

THÈSE

présentée par

Meng Xiao

pour obtenir le grade de

DOCTEUR ÈS SCIENCES DE L'UNIVERSITÉ PARIS DIDEROT

Spécialité: Particule, Noyaux, Cosmos (ED 517)

Observation d'une nouvelle particule dans la recherche du boson de Higgs se désintégrant en quatre leptons avec le détecteur ATLAS auprès du LHC

Soutenue le 24 mai 2013 devant le jury composé de:

K.A.	Assamagan	Rapporteur
P.	Bloch	Président du Jury
A.	Djouadi	
C.	Guyot	Directeur de thèse
S.	Hassani	Directeur de thèse
L.	Pontecorvo	
Y.	Sirois	Rapporteur

Thèse préparée au Service de Physiques des Particules du CEA de Saclay

THESIS

presented by

Meng Xiao

to obtain the degree of

DOCTOR OF SCIENCES OF THE PARIS DIDEROT

**Search for the Higgs boson decaying to four
leptons in the ATLAS detector at LHC
leading to the observation of a new particle
compatible with the Higgs boson.**

May 24, 2013. Committee:

K.A.	Assamagan	
P.	Bloch	
A.	Djouadi	
C.	Guyot	Thesis advisor
S.	Hassani	Thesis advisor
L.	Pontecorvo	
Y.	Sirois	

Thesis prepared at IRFU / SPP / CEA - Saclay

Abstract

The thesis is devoted to the search of the Standard Model Higgs boson in the ATLAS experiment at the Large Hadron Collider (LHC), in the decaying channel $H \rightarrow ZZ^{(*)} \rightarrow 4\ell$, where the ℓ can be electron or muon. The analysis uses 4.8 fb⁻¹ 7 TeV and 5.8 fb⁻¹ 8 TeV collision data recorded in ATLAS. The details of the analysis are presented with an emphasis on the background estimation techniques. A clear excess above the expected background is seen around 125 GeV. When the result is combined with other search channels, a Higgs-like particle of the mass ~ 126.5 GeV is observed. The updated search in the 4ℓ channel using the data corresponding to an integrated luminosity of 4.6 fb⁻¹ and 20.7 fb⁻¹ at $\sqrt{s} = 7$ TeV and 8 TeV, respectively is also presented. The fitted Higgs-like mass is measured to be $m_H = 124.3^{+0.6}_{-0.5}$ (stat) $^{+0.5}_{-0.3}$ (syst) GeV, and the signal strength (the ratio of the observed cross section to the expected SM cross section) at this mass is found to be $1.7^{+0.5}_{-0.4}$.

The thesis also includes a series of performance studies related to the muon reconstruction. The precision measurement of the wire position in MDT chambers using X-ray tomography is presented, and it is shown how it improves the muon reconstruction quality. I show that extending the use of "combined" muons to the region of $|\eta| > 2.5$ with the help of the inner detector tracklets improves the momentum resolution and the impact parameter accuracy. The muon term related to the missing energy reconstruction is also investigated, a series of optimisation on the muon term is proposed and validated in order to improve the reconstruction quality. The thesis also includes the Final State Radiation (FSR) studies in $Z \rightarrow \mu\mu$ decays. The impact of FSR on the $H \rightarrow ZZ^{(*)} \rightarrow 4\ell$ search is investigated.

Resumé

Cette thèse porte sur l’observation d’une nouvelle particule dans la recherche du boson de Higgs se désintégrant en deux bosons Z qui se désintègrent eux-mêmes en quatre leptons avec le détecteur ATLAS auprès du LHC. Les données utilisées sont celles collectées par l’expérience ATLAS durant les années 2011 et 2012 et correspondant à une luminosité de 4.8 fb^{-1} à une énergie de centre de masse de 7 TeV et 5.8 fb^{-1} à 8 TeV. Les caractéristiques de ce boson sont compatibles avec celles du boson de Higgs du Modèle Standard avec une masse de 126.5 GeV. Une étude détaillée de l’estimation des bruits de fond provenant des canaux Z+jets et $t\bar{t}$ à partir des données est présentée. L’analyse est mise à jour en utilisant toutes les données collectées en 2011 et 2012 confirmant la présence d’un boson de Higgs de masse $m_H = 124.3^{+0.6}_{-0.5} (\text{stat})^{+0.5}_{-0.3} (\text{syst}) \text{ GeV}$.

La thèse contient aussi des études de performance reliées au spectromètre à muons : La précision de la mesure de la position des fils des chambres à dérive MDT obtenue en utilisant les données du tomographe à rayons X, est exploitée pour améliorer la reconstruction des μ ; Une optimisation du terme provenant des muons dans le calcul de l’énergie transverse manquante est effectuée et est validée; Une amélioration de la reconstruction des μ dans la région vers l’avant (pseudo-rapacité $|\eta| > 2.5$) est présentée, qui utilise la combinaison des traces reconstruites dans le spectromètre avec celles formées par les coups dans les pixels. Cette combinaison améliore la résolution sur le paramètre d’impact des μ ; L’impact des émissions de photons radiatifs par les μ sur la reconstruction des bosons Z et sur l’analyse du Higgs se désintégrant en quatre leptons, est présenté.

Contents

Introduction	5
1 The Standard Model and the Higgs boson	9
1.1 The Standard Model	10
1.1.1 Quantum electrodynamics (QED)	10
1.1.2 Electroweak unification	11
1.1.3 Quantum chromodynamics (QCD)	14
1.1.4 The Higgs mechanism	14
1.1.5 Summary of the Standard Model	17
1.2 Constraints on the Higgs boson mass	19
1.2.1 Theoretical constraints	19
1.2.2 Experimental constraints	20
1.3 Higgs production at the LHC and its search modes	25
1.3.1 Higgs production at the LHC	26
1.3.2 Higgs decay modes and searches at the LHC	28
2 LHC and the ATLAS detector	33
2.1 LHC	33
2.2 The ATLAS experiment	34
2.2.1 Overview	34
2.2.2 Naming convention and coordinate system	36
2.2.3 Inner Detector	37
2.2.4 Calorimeter	40
2.2.5 Muon Spectrometer	43
2.2.6 Trigger and data acquisition	51
2.3 Object identification and reconstruction	53
2.3.1 Electron identification and reconstruction	53
2.3.2 Muon identification and reconstruction	56
3 MDT chambers wire position measurement with X-ray tomography	61
3.1 The MDT chambers	62
3.1.1 Operating principle	62
3.1.2 The drift tubes	62
3.1.3 Chamber design	63

3.2	X-ray tomography	64
3.2.1	Introduction	64
3.2.2	Working principle	65
3.2.3	X-ray tomography structure	66
3.2.4	Analysis of the scan data	67
3.2.5	Analysis results	70
3.3	Muon reconstruction and the as-built parameters	71
3.3.1	Muon trajectory reconstruction in the muon spectrometer	72
3.3.2	Wire position reconstructed with as-built parameters	74
3.3.3	Effects of the as-built wire positions on the muon reconstruction	75
3.4	Summary	77
4	Performance	85
4.1	Missing Transverse Energy (MET) Reconstruction and Optimisation	85
4.1.1	MET reconstruction and calibration	85
4.1.2	Muon term optimization	88
4.1.3	Optimization results	92
4.1.4	FSR, jet and MET	92
4.1.5	Summary	97
4.2	Pixel Tracklets Combination With StandAlone Muons	98
4.2.1	Pixel Tracklets Reconstruction and Combination with StandAlone Muons	99
4.2.2	Pixel Tracklets Combined Muons Validation	101
4.2.3	Summary	106
5	Final State Radiation (FSR) in $Z \rightarrow \mu\mu$ decays	107
5.1	Data and MC Samples	108
5.2	Event Selection	110
5.3	FSR photon candidates	111
5.4	FSR tool performance	112
5.5	FSR impact on the Z boson mass spectrum and the resolution	115
5.6	FSR impact on muon isolation	116
5.7	Summary	117
6	Search for $H \rightarrow ZZ^{(*)} \rightarrow 4\ell$ using 4.8 fb^{-1} of 7 TeV data and 5.8 fb^{-1} of 8 TeV data	119
6.1	Data and Simulation Samples	121
6.1.1	Signal	121
6.1.2	Background	122
6.2	Event Selection and Optimization	123
6.2.1	Trigger	125
6.2.2	Object selection	126
6.2.3	Quadruplet selection and Optimisation	127
6.2.4	Extra selection and Efficiency	129

6.3	Background estimation	130
6.3.1	Estimate of the $Z+\mu^+\mu^-$ background	131
6.3.2	Estimate of the $Z+ee$ background	137
6.3.3	Summary of backgrounds	146
6.4	Higgs mass resolution and Z mass constraint	146
6.5	Systematic uncertainties	148
6.6	Results of event selection	151
6.7	Exclusion limits and p -values	154
6.7.1	The CL_s method	154
6.7.2	Frequentist Limit Setting	155
6.7.3	Results	157
6.8	Summary	157
6.9	Combination with other search channels	158
7	Updated results of the new Higgs-like particle in the four lepton decay channel with the ATLAS detector	167
7.1	Event Selection	168
7.2	FSR impact on $H \rightarrow ZZ^{(*)} \rightarrow 4\ell$ analysis	169
7.3	Background Estimation	174
7.4	Results	176
7.5	4μ invariant mass error	179
7.5.1	Muon momentum resolution	181
7.5.2	Muon momentum resolution validation	184
7.5.3	Muon resolution and 4μ mass error	187
7.6	Higgs production search in VBF and VH modes and Spin-Parity measurement	188
7.6.1	Higgs production search in VBF and VH modes	188
7.6.2	Spin-Parity measurement	189
7.7	Summary	189
	Conclusion	191
	Bibliography	193
	Acknowledgements	203

Introduction

From ancient times, people realised that in the world we live in, there are so many things sharing the same characteristics. The attempt to organise the world in fundamental elements and find out the law of how they are held together led to the birth of physics. Until the 1930s, the fundamental particles are thought to be protons, electrons and photons. After quantum mechanics and special relativity had been combined to describe these particles, Max Born said that "Physics as we know it will be over in six months". However, as neutrons were discovered in 1931, followed by an explosion discoveries of new particles, physics entered the era of particle physics.

The interactions between all the particles were then categorised in four categories, the electromagnetic, the weak, the strong, and the gravitational interaction. A gauge theory that unifies all the interactions except the gravitational force was developed, and is known as the Standard Model. The model not only described the experimental measurements, but also predicted the existence of the weak interaction mediator W and Z bosons, and the top and charm quarks. The discovery of all these particles is regarded as a strong validation of the model. Furthermore, precision measurements from many experiments agree extremely well with the theoretical predictions, which makes the standard model a great success. However, of all the elements of the model, one particle was not found yet, the Higgs boson arising from a scalar field. This scalar field is essential to the model, in the sense that, only through the interaction with this field, can all the other elementary particles in the model acquire mass without breaking the beauty of the gauge symmetry.

As the probing of particle structure goes deeper, very high energy is needed, energies beyond the reach of traditional detection techniques. For this reason, large accelerators and colliders are designed to produce particle collisions at energies at the GeV and even the TeV scale. The techniques have been successful in many experiments, such as the Tevatron experiments conducted by Fermilab in the USA, which lead to the discovery of top quark. The European Organisation of Nuclear Research (CERN) on the French - Swiss border, near Geneva, designed and built the Large Hadron Collider (LHC), which is the most powerful particle accelerator to date. This collider provides proton-proton collisions to general purpose experiments destined to make discoveries, among them the long sought Higgs boson of the standard model.

The ATLAS detector installed in LHC is designed to record the particles produced in

the proton-proton collisions. Physicists reconstruct the particles according to the trails they leave in the detector, and further trace back the derived particles to the physics processes which generate the particles. The search of the Higgs boson is based on this methodology, through the predicted decay products of the Higgs boson. The $H \rightarrow ZZ^{(*)} \rightarrow 4\ell$ channel is one of the most promising channels because of its clean signature and the fine resolution of the reconstructed invariant mass. This puts a stringent requirement on the quality of the lepton reconstruction and identification.

The thesis is divided into two parts, the first being devoted to the improvement of object reconstruction, especially the muon. The second part deals with the Higgs boson search in the $H \rightarrow ZZ^{(*)} \rightarrow 4\ell$ channel.

More specifically, chapter 1 introduces the theory of the Standard Model, which includes the three interactions and the role of the Higgs boson; from the theoretical and experimental point of view, the constraints that can be put on the Higgs boson mass are listed; the Higgs production at the LHC and the various searches according to the decay modes are discussed.

The LHC machine and the ATLAS detector are introduced in chapter 2, starting with the overview and basic convention used in ATLAS, followed by the description of each sub-system. The object reconstruction and identification which is crucial for the Higgs search is also presented.

The muon reconstruction quality is important to the search, which needs both hardware precision and software optimisation. As the basic element of the precision measurement, the MDT chambers are examined with X-ray tomography to make sure the wires in the chamber are correctly placed with respect to the design. Chapter 3 introduces the structure of the MDT chambers, the techniques of the X-ray tomography, and shows how the result from the wire position measurements provided by the tomography scan are processed. The author participated in the study of the impact of the as-built detectors on the muon reconstruction. The author helped incorporating this information into the muon reconstruction software, and the improvement is shown at the end of the chapter.

In the context of software reconstruction, the author has also optimised the muon term in the missing transverse energy (MET) calculation. This work was implemented in the ATLAS software and is now used as a standard in the physics analysis. Chapter 4 introduces the MET reconstruction algorithm in ATLAS, with focus on the muon contribution. A dedicated study of the muon term optimisation is presented, with the resulting improvements shown in the context of the $H \rightarrow WW^{(*)} \rightarrow \ell\ell\nu\nu$ analysis. The effect of the final state radiation (FSR) on the MET is discussed, and a possible optimisation is proposed. For the muon reconstruction, an extension of pseudo-rapidity range of the combined muon using the pixel tracklets is performed. The reconstruction principle is introduced, and the validation of the new combined muons is achieved: lower uncertainty on track parameters, improved precision on impact parameters and momentum are demonstrated.

From the muon objects, one can reconstruct the Z boson, whose mass spectrum is important in many Standard Model processes including the $H \rightarrow ZZ^{(*)}$. The author studied

thoroughly the FSR impact in the $Z \rightarrow \mu\mu$ decay using a dedicated FSR identification tool. In chapter 5, the efficiency, purity, fake rate of the tool are investigated to optimise the FSR selection criteria. The MC modelling of the FSR is also checked and compared with data. The Z mass spectrum shift caused by the FSR is shown, and the degradation of the resolution is also evaluated. Apart from the obvious mass shift, the FSR has another effect which is to increase the muon isolation value, which is studied and presented at the end of the chapter. As a way to restore the isolation, a new way of calculating the muon isolation is proposed when the FSR is identified, and the effect is also presented.

All the performance optimisations developed by the author have been included in the ATLAS general software.

In chapter 6, the search of the Higgs boson in the $H \rightarrow ZZ^{(*)} \rightarrow 4\ell$ channel, using 4.8 fb^{-1} 7 TeV data and 5.8 fb^{-1} 8 TeV data is presented. The chapter describes the data and simulation samples used in the search, the event selection and optimisation adopted in the analysis. As in any selection, the events contain background processes which need to be estimated. The author has developed two data driven methods to estimate the background in the $\ell\ell + \mu\mu$ and $\ell\ell + ee$ final states. The first method is based on the fit of the leading di-lepton mass, which allows to extract the $t\bar{t}$ and Z+jets background simultaneously. This method is used as a baseline in the Higgs analysis. The second method estimates the $\ell\ell + ee$ background using the origin of the least energetic electron in the final state. This method is used as a cross check in the Higgs analysis. The systematic uncertainties from all sources are given, and the final result of the event selection is shown. Integrating all the information, exclusion limits are derived. Combined with the result from other search channels, a new particle compatible with the Standard Model scalar boson is declared to be found, with a mass around 126.5 GeV.

After the discovery, the ATLAS continued collecting data, and the search result using 4.6 fb^{-1} 7 TeV data and 20.7 fb^{-1} 8 TeV data is updated in chapter 7. In the updated results, the changes in the selection with respect to the previous analysis are listed. The author studied the FSR impact on the $H \rightarrow ZZ^{(*)} \rightarrow 4\ell$ search, which includes the improvement on signal resolution and mass spectrum, the potential shape change of background processes, and the check of possible FSR among the selected candidates were provided by the author. Adding FSR to the final selected events is one of the selection changes made possible by the optimisation performed by the author. The author also provided numbers for the irreducible background estimation. The final number of events in the mass region of interest is presented, and the exclusion limit is shown. For the first time, the events are categorised according to the production mechanism into ggF and VBF type, and the spin/parity of the new particle is measured. As a possible improvement for future mass measurements, the author developed a method to estimate the "per event" mass uncertainty in the 4μ channel, which is also presented in this chapter. The $H \rightarrow ZZ^{(*)} \rightarrow 4\ell$ channel alone could then reach a 6.6σ excess above the background at the mass $m_H = 124.3 \text{ GeV}$.

Chapter 1

The Standard Model and the Higgs boson

Physics is a branch of science which studies the nature of matter and energy. Integrating all known laws of matter and forces into a simple, unified theory, is the ultimate goal of physics. To date, all visible matter and force in the universe is found to be made of two kinds of particles: fermions and bosons. Fermions are building blocks of matter with spin $\frac{1}{2}$, obeying Fermi-Dirac statistics. There are 12 elementary fermion particles: 6 leptons and 6 quarks, classified into three generations with increasing masses. Within each generation, pairs of leptons (quarks) exhibit similar properties. The 12 elementary particles have each their own corresponding anti-particle with identical properties but also opposite characteristics such as electric charge. The fermions make up the matter governed by the four fundamental forces: the electromagnetic, the weak, the strong and the gravitational. Each force has one or several force carriers, called vector bosons. These vector bosons are spin-1 particles which obey Bose-Einstein statistics. The fermions interact with each other via the exchange of vector bosons.

The electromagnetic interaction is well described by the theory of quantum electrodynamics (QED), whose first formulation was written by Paul Dirac around 1930 to describe radiation and matter interaction in quantum theory. In 1960, the combination of the electromagnetic and the weak interactions by Sheldon Glashow, now known as the electroweak theory, successfully predicted the W and Z bosons, which were later discovered in 1982–1983. The theory of quantum chromodynamics (QCD), which acquired its modern form around 1973–74, describes the strong interaction between fractionally charged quarks. In 1967 Steven Weinberg and Abdus Salam incorporated the Higgs mechanism into Glashow’s electroweak theory, which resulted in a modern form of the Standard Model, which will be introduced in section 1.1. All the ingredients of the Standard Model, the electrodynamics, the electroweak theory, quantum chromodynamics and the Higgs mechanism will be described in this section. The Higgs boson is predicted by the Standard Model through the Higgs mechanism. Among all its properties, the mass is the only unknown. The constraints

on the Higgs mass from current experiments and from theory are shown in section 1.2. The production and decay modes of the Higgs boson will be presented in section 1.3.

1.1 The Standard Model

The Standard Model (SM) is a quantum field theory of the fundamental particles and the interaction among them, except the interaction via gravity. It unifies the well established electroweak theory and Quantum Chromodynamics (QCD), and describes the electromagnetic, weak and strong interactions respectively. The $SU(2)_L \otimes U(1)_Y$ gauge symmetry of the electroweak theory and the $SU(3)_C$ symmetry of QCD are well preserved when it is introduced in the SM. The missing piece in the electroweak theory is the mass term of particles, which breaks the $SU(2)$ symmetry. In the Standard Model, the problem is solved by adding a hypothetical scalar field. Through the interaction with this field, the symmetry in mass terms is preserved. As a consequence of the spontaneous electroweak symmetry breaking of the field, all particles gain mass and a new particle arises, known as the Higgs boson.

1.1.1 Quantum electrodynamics (QED)

The concept of interactions governed by gauge symmetries leads naturally to Lagrangian field theories, which connect symmetry with conservation laws. It is essential to first establish the Lagrangian density function of fermions and electromagnetic field, between which the electromagnetic interaction takes place.

Fermions Spin- $\frac{1}{2}$ free particles, known as fermions, obey the Dirac equation, which is a linear form of relativistic quantum theory

$$(i\gamma^\mu \partial_\mu - m) \psi(x) = 0, \quad (1.1)$$

where ψ is a 4-component spinor, representing the fermion field, and it becomes an operator that annihilates particles after quantisation; γ^μ ($\mu = 1, 2, 3, 4$) are Dirac matrices and m is the fermion mass.

The Lagrangian density that can yield the Dirac equation is chosen as

$$\mathcal{L}_0 = i\bar{\psi}(x)\gamma^\mu \partial_\mu \psi(x) - m\bar{\psi}(x)\psi(x). \quad (1.2)$$

Electromagnetic field The theory of electromagnetism is formulated in the Maxwell equation in terms of an antisymmetric tensor $F_{\mu\nu}$. When no external current exists, it has the form

$$\partial_\mu F^{\mu\nu} = 0. \quad (1.3)$$

$F_{\mu\nu}$ is defined as $\partial_\mu A_\nu - \partial_\nu A_\mu$, where $A_\mu = (\Phi, \mathbf{A})$ describes the field potential.

A Lorentz invariant choice for the Lagrangian density so as to derive the above equation is

$$\mathcal{L} = -\frac{1}{4}F^{\mu\nu}F_{\mu\nu}. \quad (1.4)$$

Interaction The Lagrangian of fermions in equation 1.2 is invariant under a global U(1) transformation: $\psi \rightarrow e^{-i\theta}\psi$. The word global implies that θ is independent of time and space. From this the conservation of the current is derived:

$$\partial_\mu(\bar{\psi}\gamma^\mu\psi) = 0, \quad (1.5)$$

which indicates that $\psi^\dagger\psi$ is a constant independent of time. After quantisation, this becomes an operator that counts the number of particles minus the number of anti-particles.

A stricter symmetry requirement of local U(1) is reasonable since there is no preferred inertial coordinate system for the Lagrangian. But when θ depends on x , equation 1.2 no longer satisfies the invariance under the transformation. To maintain the symmetry, an extra term that cancels out the asymmetry can be added, giving a new Lagrangian

$$\mathcal{L} = i\bar{\psi}(x)\gamma^\mu D_\mu\psi(x) - m\bar{\psi}(x)\psi(x) = \mathcal{L}_0 - qA_\mu(x)\bar{\psi}(x)\gamma^\mu\psi(x), \quad (1.6)$$

where $D_\mu = \partial_\mu + iqA_\mu$ and A_μ transforms under the law $A_\mu \rightarrow A_\mu + \frac{1}{q}\partial_\mu\theta$

Now the coupling of the electromagnetic field to the fermion spinors appear in the Lagrangian. The strength of the interaction is proportional to q , the charge of the fermion, and as a consequence of local U(1) invariance, the current $j^\mu = q\bar{\psi}\gamma^\mu\psi$ is conserved, which can be interpreted as the electric current.

With the appearance of A_μ , its corresponding kinematic term should be added to the Lagrangian. The final form of the Lagrangian is

$$\mathcal{L} = i\bar{\psi}(x)\gamma^\mu D_\mu\psi(x) - m\bar{\psi}(x)\psi(x) - \frac{1}{4}F^{\mu\nu}F_{\mu\nu}. \quad (1.7)$$

There is no mass term for the electromagnetic field, because it would break the gauge invariance.

1.1.2 Electroweak unification

Weak interactions are involved for example in the decay of muons, neutrons, charged pions and the scattering of neutrinos. As discussed above in QED, the principle of local gauge symmetry gives rise to the term of coupling. This concept can also be used for the description of the weak interactions. Weak charged current data and electromagnetic processes are invariant under weak isospin $SU(2)$ and weak hyper-charge $U(1)$ transformations [1]. This is described by the unified theory of electromagnetic and weak interactions.

To build a Lagrangian density that is invariant under SU(2) transformations, a doublet is introduced

$$\psi_{\mathbf{L}} = \begin{pmatrix} \nu_{eL} \\ e_L \end{pmatrix}, \begin{pmatrix} u_L \\ d_L \end{pmatrix} \quad (1.8)$$

where the subscript L of leptons ν_e and e , quarks u and d , stands for the left-handed part of the spinors. Similar doublets are defined for the 2^{nd} and 3^{rd} family of leptons and quarks.

Parity is not conserved in the weak interaction. Experiments show that in processes like β decay, only left-handed components of fields play a role in the weak interaction, while the right-handed fields do not. Based on this, the ψ_R is defined as a singlet, invariant under SU(2) transformation. The ν_R does not exist in the minimal version of the theory, and is not included in the discussion below. The Lagrangian of fermions takes the same form as in equation 1.2 if no gauge invariance is required. Expressed in chiral representation

$$\mathcal{L}_0 = i\psi_L^\dagger \tilde{\sigma}^\mu \partial_\mu \psi_L + i\psi_R^\dagger \sigma^\mu \partial_\mu \psi_R - m(\psi_L^\dagger \psi_R + \psi_R^\dagger \psi_L) \quad (1.9)$$

where $\sigma^\mu = (\sigma^0, \sigma^1, \sigma^2, \sigma^3)$ and $\tilde{\sigma}^\mu = (\sigma^0, -\sigma^1, -\sigma^2, -\sigma^3)$, σ^i (i=0,1,2,3) being the Pauli matrices.

The spinors change in the following way when U(1) and SU(2) local transformations are applied

$$\psi_{\mathbf{L}} \rightarrow \mathbf{e}^{-i\theta} \mathbf{U} \psi_{\mathbf{L}}, \quad \psi_{\mathbf{R}} \rightarrow \mathbf{e}^{-i\theta'} \psi_{\mathbf{R}}. \quad (1.10)$$

\mathbf{U} represents any element of SU(2), and it can be written as $\mathbf{U} = \mathbf{e}^{-i\alpha^k \sigma^k}$, the σ^k are three generators of the SU(2) group and are identical to Pauli matrices. α and θ are dependent on time and space.

It is clear that equation 1.9 is not invariant under the above transformations. In analogy with QED, a vector field W_μ^k for each generator σ^k of the SU(2) transformations and a vector field B_μ for the U(1) transformation are introduced. Let us define the covariant derivatives

$$\begin{aligned} D_\mu \psi_L &= [\partial_\mu + (ig'/2)B_\mu + (ig_2/2)\mathbf{W}_\mu] \psi_L \\ D_\mu \psi_R &= [\partial_\mu + (ig''/2)B_\mu] \psi_R \end{aligned} \quad (1.11)$$

and the transformations for B_μ and \mathbf{W}_μ

$$\begin{aligned} B_\mu &\rightarrow B_\mu + (2/g')\partial_\mu \theta \\ \mathbf{W}_\mu &= W_\mu^k \sigma^k \rightarrow \mathbf{U} \mathbf{W}_\mu \mathbf{U}^\dagger + (2i/g_2)(\partial_\mu \mathbf{U}) \mathbf{U}^\dagger. \end{aligned} \quad (1.12)$$

Replacing ∂_μ by D_μ in equation 1.9 and adding the kinematic terms due to the vector

fields, the sum of the dynamic terms in the Lagrangian is

$$\mathcal{L}_{dyn} = i\psi_L^\dagger \tilde{\sigma}^\mu D_\mu \psi_L + i\psi_R^\dagger \sigma^\mu D_\mu \psi_R - \frac{1}{4} B_{\mu\nu} B^{\mu\nu} - \sum_{i=1}^3 \frac{1}{4} W_{\mu\nu}^i W^{i\mu\nu} \quad (1.13)$$

where the field tensor $B_{\mu\nu}$ and $W_{\mu\nu}$ are defined as

$$\begin{aligned} B_{\mu\nu} &= \partial_\mu B_\nu - \partial_\nu B_\mu \\ W_{\mu\nu}^i &= \partial_\mu W_\nu^i - \partial_\nu W_\mu^i - (g_2/2) \epsilon_{ijk} W_\mu^j W_\nu^k. \end{aligned} \quad (1.14)$$

This dynamic part of the Lagrangian is invariant under $U(1) \otimes SU(2)$ local transformation. However, neither the fermion mass term nor the gauge field mass term has this property, and are therefore not added to the Lagrangian for the moment.

The interaction between fermions and gauge bosons are not straightforward in the present form of Lagrangian. But by defining

$$\begin{aligned} W_\mu^+ &= (W_\mu^1 - iW_\mu^2)/\sqrt{2} \\ W_\mu^- &= (W_\mu^1 + iW_\mu^2)/\sqrt{2} \\ \begin{pmatrix} W_\mu^3 \\ B_\mu \end{pmatrix} &= \begin{pmatrix} \cos \theta_W & \sin \theta_W \\ -\sin \theta_W & \cos \theta_W \end{pmatrix} \begin{pmatrix} Z_\mu \\ A_\mu \end{pmatrix}, \end{aligned} \quad (1.15)$$

where θ_W is the Weingberg angle, the interaction terms appear in a much clearer way. Taking electron terms as example, the term

$$\mathcal{L}_{eW} = -(g_2/\sqrt{2}) \nu_{eL}^\dagger \tilde{\sigma}^\mu e_L W_\mu^+ - (g_2/\sqrt{2}) e_L^\dagger \tilde{\sigma}^\mu \nu_{eL} W_\mu^- \quad (1.16)$$

describes the coupling of the electron and electron neutrino to the W^+ and W^- gauge fields. Terms related to A_μ imply the charge of fermions. For leptons, the fact that neutrinos are electrically neutral and electrons carry a charge -e, yields

$$g' \cos \theta_w = -g_2 \sin \theta_w = -e. \quad (1.17)$$

With the above property, another term in the Lagrangian

$$\mathcal{L}_{eZ} = -\nu_{eL}^\dagger \tilde{\sigma}^\mu \nu_{eL} \left(\frac{e}{\sin(2\theta_W)} \right) Z_\mu - e_L^\dagger \tilde{\sigma}^\mu e_L \left(\frac{e \cos(2\theta_W)}{\sin(2\theta_W)} \right) Z_\mu - e_R^\dagger \tilde{\sigma}^\mu e_R (e \tan(\theta_W)) Z_\mu \quad (1.18)$$

shows that both left-handed and right-handed leptons as well as neutrinos couple to the Z field, with strength proportional to the electric charge.

As equation 1.14 indicates, $\mathbf{W}_{\mu\nu}$ is the tensor of non-abelian fields. Therefore the kinematic terms of vector fields, $-\frac{1}{4} B_{\mu\nu} B^{\mu\nu} - \sum_{i=1}^3 \frac{1}{4} W_{\mu\nu}^i W^{i\mu\nu}$, result in the self-interactions of gauge bosons.

1.1.3 Quantum chromodynamics (QCD)

QCD is a theory that describes the strong interactions. As in the electroweak theory, it involves the application of gauge theory. Since the elementary particles that are subjected to the strong interaction, quarks, carry a quantum number "colour" that has 3 states, one can postulate that the theory is invariant under $SU(3)$ transformation.

For each flavour of quark, the three colour states can be put into a triplet, e.g. for the u-quark.

$$\begin{pmatrix} u_r \\ u_g \\ u_b \end{pmatrix}, \quad (1.19)$$

where the subscripts r,g,b stand for the colour state arbitrarily named red, green and blue.

An $SU(3)$ group has eight generators. Similar to what has been done in electroweak theory, a gauge field \mathbf{G}_μ , which can be expressed in terms of eight Hermitian matrices is introduced. The Lagrangian density is taken to be the sum of the standard Dirac form for quarks and the vector field form for the added gauge field:

$$\mathcal{L} = \sum_{f=1}^6 [i\bar{\mathbf{q}}_f \gamma^\mu (\partial_\mu + ig\mathbf{G}_\mu) \mathbf{q}_f] - \sum_{a=1}^8 \frac{1}{4} G^{a\mu\nu} G_{\mu\nu}^a. \quad (1.20)$$

The gauge bosons corresponding to the gauge fields are called gluons. There is no mass term of the gauge field for the same reason as in the electroweak theory, namely that it violates the symmetry.

As exhibited in the field tensor $G_{\mu\nu}^a = \partial_\mu G_\nu^a - \partial_\nu G_\mu^a - gf_{abc}G_\mu^b G_\nu^c$, the non-Abelian nature of the gluon fields gives rise to the self-interactions, analog to what is seen in electroweak theory.

1.1.4 The Higgs mechanism

Both electroweak and QCD theories work quite well incorporating the gauge symmetry. Nevertheless, the massless form of the Lagrangian is in contradiction with experimental observations that fermions and gauge bosons like Z and W do have mass. The Higgs mechanism solves the problem by bringing back the mass terms in an $SU(2)$ invariant form, and by giving the mass to fermions and bosons through spontaneous symmetry breaking. To achieve this, a new doublet of a complex scalar field is defined

$$\Phi = \begin{pmatrix} \Phi^+ \\ \Phi^0 \end{pmatrix} = \begin{pmatrix} \phi_1 + i\phi_2 \\ \phi_3 + i\phi_4 \end{pmatrix} \quad (1.21)$$

Consider this field as part of the fields in the existing electroweak local gauge theory

of $U(1) \otimes SU(2)$, simply by adding the Lagrangian of scalar fields

$$\mathcal{L} = D_\mu \Phi D^\mu \Phi - V(\Phi). \quad (1.22)$$

D_μ has the same format as in equation 1.11 of the electroweak theory, since the same gauge symmetry is required. The potential term, which satisfies the symmetry can be chosen as

$$V(\Phi) = \mu^2 \Phi^\dagger \Phi + \lambda \left(\Phi^\dagger \Phi \right)^2 = \mu^2 |\Phi|^2 + \lambda |\Phi|^4. \quad (1.23)$$

In this expression, the signs of the parameters μ^2 and λ are yet to be determined. For physics reasons, a minimum of the potential should be guaranteed so that the corresponding field has a ground state. Therefore, λ should always be positive. As for μ^2 , taking it to be positive, and expanding the potential in terms of Φ_i , one would get

$$V(\Phi) = \sum_{i=1}^4 \mu^2 |\phi_i|^2 + \lambda |\phi_i|^4, \quad (1.24)$$

which corresponds to four independent scalar fields, with the same mass μ , each interacting with the massless gauge bosons. Such a non-interacting form is of no interest, and furthermore, the minimum of the potential in this case corresponds to $\phi_i = 0$, which is the vacuum state. While in the context of $\mu^2 < 0$, the potential has a non-trivial minimum, as shown in figure 1.1. The ground state of Φ is around a circle of $|\Phi|^2 = -\frac{\mu^2}{2\lambda} = \frac{v^2}{2}$, and now the vacuum has a non-zero expectation value. As the Lagrangian is invariant under local $SU(2)$ transformation and knowing that there are three free parameters in the $SU(2)$ operation, it is possible that there exists a point in ground states, where $\phi_{1,2,4} = 0$, thus

$$\Phi = \begin{pmatrix} 0 \\ v \end{pmatrix} \quad (1.25)$$

Since there is a preferred direction of the ground state, the $SU(2)$ symmetry is broken, this behavior is called spontaneous symmetry breaking.

Expanding Φ about this specific ground state

$$\Phi = \begin{pmatrix} 0 \\ v + \frac{1}{\sqrt{2}} h(x) \end{pmatrix}, \quad (1.26)$$

the interactions between Φ and gauge bosons will reveal the mass in the following way.

Adding equation 1.22 to the electroweak Lagrangian, and expanding the Lagrangian

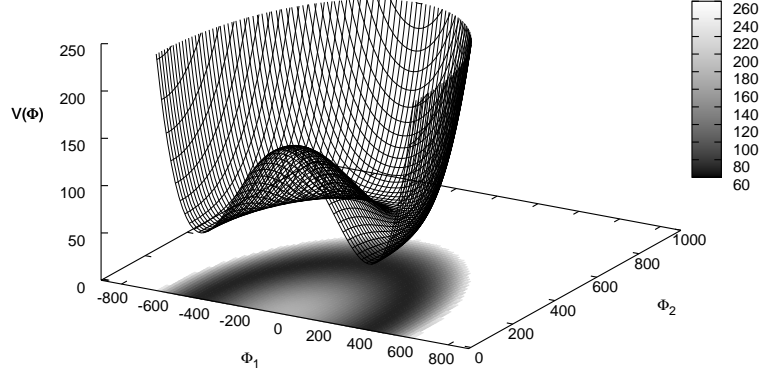


Figure 1.1: Illustration of the Higgs potential for a scalar field with $\mu^2 < 0$.

fully, one gets the following terms:

$$\begin{aligned}
 \mathcal{L}_1 = & \frac{1}{2} \partial_\mu h \partial^\mu h + 2\mu^2 h^2 \\
 & - \frac{1}{4} Z_{\mu\nu} Z^{\mu\nu} + \frac{1}{4} v^2 (g'^2 + g_2^2) Z_\mu Z^\mu \\
 & - \frac{1}{4} A_{\mu\nu} A^{\mu\nu} \\
 & - \frac{1}{2} [(D_\mu W_\nu^+)^* - (D_\nu W_\mu^+)^*] [(D^\mu W^{\nu+})^* - (D^\nu W^{\mu+})^*] + \frac{1}{2} g_2^2 v^2 W_\mu^- W^{+\mu}
 \end{aligned} \tag{1.27}$$

where $D_\mu W_\nu^+ = (\partial_\mu + ig_2 \sin\theta_w A_\mu) W_\nu^+$. This part of the Lagrangian can be identified as a compound of multiple gauge fields: a neutral scalar boson field h , of the Higgs boson particle, with mass $m_H = \sqrt{-2\mu^2}$; a neutral vector boson field of gauge boson Z_μ , acquires its mass through its interaction with the Higgs boson; And 2 massive charged vector boson fields W_μ^+ and W_μ^- , obtain their masses in the same way as the Z boson, interacting with a massless electromagnetic field A_μ mediated by photons.

The masses of the gauge bosons are

$$\begin{aligned}
 M_Z &= \frac{v}{2} \sqrt{(g'^2 + g_2^2)} \\
 M_W &= \frac{v}{2} g_2 = M_Z \cos\theta_W \\
 M_\gamma &= 0
 \end{aligned} \tag{1.28}$$

The remaining interaction terms

$$\mathcal{L}_{int} = \left(\frac{1}{4} h^2 + \frac{1}{\sqrt{2}} h v \right) (g_2^2 W_\mu^- W^{+\mu} + \frac{1}{2} (g'^2 + g_2^2) Z_{\mu\nu} Z^{\mu\nu}) \tag{1.29}$$

shows that the coupling between the Higgs and the weak bosons are proportional to their masses.

The fermion mass terms, which are missing in the electroweak theory also can be added now through the interaction between the scalar field Φ and fermions. The interaction is called Yukawa interaction. The Lagrangian can be written as

$$\mathcal{L}_{\text{Yukawa}} = c \left[\Psi_L^\dagger \Phi \Psi_R + \Psi_R^\dagger (\Phi^\dagger \Psi_R) \right]. \quad (1.30)$$

The form is invariant under local $SU(2)$ transformation, and after symmetry breaking, it becomes

$$\mathcal{L}_{\text{Yukawa}} = -cv(\Psi_L^\dagger \Psi_R + \Psi_R^\dagger \Psi_R) - \frac{ch}{\sqrt{2}}(\Psi_L^\dagger \Psi_R + \Psi_R^\dagger \Psi_R). \quad (1.31)$$

Compared with the nominal mass term of fermions eq. 1.9, the mass is identified as cv , where the different c parameters represent each generation. As seen from the Lagrangian, the coupling between the fermions and the Higgs field, is proportional to the fermion mass.

1.1.5 Summary of the Standard Model

The gauge symmetry and interactions The Standard Model, as discussed in the previous sections, combines the electromagnetic, weak and strong interactions by a gauge theory. Nevertheless, the gauge groups are not chosen due to purely theoretical reasons, but as the result of matching to the experimental observations. The gauge symmetry $SU(3)_C \otimes SU(2)_L \otimes U(1)_Y$ implies that all the interactions are involved.

$SU(3)_C$ is the group of strong interactions. The subscript C refers to the three colours of quarks. It has eight generators, thus corresponds to eight gauge bosons, which convey the interaction: the gluons. The strong interaction is between quarks, and due to its non-Abelian character, gluons also self interact through the strong interaction. The coupling strength of the eight gauge bosons are unique, and denoted as g .

The $SU(2)_L \otimes U(1)_Y$ represents the symmetry of the electroweak interactions. The three generators of the $SU(2)_L$ group imply the three gauge bosons mediating the weak interaction, which are $W_\mu^{1,2,3}$, with a unique strength g_2 , and the subscript L represent the left-handed fields related isospin. The generator of $U(1)_Y$ corresponds to another gauge boson B_μ , with coupling g' ; this group is not identical to the one of electromagnetic interaction: as the subscript Y indicates it as the hypercharge, which is a linear combination of electric charge and isospin. Though the QED $U(1)$ symmetry is not identical to $U(1)_Y$, it reappears after the spontaneous symmetry breaking of $SU(2)_L \otimes U(1)_Y$. None of the four mediators in the electroweak theory mentioned above are physical particles, but linear combination of them represent four new gauge bosons A_μ, Z_μ, W^\pm . A_μ corresponds to the gauge boson of electromagnetic interaction, the photon, and the other three are the mediators of weak interaction.

The masses of particles The masses of gauge bosons and fermions are generated through the interaction with the scalar Higgs field. Table 1.1 and 1.2 show the masses of all the elementary particles. One thing to notice is that the eigenstates of quark masses are not identical to the eigenstates of the weak interaction. This introduces a unitary matrix transformation between the two, called CKM matrix, named after Cabbibo, Kobayashi and Maskawa. It consists of a rotation matrix with three free parameters, which mix the different flavours of quarks, and an extra phase term with one free parameter to allow for CP violation, which is observed in the weak interaction of quarks.

Table 1.1: Properties of the vector bosons of the Standard Model. The experimental values for the masses of the W and Z bosons were extracted from ref. [2].

Boson	Mass (GeV)	Electric charge	Associated interaction
γ	0	0	electromagnetic
Z	91.1876 ± 0.0021	0	weak
W^\pm	80.385 ± 0.015	± 1	
g	0	0	strong

Table 1.2: Properties of the quarks and leptons of the Standard Model. Only upper limits are given for the masses of the neutrinos, although there is strong experimental evidence that they are massive [3].

Quark	Mass	Electric charge
up (u)	1.8 to 3.0 MeV	+2/3
down (d)	4.5 to 5.5 MeV	-1/3
charm (c)	1.275 ± 0.025 GeV	+2/3
strange (s)	95 ± 5 MeV	-1/3
top (t)	$173.5 \pm 0.6 \pm 0.8$ GeV	+2/3
bottom (b)	$4.20^{+0.17}_{-0.07}$ GeV	-1/3

Lepton	Mass	Electric charge
electron (e)	0.511 MeV	-1
e-neutrino (ν_e)	< 0.22 KeV	0
muon (μ)	105.7 MeV	-1
μ -neutrino (ν_μ)	< 0.19 MeV	0
tau (τ)	1777 MeV	-1
τ -neutrino (ν_τ)	< 18.2 MeV	0

The free parameters in the Standard Model In the Standard Model, there are 18 free parameters.

- The 9 fermion masses, 3 for leptons, and 6 for quarks,
- The 4 parameters of the CKM matrix, with 3 rotation parameters and 1 phase parameter.
- The 3 coupling constants of interactions, which are g' and g_2 from the electroweak interaction, and g from the strong interaction.

- The 2 parameters of the scalar Higgs field, λ , the Higgs self-interacting coefficient and μ , the parameter related to Higgs mass.

The fermion masses and CKM parameters are measured from experiments, the remaining 5 parameters, can be combined and rewritten as 5 parameters that are measurable:

- the electromagnetic coupling constant $\alpha = \frac{g_2^2 g'^2}{4\pi(g'^2 + g_2^2)}$,
- the strong coupling constant $\alpha_s = \frac{g^2}{4\pi}$,
- the weak coupling constant $G_F = \frac{\mu^2}{\sqrt{2}\lambda}$,
- the Z boson mass $m_Z = \frac{1}{2} \sqrt{\frac{-\mu^2(g'^2 + g_2^2)}{\lambda}}$,
- the Higgs mass $m_H = \sqrt{2}\mu$.

Experimentally, 4 out of the 5 parameters listed above have been precisely measured, leaving one parameter unknown: the Higgs boson mass. The constraints on the Higgs boson mass will be discussed in the next section, from both theoretical and experimental points of view.

1.2 Constraints on the Higgs boson mass

As mentioned in section 1.1, the Higgs mass is the only unknown free parameter in the Standard Model. Theoretical calculations of the perturbation theory have put some constraints on it, and experimental measurements, either through direct searches or through indirect ways, were able to set limits on the possible mass range.

1.2.1 Theoretical constraints

Theoretical constraints on the Higgs boson mass can be set, under the assumption that the perturbation theory is no longer valid and that the Standard Model breaks down at a certain energy. This includes the constraint from perturbative unitarity of the Higgs self-coupling, the unitarity in longitudinal scattering amplitudes and the stability of the electroweak vacuum.

Perturbative unitarity At the tree-level perturbation calculation, a $2 \rightarrow 2$ process cross section mathematically should not exceed an upper bound that is proportional to the inverse of the square of the energy in the centre of mass frame, s^{-1} ; this is called unitarity. However, in the case of 2 longitudinally polarised vector bosons scattering, the cross section will increase with the momentum of the bosons, which implies that as the boson's momentum rises, the cross section will eventually reach the boundary thus causing violation of the unitarity. The Higgs boson participates in these interactions through

its coupling to the gauge bosons, pushes the violation to a much higher energy, yet the violation exists unless a limit is set on parameters that can determine the cross section. The Higgs mass is one of these parameters.

At the high energy limit, $s \gg m_H^2$, the cross section for the W^+W^- scattering is proportional to m_H^2 , therefore, to maintain the unitarity, the Higgs mass should be less than 870 GeV. Similar calculation for all possible gauge bosons scattering leads ultimately $m_H \leq 710$ GeV. This means that unitarity will be violated unless new physics appears and restores unitarity when the Higgs mass exceeds ~ 700 GeV [4].

Triviality bound As the Lagrangian of the Standard Model shows in Equation 1.23, the scalar sector has a ϕ^4 term. Under the assumption of a ϕ^4 theory, the quartic coupling λ varies with the energy scale Q . If we consider only the Higgs boson contribution to the one-loop radiative corrections to the quartic coupling, and if the energy is much smaller than the electroweak breaking scale, the quartic coupling vanishes and the theory becomes trivial. On the other hand, if the energy is much higher than the weak scale, i.e. $Q^2 \gg v^2$, λ monotonically increases with Q . In this circumstance, a Landau pole is defined for the energy scale that causes an infinite λ . Perturbative theory characterised by a finite λ can not be achieved with the existence of the Landau pole. However, one can claim that the theory is still perturbative in a certain domain of energy that excludes the Landau pole. Therefore, the cut-off energy Λ_C , beyond which the perturbation is no long valid, should be smaller than the Landau pole, i.e., $Q > \Lambda_C$. The Higgs mass being $\sim \frac{1}{\log(Q/v)}$, there will be an upper bound to it if there is a cut-off energy. Simulations of gauge theories on the lattice where non-perturbative effects are properly taken into account yield the rigorous bound $m_H < 640$ GeV [4].

Stability bound The triviality considers large λ , where the Higgs boson field dominates the coupling, while in the scenario of low λ , the coupling has non-negligible contributions from fermions and gauge bosons. If λ is too small, the contribution from top quark becomes important and drives λ to negative values. As mentioned in section 1.1.4, $\lambda > 0$ guarantees the minimum of potential. Now without the minimum, the vacuum is no longer stable because it tends to fall into a lower potential. The stability argument states that, in order to keep $\lambda > 0$, the Higgs boson mass should have a lower bound. Depending on the cut-off value of the energy scale, constraints on the Higgs mass vary. When $\Lambda_C \sim 10^3$ GeV, $m_H \geq 70$ GeV, and at much larger scale, $\Lambda_C \sim 10^{16}$ GeV, $m_H \geq 130$ GeV [4].

To summarise, the theoretical limits of the Higgs mass as a function of the cut-off energy is shown in figure 1.2.

1.2.2 Experimental constraints

The results of direct Higgs searches from experiment at LEP and at the Tevatron will be introduced in this section. Electroweak measurements, which reach a very high precision

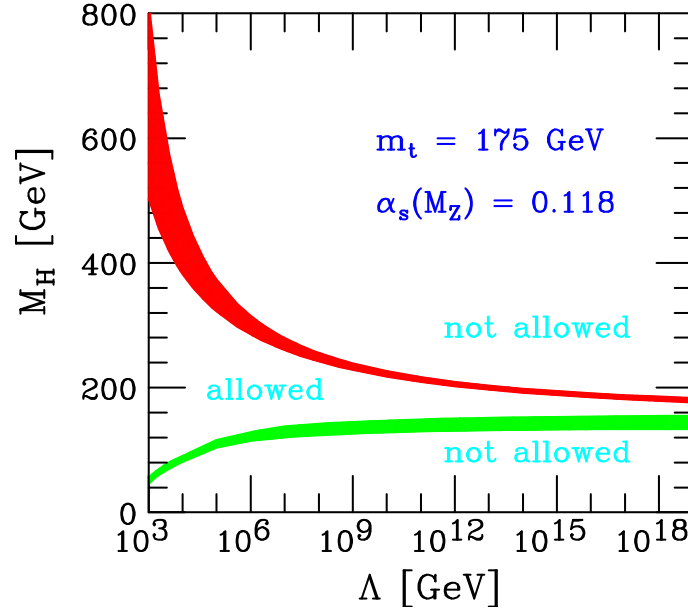


Figure 1.2: Theoretical limits on the Higgs boson mass from the triviality (upper bound) and vacuum stability arguments (lower bound), as a function of the cut-off Λ . Extracted from ref. [4].

also help constrain the Higgs mass; they will be discussed in this section.

Direct search

LEP experiments The Large Electron-Positron Collider (LEP) built at CERN, started operation in 1989 to search for the Higgs boson. By colliding accelerated electrons and positrons, it probes the possible Higgs production through the process $e^+e^- \rightarrow Z \rightarrow HZ^*$ in phase 1, and $e^+e^- \rightarrow Z^* \rightarrow HZ$ in phase 2. The corresponding Feynman diagrams are shown in fig 1.3

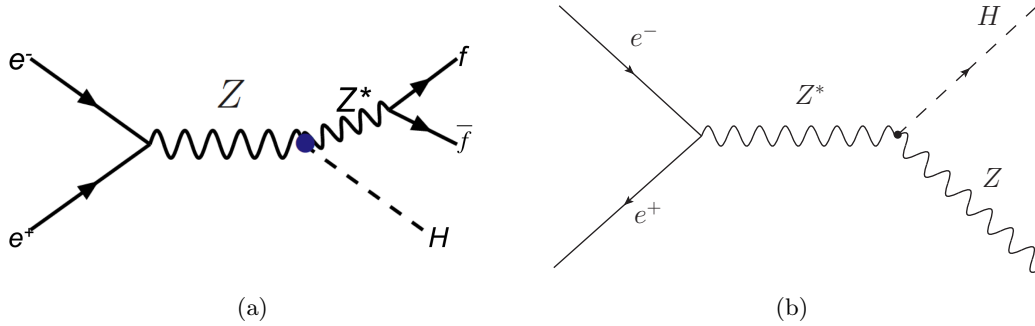


Figure 1.3: Feynman diagram of the dominant production mechanism of the Higgs boson at a) LEP1 b) LEP2.

The first phase (LEP1) produces electrons and positrons at the centre-of-mass (c.m.)

energy of the Z resonance. This detection is based on the fact that the invariant mass of the system recoiling against the Z^* decaying product, is the Higgs mass. Especially in the case of Z^* decaying to leptons, with a good knowledge of the lepton energies, excellent resolution on the Higgs boson mass can be achieved. At the energy scale of the search, the Higgs mainly decays to $b\bar{b}$, with few percent probability of decaying to $\tau\bar{\tau}$. The decay modes of the Z boson, ordered by descending branching ratio, are hadronic, invisible and leptonic. When choosing the most promising decay topology, we eliminate the $(Z \rightarrow b\bar{b})(H \rightarrow b\bar{b})$ combination because it suffers from a large $e^+e^- \rightarrow \text{hadron}$ background; any combination, which includes the Higgs boson decaying to $\tau\bar{\tau}$ is eliminated too considering the low branching ratio. Therefore, only 2 topologies are considered in LEP1: $(Z \rightarrow \nu\bar{\nu})(H \rightarrow b\bar{b})$ and $(Z \rightarrow \ell^+\ell^-)(H \rightarrow b\bar{b})$. The 2 channels exclude the Higgs in the mass range $m_H < 65.2$ at 95% confidence level [5].

In phase 2 (LEP2), the c.m.energy was raised to 209 GeV, which enables the production of an on-shell Z and a Higgs. With on-shell Z , a constraint on the invariant mass can be applied to the decay products, therefore all decay modes of Z can be considered for the search. Because of the large branching ratio of the Z boson hadronic decay, its association with Higgs decaying to $\tau\bar{\tau}$ mode provides a feasible channel of search. In summary, there are 4 topologies, the two of LEP1, and additionally, $(H \rightarrow \tau\bar{\tau})(Z \rightarrow b\bar{b})$ and $(H \rightarrow b\bar{b})(Z \rightarrow \tau\bar{\tau})$ in LEP2. The final result of LEP combining LEP1 and LEP2 is that, there is no SM Higgs of $m_H < 114.4$ GeV at the 95% confidence level while the expected limit is $m_H < 115.3$, as shown in fig 1.4. The difference of the two limits comes from an excess of observed events near 116 GeV, with a significance of 1.7σ , which is not sufficient to declare an observation.

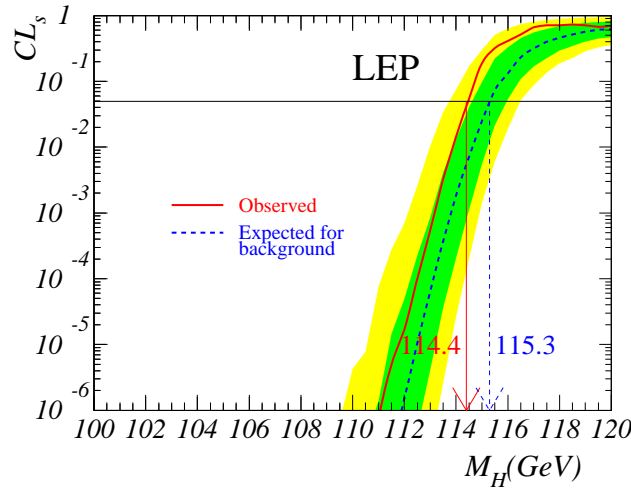


Figure 1.4: Confidence level of signal plus background hypothesis on the Standard Model Higgs boson searches at LEP. Masses below 114.4 GeV, defined by the intersection of the horizontal line at $CL_s = 0.05$ with the observed curve are excluded at 95% CL. Extracted from ref. [5].

Tevatron experiment The Tevatron experiment at Fermilab analyses $p\bar{p}$ collisions at the c.m. energy of 1.96 TeV from 2011. They search for the Higgs boson in the mass range of 100–200 GeV. The highest rate production mechanism of Higgs boson at Tevatron is gluon-gluon fusion ($gg \rightarrow H$), followed by the association production with a vector boson, Z or W through quark-antiquark annihilation, and vector boson fusion, which are shown in figure 1.10. The Higgs subsequently decays to $b\bar{b}$, WW or $\gamma\gamma$. As will be discussed in section 1.3, in the mass region below 125 GeV, the Higgs mainly decays to $b\bar{b}$, whereas for $m_H > 125$ GeV, the dominant decaying mode is WW . The Tevatron ceased its operation in 2011. The exclusion range is $156 < m_H < 177$ GeV at that time [6]. In July 2012, new results were published by including more channels with luminosities ranging from 5.4 to 10 fb^{-1} , and further optimized analysis from the two collaborations D0 and CDF. By combining all the channels, it exclude 2 regions: $100 < m_H < 103$ GeV and $147 < m_H < 180$ GeV at 95% confidence level, as shown in figure 1.5. An excess of data events over the background estimation is seen in the range $115 < m_H < 140$ GeV, the maximum local significance being 3.0σ at $m_H = 120$ GeV, as illustrated in figure 1.6, which reduces to 2.5σ after taking into account the look elsewhere effect. The largest contribution comes from $H \rightarrow b\bar{b}$, where a global 2.9σ significance is seen at $m_H = 135$ GeV.

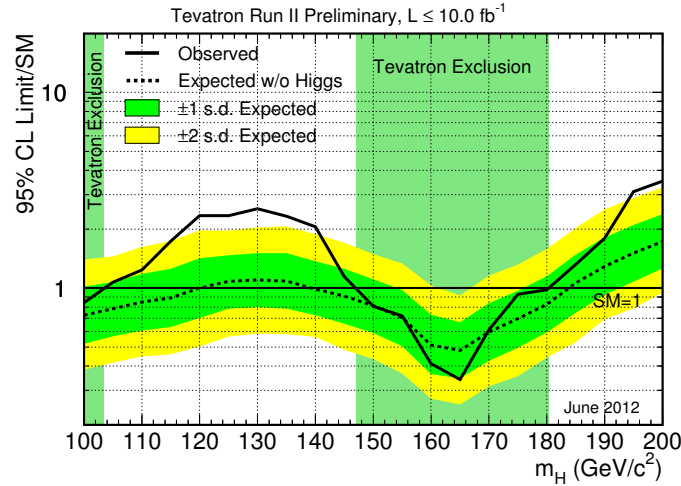


Figure 1.5: Observed and expected (median, for the background-only hypothesis) 95% C.L. upper limits on the ratios to the SM cross section, as functions of the Higgs boson mass for the combined CDF and D0 analyses. The limits are expressed as a multiple of the SM prediction for test masses (every 5 GeV) for which both experiments have performed dedicated searches in different channels. The points are joined by straight lines for better readability. The bands indicate the 68% and 95% probability regions where the limits can fluctuate, in the absence of signal. The limits displayed in this figure are obtained with the Bayesian calculation [7].

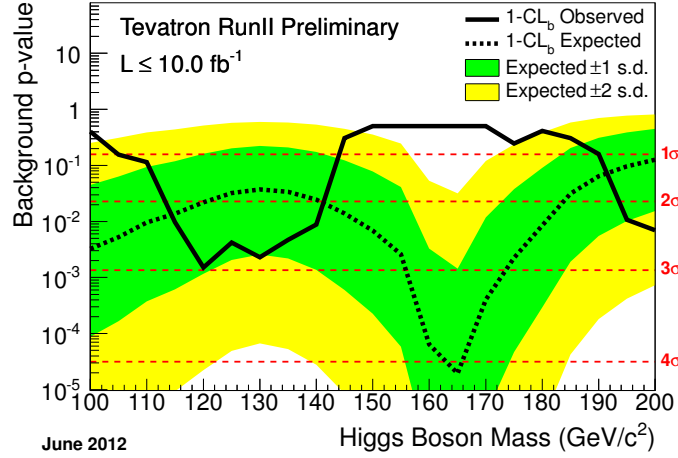


Figure 1.6: The background p-values $1-CL_b$ as a function of the Higgs boson mass (in steps of 5 GeV), for the combination of the CDF and D0 analyses. The green and yellow bands correspond respectively to the regions enclosing 1 standard deviation and 2 standard deviation fluctuations around the median prediction in the signal plus background hypothesis at each value of m_H [7].

Indirect constraints from high precision data

The existence of the Higgs boson would contribute to the radiative correction of electroweak observables, which can be measured with high precision. This produces an indirect constraint to the Higgs mass. These indirect constraints were first derived at LEP by fitting all the precision measurement data as a function of the Higgs mass. As data accumulated in Tevatron and SLC experiments, the LEP electroweak working group (EWWG) proceeded with regular updates of the fit results. The latest result published by LEP combining the Tevatron top mass measurement in July 2011 and W mass measurement in March 2012, shows that the Higgs mass should be in the range $m_H = 94^{+29}_{-24}$ GeV. The error is calculated by deviating 1σ from the lowest χ^2 fit value, as the distribution of fit $\Delta\chi^2$ shows in figure 1.7. The fit also excludes Higgs $m_H > 152$ GeV at 95% confidence level.

A similar constraint was obtained by the GFitter group [9], who provides a global fit of electroweak parameters from precision data as well as Higgs direct search. The latest result of GFitter with combination of LEP, Tevatron, SLC, and BaBar was published in September 2011, which uses the experiment data up to July 2011 (After that, GFitter still regularly updated their results, but with integration of result from LHC, therefore those results will not be quoted here). The fit yields the Higgs boson mass of

$$m_H = 95^{+30}_{-24} \text{ GeV} \quad (1.32)$$

when combining precision measurements, and the upper limit is $m_H < 166$ GeV at 95%

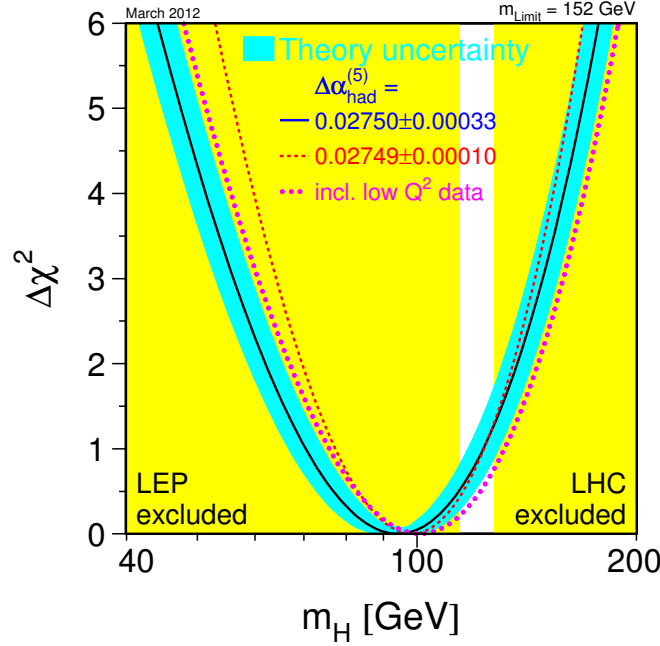


Figure 1.7: The $\Delta\chi^2$ of the fit to the electroweak precision data as a function of m_H . The solid line results from including all data and the blue band is the estimated theoretical error from unknown higher-order corrections [8].

confidence level. When including results from direct Higgs search results, the fit yields

$$m_H = 125^{+8}_{-10} \text{ GeV} \quad (1.33)$$

and the limit is $m_H < 154 \text{ GeV}$. Figure 1.8 shows the $\Delta\chi^2$ as a function of the Higgs mass when only precision measurements are used and when Higgs boson search results are included. The fitted electroweak parameters have good compatibility with the measured ones, as shown in figure 1.9 .

1.3 Higgs production at the LHC and its search modes

The LHC was designed to discover or exclude the Higgs in the entire mass range. The collision of pp with c.m energy 7 TeV in 2011 and 8 TeV in 2012 allows detection of the Higgs bosons. A prediction of Higgs production and its decay branching ratios over the mass range is needed first. The theorists documented thoroughly their results in different energy scenarios in Ref. [10] [11], and updates are available in Ref. [12]. This section is based on the above sources.

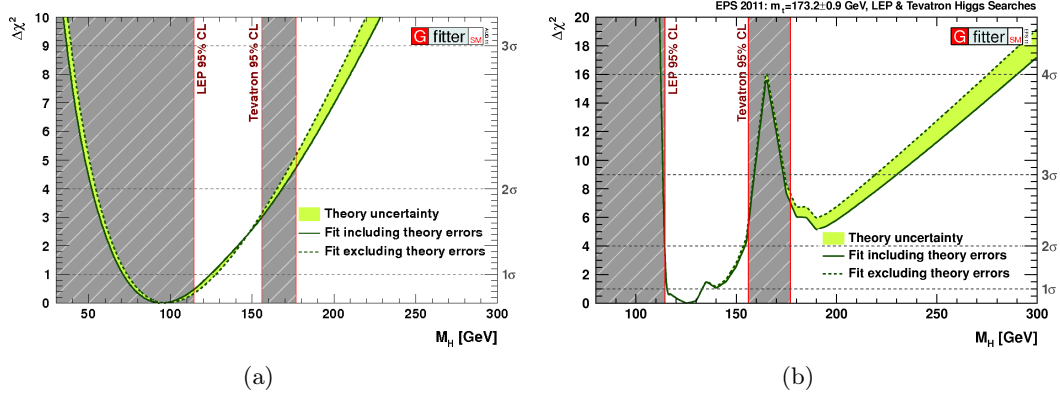


Figure 1.8: $\Delta\chi^2$ as a function of the Higgs mass for the fit of a) precision measurement only b) results including direct Higgs search. The solid (dashed) lines give the results when including (ignoring) theoretical errors. The minimum $\Delta\chi^2$ of the fit including theoretical errors is used for both curves to obtain the offset-corrected $\Delta\chi^2$ [9].

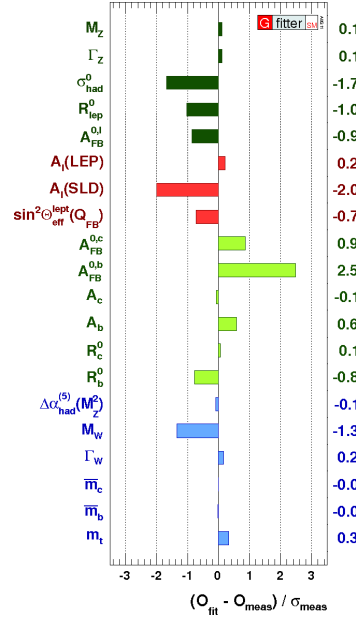


Figure 1.9: Comparing fit results with direct measurements, pull values for the fit [9].

1.3.1 Higgs production at the LHC

In a hadron collider like LHC, there are mainly four mechanisms to produce a Higgs boson. The relevant Feynman diagrams are shown in fig 1.10.

Gluon-gluon fusion (ggF) The fusion of gluons through a heavy-quark loop, and produces a Higgs boson through its coupling to the quarks. It is the dominant mechanism of the LHC in the entire mass range. This production is controlled by the strong coupling, and because the Higgs coupling is proportional to the quark mass, the top quark

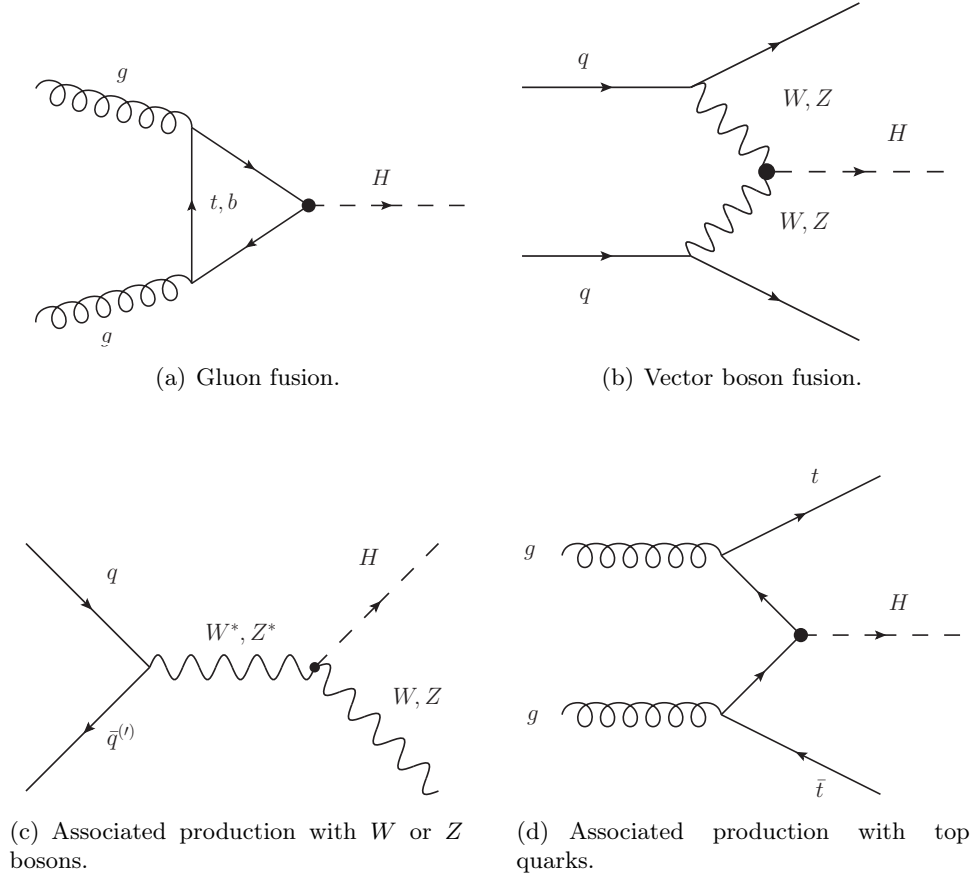


Figure 1.10: Main production modes of the Higgs boson at hadron colliders.

loop is the most probable, followed by b-quark. As to the cross section of this process, the leading order (LO) calculation is proportional to α_s^2 , which implies a sizeable QCD radiative correction at higher level. In the next to leading order (NLO) the cross section is increased by 80-100% at the LHC, with another increase of 25% at next-to-next-leading-order (NNLO). An additional 7-9% is added when soft-gluon contribution is included at next-to-next-leading logarithm (NNLL) for 7 TeV collision. Extra electroweak corrections, which depend on the Higgs mass are at the percentage level.

The final computation of the gluon-gluon fusion cross-section, uses the NNLO parton distribution functions (PDFs), with NNLL QCD corrections and NLO electroweak correction. The central value is taken from the mean of 2 independent groups of theorists, Anastasiou/Boughezal/Petriello/Stoeckli (ABPS) and de Florian/Grazzini (dFB), whose results are in good agreement with each other [10]. The difference of the central values between the two groups is +3% to +1% in the range $115 < m_H < 300$ GeV at 7 TeV. The most important uncertainties come from the high-order uncalculated QCD radiative corrections, and the uncertainty from the PDFs, which are 9-10% and 7-8%, respectively in the Higgs boson mass range 100 – 300 GeV, at 7 TeV. The final uncertainty is treated

by combining the two sources linearly, which gives $\sim 16\%$.

Vector boson fusion (VBF) In the VBF mechanism, the Higgs boson is produced through the coupling to two weak bosons radiated from the initial quarks, in association with two hard jets, with a back-to-back topology. At the LHC, there are actually three ways of producing H+2 jets: the t, u and s channels [10]. The t and u channels, have a strong tendency to produce forward-backward directed jets, while the s channel does not have the same property. In the search of VBF H+2 jet type events, there exists a large background from the topology of ggF produced Higgs together with 2 jets. To suppress the background, a cut on the jet rapidity gap is always applied. The cut will also exclude s-channel production in vector boson fusion. Thus the VBF type only refers to the t and u channels. The cross section calculation of the VBF mechanism will also eliminate this type. The VBF mode has the second largest rate to produce the Higgs. The QCD correction at NLO increases the cross section from LO by 5–10%. The NNLO correction in QCD via the structure-function approach, combined with the NLO EW correction, gives an uncertainty around 1-2%. The uncertainty from PDFs is at the same level.

Associated production with W or Z bosons (WH/ZH) The associated production, also known as Higgs-strahlung process, produces the Higgs boson through its coupling to W or Z bosons, which are produced by coupling to a quark-antiquark pair. This channel is important, in spite of its small cross section, in the sense that it offers a clean way to detect the $H \rightarrow b\bar{b}$ decay. Extracting the signal of ggF $H \rightarrow b\bar{b}$ from the QCD background is very challenging, but it becomes easier in the WH/ZH channel, with the signature of accompanying leptons from Z or W. The cross section is given at NNLO in QCD and NLO EW radiative correction, with 0.5% uncertainty from QCD scale and 4% from PDF in the WH channel. The contribution of the gg channel to ZH production increases the overall uncertainty to 0.5–1.5%.

Associated production with $t\bar{t}$ pairs (ttH) The Higgs can be radiated off top quarks in the process $q\bar{q}/g\bar{g} \rightarrow Ht\bar{t}$. It provides the possibility of measuring the top-Higgs Yukawa coupling. The cross section of this process is given at NLO, QCD uncertainty amounts to 5–10% while the PDF uncertainty ranges from 3 to 5%.

Fig 1.11 shows, at 7 TeV the overall cross section of the above channels, with their uncertainties illustrated by bands. The type of corrections included in the calculation are labeled on the bands. At 8 TeV, the cross sections are increased by 30% on average.

1.3.2 Higgs decay modes and searches at the LHC

The branching ratios of the Higgs boson decay in the Standard Model are calculated in Reference [10]. It includes all channels that are kinematically allowed, with QCD and EW

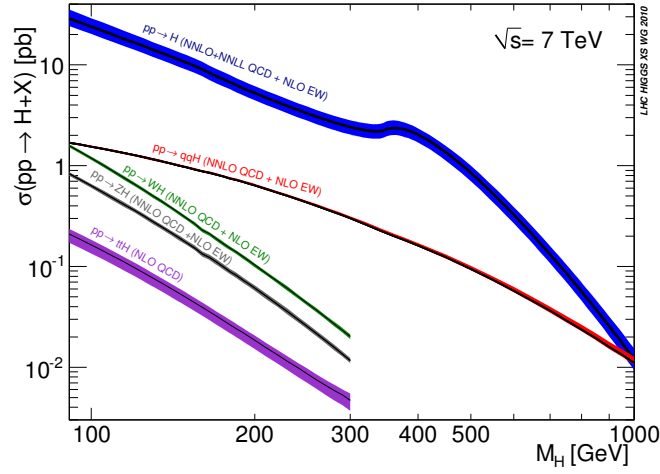


Figure 1.11: The SM Higgs production cross section at $\sqrt{s} = 7$ TeV [12].

NLO corrections. Figure 1.12 shows the branching ratios as a function of the SM Higgs-boson mass in the full mass range, and the uncertainties bands. The total width of the Higgs boson, obtained by summing up all partial widths, is shown in figure 1.13.

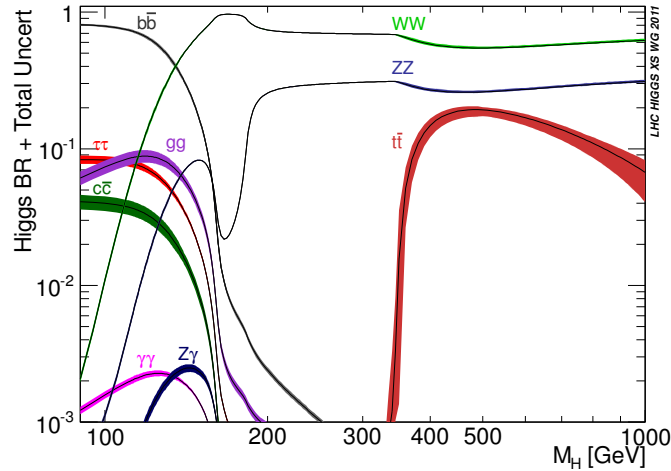


Figure 1.12: SM Higgs branching ratios as a function of the Higgs-boson mass [12].

To consider which channels to exploit, there are some basic requirements. The channel should produce a sufficient number of Higgs bosons so that the experiment can identify them among the background events. This requirement corresponds to a high branching ratio, and raises the question of signal over background ratio (s/b). To achieve a high s/b , the decaying mode should either contain objects that can be easily identified in the detector, leptons or missing energy for example, or signatures which differ from the backgrounds like special topology of back-to-back high energy jets. Therefore, in spite of high branching ratio, some channels are ruled out in the list of search channels, $H \rightarrow c\bar{c}$ and $H \rightarrow gg$ for example. The QCD background of these processes is several orders of magnitude higher

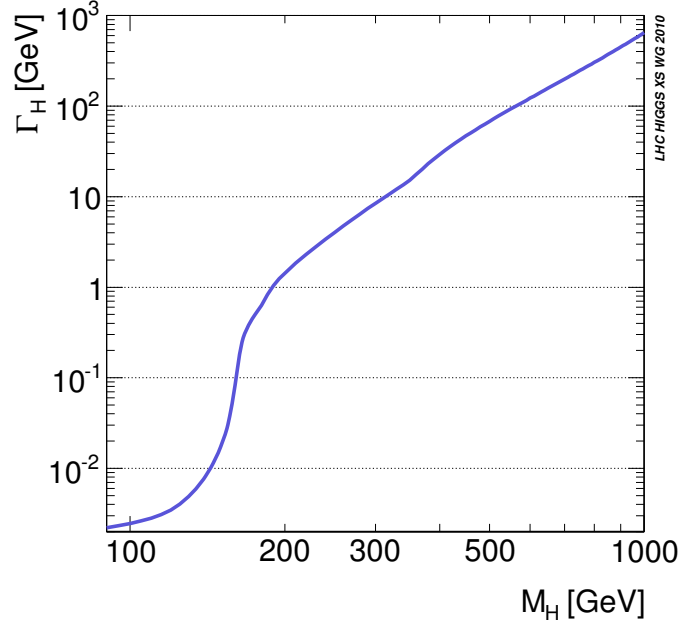


Figure 1.13: SM Higgs total width as a function of the Higgs-boson mass [10].

than the signal, yet the signal does not have a distinctive signature. Combining the above considerations, only a few channels are of interest. The SM Higgs boson production cross sections times branching ratios at 7 TeV of these channels are shown in figure 1.14. Clearly, the promising search channels depend on the Higgs mass and we will briefly discuss these channels in the three mass regions.

Low mass region, $115 \text{ GeV} < m_H < 130 \text{ GeV}$

In this region, the $H \rightarrow b\bar{b}$ has a branching ratio of $\sim 75\%$, but due to the large QCD background, it is not possible to extract the signal in the ggF mode. While in the mode of associated production with W/Z, it exhibits signatures of isolated leptons, when the W/Z decays leptonically, and additional missing energy in case of W. Although the W/Z associated production cross section is much lower than the ggF production (see Figure 1.14), the distinct signature makes the $H \rightarrow b\bar{b}$ decay a promising search channel.

The other high rate process is $H \rightarrow \tau\bar{\tau}$. The Higgs produced in the VBF mode with the semi-leptonic or leptonic decaying τ pairs in the central region leads to a signature of central isolated leptons with forward-backward jets, which is a rare topology in QCD. To fully reconstruct the mass of the Higgs boson, the collinear approximation is used to solve the problem of the undetected neutrino. This approximation assumes the visible decay products of τ to be collinear with the neutrino.

Although it does not have the highest rate in this region, $H \rightarrow \gamma\gamma$ plays a very important role in Higgs boson searches. Unlike the other processes listed here, the Higgs does not couple to the final state photons directly since they are massless. The decay involves

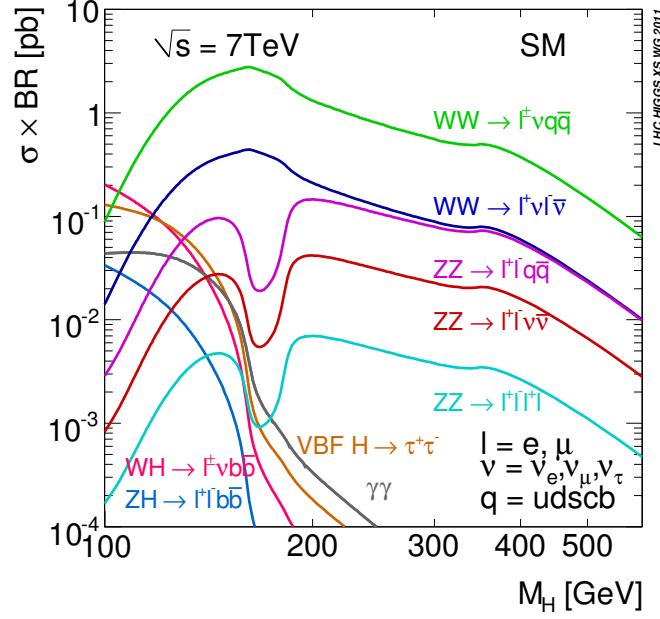


Figure 1.14: The SM Higgs-boson production cross sections multiplied by the decay branching ratios in pp collisions at $\sqrt{s} = 7$ TeV as a function of the Higgs-boson mass. All production modes are summed in the channels of $H \rightarrow t\bar{t}, gg, \text{ or } WW/ZZ(\rightarrow 4\text{fermions})$. In the $H \rightarrow b\bar{b}$ channel, only the vector-boson associated production is considered. [11].

loop of massive particles (dominantly top quark) to produce the final photons. With the requirement of two isolated energetic photons, the Higgs mass can be fully reconstructed. Since the Higgs boson width is around 1–2 GeV in this region, and a large number of events survive after the selection, the QCD background can be extracted from fitting the sideband of data, therefore leaving a clear signal peak.

Similar to $H \rightarrow \gamma\gamma$, $H \rightarrow ZZ$ has the advantage of a fully reconstructed mass when it decays to 4 leptons. In spite of the low rate in this region, because of the clean signature, the background is also considerably reduced. It benefits from the very accurate lepton measurement, which in turn provides a resolution of the Higgs boson mass around 2 GeV at $m_H = 130$ GeV, a precision which no other channels can reach.

The $H \rightarrow WW$ channel has a relatively high rate in this region. The requirement of a leptonic decay, i.e. two high energy leptons and a large missing transverse energy makes up the signature of this channel. The two leptons decaying from the Higgs boson are close to each other. But this channel cannot reconstruct the Higgs mass due to the escaping two neutrinos.

Intermediate mass region, $130 \text{ GeV} < m_H < 180 \text{ GeV}$

In this region, the Higgs mainly decays into WW and ZZ pairs. $H \rightarrow WW$ becomes dominant, especially in the region between $2m_W < m_H < 2m_Z$, the Ws are on shell while

one of the Z is still virtual. But again, the ability to fully reconstruct the Higgs mass is the advantage of the ZZ channel. If the Higgs exists in this mass range, a large excess of data over background would be seen in $H \rightarrow WW$.

High mass region, $180 \text{ GeV} < m_H < 1 \text{ TeV}$

In this range, $m_H > 2m_Z$, the $H \rightarrow ZZ$ rate is closer to the $H \rightarrow WW$ rate. With the two on-shell Z decaying to 4 leptons, it becomes the gold-plated mode. However, for $m_H > 600 \text{ GeV}$, the total Higgs width becomes very large and the cross section of the 4 leptons mode drops sharply. Adding $H \rightarrow ZZ \rightarrow \ell\ell\nu\nu$ can increase the statistics and can be identified by the Jacobian peak in the missing transverse energy spectrum. Inclusion of $H \rightarrow WW \rightarrow \ell\nu jj$ and $H \rightarrow ZZ \rightarrow \ell\ell jj$ also helps.

Chapter 2

LHC and the ATLAS detector

2.1 LHC

The Large Hadron Collider (LHC) at CERN [13] is designed to collide proton beams with an unprecedented luminosity of $10^{34} \text{ cm}^{-2}\text{s}^{-1}$ and heavy (Pb) ions with a peak luminosity of $10^{27} \text{ cm}^{-2}\text{s}^{-1}$. It is a two-ring-superconducting-hadron accelerator and collider, built in the existing 26.7 km tunnel that was constructed for the CERN LEP machine.

To reach the designed energy, the protons are accelerated in several steps by beginning with the extraction of protons from a hydrogen bottle. They reach 750 KeV by the use of accelerating RF cavities. Then a linear accelerator (LINAC 2) brings their energy to 50 MeV and passes them to the Proton Synchrotron Booster (PSB) where the beams reach 1.4 GeV. The protons subsequently enter the Proton Synchrotron (PS) and Super Proton Synchrotron (SPS), where they attain energies of 26 GeV and 450 GeV, respectively. After that, they are injected into the LHC rings where they are finally accelerated to form 3.5 TeV (2010 and 2011) or 4 TeV (2012) beams. The whole chain is illustrated in Figure 2.1.

One magnetic field cannot make the two separate proton beams counter-rotate, so the protons need to be put in two rings, deployed with opposite magnetic fields. The limited space in the tunnel led to the adoption of the twin-bore magnet design, where two coils share the same cooling infrastructure. The magnet system consists of dipole magnets, quadrupole and higher multipole magnets, responsible for bending the beams, for beam focusing and beam correction, respectively. The acceleration is generated by the radio-frequency (RF) cavities. The frequency of this superconducting system is 400 MHz, which accelerates the beam by 485 keV at each turn.

The LHC beams are made to cross at four "interaction points" (Figure 2.1). Four detectors are built, at each of these interaction points: ATLAS (A Toroidal LHC ApparatuS), CMS (Compact Muon Solenoid), ALICE (A Large Ion Collider Experiment) and LHCb for "beauty" physics. ATLAS and CMS are designed for broad physics programs, among them, the studies of Standard Model, especially the search for the Higgs boson. Looking for evidence of new physics is another important subject of the two experiments.

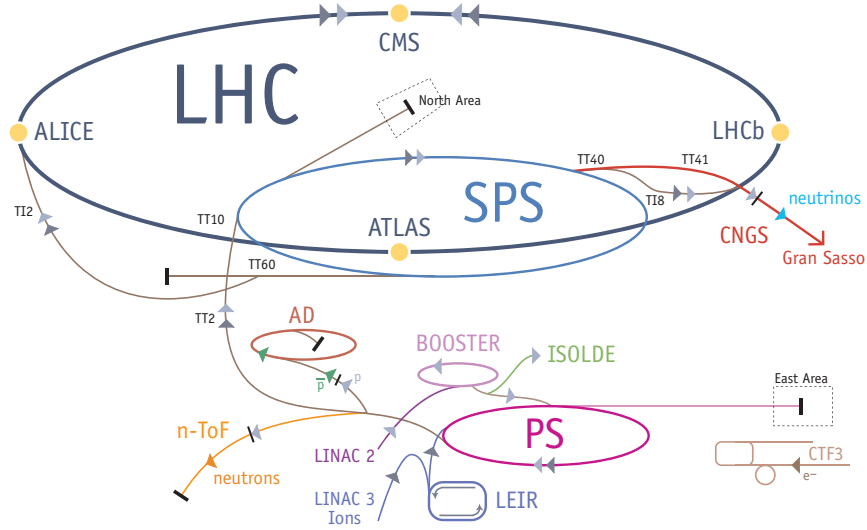


Figure 2.1: Illustration of the LHC CERN accelerator complex, including the injection system. The LHC experiments are indicated with yellow circles.

ALICE is dedicated to the studies with heavy ions, to exploring the properties of quark-gluon plasma, which is believed to have existed in the early universe shortly after the Big Bang. The focus of LHCb is b-quark physics. It will investigate the matter and antimatter asymmetry in the universe.

On March 30, 2010, LHC successfully collided proton beams at a c.m. energy of 7 TeV. Since then LHC has collected pp collision data up to the end of 2012. During 2011 the LHC has delivered 5.6 fb^{-1} of pp collisions at $\sqrt{s} = 7 \text{ TeV}$ of which ATLAS has recorded 93% (5.2 fb^{-1}) reaching an instantaneous peak luminosity of $3.65 \times 10^{33} \text{ cm}^{-2} \text{ s}^{-1}$. Figure 2.2 shows the pp collision luminosity delivered to each experiment in 2012, and Figure 2.3 shows the luminosity of ATLAS in 2010, 2011 and 2012.

2.2 The ATLAS experiment

2.2.1 Overview

ATLAS (short for A Toroidal LHC ApparatuS) is designed for a broad spectrum of detailed physics studies, which impose very stringent requirements on the detector:

- For accurate measurement and identification of the electrons and photons, the electromagnetic calorimeter must be of high performance.
- For accurate jet and missing transverse energy (E_T^{miss}) measurements, hadronic calorimetry with full-coverage is needed.

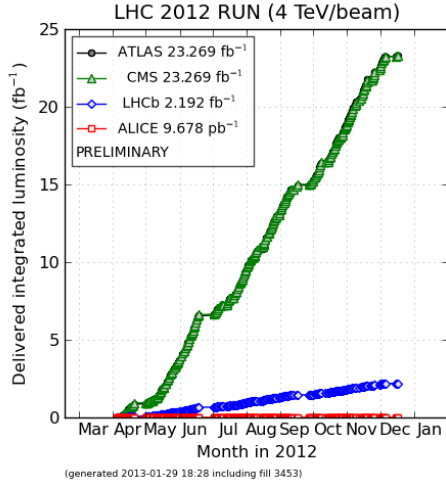


Figure 2.2: Delivered luminosity to all 4 experiments during 2012 stable beams of p-p collisions.

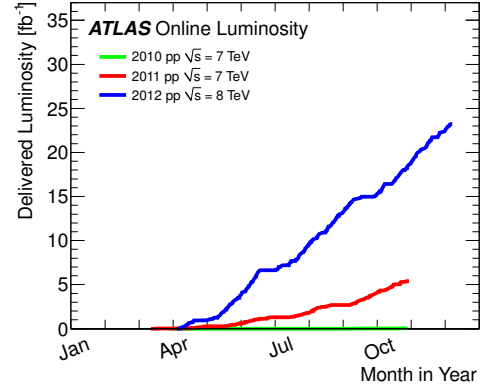


Figure 2.3: Cumulative luminosity delivered to ATLAS during stable beams of p-p collisions. 2010 (green), 2011 (red) and 2012 (blue).

- For high- p_T lepton-momentum measurements, charged particle identification and secondary vertex reconstruction at higher luminosity and full event reconstruction capability at lower luminosity, efficient tracking should be provided by the inner detector.
- For high- p_T muon momentum measurements at the highest luminosity, the external muon spectrometer should be capable of providing standalone measurements without the help of the internal tracking.
- For most physics processes of interest at the LHC, triggering and measurements of leptons and jets at low p_T , should have high efficiency.
- For high efficiency of recording events, the large space acceptance is required from each detector system.

Based on the above requirements, the following 6 sub-systems of ATLAS are designed:

- The Inner Detector (ID), for pattern recognition, momentum and vertex measurements, and electron identification.
- The electromagnetic and hadronic calorimeters, for jet and E_T^{miss} measurements and energy deposition.
- The Muon Spectrometer (MS), for muon momentum measurement and identification.
- The magnet system, provides bending power for ID and MS.
- The trigger system, to effectively reduce background before recording events.

- The data acquisition system, to store interesting events.

Figure 2.4 shows the components of the ATLAS detector. Overall ATLAS is 25m high, 44m long, and weighs 7000 tons. In the following sections, the coordinate system will first be introduced and the six detector sub-systems will be described in detail.

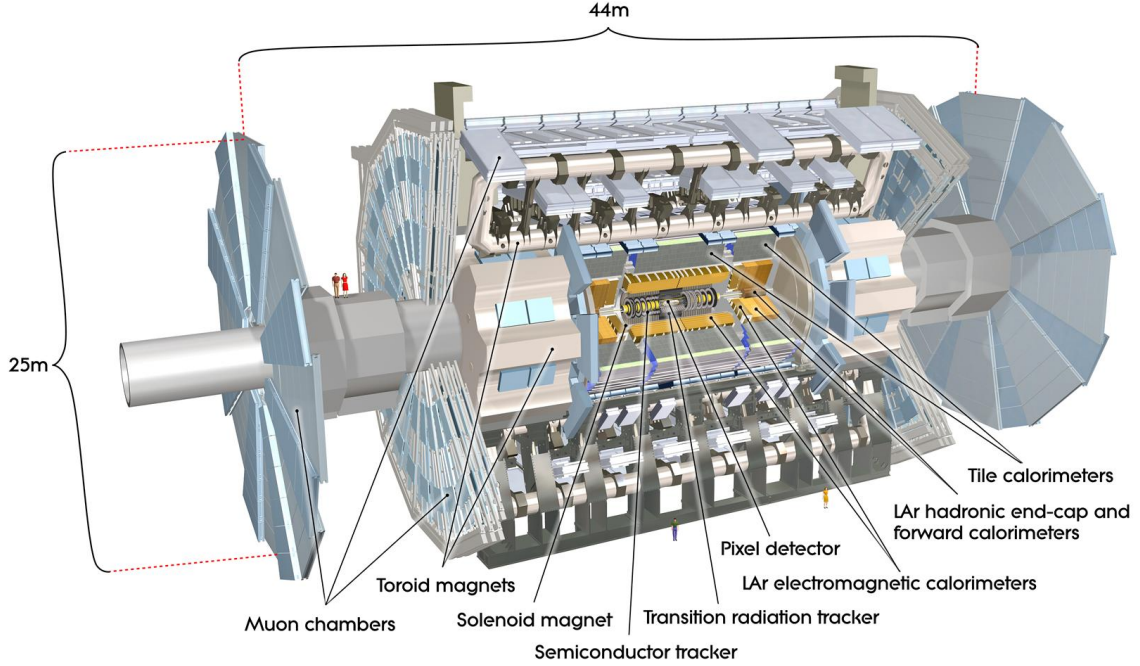


Figure 2.4: Cut-away view of the ATLAS detector, with the different sub-systems identified.

2.2.2 Naming convention and coordinate system

The centre of the detector, is at the interaction point (IP) and is defined as the origin of the system. In the Cartesian system, the beam direction defines the z axis and the positive x -axis points from the IP to the centre of the ring, the positive y axis points upwards. The scheme of the coordinate system is shown in Figure 2.5. The transverse quantities like transverse momentum p_T and transverse energy E_T refer to the projection in the x - y plane unless stated otherwise. Since ATLAS has a cylindrical shape, it's more convenient to use the polar system, where the azimuthal angle ϕ is measured around the beam axis, and the polar angle θ is the angle from the beam axis. Variables that are transformed simply in the context of relativity are used to express the angular position. The pseudo-rapidity, η , thus is defined by $\eta = -\ln(\tan\frac{\theta}{2})$, which transforms additively under a z direction boost. The quantity $\Delta R \equiv \sqrt{(\Delta\eta)^2 + (\Delta\phi)^2}$ is frequently used to measure the distance in pseudo-rapidity and azimuthal angle space.

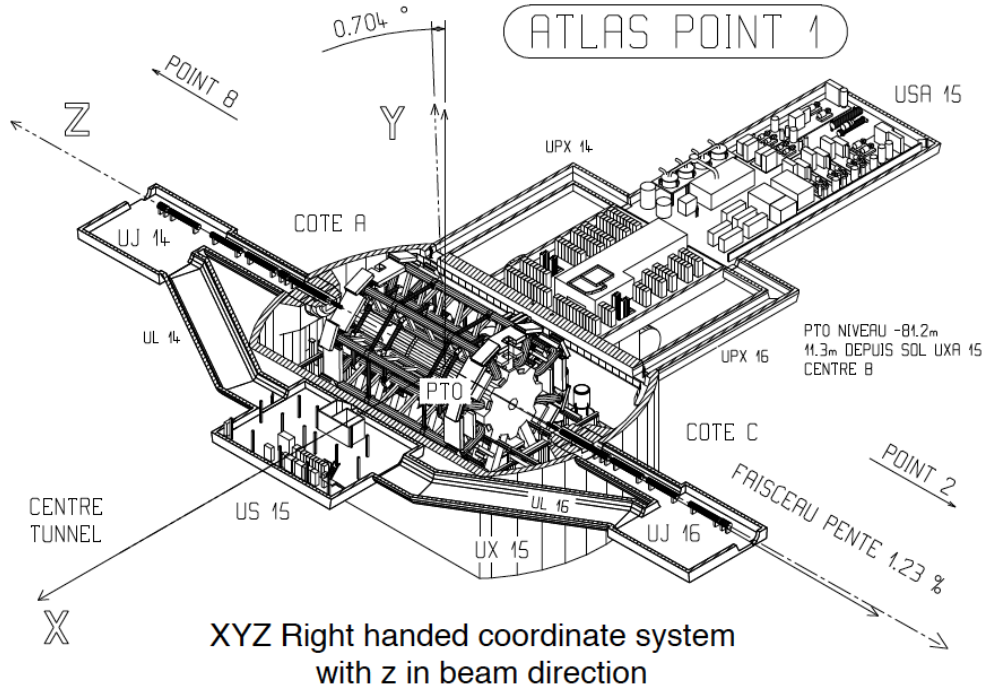


Figure 2.5: The coordinate system in the ATLAS detector.

2.2.3 Inner Detector

The inner detector is designed to provide hermetic and robust pattern recognition, excellent momentum resolution and both primary and secondary vertex measurements for charged tracks with $P_T > 0.2$ GeV, as well as electron identification. This is achieved by a combination of high bending power, provided by a solenoidal magnetic field of 2 T, and fine-granularity position measurements, provided by the three independent but complementary sub-detectors composing the inner detector. In the innermost parts, discrete space-points from silicon pixel layers (Pixel) and stereo pairs of silicon microstrip (SCT) layers, provide high-resolution pattern recognition, and the transition radiation tracker (TRT), consisting of layers of gaseous straw tube elements in the transition region, enhance the pattern recognition and improve electron identification complementary to that of the calorimeter for $|\eta| < 2.0$. The tracking system covers the range $|\eta| < 2.5$, and its layout is shown in Figure 2.6 [14].

Magnet

The superconducting solenoid provides bending power of the charged particles passing through the inner detector. The 2 T axial field is generated by a coil of length 5.3 m, of diameter 2.3 m, wound with a high strength aluminium-stabilised niobium-titanium (NbTi) conductor and operates at 4.5 K. The magnet thickness is minimised to optimise

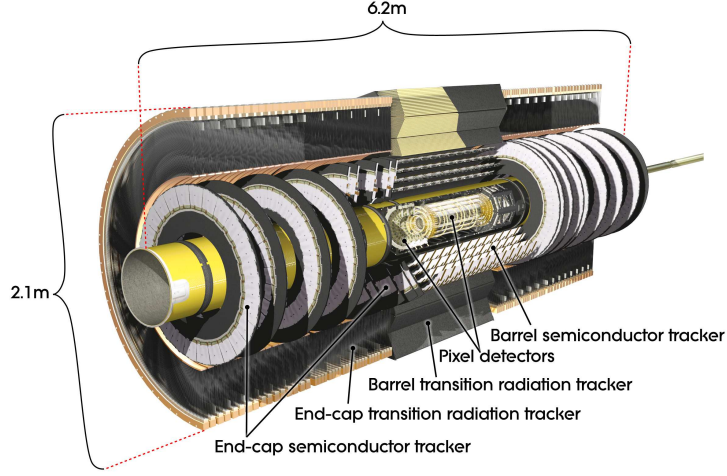


Figure 2.6: Cut-away view of the ATLAS Inner Detector.

the performance of the electromagnet calorimeter. For this reason, the cryostat uses a common vacuum enclosed with the calorimeter.

Pixel detector

The pixel detector is designed to provide a very high-granularity, high-precision set of measurements as close to the interaction point as possible. The 1744 modules of the pixel detector are arranged in three cylindrical layers in the barrel, with radial position 50.5 mm, 88.5 mm and 122.5 mm respectively, and in each of the two end-caps in three disk layers, which complete the angular coverage. Each module has a size of $50 \times 400 \mu\text{m}^2$, and an intrinsic resolution of $10 \mu\text{m}$ in the transverse plane, $115 \mu\text{m}$ in the z coordinate. A charge depleted layer of silicon in the module is used to record the charge of the particle transversing the pixel, and interpolation over adjacent pixels determines the hit position. The pixel sub-system covers the range $|\eta| < 2.5$ in space.

Semi-Conductor Trackers (SCT)

The SCT system is mounted in the intermediate radial range to provide at least four precision measurements per track. The number of layers had to be limited in order to keep the amount of material in front of the calorimeter to a reasonable level and also to reduce the cost. There are four layers of silicon microstrip detectors in the barrel and nine in the end-cap. An SCT module is composed of two detector pairs glued together back-to-back at a 40 mrad angle, which provides precision points in the $R - \phi$ and z coordinates. The intrinsic accuracy per module is $17 \mu\text{m}$ in $R - \phi$ and $580 \mu\text{m}$ in z (R) in the barrel (end-cap). The SCT system coverage is $|\eta| < 2.5$ with barrel sensors up to $|\eta| < 1.4$.

Transition Radiation Tracker (TRT)

The straw tube tracker (TRT) provides the possibility of continuous track-following with much less material per point and at lower cost. The detector consists of drift (straw) tubes of 4 mm diameter, filled with Xe : CO₂ : O₂ (70% : 27% : 3%) at an overpressure of 5–10 mbar. It's the outmost sub-system of the inner detector. Compared to the silicon, the straw hits provide a lower precision, which is compensated by the large number of measurements and the larger track length. It is capable of 36 measurements per track up to $\eta = 2.0$. The TRT provides only $R - \phi$ information in the barrel and z in the end-cap. The intrinsic accuracy is 130 μm per straw. The detection of transition-radiation photons in the straw tubes enhance the electron identification capabilities of the whole experiment. The Xe-based gas mixture absorbs transition radiation photons, and gives a distinctive signature for electrons. Figure 2.7 shows the high-threshold hit probabilities for electron candidates from photon conversions and generic Inner Detector tracks, which are assumed to be pions. Electron tracks have four times more hits than pions.

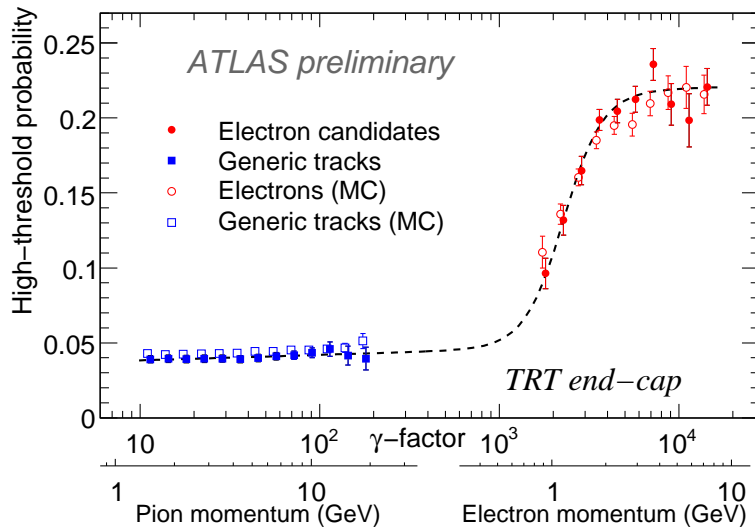


Figure 2.7: The high-threshold hit probabilities for electron candidates from photon conversions and generic Inner Detector tracks, which are assumed to be pions.

Material budget

Material in the inner detector can cause reconstruction loss of photons if they convert before reaching the electromagnetic calorimeter, the same happens to the electrons with bremsstrahlung. Therefore every effort has been made to keep the material in the tracking volume to a minimum, by careful design of the active detectors and by the use of low- z materials. In Figure 2.8 the material distribution in radiation lengths at the exit of the ID envelope is shown as a function of pseudo-rapidity.

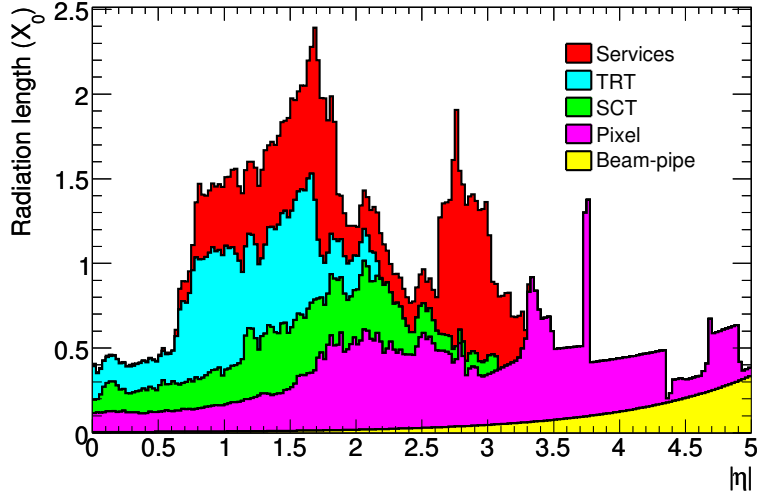


Figure 2.8: Material distribution at the exit of the Inner Detector envelope as a function of $|\eta|$ (averaged over ϕ).

Tracking performance

For particles with $p_T > 1$ GeV, the expected resolution can be expressed by $\sigma_{p_T}/p_T = 0.05\% p_T \text{ (GeV)} \oplus 1\%$ where \oplus denotes addition in quadrature. The first term represents the intrinsic resolution, dominant in high p_T , while the second term comes from multiple scattering, and contributes mostly at low p_T . The relative precisions of the 3 sub-system measurements are well matched, so that no single measurement dominates the global momentum resolution. The absence of TRT in the region $|\eta| > 2.0$ makes the resolution depend on the pseudo-rapidity.

2.2.4 Calorimeter

The sampling calorimeter is located between the Inner Detector and the Muon Spectrometer, covering the pseudo-rapidity range $|\eta| < 4.9$. It measures the energies of charged and neutral particles. Over the η region matched to the inner detector, the fine granularity of the electromagnetic calorimeter is ideally suited for precision measurements of electrons and photons. The coarser granularity of the rest of the calorimeter is sufficient to satisfy the physics requirements for jet reconstruction and E_T^{miss} measurements. An overview of the structure is presented in Figure 2.9.

The calorimeter is composed of three parts: the segmented liquid argon (LAr) electromagnetic calorimeters (EM), mainly for electrons and photons, the Hadronic Calorimeter and the Forward Calorimeter (FCal) for hadronic activities. In order to achieve good containment for electromagnetic and hadronic showers and limited punch-through into the muon system, the total thickness of the EM and hadronic calorimeter is around 10–12 radiation lengths (X_0).

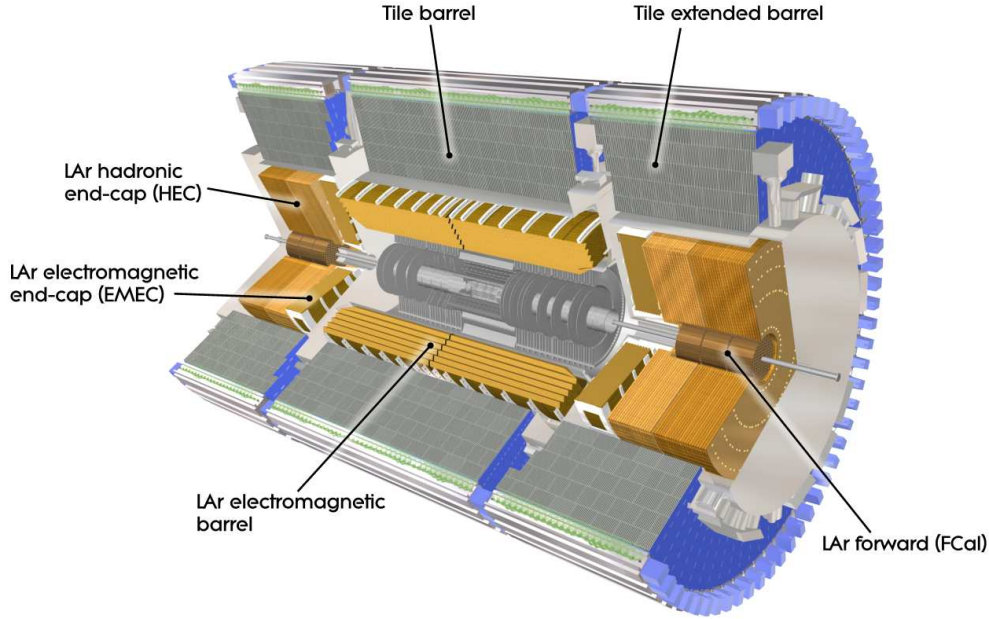


Figure 2.9: Cut-away view of the ATLAS calorimeter system.

The electromagnetic calorimeter (EM calorimeter)

The EM Calorimeter consists of lead plates as absorber and liquid argon as sensing elements. The EM calorimeter is divided into a barrel part ($|\eta| < 1.475$) and two end-cap components ($1.375 < |\eta| < 3.2$). Two identical half-barrels compose the barrel part, separated by a small gap of 4 mm at $z=0$. Each end-cap calorimeter is made of two coaxial wheels: an outer wheel covering the region $1.375 < |\eta| < 2.5$, and an inner wheel covering the region $2.5 < |\eta| < 3.2$. In the region of $|\eta| < 1.8$, a presampler detector is used to correct for the energy lost by electrons and photons upstream of the calorimeter. The accordion-shape provides complete ϕ symmetry without azimuthal cracks.

In the region overlapping with the inner detector ($|\eta| < 2.5$), where precise measurements of electrons and photons are made, the EM calorimeter is segmented in three sections in depth. The end-cap region ($2.5 < |\eta| < 3.2$) has coarser granularity. The segmentations of each part of the calorimeter are listed in table. 2.1.

The Hadronic Calorimeter

Hadron Calorimeters can measure jets, which are essential for much of the LHC physics program. The jets themselves are collections of energy detected in a limited region of pseudo-rapidity and angle as expected from the fragmentation of quarks and gluons into hadrons. The hadronic calorimeter consists of a Tile calorimeter and a LAr hadronic end-cap calorimeter (HEC).

Table 2.1: Pseudo-rapidity coverage, longitudinal segmentation and granularity of the ATLAS calorimeters. The detailed numbers can be found in ref. [15].

Calorimeter	Coverage		Granularity ($\Delta\eta \times \Delta\phi$)
EM calorimeter	barrel	end-cap	
Presampler	$ \eta < 1.54$	$1.5 < \eta < 1.8$	0.025×0.1
Sampling 1	$ \eta < 1.475$	$1.375 < \eta < 3.2$	0.003×0.1^a
			0.025×0.025^b
			$0.003 - 0.025 \times 0.1^c$
			0.1×0.1^d
Sampling 2	$ \eta < 1.475$	$1.375 < \eta < 3.2$	0.025×0.025
			0.075×0.025^b
			0.1×0.1^d
Sampling 3	$ \eta < 1.35$	$1.5 < \eta < 2.5$	0.05×0.025
Tile calorimeter	barrel	extended barrel	
Sampling 1	$ \eta < 1.0$	$0.8 < \eta < 1.7$	0.1×0.1
Sampling 2			
Sampling 3			0.2×0.1
Hadronic end-cap calorimeter			
Samplings 1-4	$1.5 < \eta < 3.2$		0.1×0.1^e
			0.2×0.2^d
Forward calorimeter			
Samplings 1-3	$3.1 < \eta < 4.9$		0.2×0.2

^a $|\eta| < 1.4$, ^b $1.4 < |\eta| < 1.475$, ^c $1.375 < |\eta| < 2.5$, ^d $2.5 < |\eta| < 3.2$, ^e $1.5 < |\eta| < 2.5$

Tile calorimeter The tile calorimeter is a sampling calorimeter using steel as absorber and scintillating tiles as active material. The scintillation light, which is emitted when a particle traverses the tiles is guided to photodetectors through wave length shifting optical fibres. The fibres are grouped in such a way as to collect the signals belonging to one calorimeter cell. The overall coverage is $|\eta| < 1.7$, with the central barrel region $|\eta| < 1.0$, and the two extended barrels, $0.8 < |\eta| < 1.7$, both segmented in depth into three layers. The structure of the scintillator tiles allows for full projective azimuthal coverage, while the readout cells built by grouping fibres imply a "pseudo-projective" geometry in η . The granularities of the samplings are shown in Table 2.1.

LAr hadronic end-cap calorimeter (HEC) The LAr hadronic end-cap calorimeter is located directly behind the end-cap electromagnetic calorimeter. It uses copper as absorber and LAr as active material. To keep the material density from dropping in the transition region, the HEC covers $1.5 < |\eta| < 3.2$, which overlaps the tile calorimeter ($|\eta| < 1.7$) and the forward calorimeter ($|\eta| = 3.1$). It consists of two independent wheels per end-cap, each built from wedge-shaped modules, divided into two segments in depth. The size of the cells is given in table 2.1.

The Forward Calorimeter (FCal)

The LAr forward calorimeter provides uniformity of the calorimetric coverage and reduces radiation background levels in the muon spectrometer in the region of $3.1 < |\eta| < 4.9$. It consists of three modules in each end-cap: the first is optimised for electromagnetic measurements, with copper as absorber, while the two others measure predominantly the energy of hadronic interactions using tungsten.

The overall performance

The calorimeter resolution is described by

$$\frac{\sigma(E)}{E} = \frac{a}{E} \oplus \frac{b}{\sqrt{E(\text{GeV})}} \oplus c, \quad (2.1)$$

where a is the noise term, b the sampling term and c the constant term reflecting local non-uniformities in the response of the calorimeter. The detailed values of b and c are shown in table 2.2 for different parts of the detector, and separately for electrons and pions. Figure 2.10 shows the resolution as a function of particle energy at two η values for electrons and pions.

Table 2.2: Resolution of the different calorimeters for pions and electrons evaluated with test beam data, given by the stochastic term a and the constant term b as in Equation 2.1. The constant term for the full electromagnetic calorimeter is expected to be around 1%.

Calorimeter	Particle	Energy Resolution	
		b (% $\sqrt{\text{GeV}}$)	c (%)
Electromagnetic	electrons	10.0 ± 0.4	0.4 ± 0.1
Hadronic End-Cap	pions	70.6 ± 1.5	5.8 ± 0.2
Forward	electrons	28.5 ± 1.0	3.5 ± 0.1
	pions	94.2 ± 1.6	7.5 ± 0.4
Tile	pions	56.4 ± 0.4	5.5 ± 0.1

2.2.5 Muon Spectrometer

The muon spectrometer is designed to provide clean and efficient muon identification and precise momentum measurement over a wide range of momentum and solid angle. It covers the pseudo-rapidity range $|\eta| < 2.7$, and allows identification of muons with momentum as low as 3 GeV and up to more than 1 TeV. It is based on the magnetic deflection of muon trajectories. The structure is shown in Figure 2.11, which comprises three part:

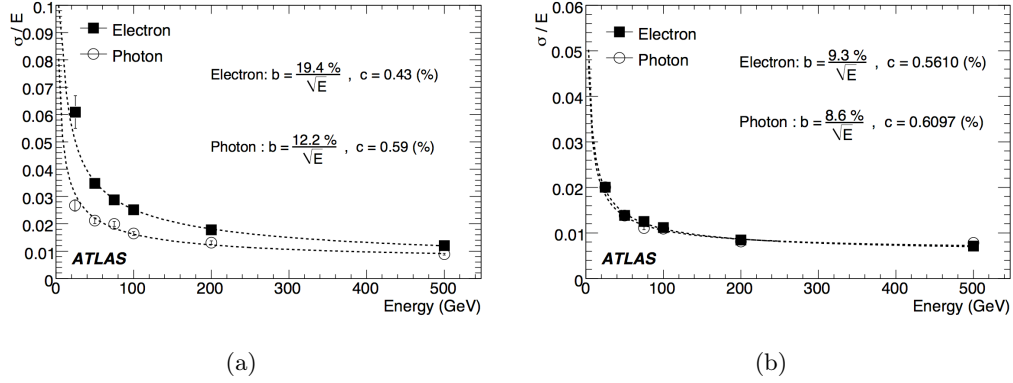


Figure 2.10: Resolution versus particle energy. (a) $|\eta| = 0.3$. (b) $|\eta| = 1.65$ [16].

- The large superconducting air-core toroid magnets, providing large integrated bending strength over the entire η range.
- The precision tracking chambers, with Monitored Drift Tubes (MDT) in the barrel and the Cathode Strip Chambers (CSC) in the end-cap.
- The trigger detectors that provide fast information on muon tracks traversing the detector, composed of Resistive Plate Chambers (RPC) and the Thin Gap Chambers (TGC).

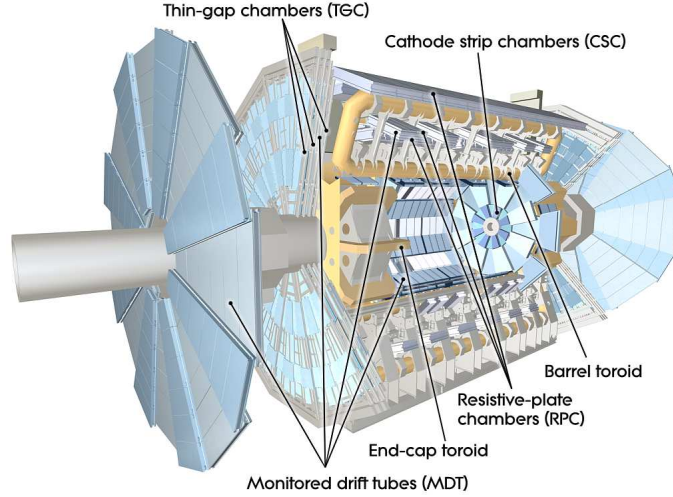


Figure 2.11: Cut-away view of the ATLAS muon system [14].

Special considerations were taken into account with respect to the design, given the requirement for the muon spectrometer, :

- Resolution requirements in barrel and end-cap regions are different. For a given p_T , the momentum increases dramatically with $|\eta|$, while the bending power does

not increase at the same rate. This leads to the necessity of an increased and η dependent granularity in the end-cap.

- Radiation levels in the end-cap region are a factor of 10 higher than in the barrel, and call for a finer granularity of the end-cap trigger readout, and more radiation-tolerance for the precision measurement chambers.
- Inhomogeneities of the magnet field in the transition region, as will be seen in the next section, imposes high precision from the trigger system to avoid fake trigger rates.

Therefore, two different technologies have been selected for the trigger detectors. In the barrel ($|\eta| < 1.05$) region, Resistive Plate Chambers (RPC) are used and in the end-cap ($1.05 < |\eta| < 2.4$), Thin Gap Chambers (TGC) have been selected. As for precision measurement, Monitored Drift Tubes (MDT) cover $|\eta| < 2.0$, substituted by Cathode Strip Chambers (CSC) in the region $2.0 < |\eta| < 2.7$.

A description of the muon magnet system will be given next, followed by the details of the four types of chambers.

Magnets

The toroidal magnetic field is provided by superconducting air-core coils. The field is mostly orthogonal to the muon trajectories, while the degradation of resolution due to multiple scattering is minimised by the air-core concept. The large barrel toroid provides magnetic bending over the range $|\eta| < 1.4$, with typical bending powers of 2.5 Tm, while two smaller end-cap magnets cover $1.6 < |\eta| < 2.7$, with 6 Tm bending power. Each of the three toroids consists of eight coils assembled radially and symmetrically around the beam axis. Owing to the finite number of coils, the field configuration is not perfectly toroidal (Figure 2.12), especially in the gap $1.4 < |\eta| < 1.6$ region, where the deflection is caused by a combination of barrel and end-cap fields. There is an angle of 22.5° between the barrel and end-cap coil system in order to optimise the interface of the two. The integrated strength over η is shown in Figure 2.13; a significant drop in the transition region ($1.4 < |\eta| < 1.6$) is seen.

Monitored Drift Tubes

Monitored Drift Tubes provide a precise measurement of the muon momentum in the bending plane, over the range $|\eta| < 2.0$. The basic element of MDT is a pressurised drift tube with a diameter of ~ 30 mm, operating with Ar/CO₂ gas (93/7) at 3 bars. The central tungsten-rhenium wire with a diameter of $50 \mu\text{m}$ at a potential of 3080 V collects electrons from muon ionisation. The wire is held in position at the tube ends by cylindrical end-plugs. The tubes are assembled in a cylindrical geometry, which results in the radial electric field, that makes the determination of tracks only depend on the radius of the circle

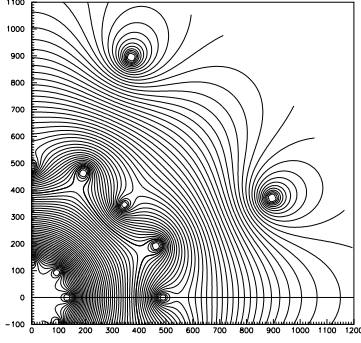


Figure 2.12: Magnetic field map in the transition region. The field lines are shown in a plane perpendicular to the beam axis and located in the middle of an end-cap toroid.

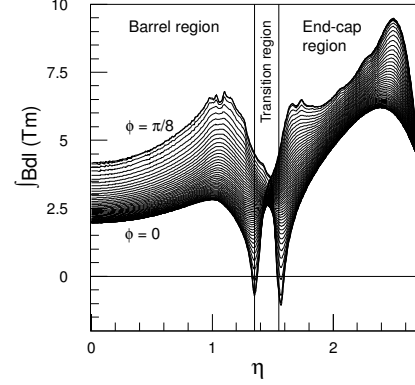


Figure 2.13: Predicted field integral as a function of $|\eta|$ and ϕ inside the Muon Spectrometer.

tangential to the track. Therefore, a precise position of a track can be read from the fine drift-time resolution. This scheme is shown in Figure 2.14. The precision per tube can reach is $80 \mu\text{m}$. The operating gas was selected because of the good ageing properties.

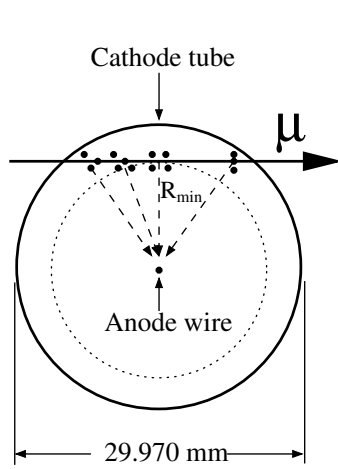


Figure 2.14: Cross-section of an MDT tube.

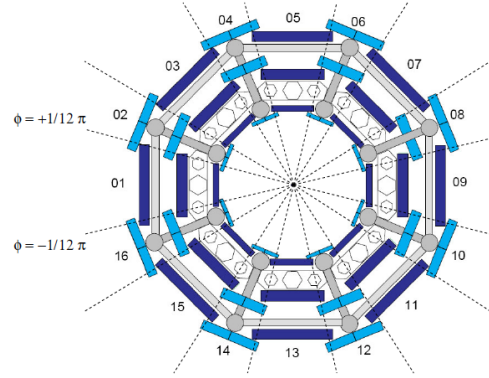


Figure 2.15: Cross-section of the barrel muon system perpendicular to the beam axis (non-bending plane), showing three concentric cylindrical layers of eight large and eight small chambers.

The direction of the tubes in the barrel and end-caps is along ϕ , assembled into chambers with rectangle shape in the barrel and trapezoidal in the end-cap. An MDT chamber consists of two groups of tubes, called multi-layers, separated by a spacer. A multi-layer then consists of 3 or 4 layers of tubes, depending on the radial position of the chamber. Furthermore, the chambers in the barrel region are located between and on the eight coils of the barrel toroid magnet, providing a ϕ symmetry of eight octants. Each octant is subdivided in the azimuthal direction in two sectors with slightly different lateral extensions, a large and a small sector. The barrel MDT chambers are segmented in 3 layers of co-axial

cylindrical shells, called inner, middle, outer respectively according to their distance from the beamline. The cross-section of the barrel muon spectrometer is shown in Figure 2.15. The end-cap chambers are in front and behind the two end-cap toroid magnets, making consecutive concentric disks: the Small Wheel (Inner), the Big Wheel (Middle) and the Outer Wheel.

Cathode Strip Chambers

Because of the very high radiation level in the region $|\eta| > 2.0$, the limit of safe operation of MDT will be exceeded, they are replaced by cathode-strip chambers, which have a safe counting rate of 1000 Hz/cm^2 , far above the 150 Hz/cm^2 of MDT chambers, and this rate is sufficient up to the forward boundary of the muon system at $|\eta| = 2.7$.

The CSCs are multi-wire proportional chambers with cathode strip readout. The location of a track is obtained by measuring the charge induced on the segmented cathode by the avalanche formed on the anode wire. The wires are oriented in the radial direction, and there are two sets of cathodes, one perpendicular to the wires, providing the precision measurement, and the other parallel to the wires, giving the transverse coordinate. The position interpolation between the charges of the neighbouring cathodes provides the track. Four layers of such wire-strip combinations form a chamber, which gives 4 independent measurements in η, ϕ , the structure of a chamber is shown in Figure 2.16. On each end-cap, there are 2 disks configured with 8 chambers, one with small chambers, the other with large chambers. The layout is shown in Figure 2.17.

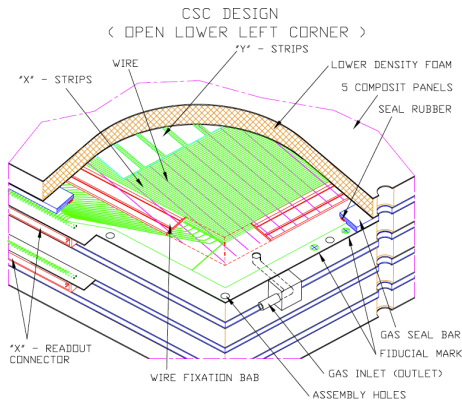


Figure 2.16: Structure of the CSC

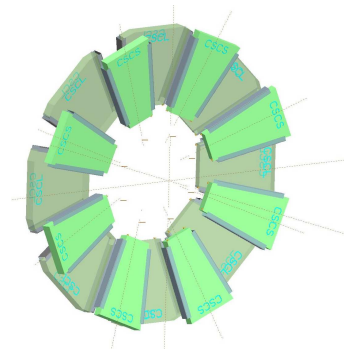


Figure 2.17: Layout of a CSC end-cap with eight small and eight large chambers.

The CSC resolution is $60 \mu\text{m}$ per layer, which is slightly better than the $80 \mu\text{m}$ of the MDT, due to the small electron drift times ($\leq 30 \text{ ns}$). The good time resolution (7 ns) is useful for bunch crossing identification. In the non-bending direction ϕ , the cathode segmentation is coarser, leading to a resolution of 5 mm . Since the measurement has a second coordinate, the ambiguity in the track due to multiple pairing can be resolved via

the pulse height. The gap between 4 planes is filled with a non-flammable mixture of 30% Ar, 50% CO₂ and 20% CF₄ gas. The absence of hydrogen makes CSC less sensitive to neutron background.

Resistive Plate Chambers

The RPC is a gaseous parallel electrode-plate (i.e. no wire) detector. The detector consists of two resistive plastic plates held parallel by insulating spacers. The 2 mm gap is filled with a nonflammable mixture of $C_2H_2F_4/Iso - C_4H_{10}/SF_6$ (94.7/5/0.3%). An electric field of 4.9 kV/mm is applied through electrodes located on the outer side of the plates. The avalanche formed along the ionising track is detected on outside conducting strips via capacitive coupling. Two such detectors independently measure η and ϕ and are combined in a unit. Two units are then put side by side to form a chamber, as shown in Figure 2.18.

The RPC chambers are then mounted in three concentric cylindrical layers around the beam axis, referred to as the three trigger stations, as seen in Figure 2.19. In this way, a track going through all three stations delivers six measurements in η and ϕ . The redundancy rejects fake tracks from noise hits and greatly improves the trigger efficiency. The resolution is around 10 mm for both coordinates, with timing resolutions below 2 ns.

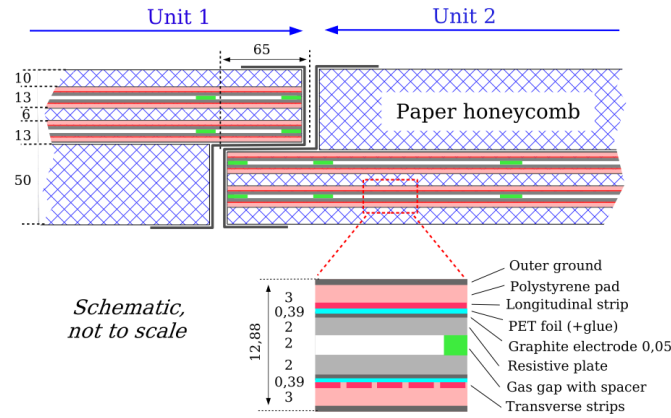


Figure 2.18: Cross-section through an RPC, where two units are assembled to form a chamber. Each unit has two gas volumes supported by spacers, four resistive electrodes and four readout planes, reading the transverse and longitudinal direction.

Thin Gap Chambers

The Thin Gap Chambers (TGC), as opposed to the wireless RPC, are multi-wire proportional chambers similar to the CSC, with very small wire-to-cathode distance of 1.4 mm, and the wire-to-wire distance of 1.8 mm. It provides the capability of triggering, as well as the second coordinate measurement in the end-cap. The chambers are filled with a gas mixture of CO₂ and $n - C_5H_{12}$ (n-pentane) with fractions of 55 and 45%, respectively. A

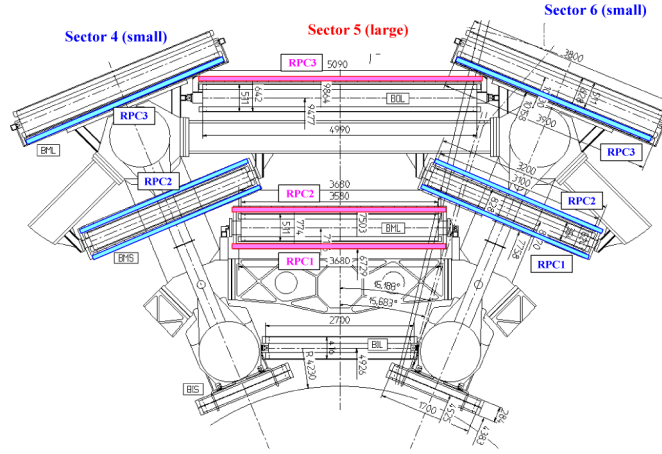


Figure 2.19: Cross-section through the upper part of the barrel with the RPC marked in colour

voltage of 2900V is applied on the anode wires. The TGC has a good time resolution to tag the beam-crossing with high efficiency (99%) within a 25 ns gate.

Alignment

The track sagitta in the magnetic field is the fundamental quantity for the momentum measurement. To reach the design resolution of 10% for a 1 TeV track, the accuracy of sagitta should be of the order $50\mu m$. After installation, the muon chamber positions are known within 5 mm. In addition, deformations due to thermal gradients and gravity are of the order of several hundred microns. An alignment system must be used to obtain the required $50\mu m$ accuracy of the chamber relative position and deformation. The alignment system used for ATLAS is based on optical straightness monitors, and has 2 basic types, the in-plane alignment, and the chamber relative position alignment.

The in-plane alignment, which monitors the MDT deformation, uses four light rays to measure the relative movement of three cross-plates that are part of the chamber support structure for large chambers. The accuracy reaches $10\mu m$. After the corrections from in-plane alignment, the alignment of the relative positions assumes the chambers are rigid planar bodies.

The relative position alignment system monitors the homogeneous thermal expansion of chambers. Due to different geometries, different strategies are used in the barrel and in the end-cap. In the barrel, the chambers inside an MDT layer are referenced to each other by chamber-to-chamber alignment sensors (paraxial and axial systems), while the projective system radially connects the inner, middle, and outer MDT layers. This network detects the relative chamber position changes with an accuracy of $20\mu m$. The system is not sufficient to provide absolute position information without linking MDT chambers to the toroid cryostat. Furthermore, the alignment is only applied to large chambers for reasons

of cost, which leaves the small sectors unaligned. Aligning the small sectors requires using particle track alignment, with the tracks crossing large chambers and small chambers in their overlap regions.

In the end-cap, the toroid cryostats prevent the use of projective rays and requires a different scheme. A network of precision alignment bars are mounted on the chambers to form a grid precisely aligned within $20\ \mu\text{m}$. Using optical sensors, the chambers are aligned with respect to the bars. Deformations of the bars themselves and the chambers are monitored with an internal alignment system. Overall with this scheme, in the end-cap the relative positions of the chambers are known with $40\ \mu\text{m}$ accuracy and the absolute position within $300\ \mu\text{m}$. The overall alignment scheme for a large sector is shown in 2.20.

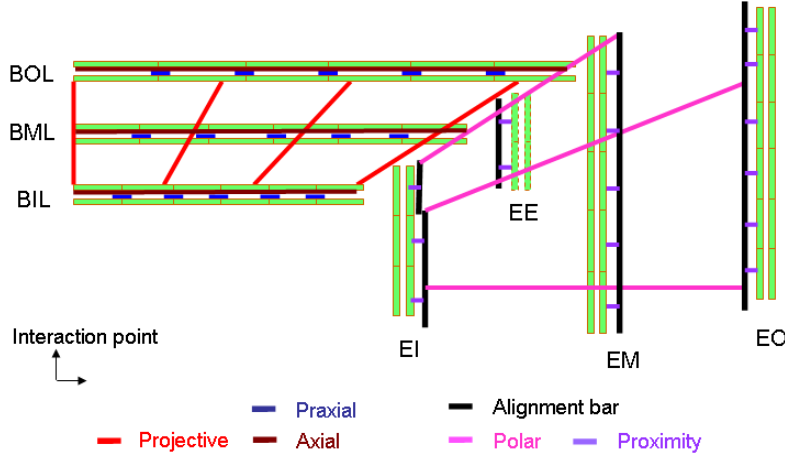


Figure 2.20: Principle of the alignment of the ATLAS muon spectrometer.

The overall performance

A high p_T muon typically traverses 3 stations of the muon spectrometer, and a precision measurement can be obtained. The resolution is degraded when the track crosses support structures or services like cables or tubing and also when it traverses one or two stations only. Other factors like energy loss in the calorimeter because of ionisation, also play an important role in momentum determination. Figure 2.21 shows how all contributions to the muon spectrometer momentum resolution vary as a function of p_T . At low momentum, the energy loss dominates; as the momentum rises, multiple scattering takes over, and at high momentum, the muon spectrometer characteristics, like alignment and calibration become the most important factor.

As will be discussed in section 2.3.2, high performance in muon identification and momentum measurement is achieved by combining other ATLAS detector systems; the inner detector and the calorimeter, which provide a measurement of momentum for $|\eta| < 2.5$ and of energy loss, respectively. The precision given by the inner detector or the muon

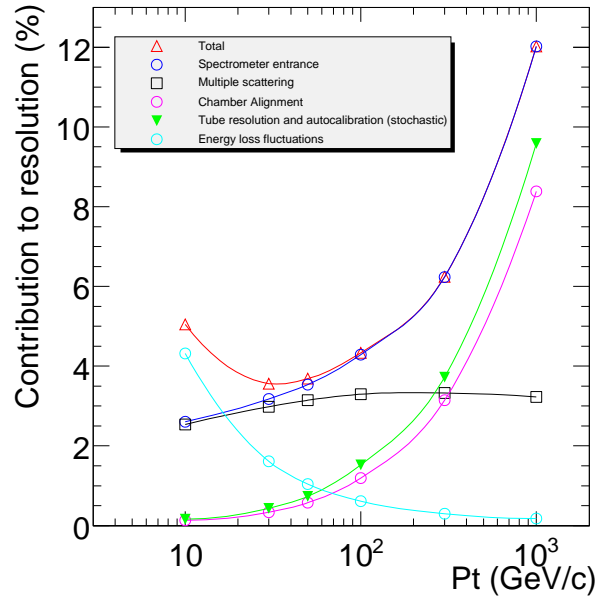


Figure 2.21: Contributions to the momentum resolution for muons reconstructed in the Muon Spectrometer as a function of transverse momentum for $|\eta| < 1.5$. The alignment curve is for an uncertainty of $30 \mu\text{m}$ in the chamber positions.

spectrometer alone is not as good as the combination in a large p_T range between 30 and 200 GeV. Below that, the ID dominates and above the MS dominates.

2.2.6 Trigger and data acquisition

Proton-proton collisions and interactions are produced in enormous numbers at the LHC, but not all of them are of interest. Furthermore, the available technology limits the recording of data to the rate of 400 Hz, while at the design luminosity, the rate is approximately 40 MHz. Therefore, a preliminary selection must be made. The ATLAS trigger system is designed for this task.

The trigger system has a 3 level hierarchy, illustrated in Figure 2.22. The first level (L1) is based on custom-made electronics, while the Level-2 trigger (L2) and event filter (EF) use computers and networking hardware. The latter two are referred to as high level trigger (HLT).

The L1 trigger, the first trigger in the sequence, thus must be fast and robust to eliminate most of the background. For this reason, it only uses reduced granularity information—RPC and TGC for muons and the calorimeter towers for electromagnetic clusters, jets, τ -leptons, E_T^{miss} , and large total transverse energy. At this level, events with signature of high p_T objects are kept, such as muons, electrons, photons, jets and τ decaying to hadrons, as well as large missing E_T and large total transverse energy. With these selections, the rate is reduced to 75 kHz in $2.5 \mu\text{s}$.

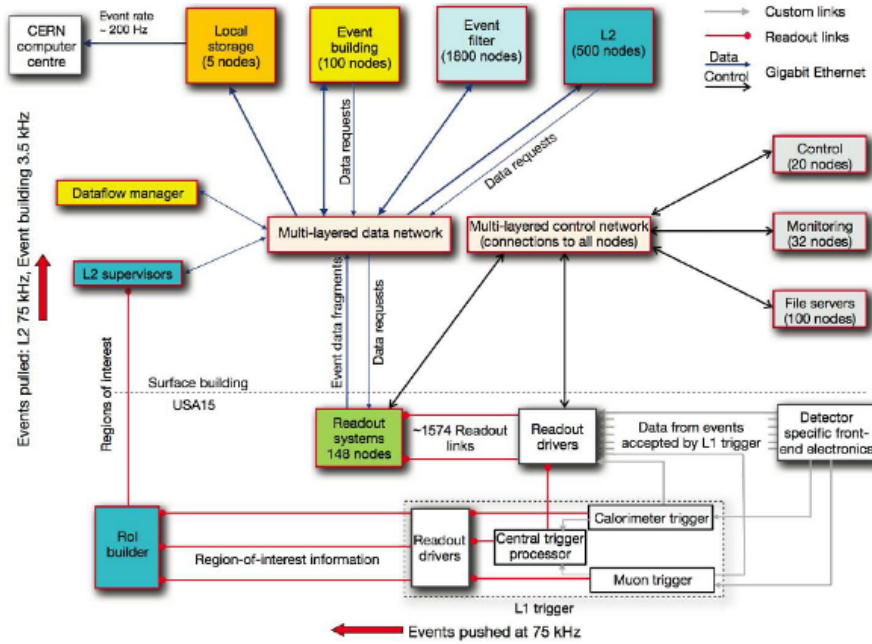


Figure 2.22: Block diagram of the ATLAS trigger and data acquisition systems

The detector regions where L1 objects are detected are called the regions of interest (RoI) and are analysed in detail by the L2 trigger. More accurate coordinates, energy, and signatures will further reduce the amount of data. This requires using the full granularity in the calorimeter and in muon chambers, as well as data from the inner detector. Due to the finer resolution, the thresholds of cuts are raised in L2. The data coming out of L2 is 3.5 kHz, in a processing time of 40 ms.

The event filter uses offline analysis procedures on fully-built events to further select events so that they can be recorded for subsequent offline analysis. This rate is approximately 200–400 Hz. The average processing time is of the order of 4 seconds per event.

The data transfer between the different trigger levels is performed by the data acquisition system (DAQ). It receives and buffers the data from the readout electronics at the L1 trigger rate, and transfers the RoI events to the L2 trigger. The events fulfilling the L2 selection criteria go through event-building and are assembled for the event filter. The finally selected events are then stored permanently.

The data acquisition system also has the function of configuring, controlling and monitoring the detector during data-taking. Another system, Detector Control System (DCS) is in charge of monitoring the detector hardware. The DCS puts the detector hardware into selected operational conditions, continuously monitors and archives its run-time parameters, and automatically performs corrective actions if necessary. Furthermore, DCS provides a human interface for the full control of ATLAS and its sub-detectors.

2.3 Object identification and reconstruction

The abundant particles produced at the LHC, mainly QCD jets, constitute a huge background to the objects of the interesting physics channels. Robust algorithms to reconstruct these objects like electrons, photons and muons are developed in ATLAS, allowing for physics analysis based on their accurate measurement. Full use of all detector systems allows for the identification of electrons and muons over a large energy range (5 GeV to 1 TeV).

2.3.1 Electron identification and reconstruction

Electrons are characterised by a charged track in the inner detector and an energy deposition in the electromagnetic calorimeter. Therefore, the reconstruction of electrons selects candidates by matching reconstructed tracks with clusters formed by the energy deposited in the electromagnetic calorimeter. Afterwards, the electron Particle Identification (PID) uses a set of variables with discrimination power against other particles like pions, photons and jets to help identify electrons.

Reconstruction of electron

The two key ingredients for electrons, are the inner detector track and the electromagnetic cluster. Reconstructed tracks, inside the tracking volume of $|\eta| < 2.5$, are extrapolated from their last measurement point to the middle layer of the calorimeter and are very loosely matched to the seed clusters. An electron is reconstructed if at least one track is matched to the seed cluster. In the case where several tracks are matched to the same cluster, tracks with more silicon hits are preferred, and the one with the smallest $\Delta R = \sqrt{\Delta\eta^2 + \Delta\phi^2}$ distance to the seed cluster is chosen.

The sliding window algorithm is used to find and reconstruct electromagnetic clusters. This forms rectangular clusters with a fixed size, positioned so as to maximise the amount of energy within the cluster. The optimal cluster size depends on the particle type being reconstructed and on the calorimeter region: electrons need larger clusters than photons due to their larger interaction probability in the upstream material and also due to the fact that they are bent in the magnetic field, radiating soft photons. In the 2012 reconstruction, seed clusters of longitudinal towers with total deposited transverse energy above 2.5 GeV are used for electrons. The window size is 3×5 in units of 0.025×0.025 in $\eta \times \phi$ space, corresponding to the granularity of the calorimeter middle layer.

The track reconstruction starts from track seeds, they are formed of pixel hits and space points of the SCT first layer, then track candidates are fitted after extrapolating the seeds through the SCT. The extension to the TRT drift circles, followed by refitting tracks to exclude outliers that result in bad fit quality, builds the tracks in the inner detector. The whole procedure treats the charged tracks using a pion particle hypothesis to estimate the

material effects. Bremsstrahlung increasing with material encountered causes energy loss of 20—50 % for electrons when leaving the SCT, which is not considered in the reconstruction. This will result in inefficiencies in reconstruction and a degradation of the estimated track parameters. A refitting of selected tracks is therefore performed, taking into account the non-linear bremsstrahlung effects with the so-called Gaussian Sum Filter (GSF) [17]. The GSF is a non linear generalisation of the Kalman filter, which has been implemented in ATLAS, it assumes the trajectory state can be approximated as a weighted sum of Gaussian functions.

A preselection of tracks for GSF refitting is made to speed up the algorithm. The tracks include both those tracks that match well the cluster and those that potentially have lost a lot of energy due to bremsstrahlung and could match the cluster well after correcting for this energy loss. These preselected tracks with silicon hits are refitted using the GSF yielding better estimates of the track parameters in the transverse plane. TRT hits do not have enough precision for such a refit to be beneficial and hence standalone TRT tracks are not used.

Although all tracks assigned to a cluster are kept for further analysis, only the best matched one is used to determine the kinematics and the charge of the electron. Thus the choice of the primary track is one of the most critical decisions in the electron reconstruction chain.

Previously, a track with more than three silicon hits takes precedence over a track with less (TRT standalone). In case of two tracks having more than three silicon hits the one with the smallest distance between its extrapolated impact point and the cluster barycentre is preferred (both quantities are calculated in the 2nd layer of the EM calorimeter). The improved track matching strategy continues to rely heavily on the distance between the cluster barycentre and extrapolated track. The selections favour the primary electron track with the longer track and aim to avoid random matches between nearby tracks in case of cascades/trident due to bremsstrahlung.

The reconstruction efficiency (including criteria on the number of pixel hits and silicon hits exceeding 1 and 7, respectively) is shown as a function of the pseudorapidity η for electrons with transverse energy between 30 and 50 GeV, for data and MC from 2011 (default track) and 2012 (track with GSF) (Figure 2.23(a)). Over this E_T range, the absolute increase in reconstruction efficiency in 2012 as compared to 2011 for both data and MC is $\sim 1\%$ in the barrel region of the calorimeter and $\sim 5\%$ in the end-caps (where there is more material in front of the calorimeter, hence more electrons undergo bremsstrahlung emissions).

Averaging over the pseudo-rapidity coverage of the central calorimeter ($|\eta| < 2.47$) (Figure 2.23(b)), the absolute increase in reconstruction efficiency in 2012 as compared to 2011 for both data and MC is $\sim 2\%$ for the high E_T region and up to 6-8% for the low E_T (< 20 GeV) region, which is particularly important for searches using low momentum leptons.

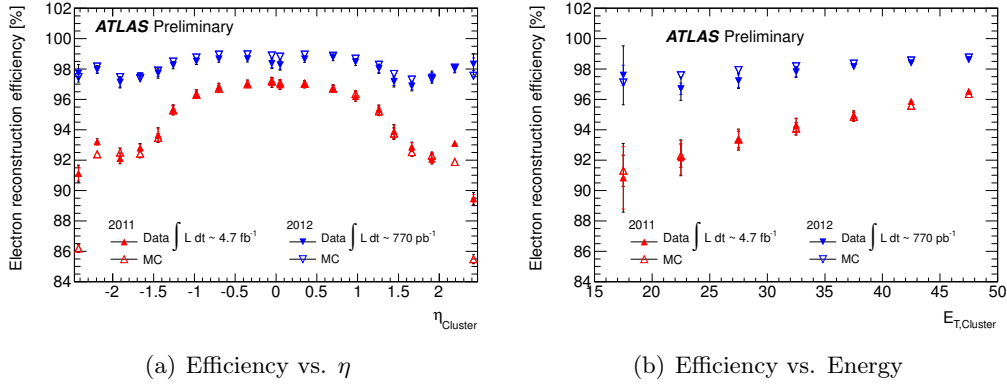


Figure 2.23: *Electron reconstruction efficiency with the old and new reconstruction for $Z \rightarrow e^+e^-$ samples in data and MC*

Identification of electrons

To make use of the new information at hand from the improved track fit, an improved electron PID menu (referred to as the "MultiLepton" menu) was created that was both more robust against pileup and ensured that background rejection remained constant. The strategy to obtain the stated goals was to relax cuts on known pileup sensitive variables (mostly calorimeter variables) and to add additional cuts on the track matching variables, which depend on whether the track had a significant energy loss or not.

The menu is based on the same calorimetric variables as those used in the trigger menu that can discriminate electrons from jets and π s. These calorimetric variables are:

- w_{tot} the total shower width in the first sampling,
- $w_{\eta 2}$ lateral width in the second sampling,
- E_{ratio} ratio of the energy difference between the largest and second largest energy deposits in the cluster over the sum of these energies in the first sampling,
- R_{had1} the ratio of energy in the first sampling of the hadronic calorimeters behind the cluster over the energy of the cluster,
- R_{η} the ratio of energy around the cluster centre in a square of 3×7 divided by the energy in a square 7×7 ,
- f_3 the fraction of energy reconstructed in the third sampling .

To ensure that the fake rejection of the electron PID menu was not decreased, additional pileup robust variables of the shower shapes in the calorimeter were introduced, in particular tighter track matching requirements.

The final identification efficiency measurement for the "MultiLepton" selection criteria has been evaluated with MC and data. The robustness against pileup is shown in Figure 2.24, where the reconstruction efficiency is stable as a function of the number of reconstructed primary vertices. The efficiency measurement (full triangles) is constant within 2% in data and deviates from the MC simulation (open triangles) over the full range by less than 0.5%.

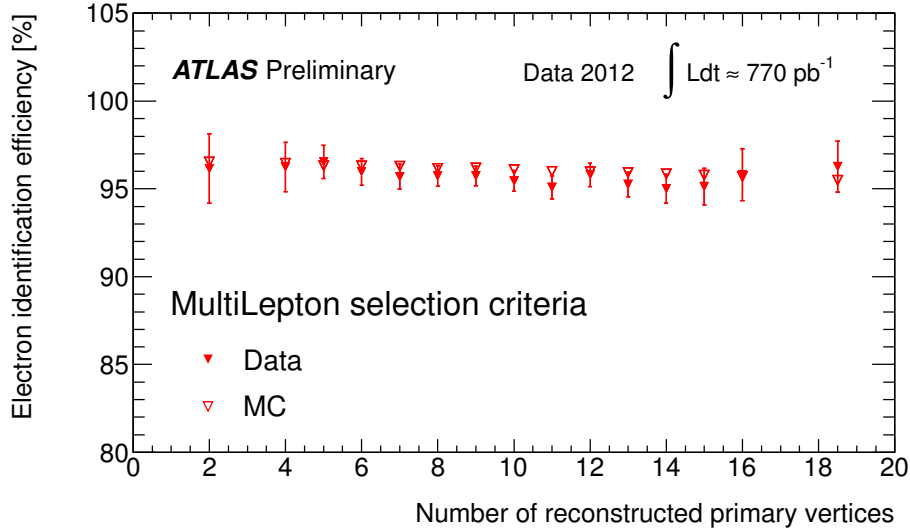


Figure 2.24: Efficiency of the new electron selection criteria as a function of the number of reconstructed primary vertices in data and MC

2.3.2 Muon identification and reconstruction

The collisions at the LHC will produce a broad spectrum of final-state muons. The Muon Spectrometer can detect muons with momenta ranging from approximately 3 GeV to 3 TeV in $|\eta| < 2.7$. Further accurate track parameter measurement can be achieved by combination with the inner detector track, but only up to $|\eta| < 2.5$ due to the limited coverage of the inner detector. Improvement is also seen when using the calorimeter to take into account the multiple scattering and energy loss. Two independent algorithms, STACO and MUID are developed with three track reconstruction strategies respectively. The default algorithm used in this analysis and described below is STACO, unless stated otherwise.

The reconstruction starts with track finding in the muon spectrometer, which is logically sub-divided into the following steps:

- Identification of ROA (region of activity) through trigger chambers (RPC and TGC).
- In the ROA, a pattern is formed with a pair of hits in a precision chamber (MDT or CSC), associated with nearby hits in the chamber.

- A segment is built by a straight line fit to all hits in the pattern, a valid approximation considering the size of the chamber compared with the total trajectory in the MS.
- A global track fit is performed linking nearby segments. It takes into account in full detail the geometrical description of the traversed material and the magnetic field inhomogeneities along the muon trajectory

The details of the segment forming will be discussed in section 3.3. After the track is reconstructed in the muon spectrometer, the full trajectory of the muon across the whole detector is determined either by matching with the inner detector track, or simply by extrapolation to the perigee. Depending on the strategy, the following three categories of muon will be reconstructed

- Stand-alone (SA): The muon track reconstruction is based solely on the muon spectrometer track over the range $|\eta| < 2.7$. The track is then extrapolated to the beam line by taking into account the multiple scattering and energy loss in the calorimeter. For STACO, the energy loss is parameterised according to the material in the path crossed by the muon in the calorimeter.
- Segment-Tagged (ST): Muons with low momentum may not have enough energy to reach the 2nd or 3rd station in the muon spectrometer, due to the energy loss upstream of the MS and the bending in the toroidal field, which make it difficult to form a track in the SA algorithm. Similar problems arise in certain regions of the muon spectrometer, where the number of stations is less than 3, e.g. at $|\eta| \sim 1.3$. In such conditions, the individual segments will look for a possible matching track in the inner detector, to form a complete muon trajectory. The parameters from the ID track will be taken.
- Combined Muons (CB): By statistically combining the independently reconstructed MS tracks and ID tracks combined muon candidates are obtained. The parameters of the reconstructed tracks and their covariance matrices are used to select the best pair. Taking advantage of the precise inner detector measurement of track parameters, the momentum resolution is improved below 100 GeV. In addition, a higher purity, i.e. muon identification compared with the other two categories is obtained, because the inner detector information can suppress backgrounds from pion punch-through and from pion or kaon decay in flight.

The three categories of muons are exclusive. If the muon is in the range $|\eta| < 2.5$, given the better resolution and higher purity, the combined muon will be kept instead of the standalone muon. In this way, stand-alone muons are only used for $|\eta| > 2.5$. In the region $|\eta| \sim 0$, there is no coverage by the muon spectrometer, so that another way of reconstructing the muon is used, namely the Calorimeter-Tagged muon. The missing information of MS is substituted by the calorimeter, by requiring the presence of a minimal

energy deposit in all calorimeter layers along the projected track trajectory found by inner detector.

Figures 2.25(a) and 2.25(b) show the expected reconstruction efficiency at a c.m. energy of 14 TeV, as a function of transverse momentum and pseudo-rapidity. Above 6 GeV, 95% efficiency is achieved. Figure 2.26(a) shows the reconstruction efficiency of CB+ST muons by STACO using 2011 MC and data, as a function of p_T . Figure 2.26(b) shows the same efficiency as a function of η for muons with $p_T > 15$ GeV. An overall efficiency $> 95\%$ is observed, except in the $\eta \sim 0$ region, where the efficiency is recovered by calorimeter tagged muons.

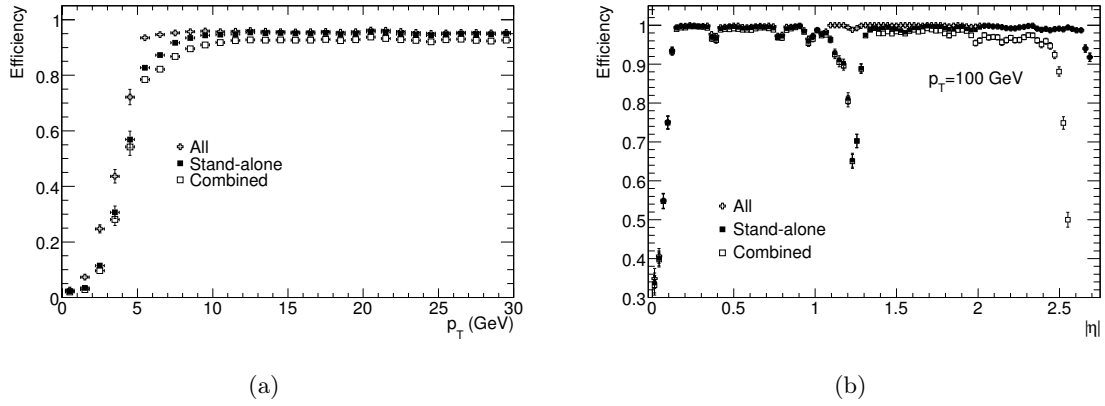


Figure 2.25: Expected efficiencies of the muon reconstruction algorithms for prompt muons as a function of (a) transverse momentum and (b) pseudo-rapidity. The label ‘All’ groups combined, stand-alone and tagged muons at c.m. energy of 14 TeV.

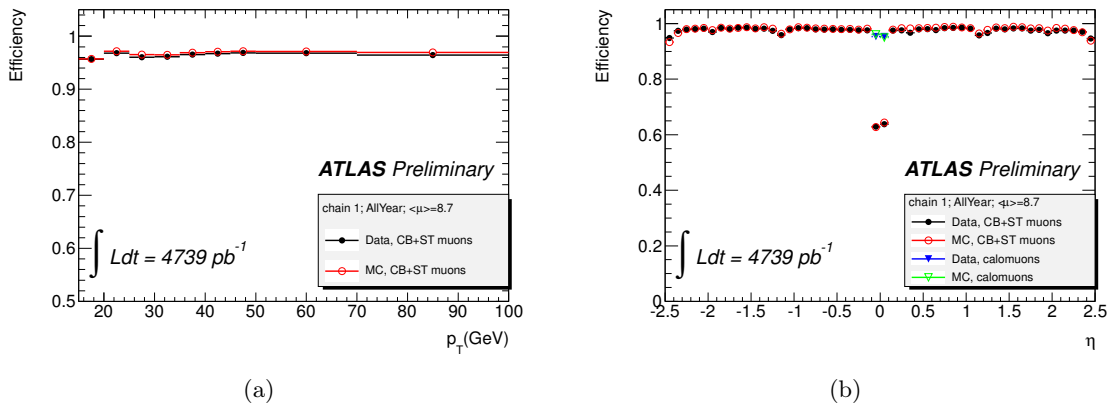


Figure 2.26: Efficiency for CB+ST muons as a function of (a) transverse momentum and (b) pseudo-rapidity of the muons [18].

Further criteria to improve the rejection against background are applied in the analysis. Different types of muon need to fulfil specific requirements. As an example, for combined muons the inner detector tracks entering the combination may have to satisfy a set of

criteria linked to the detector conditions. The details on the selection will be discussed in the analysis section.

Chapter 3

MDT chambers wire position measurement with X-ray tomography

The ATLAS Muon Spectrometer is designed to resolve muons over a wide momentum range. For the purpose of providing precise tracking, the MDT chambers are installed everywhere except in the forward region ($|\eta| > 2.0$) where they are replaced by CSC. The momentum is determined from the curvature of the three point track measured by MDT chambers. The curvature is expressed as a sagitta, which is defined as the distance from the centre of the track arc to the straight line connecting the arc ends. The momentum accuracy of the spectrometer is designed to reach 10% in the high momentum range. This imposes a stringent requirement on the chamber precision: the sagitta of a 1 TeV p_T muon is $500 \mu m$, hence its resolution should be $50 \mu m$. The drift tube, which is the basic element of the MDT chambers, has an intrinsic resolution of $80 \mu m$. The overall design precision is obtained because there are three or four layers of tubes in each MDT chambers. Furthermore the wire within single tubes must be positioned with an accuracy of $20 \mu m$ within a MDT chamber. This is achieved by both precise assembly of the element tubes to their fiducial positions and correct placement of the chamber in the spectrometer. Two systems, the X-ray tomography system and the alignment system are exploited to monitor the two aspects, respectively. The alignment system is used to verify the chamber position in the muon spectrometer. It monitors possible deformation and displacements of the chamber with respect to their nominal position. The X-ray tomography, on the other hand, is devoted to controlling the mechanical precision of each chamber [19]. It measures the relative position of the tube wires inside the chamber. This is achieved by distinctive absorption of an X-ray beam in the different materials composing the tube and the wire.

This section will focus on the verification of the inertial position of the MDT chambers by using the X-ray tomography. The basic structure of the MDT chamber will be introduced in section 3.1. The working principal of the X-ray tomography and the result of the X-ray analysis will be shown in section 3.2. The impact on the muon resolution is discussed in section 3.3.

3.1 The MDT chambers

The measurement of the precision coordinate in the bending direction of the muon track is provided by the MDT chambers. The basic detection element of a chamber is a cylindrical aluminium drift tube as described in section 2.2.5. In this section, the operating principle of the drift tube will be introduced. The composition of the tube and the structure of the MDT chamber assembled from tubes will be shown in section 3.1.3.

3.1.1 Operating principle

The drift tubes are installed to provide hit position measurement, which will be collected and further used to reconstruct a complete track. The key elements are W-Re (Tungsten-Rhenium) wires at high voltage, non-flammable gas, and a time-to-digital converter (TDC). When the charged particle transverses the tube, the gas is ionised. The produced electrons drift to the wire under the electric field generated by the voltage difference between anode and cathode. Near the wire, an avalanche is produced due to the very high electric field, which results in a larger signal. Then the signal is propagated to an amplifier and the timing pulse will be transferred to a TDC located at the end of the tube. The time between the muon passage and the arrival of the signal to the wire reflects the distance of the track to the wire. It is used to determine the position of the hit via the r-t relation introduced in section 2.2.5, and shown in Figure 3.1. The precise r-t relation is obtained by a calibration procedure using data.

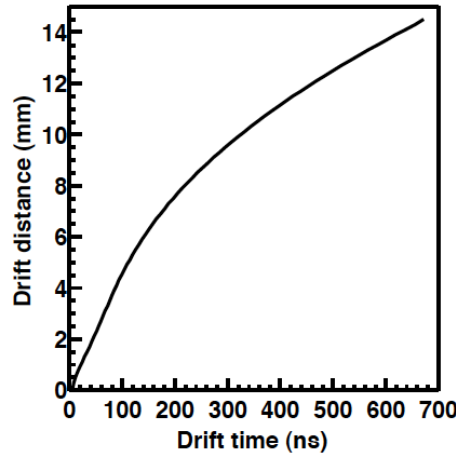


Figure 3.1: Measured relation between drift distance and drift time for the ATLAS operating point [20].

3.1.2 The drift tubes

The drift tubes are designed for optimal performance, taking into account the LHC operating conditions, the need for uniformity of the spectrometer layout and financial constraints.

Figure 3.2 shows a schematic drawing of its structure. The components are: a 30 mm diameter tube with a 400 μm wall as the cathode, a W-Re wire of 50 μm diameter as the anode, the Ar-CH₄-N₂ mixture gas for producing the avalanche, and the end-plugs at both ends for accurate positioning of the anode wires, wire tension, gas tightness, and electrical and gas connections. The fabrication of the drift tube follows strict rules. Measured along the tube axis, the deviation from straightness is required to be less than 30 μm . The gas mixture is chosen to avoid after-pulsing and to limit the maximum occupation time to 500 ns. The end-plugs should hold the wire in the centre of the tube with a precision of 10 μm . The gas leak rate should be less than 10^{-8} bar l/s and the wire tension of 350 ± 7 g (r.m.s) [21].

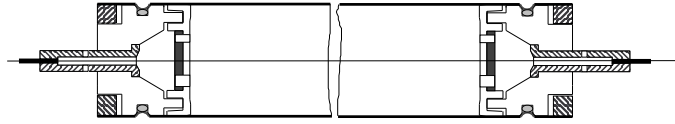


Figure 3.2: Schematic view of a monitored drift tube [21].

3.1.3 Chamber design

To improve the resolution of a chamber beyond the single-wire limit and to achieve adequate redundancy for pattern recognition, the MDT chambers are constructed from 2×4 monolayers of drift tubes for the inner, and 2×3 monolayers for the middle and outer stations. The number of tubes in each layer varies according to the geometry of the spectrometer. The three or four layers compose a multilayer, and the two multilayers in a chamber are separated by a spacer and support structure. The support structures provide accurate positioning of the two multilayers with respect to each other and mechanical integrity under effects of temperature and gravity. There are three cross plates to which the multilayers are attached, and two long beams connecting the cross plates. The layout in the spectrometer was optimised in view of standardisation to reduce the number of different chamber sizes. The spacers are 170 and 317 mm in the barrel and 121 and 170 mm in the end-caps. The schematic drawing of a MDT chamber is shown in Figure 3.3.

The total number of MDTs is 1194 making a total area of 5500 m^2 . The number of drift tubes is 371 488. Considering the enormous number of chambers, their different sizes, shapes and structures, a naming system is needed. The following nomenclature is used.

- **Region** The chambers are first distinguished between barrel (B) ($|\eta| < 1$) and end-cap (E) region, where the typical chamber shapes are different. The end-cap chambers are subdivided into an inner and outer ring, denoted as F (for forward) and E (for external) respectively.
- **Location** Depending on the location of the chamber, it is named as I (inner), E (extra), M (middle), and O (outer).

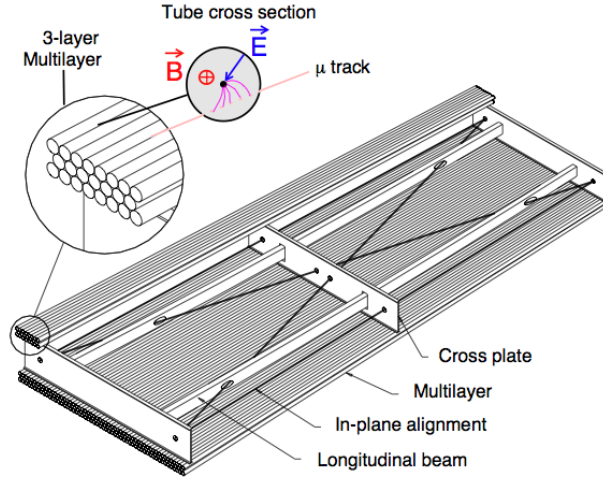


Figure 3.3: Schematic drawing of a rectangular MDT chamber constructed from multilayers of three monolayers each, for installation in the barrel. The chambers for the end-cap are of trapezoidal shape, but are of similar design otherwise. In the toroidal magnetic field, the tubes are oriented essentially parallel to the field lines [21].

- **Sector** As introduced in section 2.2.5, there are large (L) and small (S) sectors according to the azimuthal region of the chamber location. The chambers are also labelled from 1-16 in the azimuthal direction, as shown in Figure 3.4.
- **Projective tower** The octant structure is repeated along the z direction. The chambers at the same azimuthal angle are counted from 1-6 along z axis in both directions, starting at $z = 0$.
- **Side** The two detector hemisphere are defined by the positive (A) and negative (C) z -direction.

Based on the above rules, a typical chamber name can be written as BIL1A15, B: barrel chamber; I: inner; L: large sector; 1: first tower near $z=0$; A: z positive; 15: sector number 15.

3.2 X-ray tomography

3.2.1 Introduction

To verify a wire positioning accuracy of $20 \mu m$, a quality control device with a precision of $\sim 5 \mu m$ is needed. Such a dedicated X-ray tomography has been developed at CERN since 1996 [19]. X-ray tomography was chosen to measure the precise position of the wire thanks to its two features:

1. It is capable of detecting micron-sized tungsten wires hidden inside the aluminium drift tubes. This is due to the absorption coefficients of X-ray photons being different

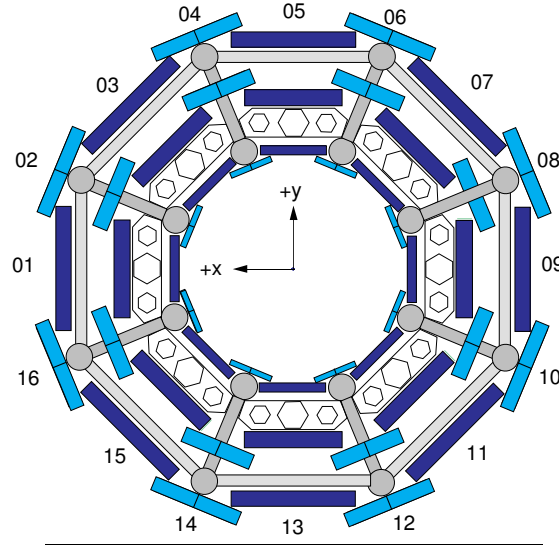


Figure 3.4: Definition of sectors of the ATLAS muon spectrometer [21].

for various materials.

2. The narrowly collimated X-ray beams allow for a precise peak position accuracy of $1-2 \mu m$.

The absorption coefficient depends on the X-ray energy (W) and the atomic number (Z) of the attenuating material and varies as $(Z/W)^3$ at $W=40$ KeV. Thus the large difference between tungsten and aluminium atomic number (79 and 13, respectively) makes it possible to detect the wire in the MDT chambers. The energy of the X-ray is chosen at a moderate value, so that the distinction between the materials is still possible when the energy is high, nor that the absorption is too high when the energy is low. The optimum energy range then is between 30 and 50 KeV. The photons not absorbed by the material are detected by scintillators.

The working principle of X-ray tomography will be explained in section 3.2.2, and the X-ray tomography structure suited for the MDT chamber will be presented in section 3.2.3. To interpret the output from X-ray tomography, a program "scana" was developed. The method will be introduced in section 3.2.4.

3.2.2 Working principle

The X-ray beam is set to move along the cross section of the MDT chambers, it aims to provide projective measurement of the wire positions in a two-dimensional map. While scanning, the photon absorption is different among the wire, the tube and the gas, which leads to a characteristic scintillator counting rate for each. This is used to identify the position of the wire. There are two methods of scanning, passive and active.

Passive method The passive procedure exploits the absorption contrast between different materials. The MDT chamber is transparent to the X-ray, while strong absorption occurs at the tungsten wire, and relatively weak absorption for the aluminium tube wall and the gas. This is reflected in the output intensity of the scintillator, as shown in Figure 3.5 (top), where four wires are seen as the peaks in the "shadowgram". Then the position of the peak can be reconstructed as the wire position.

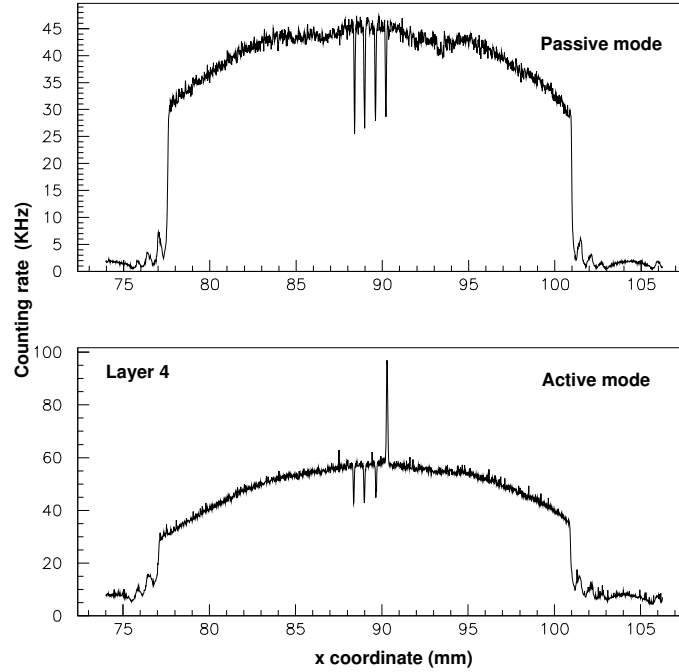


Figure 3.5: Count rate in the scintillator in passive (upper frame) and the active tube layer in active method (lower frame) as a function of the X-ray source position [21].

Active method When the X-ray beam hits the wire with high voltage turned on, photoelectrons, Auger electrons and fluorescence are produced at a much higher rate than in the gas or in the walls. These radiations cause direct ionisation in the gas if they escape from the surface of the wire. The ionisation will produce a signal to the tube readout, which leads to a positive peak in the shadowgram in contrast with the shadow peaks read from scintillators. The output from this mode is shown in Figure 3.5 (bottom).

3.2.3 X-ray tomography structure

The scheme of the X-ray tomography is shown in Figure 3.6. The X-ray tomography consists of two X-ray beams so that it can provide stereo measurement of the tube position in the chamber plane where the precision measurement is made. The direction of the two beams are $+30^\circ$ and -30° w.r.t the vertical direction. This stereo angle ensures that each beam can cross one tube per layer. The X-ray sources are mounted on a carrier,

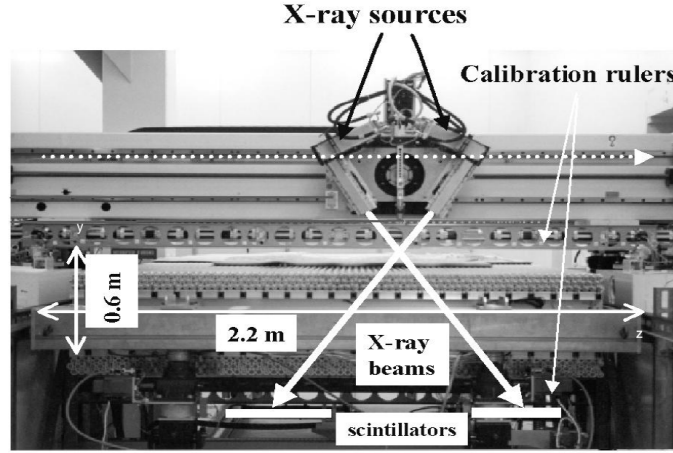
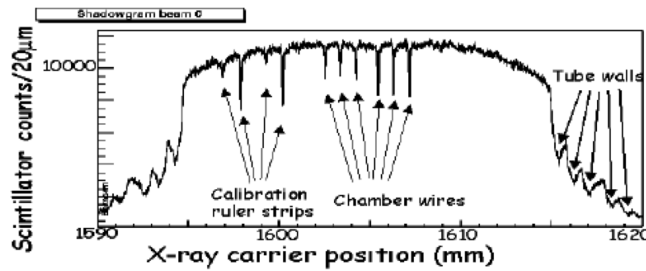


Figure 3.6: The structure of the X-ray tomography [22].

which moves linearly perpendicular to the tubes. The photons are detected by two NaI (Tl) crystals, each coupled to two photomultiplier tubes read out in coincidence. Two externally measured reference strip systems define a spatial grid for the vertical scale and for the orthogonality of the tomography coordinate system. One of these so-called calibration rulers is installed above and one below the chamber to be measured.

As the X-ray beams scan across the chamber, the scintillators record the counts so that a "shadowgram" can be produced as shown in Figure 3.7. In this figure, the three small and large peaks originate from a beam across the three layers of the upper and bottom multilayer.

Figure 3.7: Part of a full chamber absorption diagram along the z direction [23].

3.2.4 Analysis of the scan data

Coordinates and convention The coordinates are defined in the chamber plane, which is therefore called local chamber frame in contrast with the global ATLAS detector coordinate system.

The measurement plane is defined by x and z . Tubes are counted along the positive z direction and the y -axis points up-wards (out of the chamber plane), as shown in Figure 3.8.

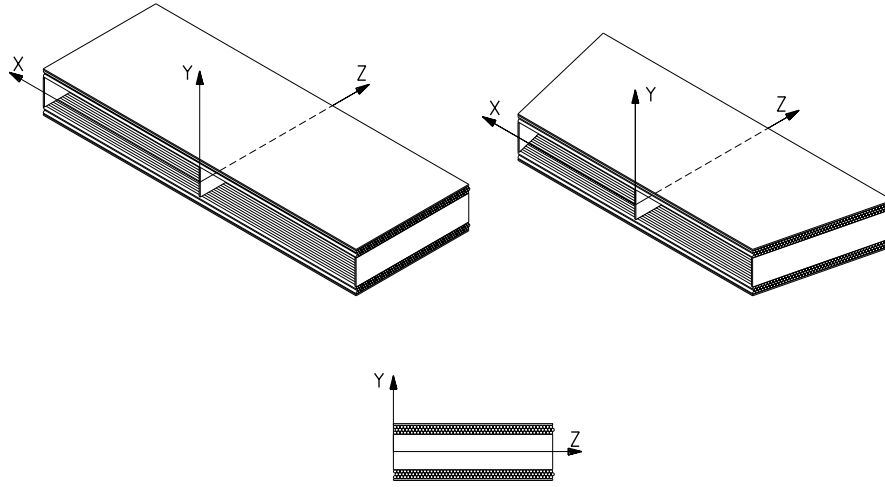


Figure 3.8: Local chamber frame

The x-axis is along the tube direction. The origin of the coordinate system lies in the mid plane of a chamber. It is defined as the point in the mid-plane, which is closest to the interaction point if the chamber were positioned in the spectrometer. In the trapezoidal end-cap chambers it is in the middle of the shorter edge.

Since the chambers are placed differently in the barrel and endcap, the local coordinates differ. Figure 3.9 shows the chamber coordinates xyz (sometimes described as szt with $s=x$, $z=y$, $t=z$) viewing from the global system rotated with the chamber direction.

X-tomography analysis The X-ray tomography data are a sequence of values of interferometer measurements of the scanner position and the intensity of the beams. The pattern recognition of the peaks is first performed. All recorded absorption peaks are fitted with a Gaussian shape and a linear background. Then the peak positions are determined with an average precision of $1.7 \mu m$ [22]. Subsequently, every peak is associated with a chamber layer or with a calibration ruler layer. The procedure is based on the fact that the wires are equidistant in each layer, with the typical space of $30 \mu m$. This value is let floating within a certain range to fit the data. After being reconstructed, the layers are ordered into a chamber. Finally, the two beams are matched to find the first and last wires in every layer.

Up to now, the relative position of the wires to the X-ray source are known. In order to reconstruct precise maps, the geometrical parameters of the X-ray carrier are calibrated. The procedure consists in minimising the residuals between the precisely known positions of the calibration ruler strips and the tomograph measurements. The two dimensional wire positions are then reconstructed using the geometry fit results. The relative displacement of each wire compared with the nominal design is plotted, Figure 3.10 shows such an example.

With the knowledge of the chamber wire position, one can derive the overall chamber

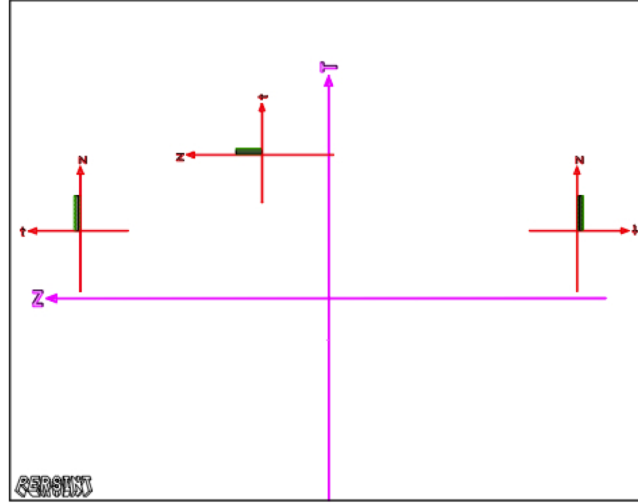


Figure 3.9: Local chamber frame, projected on global X direction. The szt system corresponds to the xyz system in the transfer form: $s=x$, $z=y$, $t=z$ [24].

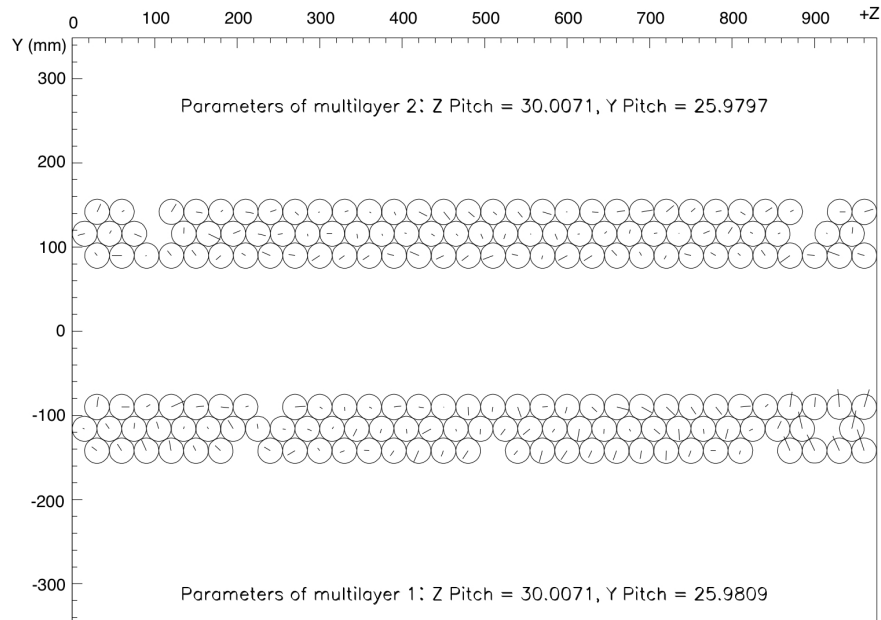


Figure 3.10: Wire displacements in BML prototype: The line inside each circle represent wire displacement in both value and direction

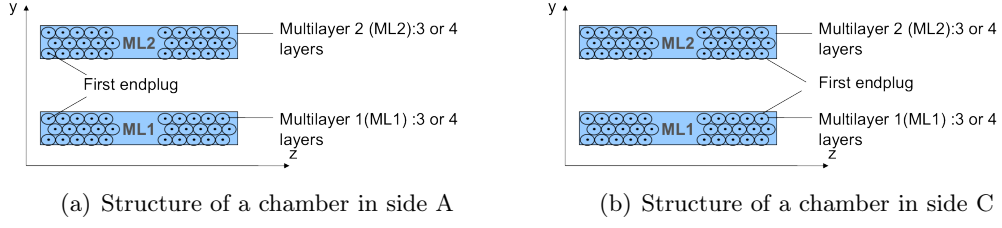


Figure 3.11: The first end-plug position in a chamber

quality. This can be evaluated by a set of parameters, also called as-built parameters :

1. δy : Vertical shift between multilayers
2. δz : Horizontal shift between multilayers
3. $\delta\alpha$: Angle between multilayers
4. y_{pitch} : Adjacent distance between layers in the y direction
5. z_{pitch} : Adjacent distance between tubes in the z direction
6. y_0 : Shift of the first tube in a multilayer in the y direction; here the definition of "1st tube" is defined in Figure 3.11. 1st means first tube in the layer and first layer of the multilayer.
7. z_0 : Shift of the first tube in a multilayer in the z direction

The illustration of the parameters is shown in Figure 3.12. The parameters are obtained from a grid fit of the wire positions. The fit minimises the residuals between the measured wire positions and the knots of the ideal hexagonal grid with the parameters:

$$\chi^2 = \sum_i (z_i^{meas} - z_i^{grid})^2 + (y_i^{meas} - y_i^{grid})^2$$

where the $z(y)_i^{meas}$ and $z(y)_i^{grid}$ represent the measured coordinates and the fiducial coordinates calculated by the above parameters, respectively. Note that here only five parameters are entered in the fit, y_0 and z_0 can be calculated from these five parameters.

3.2.5 Analysis results

The 1196 MDT chambers in ATLAS were constructed by 13 institutes around the world. Deviations from the design are inevitable. For the chambers manufactured by the same institute, there is a characteristic value of the 7 parameters. They are obtained from the tomography scan result of the prototype. These sets of parameters are referred to as nominal hereafter. After all the chambers are built, 15% of them are scanned by X-ray tomography for quality checks.

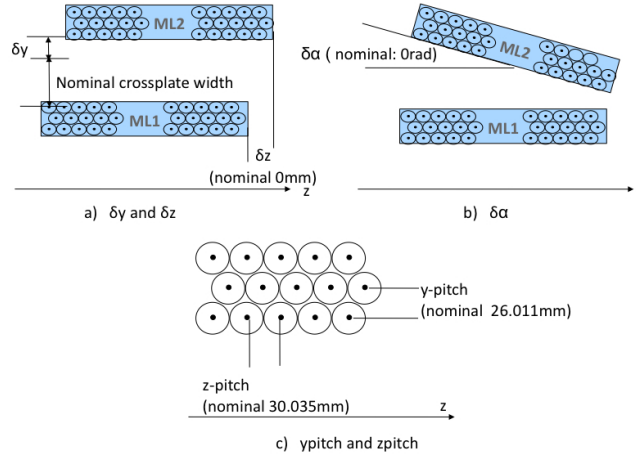


Figure 3.12: Parameters of the MDT chambers

The set of parameters for each chamber are summarised in a table. An example for a BIS chamber with 2×4 layers of tubes is given in Table 3.1. The first row gives its basic information, such as chamber name, constructor, whether it is scanned or not. Rows 2-5 give 4×7 parameters representing the quality of the chamber. Rows 2 and 3 give the first multilayer information on positive and negative x side respectively, and row 4 and 5 concern the second multilayer. $\delta\alpha$ is always 0 in multilayer 1 since it represents rotation between the two multilayers. The last row lists the nominal value of all parameters. For those chambers not scanned, the nominal values are taken.

Figure 3.13 shows the distribution of the chamber parameters from each constructor. The red entry represents the nominal value, whereas the black dots show the parameters of scanned chambers. As seen from the figure, the deviation of the parameters differs from site to site. In general, the z pitches are distributed around the nominal values within $\sim 2\mu m$. Considering that there are around 30 tubes in the layer of a small chamber, the overall shift will amount to $60\mu m$. The average shift in y pitches is at the level of $10\mu m$. The vertical deviation between multilayers in some chambers are as large as $300\mu m$. The rotation between the two multilayers are less than $100\mu rad$, with one exceptional chamber of $400\mu rad$.

The most spectacular displacement is seen in the z direction, as shown in Figure 3.14. Two chambers show displacements of 1.5 mm and 3 mm respectively, and the displacement has opposite direction at the two ends of the chamber, which indicates a rotation around x axis. The schema of the two chambers are shown in Figure 3.15.

3.3 Muon reconstruction and the as-built parameters

In the context of ATLAS muon reconstruction, the geometry information such as the position of the chambers and the wires are essential for determining the curvature of the

track. This information is provided by the ATLAS Muon DataBase description (AMDB). Currently still the design values for the wire positions are used, but these values can be wrong as demonstrated by the tomography measurements. In section 3.3.1, the impact of the wire position in the muon reconstruction will be studied. A possible way to include the as-built parameters in the AMDB is exploited in section 3.3.2, and the effects of the incorrect wire positions are shown in section 3.3.3.

3.3.1 Muon trajectory reconstruction in the muon spectrometer

The chain of reconstructing a complete track has been described in section 2.3.2; more details on the segment reconstruction will be given here to better understand the importance of the wire position.

A segment is a part of the track within one chamber. The size of the chamber is small enough to neglect the curvature of the track, thus, the segments are reconstructed as straight lines. The segment reconstruction starts from a hit. Whenever there is a hit detected in the tube, a circle with the radius r is drawn according to the recorded drift time t and the r - t relation. In this way, a series of circles describe the trajectory of the muon. The next step is to find the best path matching all these circles. The matching starts from a pair of hits: one from the bottom multilayer and one from the top. There are four possible tangent lines passing through the two chosen circles, and each line may be a possible track of the muon, as shown in Figure 3.16. To reduce the ambiguity, all four

chamber	constructor	xray flag	N_{tube}^{ml1}	N_{tube}^{ml2}	N_{ml}	N_{layer}
BIS6A10	THE	1	30	30	2	4
y_0	z_0	δy_0	δz_0	$\delta \alpha_0$	$ypitch_0$	$zpitch_0$
-15	15	0	0	0	-26.0157	30.0350
y_1	z_1	δy_1	δz_1	$\delta \alpha_1$	$ypitch_1$	$zpitch_1$
-15	15	0	0	0	-26.0147	30.0352
y_2	z_2	δy_2	δz_2	$\delta \alpha_2$	$ypitch_2$	$zpitch_2$
15.029	14.993	0.035	-0.007	-0.00001300	26.0134	30.0339
y_3	z_3	δy_3	δz_3	$\delta \alpha_3$	$ypitch_3$	$zpitch_3$
15.032	15.000	0.036	-0.000	-0.00000900	26.0156	30.0343
y^{nom}	z^{nom}	δy^{nom}	δz^{nom}	$\delta \alpha^{nom}$	$ypitch^{nom}$	$zpitch^{nom}$
15	15	0	0	0	26.011	30.035

Table 3.1: Chamber information, units are mm and $mrad$. The first row gives its basic information, such as chamber name, constructor, whether it is scanned or not. Rows 2-5 give 4×7 parameters representing the quality of the chamber. Rows 2 and 3 give the first multilayer information on positive and negative x side respectively, and row 4 and 5 concern the second multilayer. $\delta \alpha$ is always 0 in multilayer 1 since it represents rotation between the two multilayers. The last row list the nominal value of all parameters. For those chambers not scanned, the nominal values are taken.

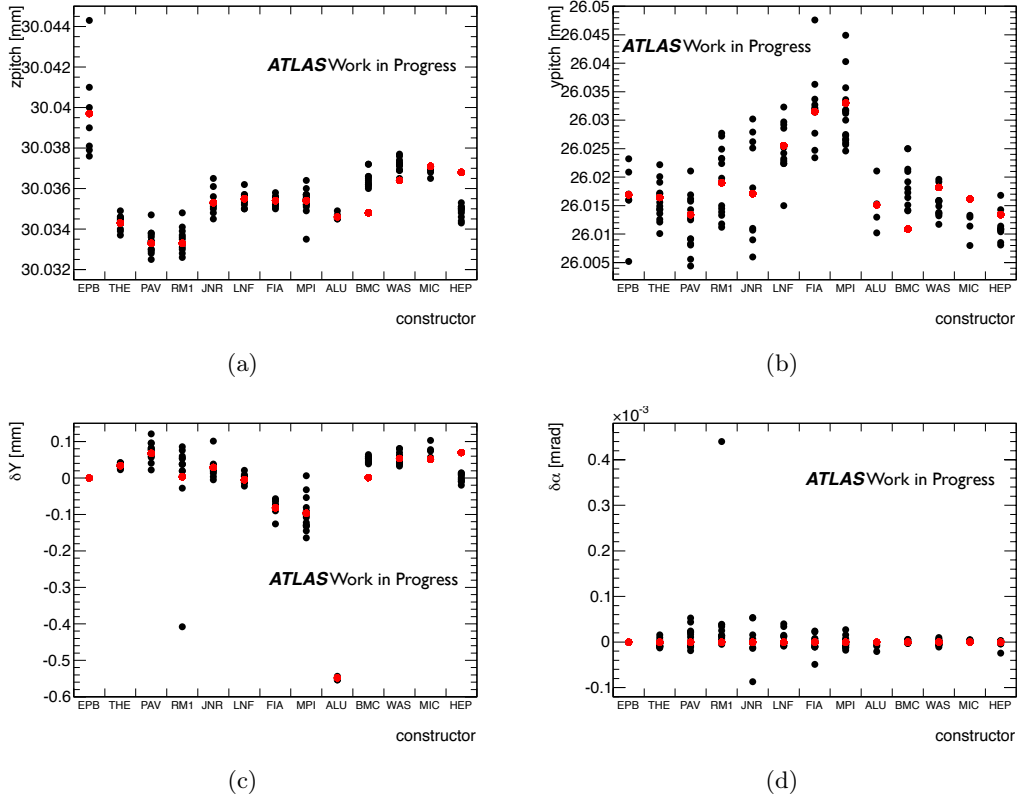


Figure 3.13: The quality parameters of MDT chamber. (a) z pitch (b) y pitch (c) δy (d) $\delta \alpha$. The red entry represent the nominal value, whereas the black dots shows the parameter of scanned chambers.

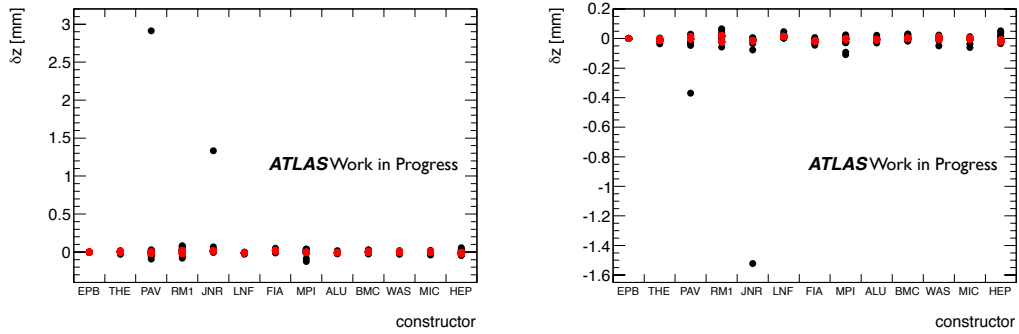


Figure 3.14: The δz distribution in both ends of the MDT chambers.

candidates are extrapolated to all the other hits in the chamber, which are less than 5 mm away from the line, which results in multiple combinations. An additional requirement that each set of extrapolation should consist of at least four hits (two hits per multilayer) reduces the random combinations. The candidate lines passing the selection are called patterns. Duplication removal is implemented by eliminating patterns sharing the same

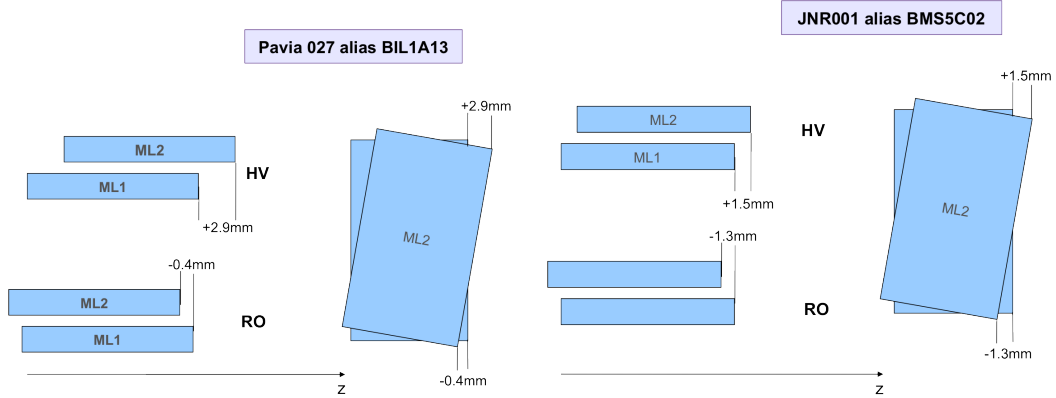


Figure 3.15: The (a) BIL1A13 (b) BMS5C02 chamber scheme, which shows a large shift in the z direction resulted from rotated multilayers.

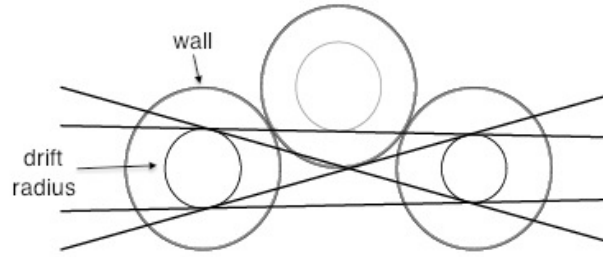


Figure 3.16: 4 tangent line for two hits

hits or being a subset of each other. Usually only one pattern per chamber will survive. Then a χ^2 fit is performed with the assumption that the track is straight. The fit begins with all hits in the pattern, if the χ^2/N , where the N is the number of degree of freedom, is smaller than 5, a segment is declared valid, otherwise, 1 hit which causes the largest χ^2/N will be excluded and the procedure repeated until the fit quality reaches the $\chi^2/N < 5$ requirement.

As seen from the above procedure, whether or not the position of the wire is correct is very important. When the actual position is different from the design value, the extrapolation may lose hits in the track or bring wrong hits to the track; it may as well affect the quality of the final fit, the χ^2 being a quadric sum of the distance to the line to each hit. By using the correct wire position obtained from X-tomograph, the reconstruction will be of a better quality.

3.3.2 Wire position reconstructed with as-built parameters

The X-ray tomography provides very precise position coordinates of each wire. However, if all the 371488 wire coordinates are recorded in the AMDB, the reading of the database and further reconstruction will be very time-consuming. Given that the wires are at quasi

equal distances, the seven parameters which define the quality of the chamber are used instead of the wire positions. For those chambers that are scanned by X-ray tomography, the parameters are from the grid fit, while for the others, the nominal values are taken.

Among the seven parameters, two can be derived from the others, namely the first tube coordinates y_0 and z_0 :

$$y_0 = y^{nom} + \delta y + \frac{1}{2} \times N_{tube} \times zpitch \times \sin(\delta\alpha)$$

$$z_0 = z^{nom} + \delta z - \frac{1}{2} \times N_{tube} \times zpitch \times (1 - \cos(\delta\alpha))$$

Here, y^{nom} and z^{nom} are the distances between the first tube and the origin of the local plane. The value is 15 mm or -15 mm depending on where the chambers are located (positive on A side and negative on C side).

Then, the position of each wire in the chamber is determined from the pitch and angle:

$$y = y_{1st} + i_{layer} \times ypitch \times \cos(\delta\alpha) - i_{tube} \times zpitch \times \sin(\delta\alpha) + y_{cor}$$

$$z = z_{1st} + i_{layer} \times ypitch \times \sin(\delta\alpha) + i_{tube} \times zpitch \times \sin(\delta\alpha) + z_{cor}$$

i_{layer} and $i_{end-plug}$ are the index of the layer and of the tube in this layer.

The correction is added because of the way the tubes are assembled in the chamber. There is a 15 mm shift between each layer, so the correction is expressed as:

$$y_{cor} = \begin{cases} -\frac{1}{2} \times zpitch \times \sin(\delta\alpha), & \text{when } i_{layer} \text{ is even} \\ 0, & \text{when } i_{layer} \text{ is odd} \end{cases}$$

$$z_{cor} = \begin{cases} \frac{1}{2} \times zpitch \times \cos(\delta\alpha), & \text{when } i_{layer} \text{ is even} \\ 0, & \text{when } i_{layer} \text{ is odd} \end{cases}$$

The wire positions will be transformed from the local system to the global system in AMDB.

3.3.3 Effects of the as-built wire positions on the muon reconstruction

As the signal in the tube provides only information of the distance between the track and the wire, a wrong absolute wire position will result in a wrong estimate of the track hit, which in turn leads to a wrong direction when combining hits into segments. The direct impact on the track reconstruction is then reflected in the sagitta. A MC study is done to quantify this effect. Straight tracks are generated in the $\eta - \phi$ space. The tracks are required to cross exactly six multilayers, namely three chambers so that one can derive the sagitta. If the wire are at their nominal positions, the sagitta will be 0. Now the vectors between the track and the nearest wires are calculated, and in the reconstruction, this

information will be read as input. Then, the vectors describing the wire misplacement are added to the nominal position of the wires, as what would happen in reconstruction, and the track sagitta is calculated from the gravity centre point of each segment. The deviation of the computed sagitta from 0 reflects the impact of the wire position. Figure 3.17 shows the sagitta of the tracks in the geometry map. Except for two regions where the sagitta deviation is of the order of $400 \mu m$, which is actually caused by the two problematic chambers shown in section 3.2.5, the sagittas mostly are below $100 \mu m$. A zoom in these regions in a smaller magnitude of the sagitta are shown in Figure 3.17 (b), which indicates that, to get the resolution under $60 \mu m$, the X-ray tomography data must be included in the database.

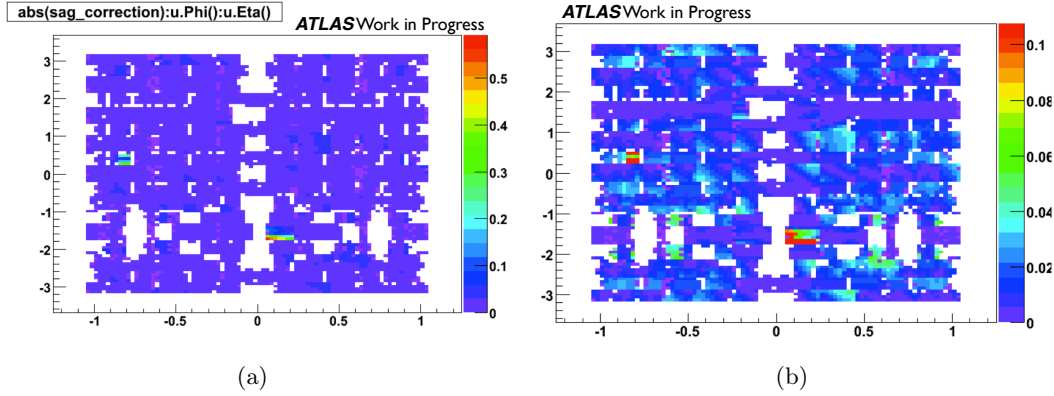


Figure 3.17: The wire position contribution to a straight track sagitta. The zooming in the range smaller than 0.1 mm is shown in (b) [25].

Further impacts are investigated by studying the reconstruction quality of the tracks crossing the chambers. Here the scanned BIL chambers are used. They are grouped according to the deviation with respect to the nominal parameters. Table 3.2 summarises the chamber information from X-tomography scanning. The problematic chambers are listed in the first two rows, and have a very large δz or $\delta \alpha$. Rows 3-6 show the chambers with $\delta z > 75 \mu m$, and the chambers in the rest of the table are assumed to be well constructed.

Then a set of variables is chosen to quantify the reconstruction quality: the segment residual, the track residual, the χ^2 of the segment fit and the χ^2 of the track fit. As the real wire positions are not included in the database, the deviation from the nominal positions will cause poor reconstruction quality. A high p_T single muon MC sample is used. Tracks that pass the chambers listed in Table 3.2 are selected. The corresponding segment residual and track residual distribution are then fitted with a double Gaussian function. The fraction between the two Gaussian is fixed to 7:3. Figure 3.18 and Figure 3.19 show the distribution of the segment residuals and track residuals for some of the chambers. As seen from the figures, the "extremely bad" constructed chambers have a clearly wider residual distribution, which is also referred in the width of the Gaussian. However, the

"relatively bad" chambers do not seem to have worse residual resolution than the "good" ones, which implies the impact of the wire positions is relatively minor. The fitted widths of the dominant Gaussian are summarised in Table 3.3 for all the scanned BIL chambers. They reflect the core of the distribution and thus the construction quality of the chamber.

Figure 3.20 and 3.21 show the segment fit and track fit χ^2 distributions for the three categories of chambers. The first two chambers, which have severely distort wire positions show large tails in the distribution. Table 3.3 shows the summarised mean value of the χ^2 distributions of all the scanned BIL chambers. Large differences are seen in the "extremely bad" chambers, while the others show similar behaviours.

More chamber types of bad quality have been investigated (BM, BO, EM). Figure 3.22 shows the track residual distribution of these chambers, two good quality chambers are also shown for comparison. The σ of the fitted dominant Gaussian are summarised in table 3.4: the bad chambers show large track residual compared to good ones, as has been seen in BIL chambers.

3.4 Summary

In this chapter the parameters on which the precision measurements provided by the MDT chambers have been examined. To verify the accuracy of the wire position within the structure of a chamber, X-ray tomography was performed at CERN. The working principle

chamber	δy [mm]	δz [mm]	$\delta\alpha$ [mrad]	y_{pitch} [mm]	z_{pitch} [mm]
Extremely "bad" chambers					
BIL1A13	0.077	2.912	0.00001100	26.0091	30.0329
BIL1A05	-0.408	-0.057	0.00044000	26.0133	30.0328
Large z shift chambers					
BIL2A03	0.121	-0.091	0.00000200	26.0169	30.0337
BIL2A05	0.060	-0.079	0.00000500	26.0272	30.0348
BIL2A01	0.053	0.076	0.00001400	26.0145	30.0337
BIL5C05	-0.028	0.084	0.00003800	26.0150	-30.0333
Good chambers					
BIL5A01	0.019	0.014	0.00001000	26.0112	30.0326
BIL1C05	0.003	0.066	0.00003400	26.0233	-30.0331
BIL1C09	0.038	0.043	-0.00000200	26.0249	-30.0333
BIL2A09	0.020	0.016	0.00002500	26.0118	30.0330
BIL3A01	0.037	0.039	-0.00000500	26.0224	30.0333
BIL3A05	0.086	-0.011	0.00003900	26.0277	30.0339

Table 3.2: BIL chamber information, units are *mm* and *mrad*. Among the 4 sets of parameters (2 multilayers \times 2 sides), the worst set is listed in the table

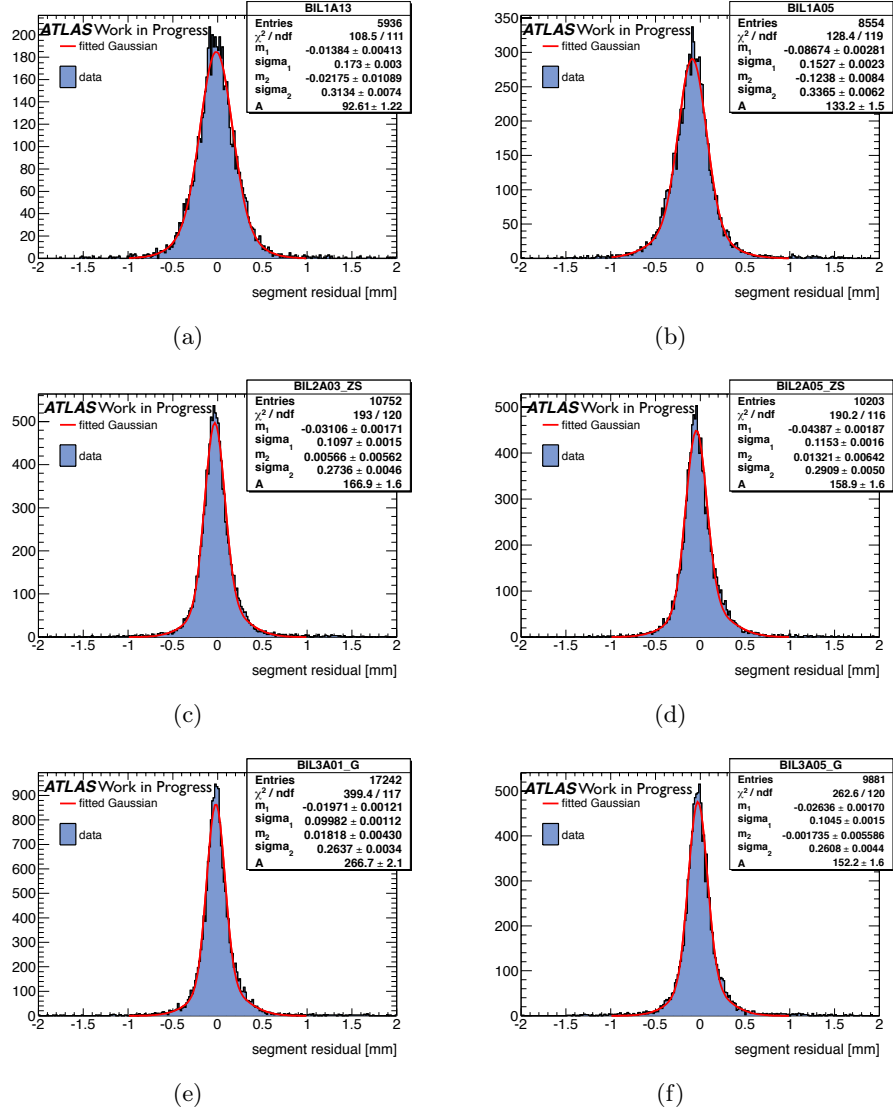


Figure 3.18: Segment residual distribution of (a), (b) Extremely "bad" chambers, (c), (d) relatively "bad" chambers and (e), (f) "good" chambers.

of the X-ray tomography is based on the distinctive absorption coefficient of different materials in the detection tubes. 15% of the chambers have been scanned and analysed results were stored as two-dimensional coordinates of the wires. A set of five parameters are extracted from the wires' position, representing the chamber construction quality, which are later used to re-calculate the wire position in the equal distant simplification. The information can be recorded in the AMDB for muon reconstruction. The impact of the precise knowledge of the wire position is evaluated, from the perspective of trajectory reconstruction in the MS. The effect on the sagitta is of the order of 60 μm on average; however the effect can be quite spectacular in special cases when the chambers deviate severely from design. The effect is reflected in both residuals and fit quality of segments

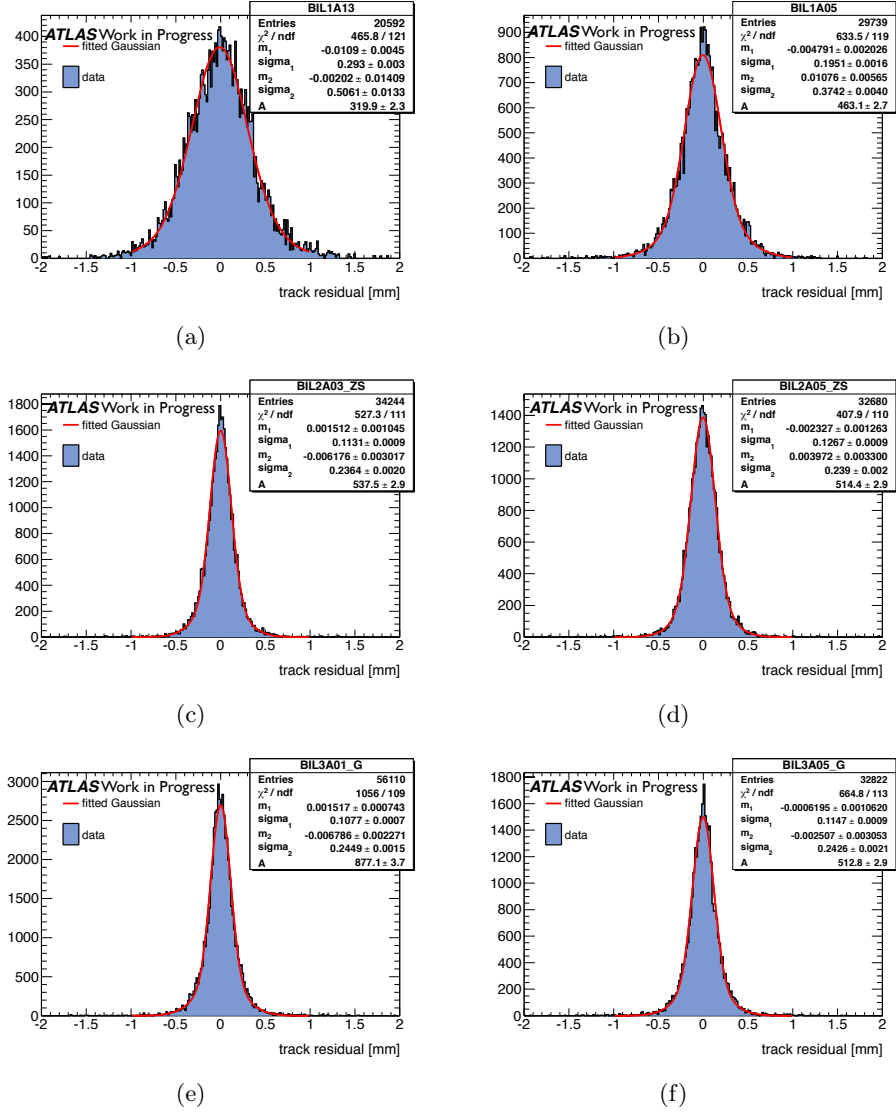


Figure 3.19: Track residual distribution of (a), (b) Extremely "bad" chambers, (c), (d) relatively "bad" chambers and (e), (f) "good" BI type chambers.

and tracks. The information from the X-ray tomography is now fully included in the default geometry database, as a result of this work.

chamber	track residual [mm]	segment residual [mm]	track χ^2	segment χ^2
Extremely "bad" chambers				
BIL1A13	0.33008	0.17298	3.06596	1.70544
BIL1A05	0.195142	0.152712	1.98802	1.6535
Large z shift chambers				
BIL2A03	0.113116	0.109732	1.33136	1.06348
BIL2A05	0.126683	0.115278	1.40635	1.204
BIL2A01	0.123062	0.117651	1.4529	1.31834
BIL5C05	0.107005	0.109649	1.41731	1.02404
Good chambers				
BIL5A01	0.118414	0.118394	1.51104	1.232
BIL1C05	0.119499	0.112612	1.53856	1.18476
BIL1C09	0.160847	0.12439	1.78038	1.52752
BIL2A09	0.134032	0.119142	1.48431	1.20898
BIL3A01	0.107694	0.0998165	1.34889	1.12259
BIL3A05	0.11471	0.104526	1.33184	1.03735

Table 3.3: BIL chamber qualities, units are *mm*

chamber	track residual
Big shift in Z	
BMS5C02	0.233221
BMS5C04	0.150819
Good chamber	
EML2A03	0.082642
BOS1C10	0.0850525

Table 3.4: Some bad constructed chambers track residual, units are *mm*

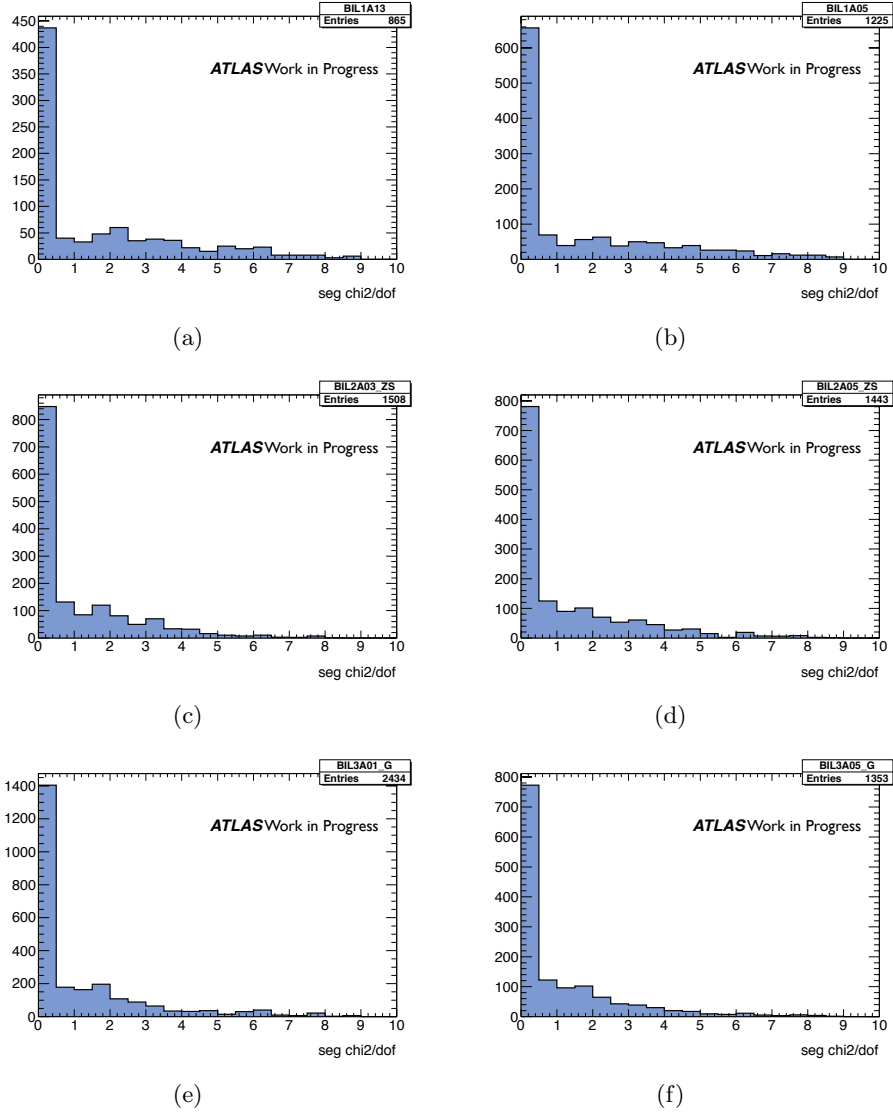


Figure 3.20: Segment fit χ^2 distribution of (a), (b) Extremely "bad" chambers, (c), (d) relatively "bad" chambers and (e), (f) "good" chambers.

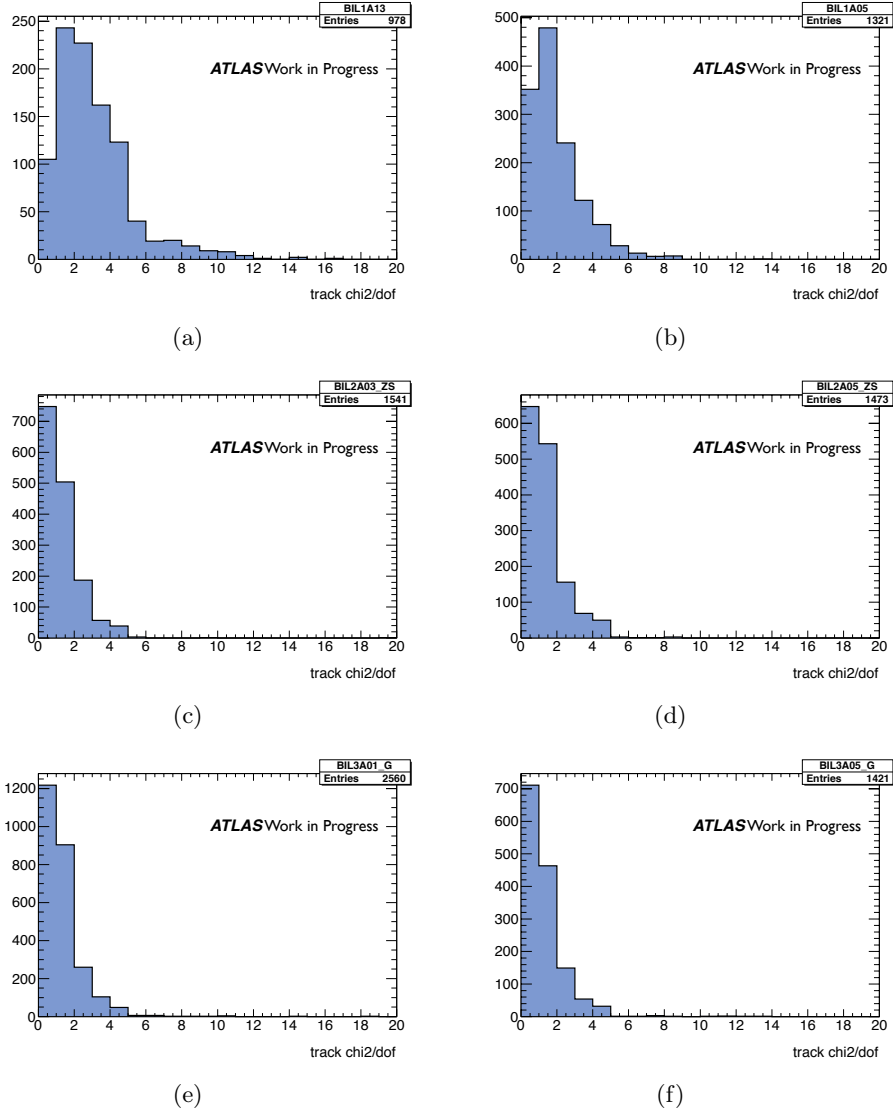


Figure 3.21: Track fit χ^2 distribution of (a) and (b) Extremely "bad" chambers, (c) and (d) relatively "bad" chambers (e) and (f) "good" chambers.

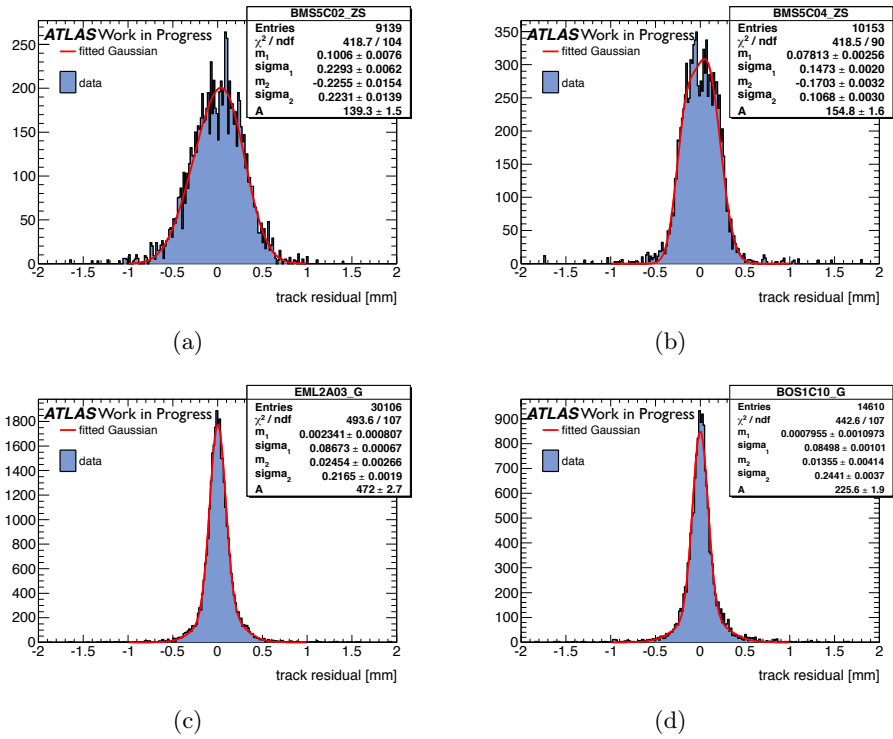


Figure 3.22: Track residuals of the badly built chambers in (a), (b), compared with good quality chamber in (c) and (d). These chambers are of the BM, BO, EM type.

Chapter 4

Performance

4.1 Missing Transverse Energy (MET) Reconstruction and Optimisation

The missing transverse energy (MET) in an event, is defined as the energy imbalance in the transverse plane perpendicular to the collision beam. As the law of energy conservation requires, the initial and final energy sum should be 0. Therefore, an imbalance implies the presence of undetectable or non-interacting particles. In the case of ATLAS, the particle may be neutrino, or a stable weakly interacting supersymmetry particle (if SUSY exists). A precise measurement of the missing transverse energy, whose magnitude is denoted as E_T^{miss} , is essential for physics at LHC. The $t\bar{t}$ production for example, which is the background of many Standard Model processes and Higgs decay channels, has a large energy imbalance due to the presence of two neutrinos, and its reconstruction depends largely on the quality of the missing energy measurement. In the Higgs search channels like $H \rightarrow WW^{(*)}$, the E_T^{miss} also determines the quality of the reconstructed Higgs mass resolution.

The ATLAS MET reconstruction algorithm will be introduced in section 4.1.1. In order to improve the performance of MET, the optimisation of the muon term is developed in ATLAS software release 17. The detailed study of the performance will be shown in section 4.1.2. The result of the optimisation is shown in section 4.1.3 and other impacts from FSR photons and jets are discussed in section 4.1.4. The validation of the developed procedure performed in the context of the $H \rightarrow WW$ analysis is summarised in section 4.1.5.

4.1.1 MET reconstruction and calibration

The transverse missing energy is calculated as the negative vector sum of the energy of all particles detected in a pp collision. The contributions considered include energy depositions in the calorimeter in the range $|\eta| < 4.5$ and reconstructed muons covering $|\eta| < 2.7$. Low p_T particles that are not able to reach the calorimeters are also taken into account by

adding their track momentum to the sum. The total MET, i.e. the magnitude of the vector, is expressed as the quadratic sum of components in the x and the y direction:

$$E_T^{\text{miss}} = \sqrt{(E_x^{\text{miss}})^2 + (E_y^{\text{miss}})^2} \quad , \quad (4.1)$$

the direction of the MET is:

$$\phi^{\text{miss}} = \arctan(E_y^{\text{miss}}, E_x^{\text{miss}}). \quad (4.2)$$

Calorimeter term

The energy summing in the calorimeter is cell-based. Nevertheless, given the high granularity, it is crucial to suppress the noise contributions and carefully select the cells to be used. The three dimensional topological clusters, which are constructed, are referred to as topocluster hereafter. Only cells belonging to the topoclusters are used. The topoclusters [28] are seeded by cells with deposited energy ¹ $|E_i| > 4\sigma_{\text{noise}}$, and are built by iteratively adding neighbouring cells with $|E_i| > 2\sigma_{\text{noise}}$ and finally by adding all neighbours of the accumulated cells. The hadronic energy of the cells needs to be calibrated to properly take into account the detector response [29]. Local Cluster Weighting (LCW) calibration was chosen in the initial MET reconstruction, where the cells are calibrated according to the topocluster properties and topology. Compared to this overall calibration a more refined treatment is considered for MET, where the calibration is based on the physics object the cells belong to. This reconstructed MET is called MET_{RefFinal} . In this calibration scheme, it can happen that one individual cell belongs to two objects at the same time, thus the association of cells to a given object is ordered with priority, once the cell is mapped to the higher priority object with more than 50% of its p_T , it cannot be used by lower ordered ones. The priority list is: electrons, photons, hadronically decaying τ leptons, jets and muons. The E_T^{miss} calorimeter term is then calculated as follows:

$$E_{x(y)}^{\text{miss,calo}} = E_{x(y)}^{\text{miss,e}} + E_{x(y)}^{\text{miss,\gamma}} + E_{x(y)}^{\text{miss,\tau}} + E_{x(y)}^{\text{miss,jets}} + E_{x(y)}^{\text{miss,softjets}} + E_{x(y)}^{\text{miss,CellOut}}. \quad (4.3)$$

The $E_{x(y)}^{\text{miss,e}}$ and $E_{x(y)}^{\text{miss,\gamma}}$ terms stand for the calorimeter cell energies of the electrons and photons projected on the x and y coordinates in the opposite direction of the object. To reduce fake electrons and photons, $p_T > 10$ GeV is required. Electrons are selected using medium criteria and calibrated with the default electron calibration. Photons passing tight criteria are calibrated to the electromagnetic scale [30]. $E_{x(y)}^{\text{miss,\tau}}$ represents the contribution from tight τ , calibrated using the LCW scheme. The jets are reconstructed with the *anti* - k_t algorithm with a cone of $\Delta R = \sqrt{(\Delta\eta)^2 + (\Delta\phi)^2} = 0.6$ and $p_T > 20$ GeV, calibrated with the LCW scheme with subsequent application of the Jet Energy Scale [31]. The soft-

¹ σ_{noise} is the Gaussian width of the EM cell energy distribution measured in randomly triggered events far from collision bunches.

jets term covers jets with $7 < p_T < 20$ GeV, calibrated with LCW. The cells belonging to muons are also added, but in another form that will be explained in section 4.1.1. Finally, all cells inside a topocluster without any link to the used object, are added as $E_{x(y)}^{\text{miss,CellOut}}$. This term also includes the contribution from the tracks of $p_T > 400$ MeV, which are not associated with high- p_T objects used by the higher priority objects. Sets of requirements are imposed on the tracks, e.g. the number of hits and the χ^2 of the fitted track in order to select good quality tracks.

Muon term

The muons included in the MET reconstruction in ATLAS software release 16 are mainly combined muons (the different types of muons are defined in section 2.3.2). Stand-alone muons are used in the range $2.5 < |\eta| < 2.7$. Due to the efficiency loss in the transition region $1.0 < |\eta| < 1.3$, the tagged muons are added.

In order to deal with the energy deposited by the muon in the calorimeter, the muon term and the calorimeter term are treated differently for isolated and non-isolated combined muons. A muon is defined to be isolated if the $\Delta R = \sqrt{(\Delta\eta)^2 + (\Delta\phi)^2}$ to any $p_T > 7$ GeV jet is larger than 0.3. This isolation is used to avoid double counting of muon energy loss in the calorimeter. As in the reconstruction of a combined muon, the energy loss is already taken into account, simply adding muon momentum to the MET together with the energy belonging to the cells linked to a muon in the calorimeter ($E_{x(y)}^{\text{miss,calo},\mu}$) actually counts the energy loss twice. One can either take only the combined momentum and ignore the $E_{x(y)}^{\text{miss,calo},\mu}$ term, or take the momentum at the entrance of the muon spectrometer where the energy has been lost in the calorimeter, and add the $E_{x(y)}^{\text{miss,calo},\mu}$ afterwards. If the muon is isolated, the first way is favoured, since the latter one treats the muon momentum as a simple summation of energy in two parts of detector, effectively not using the inner detector information. Nevertheless, in the case of non-isolated muons, one cannot add the muon momentum and ignore the $E_{x(y)}^{\text{miss,calo},\mu}$ term, since by definition, the cells overlapping with the jet have already been counted in the $E_{x(y)}^{\text{miss,jets}}$ term. Thus, one adopts the second method: add the momentum at the entrance of the muon spectrometer, identify all calorimeter cells traversed by the muon, and add to $E_{x(y)}^{\text{miss,calo},\mu}$ the cells not yet assigned to the jet. One difficulty in the treatment of the non-isolated muons is the occasional very bad quality of the spectrometer measurement, which may cause fake MET. An additional check is done to avoid this: if there is a big mis-match between the MS energy and the ID measurement, the combined momentum measurement obtained by subtracting the parameterised energy loss is used as the MS measurement. In summary, the contribution from the muons can be expressed as

$$E_{x(y)}^{\text{miss,muon}} = E_{x(y)}^{\text{MuonBoy,Track}} + E_{x(y)}^{\text{MuonBoy,Spec}} + E_{x(y)}^{\text{RefMuon,Spec}} \quad (4.4)$$

where the $E_{x(y)}^{\text{MuonBoy,Track}}$ stands for the negative momentum sum of isolated muons at the perigee, $E_{x(y)}^{\text{MuonBoy,Spec}}$ represents the ones from non-isolated muons at the entrance of the spectrometer, and the $E_{x(y)}^{\text{RefMuon,Spec}}$ is the $E_{x(y)}^{\text{miss,calo},\mu}$ term for the non-isolated muons.

4.1.2 Muon term optimization

As seen in section 4.1.1, the tagged muons are only used in the transition region $1.0 < |\eta| < 1.3$, which may lead to a fake MET due to the incomplete inclusion of all muons. Enlarging the coverage of tagged muon is discussed in this section, and further optimisation for all muons types (combined, standalone and tagged) is studied.

Enlarging the η coverage of tagged muons

In release 17, the reconstruction purity of tagged muons is largely improved compared to release 16. For this reason, these muons in all pseudo-rapidity ranges were included in the analysis. Thus, the enlargement of the η coverage of tagged muons also in the MET calculation was investigated. The properties of the reconstructed tagged muons are studied with simulation to look for possible discriminants against fakes.

Figure 4.1 shows the source of the fake muons in the transition and the non-transition regions. Most of the fakes come from pions and kaons, the "Rootino" in the figure means no source is found at generator level, which indicates possible bremsstrahlung from particles crossing the detector. Figure 4.2 shows the η of fake and true tagged muons. As illustrated in the plot, most of the fakes are located out of the transition region, where the amount of true muons are overwhelmed by the fakes. This seems to confirm the objection to add tagged muons in regions other than $1.0 < |\eta| < 1.3$. But as the p_T distribution shows in figure 4.3, for transition and non-transition regions, the majority of the fakes are very soft, even in the non-transition region where they are dominant. A simple p_T cut at 10 GeV will rule them out, without scarifying too much the efficiency of the true muon.

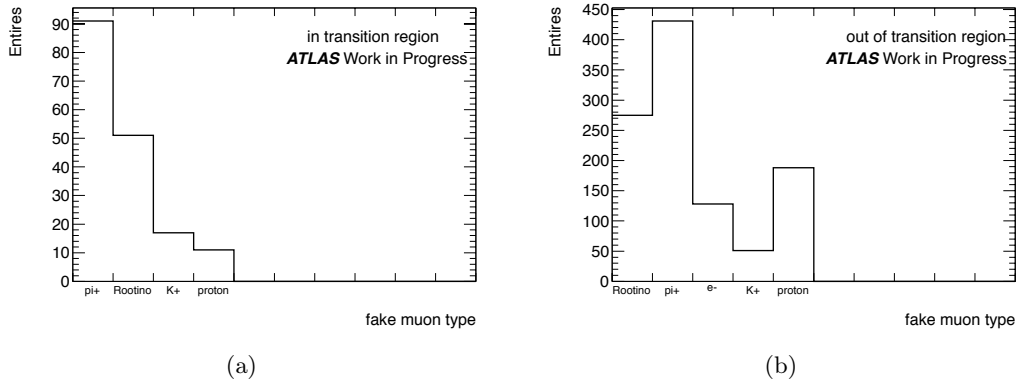
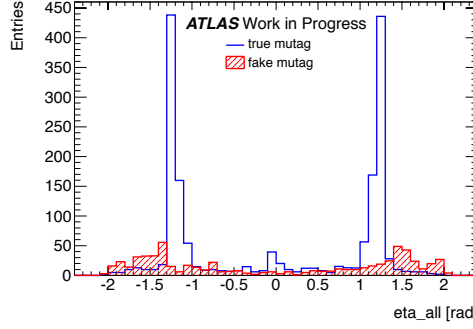
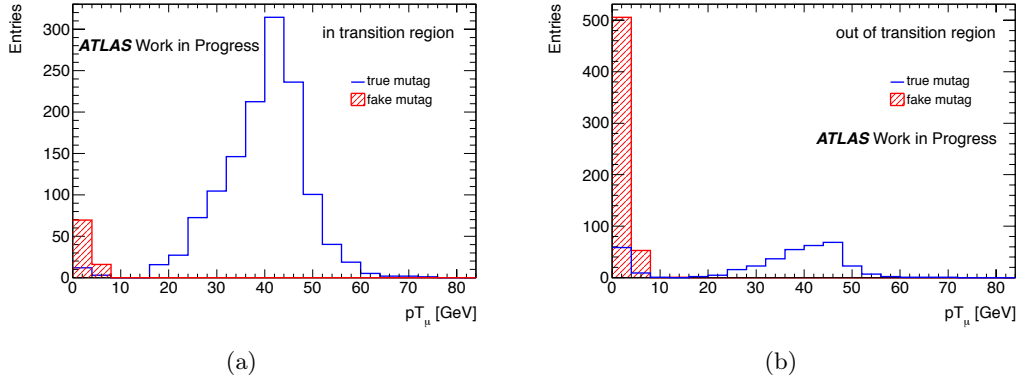


Figure 4.1: Fake sources of reconstructed tagged muons in (a) transition region (b) non-transition region from simulation.

Figure 4.2: η distribution of reconstructed tagged muons.Figure 4.3: p_T distribution of reconstructed tagged muons in (a) the transition region (b) the non-transition region for selected $Z \rightarrow \mu\mu$ events.

Adding all tagged muons without any requirement is tested in the $Z \rightarrow \mu\mu$ Monte Carlo sample. To quantify the validity of the MET reconstruction, the resolution is defined as the difference between the reconstructed MET x(y) component and the true MET, which is obtained by adding the momentum of all non-interacting generated particles. Adding the tagged muons is done in the MET reconstruction, and is labelled as "ESD (Event Summary Data) level recovery", a label derived from the format of raw MC samples. An attempt to add them at the analysis level is also made. As the format of the MC in the analysis is D3PD (Derived Physics Data), this correction is denoted as "D3PD level". The treatment of the non-isolated muons is slightly different at the D3PD level. The cell by cell overlap removal is not possible due to the missing information in D3PDs, an approximation is used instead by removing the overall energy left by the muon in the calorimeter. Figure 4.4 shows the resolution before and after adding the tagged muons at the ESD level and at the D3PD level. As the plots illustrate, when all the reconstructed tagged muons are the true muons, the resolution is significantly improved for both levels of correction. When there are fakes, the resolution does not get worse because of the soft spectrum of fakes.

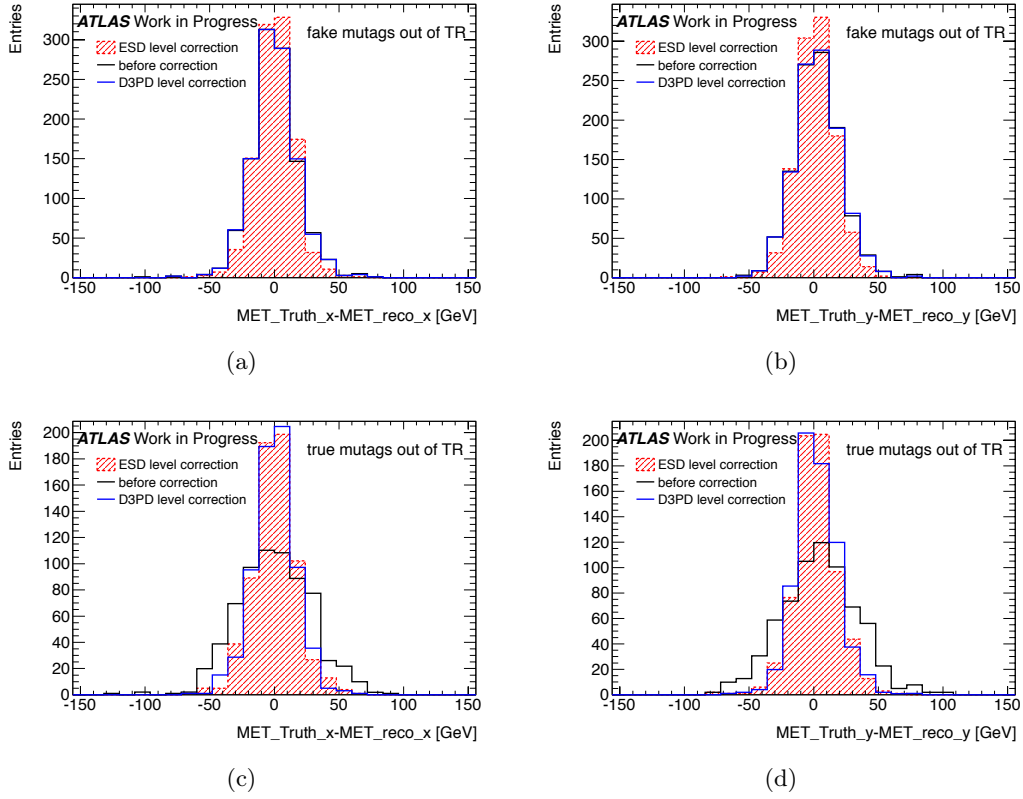


Figure 4.4: The resolution of MET x component when (a) there are fake tagged muons ((b) for y component), and (c) all tagged muons are true ones in the non-transition region ((d) for y component).

Further optimization

The previous section indicates that the p_T requirement on tagged muons can be imposed to reduce the fake sources. In addition, as the old algorithm always considers the tagged muons as isolated, there is a potential double counting. The separation between isolated and non-isolated is made for the new release (17). In the MET calculation, there was no requirement on muons, be they tagged or not. A set of stringent selection consistent with the analysis are added to further improve the quality of muons. First, the definition of isolation is changed. The initial definition considers a muon non-isolated if it overlaps with a jet with E_T more than 7 GeV, which has a large probability to be a fake. Thus the p_T threshold of the jet is raised to 20 GeV. Then a more refined scheme is proposed according to the types of the muons, It can be summarised as follows:

- Tagged muons: Besides removing the restriction on the η range of the transition region, a cut of $p_T > 10$ GeV is applied in order to exclude fake muons. To improve the resolution, a set of cuts are applied:

1. if the muon is isolated, the inner detector measurement is taken, $E_T^{\text{MuonBoy,Track}} =$

$$E_T^{\text{ID}},$$

2. for non-isolated muons, the standard procedure is to add to the MS measurement the energy of the calorimeter cells not linked to other objects. But the tagged muons are reconstructed with segments in the MS, which provides a very poor measurement; in this case, the parameterised energy loss is subtracted from the ID measurement, so that $E_T^{\text{MuonBoy,Spec}} = E_T^{\text{ID}} - E_T^{\text{ParaELoss}}$.
- Stand-alone muons: In order to include only good quality stand-alone muons, a cut on $p_T > 5$ GeV is required, and the number of the CSC η hits should be no less than 3. Stand-alone muons only have the MS measurement, so that the contribution to MET is always the MS momentum plus the energy loss in the calorimeter.
 - Combined muons: $p_T > 5$ GeV is required to reduce fakes. To better make use of the resolution of both the ID and the MS measurements, the scheme is made dependent on the quality factor (χ^2):

1. Isolated muons

- (a) A χ^2 larger than 10 is an indication of poor agreement between the ID and the MS measurements. In that case, the measurement with the best resolution is taken:
 - i. If the ID resolution on q/p ($\sigma_{q/p}/(q/p)$) is better, the ID measurement is used, and the total contribution to MET from the muon is $E_T^{\text{MuonBoy,Track}} = E_T^{\text{ID}}$.
 - ii. If the MS resolution is better, the muon is treated as non-isolated. The MS measurement is used, and the muon term is then $E_T^{\text{MuonBoy,Spec}} = E_T^{\text{MS}}$, with extra energy loss added.
- (b) If χ^2 is smaller than 10, the combination is of a high quality. Thus the combined (CB) momentum is used, and as the muon is isolated, $E_T^{\text{MuonBoy,Track}} = E_T^{\text{CB}}$.

2. The non-Isolated muons contribution to MET is always composed of the momentum at the entrance of the spectrometer, $E_T^{\text{MuonBoy,Spec}}$, and the cell level energy loss in $E_T^{\text{RefMuon,Spec}}$. The resolution of ID, MS, and CB are compared to decide which one to use in order to obtain the $E_T^{\text{MuonBoy,Spec}}$ term.

- (a) If χ^2 is larger than 10
 - i. If the ID resolution is better, ID momentum minus the parameterized energy loss is used, $E_T^{\text{MuonBoy,Spec}} = E_T^{\text{ID}} - E_T^{\text{ParaELoss}}$.
 - ii. If the MS resolution is better, the MS momentum is taken directly, $E_T^{\text{MuonBoy,Spec}} = E_T^{\text{MS}}$,
- (b) If χ^2 is smaller than 10, the CB and MS measurements are compared:

- i. if the muon passes through 3 stations in the MS, then the MS measurement is accurate enough to be taken, $E_T^{\text{MuonBoy,Spec}} = E_T^{\text{MS}}$.
- ii. if the muon passes through less than 3 stations in the MS, the CB momentum minus the parameterised energy loss is adopted, $E_T^{\text{MuonBoy,Spec}} = E_T^{\text{CB}} - E_T^{\text{ParaELoss}}$.

The scheme is summarised in figure 4.5. The red boxes represent optimised muon terms, whereas the blue boxes describe the initial scheme. The new scheme is much more complicated with the consideration of resolution conditions and fake effects.

4.1.3 Optimization results

To validate all the optimisation described above, the MET resolution is compared with the resolution before correction. Both the muon term and the overall MET are checked on different MC samples. Figure 4.6 shows the resolution of the x and the y components of MET in the $t\bar{t}$ sample. The vertical line seen around $x=0$, demonstrates the pronounced effect of the corrections applied to MET in the new scheme. It makes the original tail move to the core. The same effect is visible in both the muon term and the overall MET term. Similar improvements are also seen in $Z \rightarrow \mu\mu$, W' samples as shown in figure 4.7.

The performance of the MET muon term is also checked in the $H \rightarrow WW^{(*)}$ analysis, using 4.7 fb^{-1} data of 2011 [32]. Figure 4.8 shows the term from isolated muons ($E_T^{\text{MuonBoy,Track}}$) and from the calorimeter cell energy belonging to the muon ($E_T^{\text{RefMuon,Spec}}$). MC contributions are stacked, with data added on top. Quite good agreement is seen between data and MC for these two terms.

4.1.4 FSR, jet and MET

As explained in the previous section, the treatment on the non-isolated muons is performed to avoid double counting of the calorimeter energy shared by a jet and a muon. However, a muon cannot only overlap with a jet, but also a photon in the case of FSR, due to the fact that the FSR photons are usually collinear with the muons. This type of overlap is not considered in the MET reconstruction, i.e. despite that the photon contains part of the muon energy in the calorimeter, the muon is still identified as isolated. Therefore, the combined measurement of the muon momentum and the full energy of the photon are added in the MET, which results in a double counting of the energy shared by the two objects: the muon energy loss in the calorimeter.

A study is performed on $Z \rightarrow \mu\mu$ MC sample to investigate the impact from the FSR. The Z events were selected by requiring two isolated muons of $p_T > 20 \text{ GeV}$. The FSR candidates were identified using the the FSR tool, referenced in chapter 5. The FSR photons are selected to be within a cone $\Delta R = 0.15$ around the muon direction, with $p_T > 3 \text{ GeV}$. Figure 4.9 shows the correlation between the $\phi(\text{photon})$, the angle of the

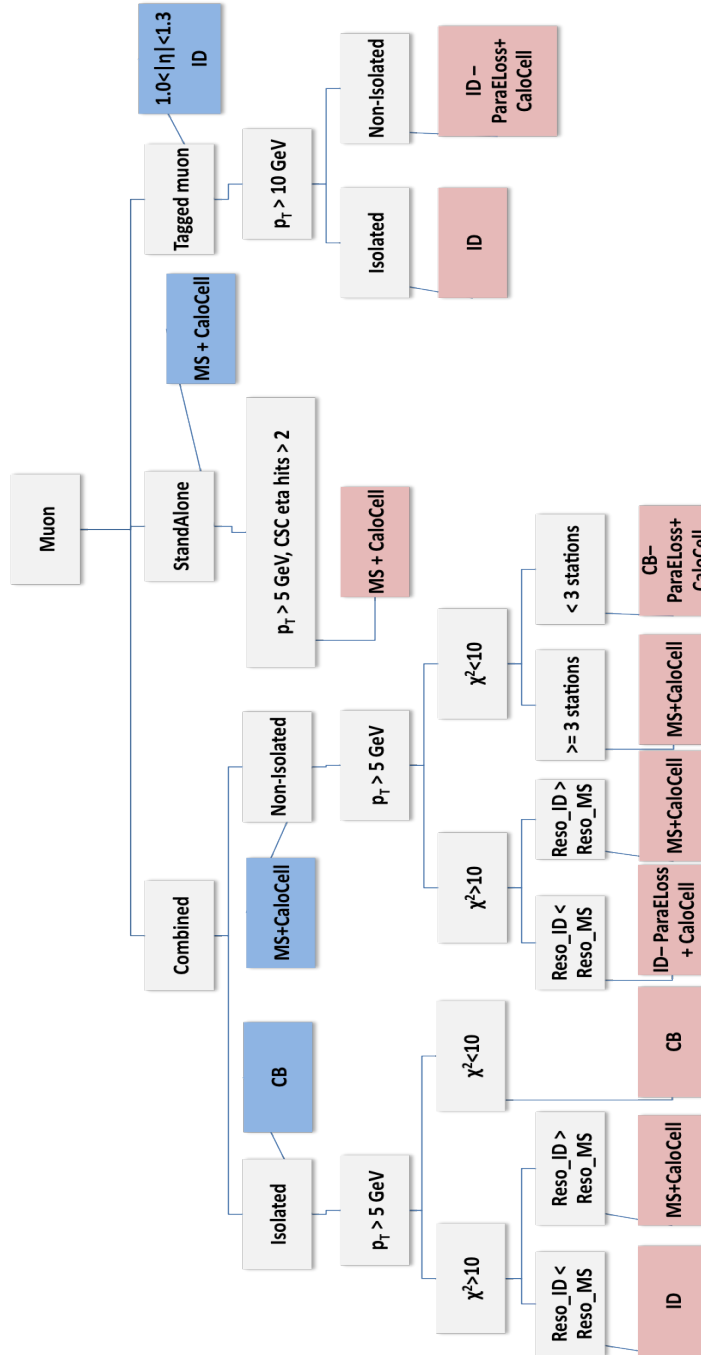


Figure 4.5: Scheme for obtaining the muon term in MET. The red boxes represent optimised muon terms, the blue boxes show the initial scheme.

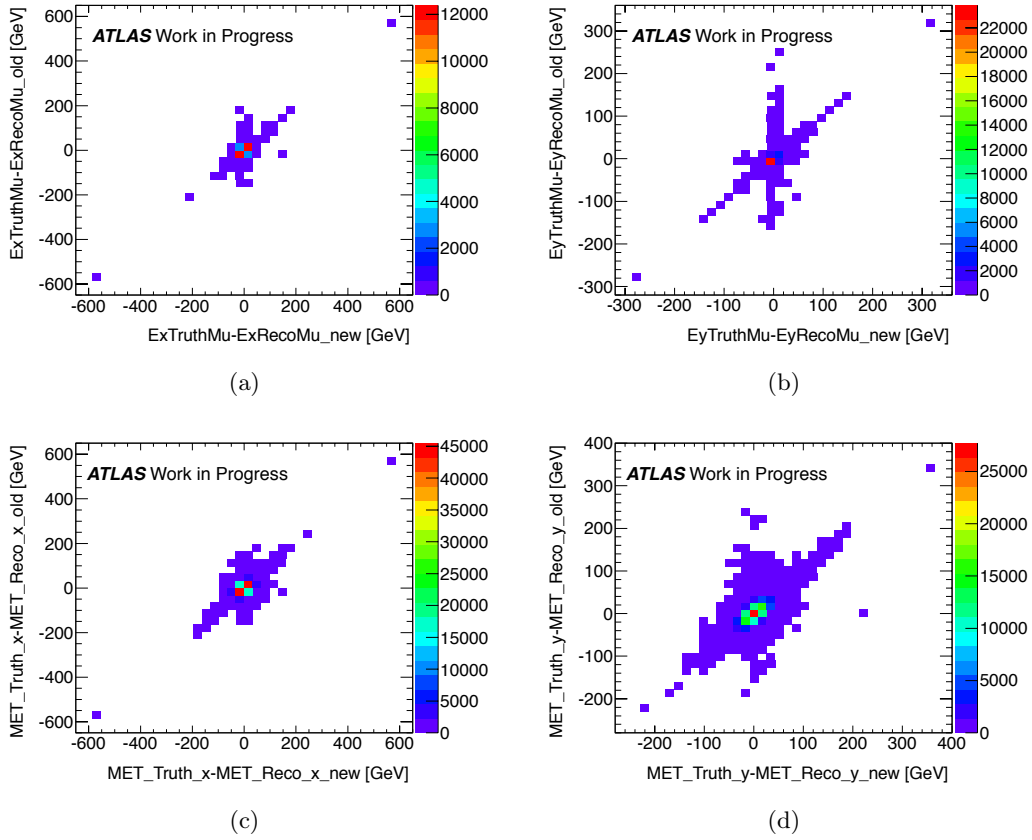


Figure 4.6: x (y) component of MET resolution on left (right) for $t\bar{t}$ sample, the muon terms are shown in (a), (b) and the overall term is shown in (c), (d)

identified photon, and the $\phi(MET - MET_{truth})$ the angle between the reconstructed MET and the true MET. An anti-correlation between the two variables is observed for $E_T < 10$ GeV, which means that the direction of the MET reconstruction deviation is opposite to the FSR candidates. In other words, in the presence of the FSR, the missing energy calculation is overestimated because the muon energy loss is counted twice. For higher E_T photons, no obvious anti-correlation is observed, this may be due to the few statistics in this region. Another explanation is that, as the photon energy increases, the probability for it to be reconstructed as a high energy jet gets higher. The overlap is then taken into account when the jet p_T reaches 20 GeV.

The FSR photons are not always reconstructed as photon objects. This may possibly be caused by rather low electromagnetic energy fraction. As a consequence, they are likely to be included in the E_T^{miss} calculation as hadronic contributions instead of photons. Since the calibration of the two objects are different, the associated energy can be wrong. The effect of mis-calibration is studied in the $H \rightarrow WW^{(*)}$ analysis.

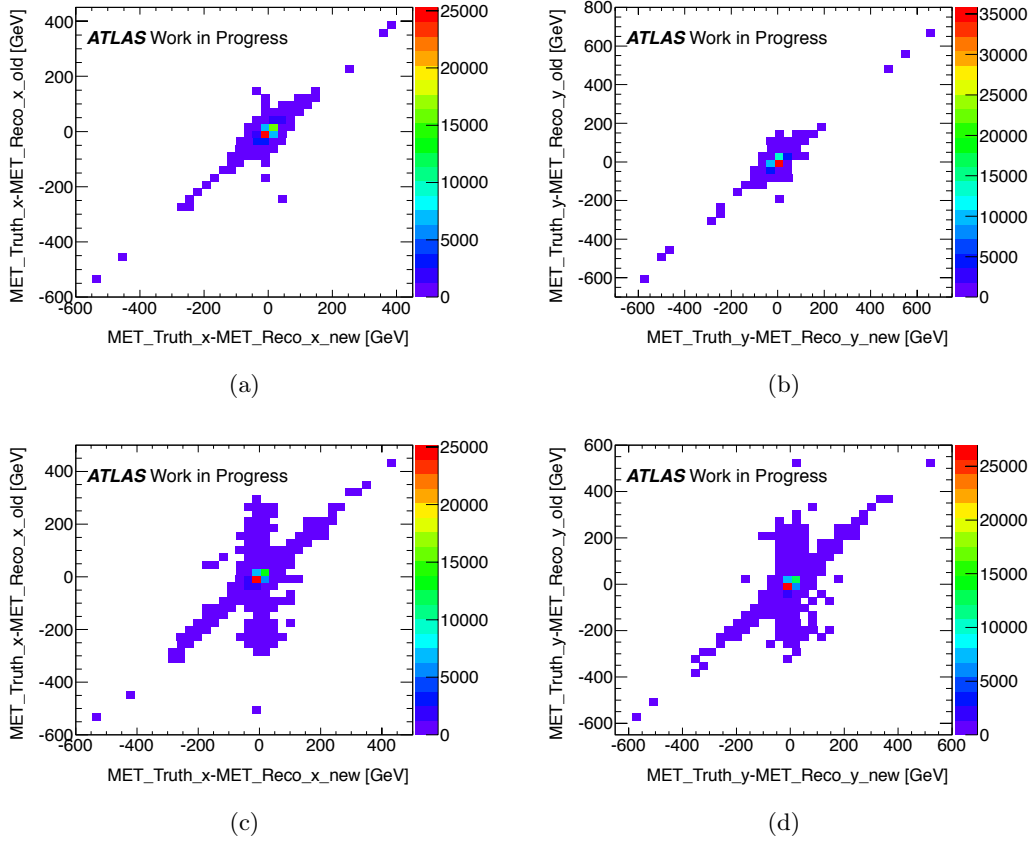


Figure 4.7: MET resolution for (a) x component (b) y component of $Z \rightarrow \mu\mu$ sample, (c) and (d) are for W' sample

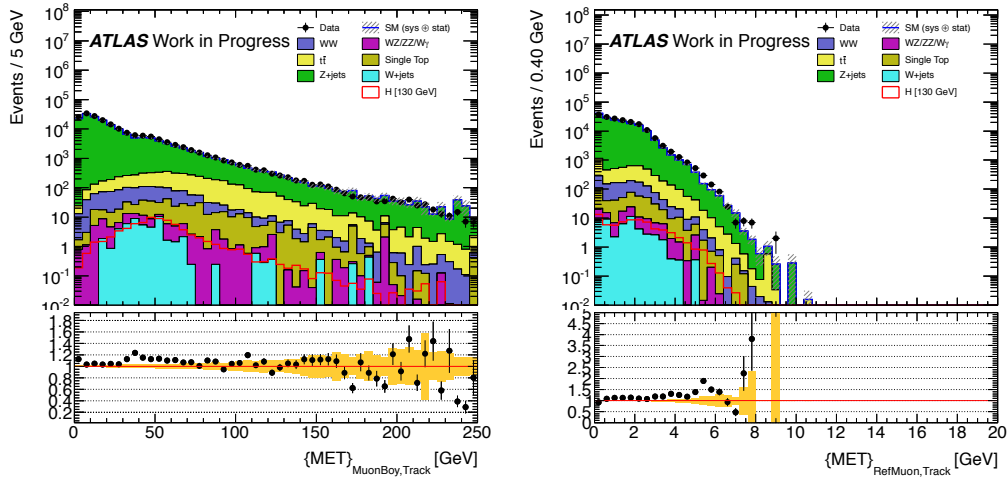


Figure 4.8: Distributions of muon terms E_T^{MuonBoy} and E_T^{RefMuon} in data and Monte Carlo for the $H \rightarrow WW^* \rightarrow \mu\mu\nu\bar{\nu}$ after the Z veto cut. The ratio between data and Monte Carlo is also shown.

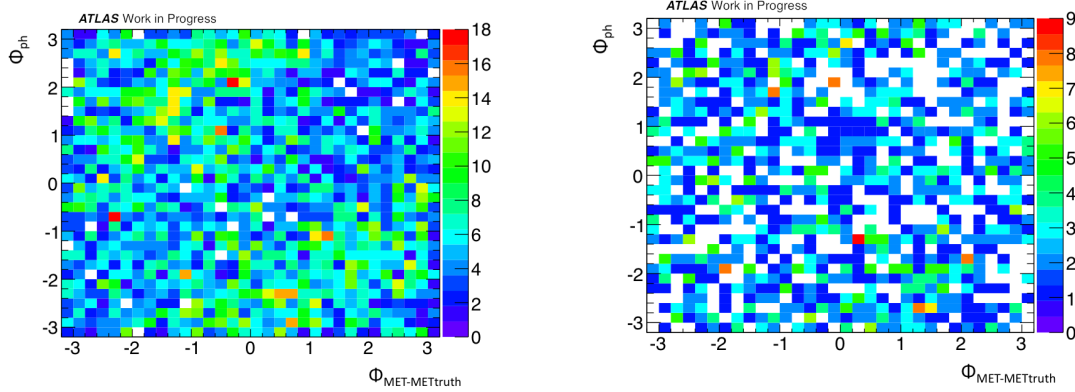


Figure 4.9: Distributions the correlation between the $\phi(\text{photon})$ of the identified photon and the $\phi(\text{MET} - \text{MET}_{\text{truth}})$ of the difference between the reconstructed missing energy and the truth one : (left) for FSR of $E_T < 10$ GeV, (right) for FSR of $E_T > 10$ GeV

$H \rightarrow WW$ analysis

Events which have a primary vertex that is consistent with the beam spot position, with at least three associated tracks with $p_T > 400$ MeV are selected. Overall quality criteria are applied in order to suppress non-collision backgrounds such as cosmic-ray muons, beam-related backgrounds, or noise in the calorimeters.

$H \rightarrow WW^{(*)} \rightarrow \ell \nu \ell \nu$ candidates (with $\ell = e, \mu$) are pre-selected by requiring exactly two oppositely charged leptons with p_T thresholds of 25 GeV and 15 GeV for the leading and sub-leading lepton, respectively. For muons, the range $|\eta| < 2.4$ is used; for electrons, the range $|\eta| < 2.47$ is used, with the region $1.37 < |\eta| < 1.52$ excluded. Leptons from heavy-flavour decays and jets satisfying the lepton identification criteria are suppressed by requiring the leptons to be isolated: the scalar sum of the p_T of charged particles and of the calorimeter energy deposits within $\Delta R = \sqrt{\Delta\phi^2 + \Delta\eta^2} = 0.3$ of the lepton direction is required to be less than approximately 0.15 times the lepton p_T , with slight differences between track- and calorimeter-based criteria and between electrons and muons.

The Drell-Yan process leads to two same-flavour, opposite-sign high- p_T leptons. In the ee and $\mu\mu$ channels (the channels are indicated by the charged lepton flavours), this background is suppressed by requiring the dilepton invariant mass to be greater than 12 GeV, and to differ from the Z -boson mass m_Z by at least 15 GeV. For the $e\mu$ channel, the dilepton invariant mass is required to be greater than 10 GeV.

Multijet production via QCD processes and Drell-Yan events are suppressed by requiring large E_T^{miss} . Further cuts on the MET are applied for the ee and $\mu\mu$ channels, to suppress the multijet and Drell-Yan events.

In this analysis, the electron and muon objects that overlap are removed. Furthermore, jets that are close to electrons are also excluded. In addition, the muon is required to be isolated. Still, one observes very close-by jet-muon pairs. Figure 4.10 shows ΔR , the

angular distance between the leading (sub-leading) muon on the left (right) and the closest jet after the selection of events with opposite sign muons of invariant mass above 12 GeV and outside the Z mass window. The jets with $p_T > 10$ GeV are used.

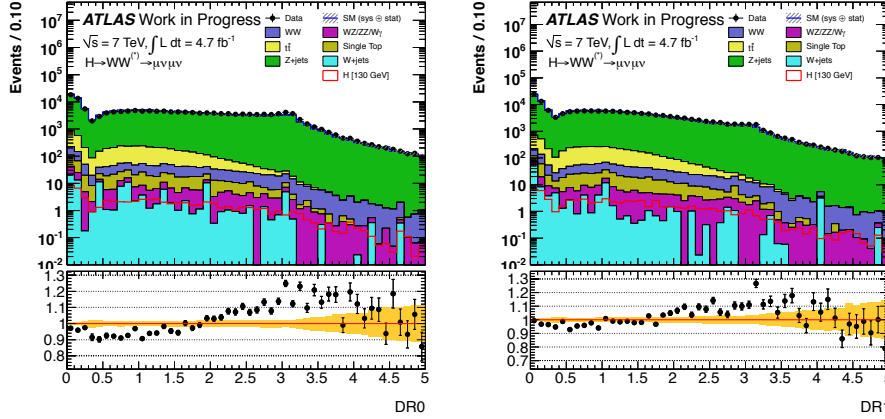


Figure 4.10: left (right): ΔR between leading (sub-leading) muon and jets after Z veto.

The source of the jets is investigated through the variable E_T^{core} , which is defined as the energy of the muon deposited in the calorimeter around its $\Delta R = 0.1$ cone. The assumption is that these nearby jets are FSR photons. The correlation between the identified FSR photon energy and the E_T^{core} is shown in figure 4.11 (left) using a $Z \rightarrow \mu\mu$ MC sample. The plots clearly indicate that most of the FSR photon energy is included in the E_T^{core} term. The correlation between the close-by jets (defined as $\Delta R < 0.1$ to the muon) and E_T^{core} is shown in figure 4.11 (right) where similar behaviour is seen. Thus, one can postulate that the jets are quite possibly FSR photons.

As in the MET reconstruction, the jets are LCW calibrated while the photons are calibrated at the EM scale, the difference is examined. A linear fit to the mean p_T for Anti-Kt LCW calibrated jets as a function of the Anti-Kt electromagnetic scale calibrated p_T is performed, as shown in figure 4.12. Using LCW calibration for these objects would lead to an overestimation of at least 6 GeV of their energy and a fake E_T^{miss} component would be built up in a direction opposite to the muon [32].

In conclusion, FSR photons affect the E_T^{miss} reconstruction, due to either ignorance of the overlap with the muon or wrong calibration mechanism. This can be improved in a future MET reconstruction.

4.1.5 Summary

The MET reconstruction scheme is introduced in this section. With a focus on the muon term, a possible optimisation of this term is proposed and validated with various MC samples. Good consistency is seen also in data for the $H \rightarrow WW^{(*)}$ analysis. An investigation on the possible impact of FSR photons is performed, which shows an overestimation in the

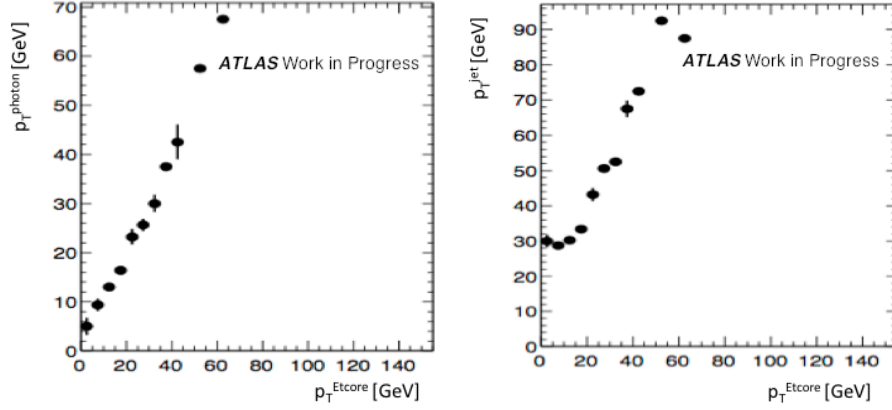


Figure 4.11: left (right): Correlation between photon(jet) E_T and E_T^{core}

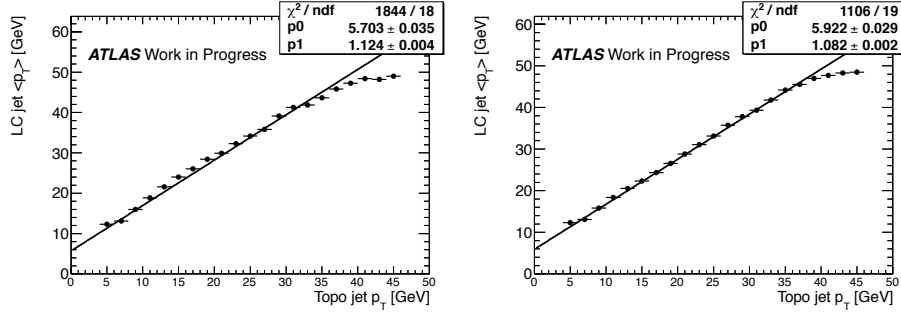


Figure 4.12: Mean p_T for AntiKt4LC jets as a function of the AntiKtTopoEM p_T calibrated at the electromagnetic scale for jets close to the leading muon (left) or the sub-leading muon (right), after Z veto.

current reconstruction scheme. Possible improvements are possible in the future.

4.2 Pixel Tracklets Combination With StandAlone Muons

The muons reconstructed in ATLAS are classified in four types, as introduced in section 2.3.2. The combined muon surpasses the other types in many aspects. It combines the inner detector and the muon spectrometer measurements by properly taking into account the uncertainties of each. Thus, it has more accurate p_T and impact parameter measurements than the StandAlone (SA) muons, which take only MS informations. Due to the limited coverage of the inner detector, the track reconstruction is restricted to $|\eta| < 2.5$. Beyond this range, one can only use SA muons, which solely take extrapolated MS measurements.

As the multiple interactions per bunch increase in ATLAS, it is crucial to identify muons coming from the primary vertex. The impact parameter is a key quality for the

identification. The SA muons in the forward region ($|\eta| > 2.5$) have relatively bad impact parameter resolution due to the long distance of extrapolation to the interaction point. However, it is still possible to find the ID information of these muons, since the ID coverage does not stop immediately at $|\eta| = 2.5$. As seen from the cross section view of ID in figure 4.13, though most of the SCT modules are within $|\eta| < 2.5$, some pixel modules cover a region as far as $|\eta| < 3.0$. With adjusted criteria, one may reconstruct "tracks" from sole pixel hits in the forward region, which can potentially be combined with the SA muons. The tracks which are reconstructed from pixel hits are called "tracklets". The procedure to build combined muons using tracklets will be introduced in section 4.2.1. The validation of these newly combined muons will be shown in section 4.2.2;

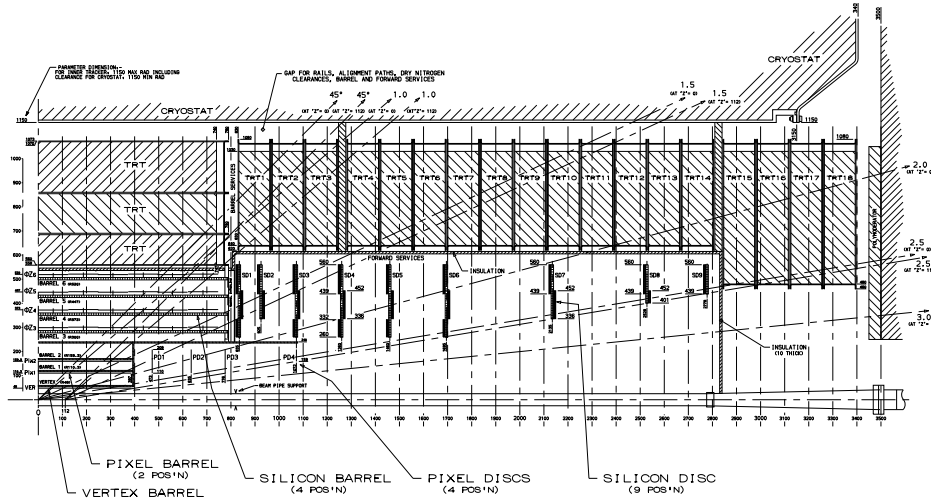


Figure 4.13: Cross section view of the inner detector.

4.2.1 Pixel Tracklets Reconstruction and Combination with StandAlone Muons

Pixel tracklets reconstruction As introduced in section 2.3.1, the standard ID track reconstruction algorithm starts from pixel and SCT space point seeds, which are then extrapolated out to the TRT. The procedure is restricted to $|\eta| < 2.5$, and a minimum number of 6 silicon hits is required. For the forward region ($|\eta| > 2.4$), tracklets are reconstructed based on the same algorithm, but the criteria on silicon hits are removed. In order not to associate arbitrary hits with a track, at least three pixel hits are required, and the p_T of the track should have a minimum value of 2 GeV. The hits which are used in the standard track reconstruction are not used.

Track parameterisation A track in ATLAS is parametrized at the point of closest approach with the global Z-axis using five parameters, also known as "the Perigee parameters". They are the helix parameterisation in a frame where the Z-axis is parallel to the solenoid magnetic field. They are defined as follows:

- q/p charge over momentum magnitude,
- ϕ azimuth angle of the momentum at the point of closest approach, measured in the range $[-\pi, \pi)$,
- θ polar angle in the range $[0, \pi]$,
- d_0 transverse impact parameter, the distance of the closest approach of the helix to the beam,
- z_0 longitudinal impact parameter, the z value at the point of closest approach.

Figure 4.14 shows the five parameters in ATLAS coordinates. Using the above five parameters, the transverse momentum can be derived. The measurement uncertainties of the five parameters are not independent, thus a 5×5 covariant matrix is used to describe them.

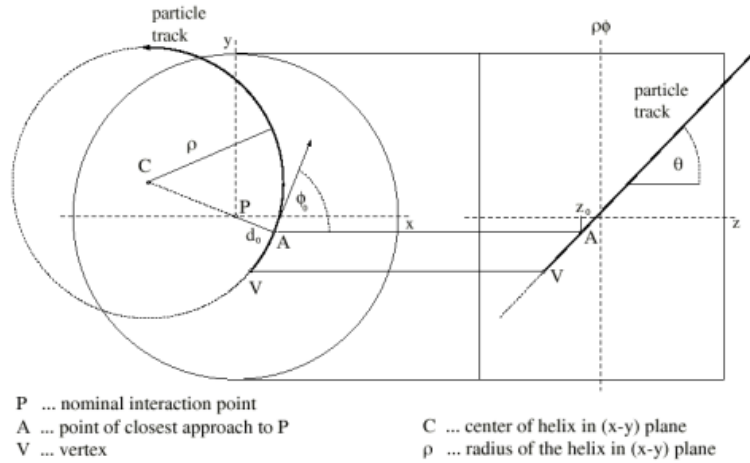


Figure 4.14: The five track parameters, split into three transverse parameters (x-y plane) and two longitudinal parameters (r-z view)

Combination with standalone muons After the reconstruction, the tracklets are then treated as regular tracks, and used in the procedure of combined muon matching (If not stated otherwise, the algorithm used for the muon reconstruction is STACO). The MS tracks first seek possible matching with the ID tracks in the standard ID collection; if none is found, one searches for tracklets. The statistical combination makes no difference between the standard tracks and the tracklets.

4.2.2 Pixel Tracklets Combined Muons Validation

Since the tracklets only use pixel hits, one needs to verify the performance of the combination by checking the quality of the newly combined muons. This is performed on single muon MC samples, generated with $p_T = 10$ GeV, uniformly distributed in η above 2.2. Compared to the standard reconstruction, it is expected that some SA muons will migrate to the CB category, due to their combination with tracklets. This is quantified in figure 4.15, where the generated muons are shown in the $\eta < 2.5$ and $\eta \geq 2.5$ regions (in blue lines), while the total number of CB and SA muons are shown in red lines. Counting the SA and CB muons together, 93% of the generated muon can be successfully reconstructed in $\eta < 2.5$ and the corresponding number in $\eta \geq 2.5$ is 94.5%. Given this high reconstruction efficiency, the CB muons only contribute 25% in the region $\eta \geq 2.5$, as shown by red shadows, which means that in the forward region, the SA muons have a low probability to be combined with the standard ID tracks. By searching possible matching ID tracklets, the probability of the SA muons to be combined is increased by 12%, as shown by the yellow shadow.

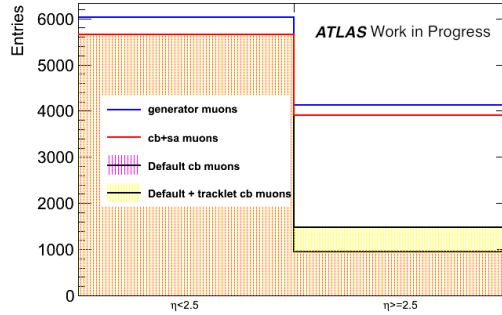


Figure 4.15: Number of reconstructed standalone and combined muons, compared to the generated muons. The blue line represents the generated muons, and the red line denotes the sum of reconstructed standalone and combined muons. The number of combined muons reconstructed with the standard algorithm is also shown in the plot with red shadows. The additional number of combined muons using the ID tracklets is shown in yellow shadow.

The ID track reconstruction in the forward region is more challenging in the presence of multiple tracks and high pileup, where more fake tracks will be produced. For this reason, the validation is also performed with $t\bar{t}$ MC samples, with an average number of interactions equal to 20. Figure 4.16 shows, for the muons combined with tracklets, the η and ϕ correlation between the ID and MS measurements. Both distributions indicate that the positions of the MS track and tracklet are well matched. To study the quality of combined muons, one defines the pull as the difference between the measured and generated values, scaled by the error from the combined measurement. Figure 4.17 shows the pull distributions of η , ϕ and q/p , which have a width ~ 1 and mean value close to 0 if fitted with a Gaussian function.

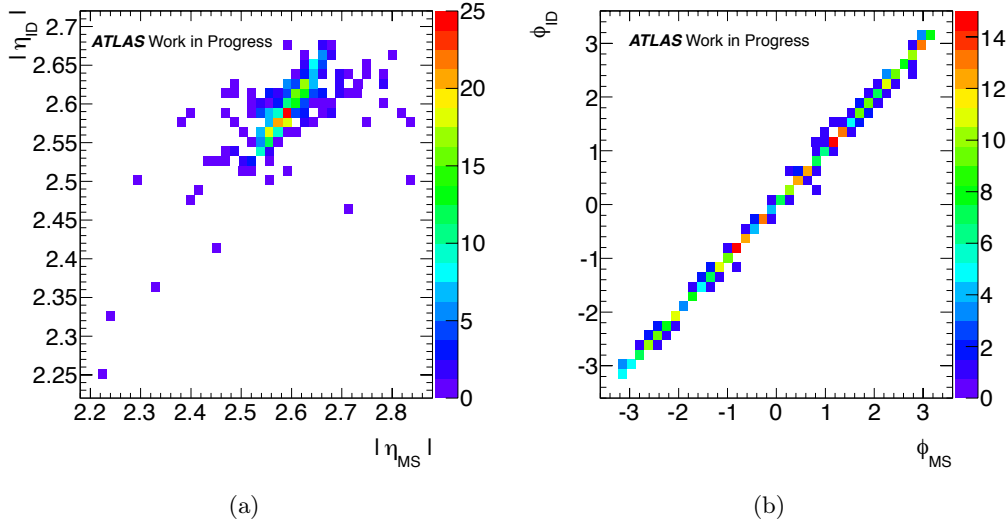


Figure 4.16: Correlation between the ID and MS measurements of (a) η and (b) ϕ for the combined muons using tracklets.

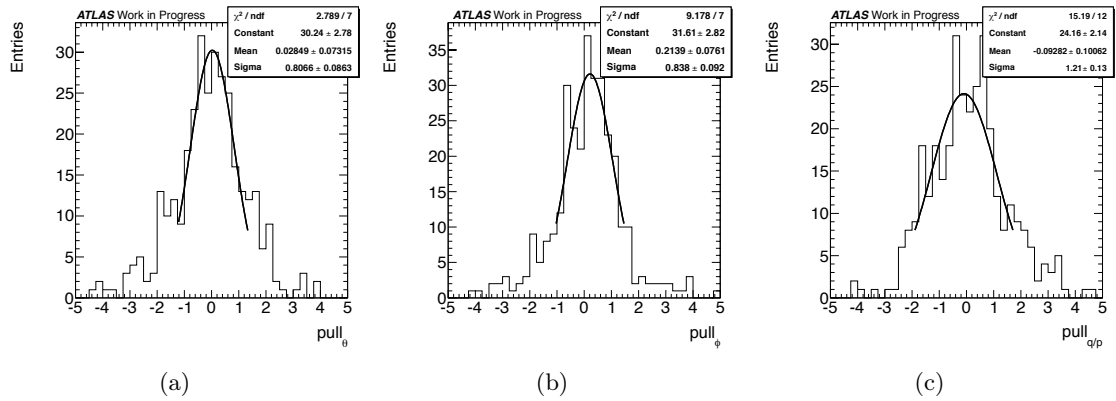


Figure 4.17: Pull distribution of the tracklet combined muons (a) θ (b) ϕ (c) q/p .

The correlation and the pull study demonstrate that the new reconstruction is performing well. However, the limited number of hits in the tracklet may cause fake tracks, which in turn produce fake combined muons. The rate of reconstructing fake muons is examined by comparing the generated muons in the vicinity of the reconstructed muons. Figure 4.18 shows the ΔR of the reconstructed CB muons with tracklets to the nearest generated muon. If the muon is not an artificially reconstructed fake, the ΔR should be small. As seen from Figure 4.18, most of the muons enter the region of $\Delta R < 0.1$, which is quite close to the true muon, while the others are clearly fakes, far away from any generated muon, and have a rather small p_T . The fake muons are then defined as the ones with $\Delta R \geq 0.1$, otherwise they are called true muons. The ratio of reconstructed true CB muons to all the generated muons is defined as the efficiency ϵ , which will be used later. The fake rate is determined by finding fakes among the reconstructed muons.

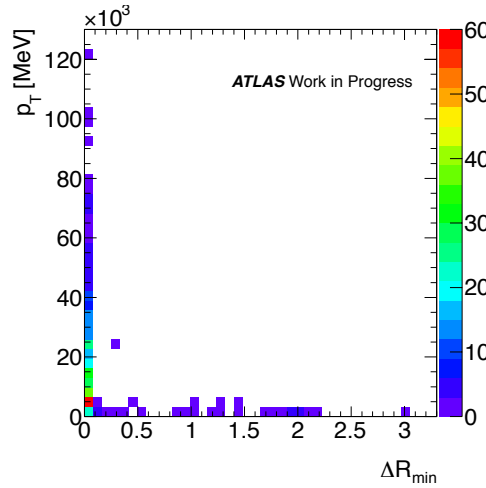


Figure 4.18: Correlation between the p_T of tracklet combined muons and the minimum distance ΔR to the generated muons.

Figure 4.19 shows the ϵ as a function of η and ϕ in the standard reconstruction, with comparison with the efficiency after including tracklets combined muons. The efficiency is close to one and is flat for $|\eta| < 2.4$. A drop is seen starting from $|\eta| = 2.5$. There is a clear increase in the efficiency after the tracklets combined muons are added, around 10% near $|\eta| = 2.5$ and more as η increases. A uniform increase is seen in the entire ϕ range for muons in $|\eta| > 2.2$. The efficiency for muons in $|\eta| > 2.2$ in different p_T ranges is also shown in figure 4.20, a similar uniform increase is seen. The efficiency is quite low below 10 GeV, and a zoom of this region is shown in figure 4.20 (b), which indicates that the low efficiency is mostly caused by $p_T < 2$ GeV muons.

The fake rate as a function of η and ϕ is shown in figure 4.21. The tracklets combined muons do not increase the fake rate neither in the low η region nor in forward region. On the contrary, the overall fake rate is uniformly decreased in ϕ . Similarly, no clear change is seen in the fake rate distribution in p_T bins, as shown in figure 4.22. The fake rate is

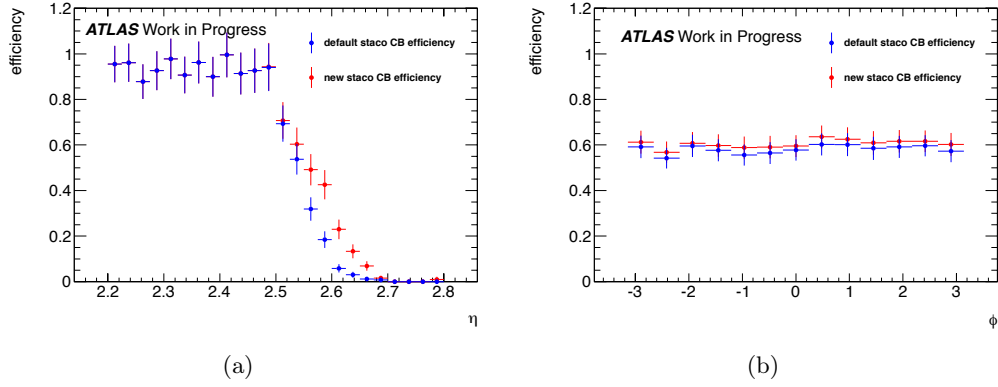


Figure 4.19: Reconstruction efficiency of the Staco combined muons in ranges of (a) η (b) ϕ for those in $|\eta| > 2.2$.

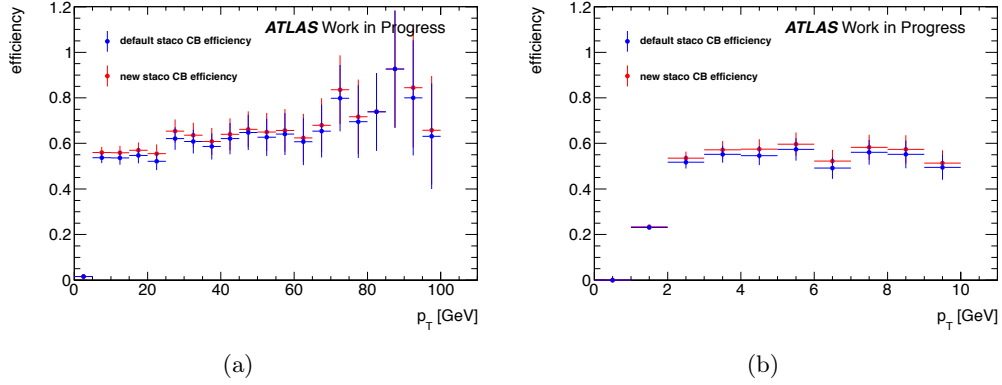


Figure 4.20: Reconstruction efficiency of the Staco combined muons in ranges of (a) p_T (b) below 10 GeV for those in $|\eta| > 2.2$.

quite high below 6 GeV, but not increased by the tracklet combined muons.

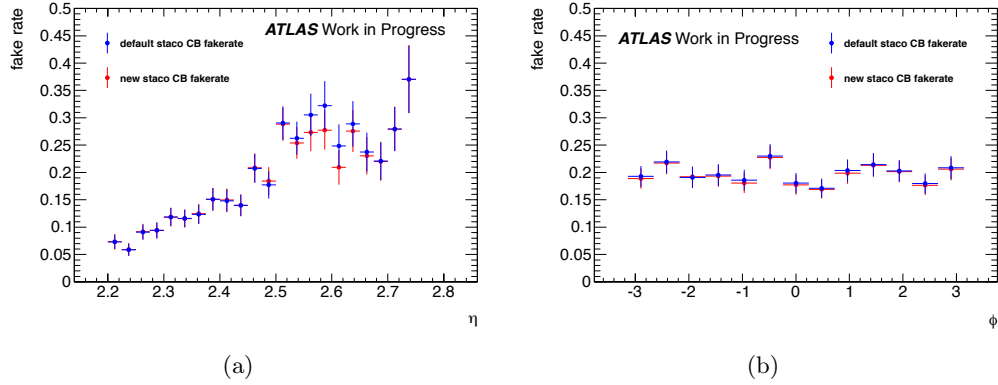


Figure 4.21: Fake rate of the staco combined muons as a function of (a) η (b) ϕ in the range of $|\eta| > 2.2$.

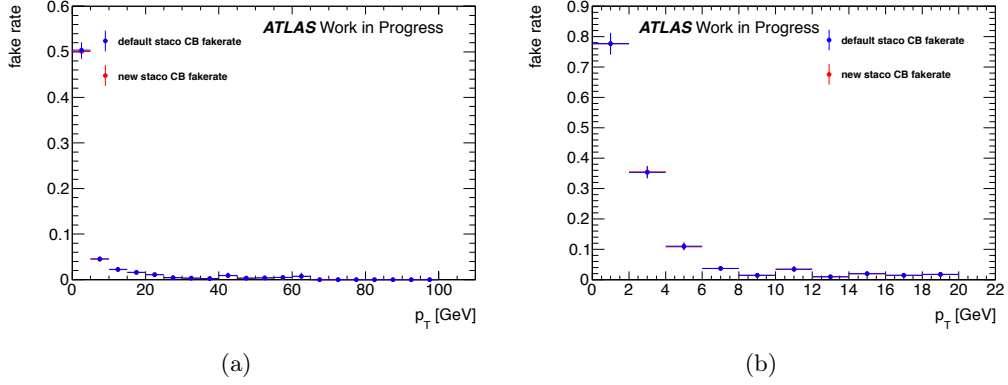


Figure 4.22: Fake rate of the staco combined muons as a function of (a) p_T (b) below 10 GeV in the range of $|\eta| > 2.2$

The advantage of transformation from a SA muon to a combination with the tracklet, is that an impact parameter and good p_T resolution can be obtained. This is validated by comparing the CB and the MS measurement of the tracklet muons. Figure 4.23 shows the deviation of reconstructed d_0 and z_0 compared to truth. A very dramatic difference is seen between the CB and MS, which indicates a much more precise measurement with the CB. The p_T resolution, defined as $\frac{p_T^{Reco} - p_T^{Truth}}{p_T^{Truth}}$, is shown in figure 4.24. The CB measurement has a better resolution than the MS, as there are more events seen in the core and less in the tail. This is expected considering the long lever arm between the SA muon and the tracklets.

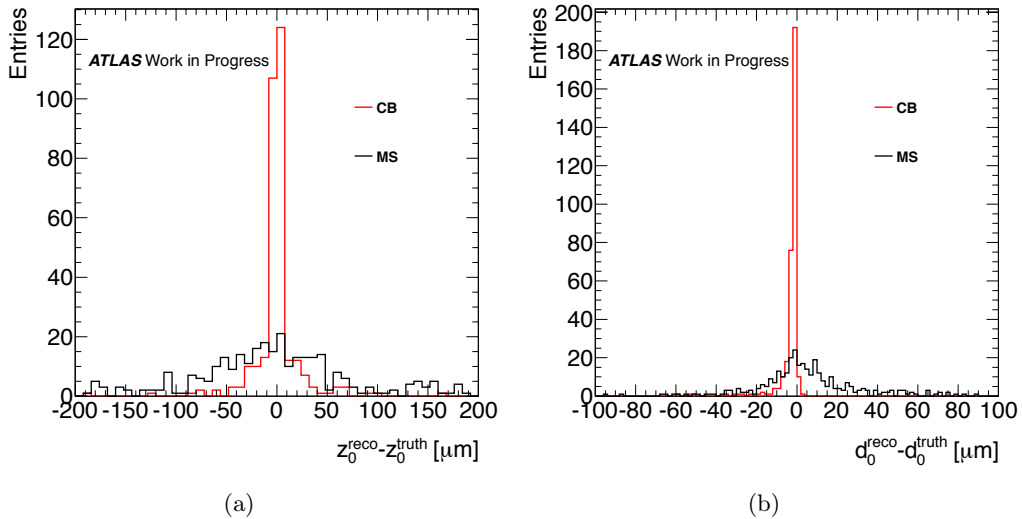


Figure 4.23: For the tracklet combined muons, the difference between reconstructed and generated (a) d_0 (b) z_0 , is shown. Combined and MS measurements are compared.

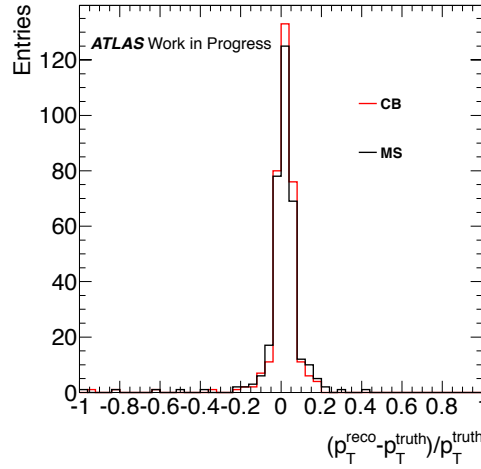


Figure 4.24: For the tracklet combined muons, the difference between reconstructed and generated p_T , is shown. Combined and MS measurements are compared.

4.2.3 Summary

ID tracks reconstructed softly with pixel hits (tracklets) are combined with STACO standalone muons and tested in the forward region. This new type of combined muons can be successfully reconstructed with no abnormal behaviour even in high pileup conditions. This increases the efficiency of combined muons in the high η range, uniformly in ϕ and p_T . The rate of fake muons does not increase by including these muons. With the combination, the resolutions of impact parameter and p_T are greatly improved. The tracklets combined muons are now included in the official reconstruction of ATLAS, and are used in the $H \rightarrow ZZ^* \rightarrow 4\ell$ analysis.

Chapter 5

Final State Radiation (FSR) in $Z \rightarrow \mu\mu$ decays

The measurement of the Z mass spectrum is an important standard model benchmark for ATLAS. It provides stringent tests of perturbative quantum chromodynamics (QCD) and significant constraints on the evaluation of the parton distribution functions (PDFs). Furthermore, the production of Z lepton pairs constitutes a major source of background for $t\bar{t}$ and diboson measurements, as well as for searches for New Physics. However, muons can radiate nearly collinear photons in a process called final state electromagnetic radiation (FSR), which significantly alters the shape of the di-muon mass spectrum, as well as the signal acceptance. The Feynman diagram of the FSR production is shown in Figure 5.1.

One may actually want to reconstruct and measure the FSR photons, especially in the Z resonance region, in order to improve the Z invariant mass reconstruction by including them in the calculations. In ATLAS, the FSR photons emitted at large angle from the Z decay muons' direction are reconstructed and identified with the standard reconstruction algorithms. The efficiency for reconstructing FSR photons can be significantly improved by

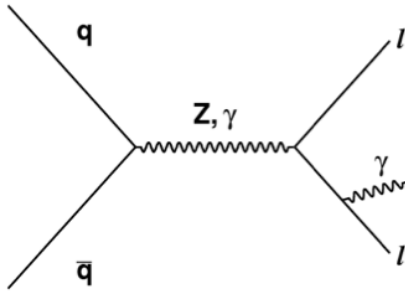


Figure 5.1: Feynman diagram of final state radiation in Z decay

also including photons emitted collinear to muons. Collinear photons can be reconstructed with the liquid argon (LAr) calorimeter by searching for electromagnetic (EM) clusters. The longitudinal segmentation of the LAr calorimeter can be exploited to reduce fake photon clusters produced by muon energy loss in the calorimeter. An FSR tool is thus developed [33], which searches for hard FSR photon radiated collinearly with the outgoing muon. For each muon, the tool searches EM clusters within a narrow cone around the axis defined by the muon momentum direction at the primary vertex. Topological clustering is used below 3.5 GeV, because it provides higher efficiency for identifying low-energy depositions in the EM calorimeter compared to the standard sliding-window clustering. Above 3.5 GeV standard photons are used. With the deposited energy in the calorimeter and a nearby inner detector muon track, the FSR photon can also be reconstructed as an electron. Therefore electrons are also treated as FSR photon candidates by the tool.

A significant background contribution is expected for the selected low energy EM clusters. To reduce the background, three additional selection cuts are applied to the reconstructed FSR photon candidates: i) the minimum transverse energy, ii) the angular distance between the FSR candidate and the muon, and iii) the longitudinal shower shape discriminant f_1 , which is the fraction of energy reconstructed in the first sampling of the EM calorimeter (strips) with respect to the total energy of the cluster. The values of the cuts are chosen by the user, depending on the desired efficiency and purity. If the tool succeeds in finding a candidate satisfying all the requirements, it will provide the photon information e.g. E_T , ΔR and types (reconstructed as electron or photon). If multiple FSR candidates are found, the closest one to the muon will be selected.

This chapter examines the properties of FSR photons, by using the tool. The performance in both MC and data are shown, which also serves as a test of the FSR modelling in the simulation. Based on the performance of the tool, the sets of cuts are optimised for the Z boson analysis. By applying the criteria to the $Z \rightarrow \mu\mu$ FSR selection, the effects on the di-muon spectrum are shown. The collinear FSR photons have an impact on the muon isolation. This is also investigated and shown in this chapter.

In processes where a Z boson is produced in the final state, e.g. $H \rightarrow ZZ^{(*)} \rightarrow 4\ell$, the FSR photons play a role as well. They deteriorate the 4-lepton mass resolution, which in turn leads to reduced sensitivity to the Higgs boson signal. The impact on the Higgs mass spectrum, will be discussed in Section 7.2.

5.1 Data and MC Samples

The proton-proton collision data at 7 TeV collected in 2011 is used for the FSR study, using an integrated luminosity of 2.5 fb^{-1} of data taken in a low pileup environment. The Monte Carlo sample that simulates the $Z \rightarrow \mu\mu$ process is generated with PYTHIA [34] and interfaced with POWHEG [35] for showering and hadronisation. The effects of QED radiative corrections are included using the package PHOTOS [36], which is executed in the

exponentiated mode, allowing for multiple photon emission. The infrared cut-off parameter in PHOTOS, E_γ^{min}/m , where the E_γ^{min} is the minimal energy of generated photons and m is the particle mass, is set to 10^{-7} . The ATLAS detector is modelled by GEANT4 [37]. The extra interactions in single and nearby bunch crossings are also simulated in MC, and weighted according to the observed data.

The study is first performed with generator level photons so that experimental effects coming from reconstruction can be excluded. Events which are generated with photons of transverse energy $E_T^\gamma > 3$ GeV are selected in a simulated $Z \rightarrow \mu\mu$ sample. The same criteria that are later applied at the reconstruction level are also applied here for consistency. Figure 5.2 shows the number of generator level photons per muon for all selected events in the MC sample. A single muon may produce more than one FSR photon, but in general only one of them will have enough energy to reach the detector. Figure 5.3 shows the E_T^γ spectrum and the pseudo-rapidity distributions of the photons. For comparison, non-FSR photons with $E_T^\gamma > 3$ GeV are also shown in the plots. As seen from the figure, above the threshold of 3 GeV, FSR photons are in general dominant in quantity over other types of photons. The non-FSR photons are characterised by low energy, while the FSR photons has a long high energy tail. The η distribution of the FSR photons in figure 5.3 shows that the FSR photons distribution is similar to the background photons. The FSR photons tend to be collinear with the muons, as illustrated by the distribution of $\Delta R(\mu, \gamma)$ in Figure 5.4. The figure also shows the angular distance between the photon and the muon, the $\Delta\phi(\mu, \gamma)$ and $\Delta\eta(\mu, \gamma)$. The distributions show that FSR photons are emitted close to the muon, while photons from other sources are generally uncorrelated with the muon and evenly distributed. The di-muon invariant mass is show in Figure 5.5 and is calculated before ($M_{\mu\mu}$) and after ($M_{\mu\mu\gamma}$) including the FSR photons. Including the FSR photons moves events from the low mass tail to the Z peak. The fraction of muons which undergo a FSR radiation of $E_T^\gamma > 3$ GeV and $\Delta R(\mu, \gamma) < 0.5$ is estimated to be 2%.

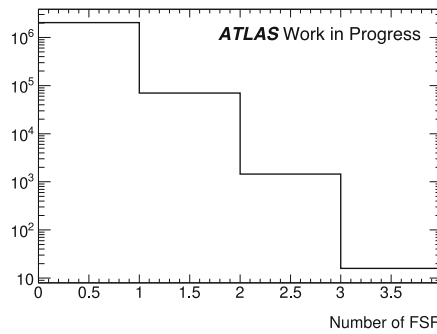
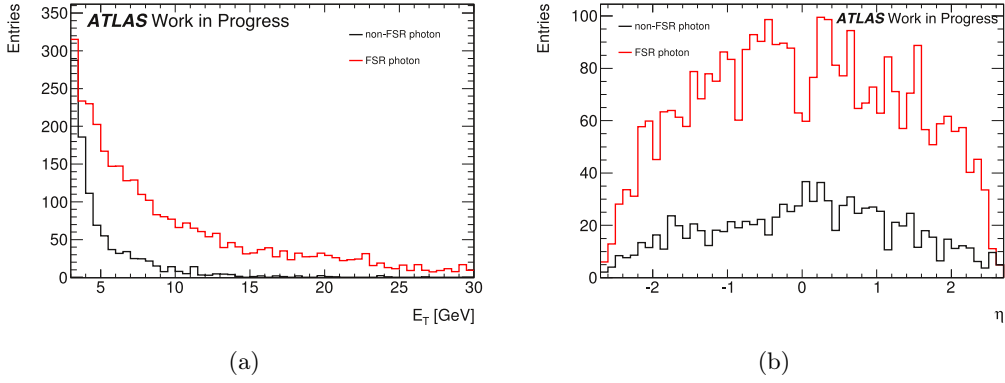
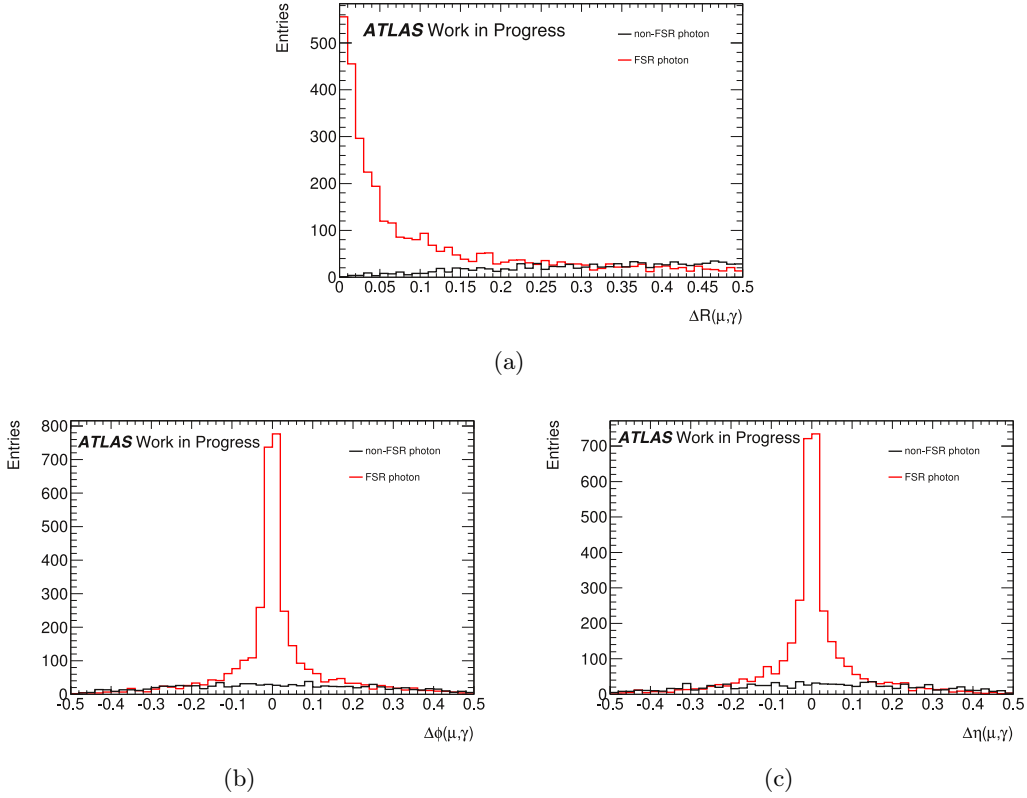


Figure 5.2: Number of FSR photons with $E_T > 3$ GeV per muon at the generator level.

Figure 5.3: Generator level photon E_T (left) and η (right) distributionFigure 5.4: (a) ΔR , (b) $\Delta\phi$ and (c) $\Delta\eta$ of generator level muon and nearest FSR photons and other types of photons.

5.2 Event Selection

At the reconstruction level, Z events are selected by requiring two combined muons with $p_T > 20$ GeV and $|\eta| < 2.4$. To reject cosmic muons or secondary muons the candidate is required to have absolute distance from the primary vertex (z_0) less than 10 mm and the transverse impact parameter d_0 less than 1 mm. A set of ID hit requirements [18] is

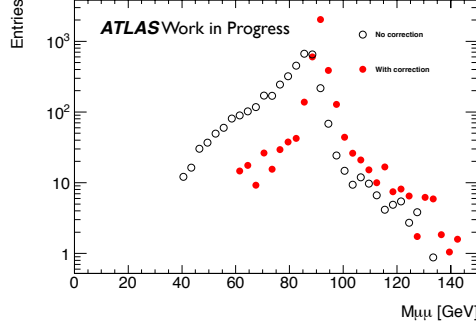


Figure 5.5: Simulated di-muon invariant mass before (black) and after (red) the FSR photon correction.

applied to select high quality tracks.

A track-based isolation criterion is defined as $\Sigma p_T^{ID}/p_T < 0.2$, where Σp_T^{ID} is the sum of transverse momenta of ID tracks with $p_T > 1$ GeV within a cone of $\Delta R < 0.2$ around the muon direction, and p_T is the muon transverse momentum p_T . After all other selection cuts are applied, this requirement has a high QCD background rejection power, while keeping more than 99% of the signal events. In the $Z \rightarrow \mu\mu$ channel, the relative background contributions from $t\bar{t}$ events, $Z \rightarrow \tau\tau$ and diboson decays are less than 1% and are thus neglected.

QED FSR photons emitted in $Z \rightarrow \mu\mu$ are selected by the FSR tool. The candidates are required to have a minimum transverse energy of 3.5 GeV. A longitudinal shower shape cut $E_{strip}/E_{cluster} > 0.15$ is applied to further reduce the background. The value of the cut is set according to reference [33]. The ΔR cut is used to decrease the number of fake FSR photons. But to study the properties of all types of photons, this cut is relaxed to $\Delta R < 0.5$.

5.3 FSR photon candidates

The selected FSR photon candidates may be true FSR photons or come from various sources of background. They enter into three categories based on the availability of the MC truth information:

Underlying Events (UE) The underlying events of the proton-proton collision produces abundant neutral pions, which decay to photons. The pile-up events that originate from non-primary interactions produce photons in a similar way. Initial state radiation also produces photons. As the events are simulated in MC, one can always use the truth information to determine the source of the photon. This kind of photons will be labelled as "underlying event" (UE) type.

Unmatched There is another type of photons that cannot be traced using MC truth information. Instead of being produced in the interactions simulated by the event generator, the photons come from detector effects, for example from the bremsstrahlung of charged particles through their interaction with material. These photons are simulated by GEANT4 and are called "unmatched".

True muon The MC truth matching algorithm classifies the photons into two categories of true muon: the photons from muon ionisation and the "true FSR" photons. The electromagnetic calorimeter cells seeded as a photon candidate sometimes get their energy deposition from the muon ionisation. Therefore these photons are labelled as true muons. The other composition of true muon, the FSR photon, is obtained by the ATLAS truth matching algorithm. A FSR photon that is extremely close to the muon, can be reconstructed as an electron, as explained in the introduction, where the track in fact belongs to the muon. The truth matching algorithm links the reconstructed inner detector track to a generator level particle, which in this case, is the muon track. The FSR photon is then categorised as a true muon in the MC truth information. In previous reconstruction versions, there was no way to distinguish the muon ionisation from FSR in the true muon category.

The properties of the different sources of photons are studied using the FSR tool. Figure 5.6 shows the ΔR between the photon and the muon of the selected Z events in different E_T regimes. The contribution from true FSR and backgrounds in MC are also shown and compared with data. As seen from the figure, most of the underlying event type photons (red) and unmatched photons (green) are low E_T , they vanish quickly around $E_T > 7$ GeV; above 10 GeV, the selected photons are mainly true FSR and muon ionisation types. There is a clear signature of the UE and unmatched photons are well separated from the muon, while the other two types are mostly collinear with the muon. The data is well described by the MC in all E_T ranges.

5.4 FSR tool performance

As explained in Section 5.3, the tool can select fake FSR photons. An optimisation is made to reduce the fake FSR photons while still keeping high efficiency. To quantify, the purity and efficiency of the tool are defined. The purity is calculated as the ratio between the number of true FSR photons and the number of the photons selected by the tool. It varies according to various cuts imposed on the photons. Figure 5.7 shows the purity as a function of the ΔR cut, in different E_T regions. As most of the fakes are low E_T and far away from the muon, the purity decreases as the ΔR cut increases, and the low E_T region has an overall lower purity than the high E_T region. A purity of 50% is obtained at very low E_T range of 3–4 GeV, and this number increases to 95% for $E_T > 15$ GeV for the same ΔR cut of 0.15.

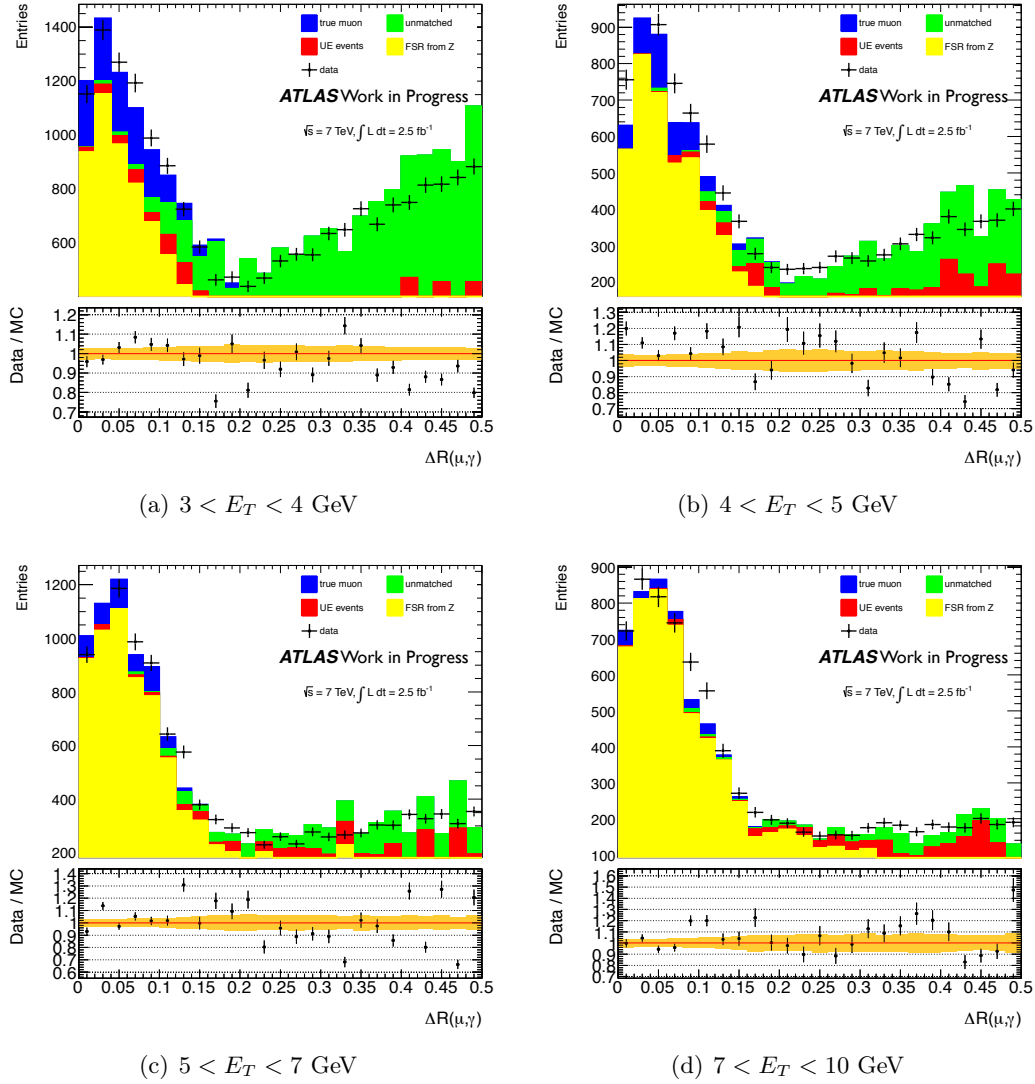


Figure 5.6: Distribution of the distance ΔR between muon and the selected FSR candidates in different E_T regions.

The efficiency of the tool on the other hand, is defined by the ratio of the number of photons selected by the tool over the number of generated FSR photons. This reflects the tool's capability of correcting the Z mass spectrum. The variation as a function of the ΔR cut is shown in figure 5.8 for different values of the photon E_T . The efficiency decreases as the selected E_T cut increases. At the default value of E_T cut, 3.5 GeV, the efficiency is 60%, if the ΔR is required to be smaller than 0.15.

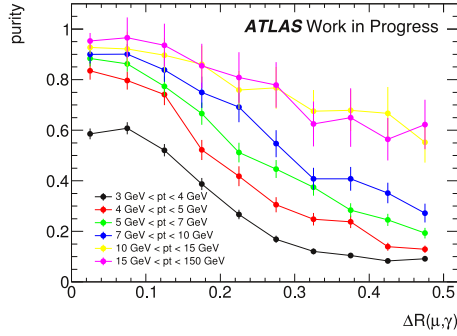


Figure 5.7: Purity determined with the FSR tool as a function of $\Delta R(\mu, \gamma)$ for different E_T^γ cuts

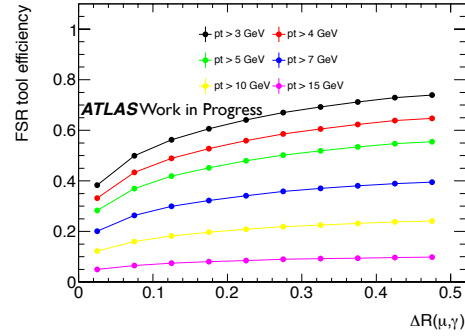


Figure 5.8: Efficiency of the FSR tool as a function of $\Delta R(\mu, \gamma)$ for different E_T^γ cuts

Adding fake FSR photons can distort the shape of the Z boson mass distribution. The overall effect on the whole mass spectrum is studied by calculating the mistag rate r_{mistag} of the tool. The mistag rate is defined as the probability to find fake FSR photons for all the $Z \rightarrow \mu\mu$ events. It can be expressed in terms of purity:

$$r_{mistag} = (1 - p) \times r_{FSR}$$

where p is the purity of the tool, and r_{FSR} is the rate of FSR candidates in the $Z \rightarrow \mu\mu$ events. Figure 5.9 shows the distribution of the mistag rate as a function of ΔR cut, and this rate is far below 0.5% in all circumstances, which guarantees the safety of using the tool.

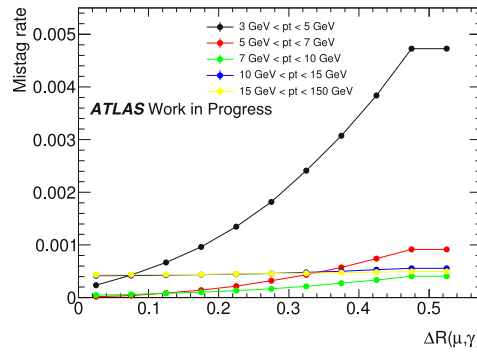


Figure 5.9: Fake rate of FSR tool as a function of $\Delta R(\mu, \gamma)$ for different E_T^γ cuts.

5.5 FSR impact on the Z boson mass spectrum and the resolution

The tool is aimed at correcting the Z boson mass spectrum and improving the resolution. This is validated by adding the identified FSR photon to the reconstructed invariant mass. Figure 5.10 shows in its top part the invariant mass of $\mu\mu\gamma$ versus $\mu\mu$ when the tool finds a FSR candidate with cut $\Delta R < 0.5$ (left) and $\Delta R < 0.2$ (right). The different colours represent the types of photons. As the bottom part in Figure 5.10 shows, adding the FSR moves the low mass tail to the Z pole. The true muon type, which is a combination of muon ionisation and true FSR photon, has a similar effect as adding FSR photons on the spectrum. The background photons, which are more visible in the large ΔR region, have an opposite effect on the Z mass: adding them moves the Z mass tails to higher values. This impact can be effectively reduced by a tighter ΔR cut as shown in figure 5.10(b) and (d) where most of the fake photon sources disappear.

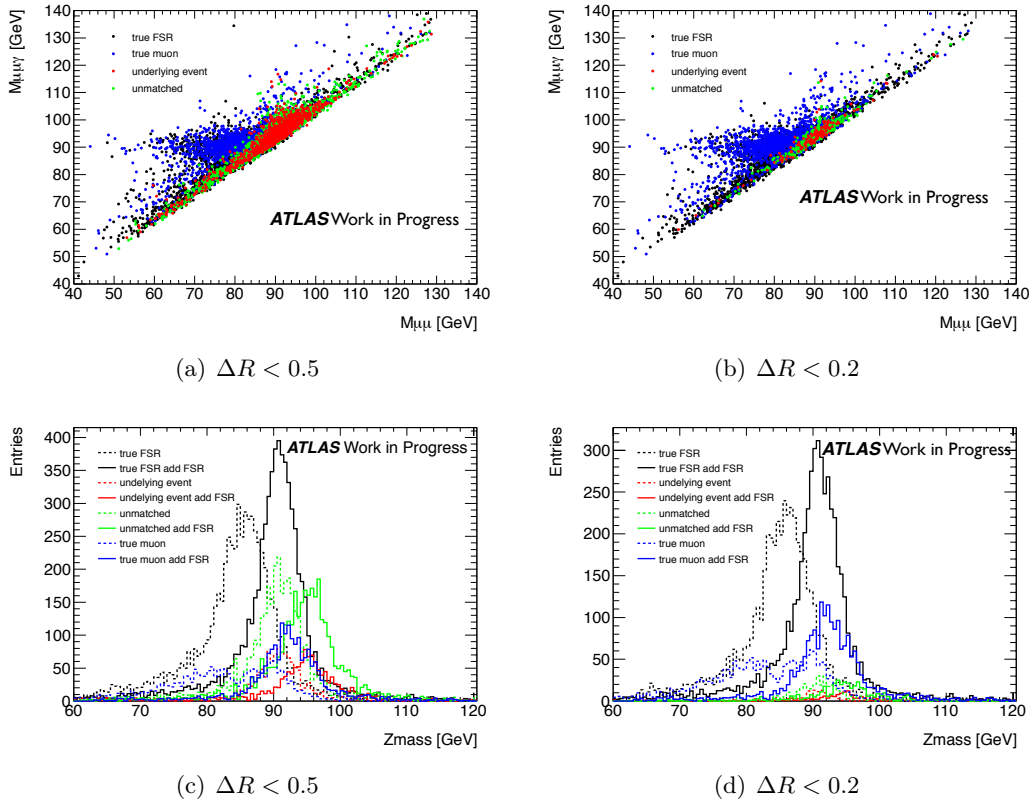


Figure 5.10: For events where FSR photons are found by the FSR tool, the two-dimensional comparison between $m_{\mu\mu\gamma}$ and $m_{\mu\mu}$ is shown for two ΔR cuts: $\Delta R < 0.5$ (a) and $\Delta R < 0.2$ (b). The effect of including the FSR photons for calculating the $Z \rightarrow \mu\mu$ mass is shown in (c) and (d) for the two ΔR cuts.

The effect on the mass resolution of the Z is examined by fitting the Z mass before

and after adding the selected FSR photons with ΔR cut of 0.2. The fraction of events containing FSR photons according to the tool is 2%. The model used in the fit is a Breit-Wigner convoluted with a Gaussian resolution function [38]. The result of the fit is shown for both MC and data in figure 5.11. The resolution improves by 1% in data as well as in MC when FSR photons are included. The deviation from the PDG value of the Z mass denoted as μ in the plot, is also improved by ~ 30 MeV.

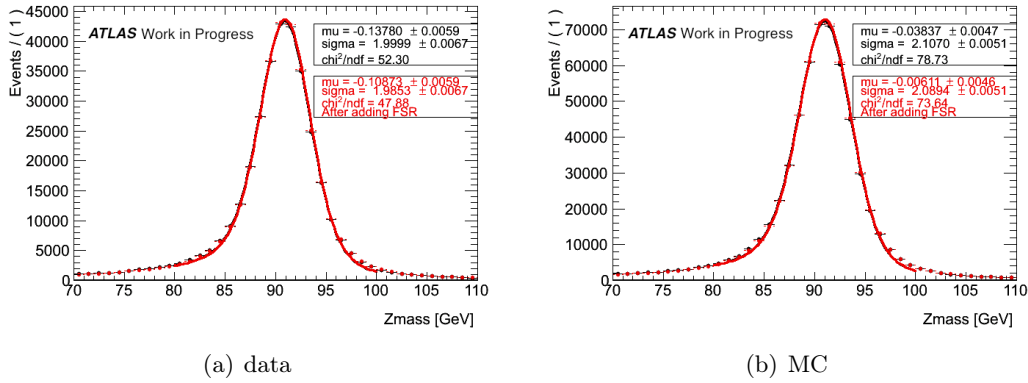


Figure 5.11: Di-muon invariant mass resolution in data and MC without (black) and with (red) FSR photons.

5.6 FSR impact on muon isolation

A conventional calorimeter isolation requirement is to use the sum of the transverse calorimeter energy deposited around a muon within a cone of $\Delta R = 0.2$ or 0.3 , which after subtracting its own energy, should not exceed 20% or 30% of its transverse momentum. As in most cases, the FSR photon is quite close to the muon, its energy deposition in the calorimeter can affect the isolation performance of the muon. Figure 5.12 shows the efficiency of the muon to pass the calorimeter isolation cut $\Sigma E_T^{20}/p_T < 0.2$ and $\Sigma E_T^{30}/p_T < 0.3$ as a function of the reconstructed di-muon mass. The efficiencies are obtained using the tag and probe method on the $Z \rightarrow \mu\mu$ events. The probe muon should satisfy $p_T > 20$ GeV. The calorimeter efficiency of the probe muon shown in Figure 5.12 is calculated after applying track isolation requirement, which is $\Sigma p_T^{20}/p_T < 0.14$. The black and blue curves which represent the MC and data respectively show a drop around 80 GeV, where most of the FSR events are located. To validate the assumption that this effect is due to FSR, events with FSR photons identified by the tool are removed and the efficiency is recalculated. As the red and yellow curves show for MC and data, the efficiency is recovered and reaches the same level at all masses. Since the tool has some inefficiency at identifying FSR photons, the procedure is repeated by removing events containing FSR photons at the generator level, and the overall efficiency is shown in green, which is flat over the mass spectrum. This leads to the conclusion that the FSR photons cause a 10% drop in the

isolation efficiency for muons under the Z mass peak.

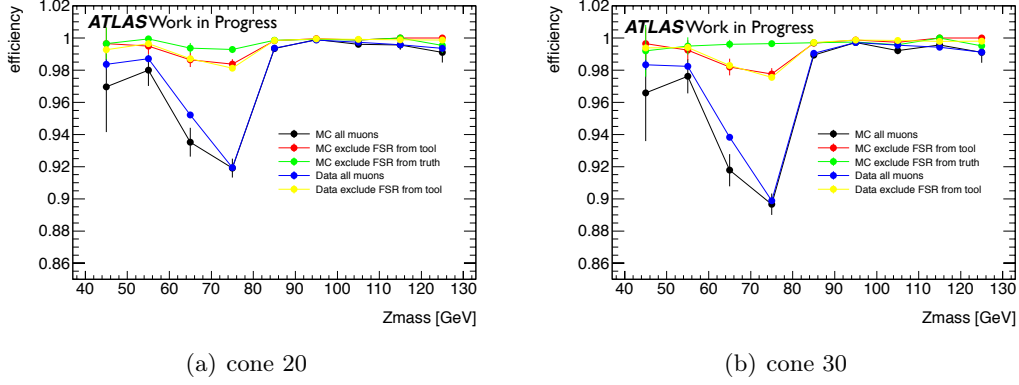


Figure 5.12: Calorimeter isolation efficiency as a function of the reconstructed $Z \rightarrow \mu\mu$ mass, after applying track isolation ($\Sigma p_T^{20}/p_T < 0.14$).

To compensate for the loss, one needs to remove the FSR contribution to the cone around the muon. This can be achieved by removing all the electromagnetic energy part of calorimeter isolation when a FSR is identified. Figure 5.13 shows the comparison between the efficiency of the muon passing the isolation criteria ($\Sigma E_T^{20}/p_T < 0.2$) by using the default isolation variable and the new variable. The drop of 10% in efficiency near the Z peak is compensated by the use of the new variable. This variable is now used in the ATLAS software.

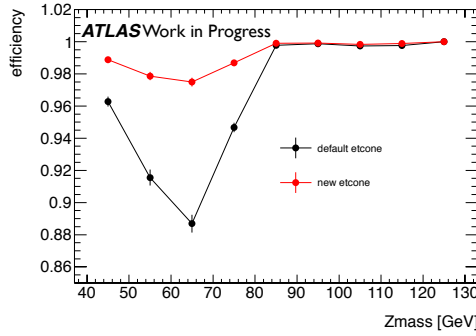


Figure 5.13: Calorimeter isolation $\Sigma E_T^{20}/p_T < 0.2$ efficiency using the default and the new variable.

5.7 Summary

In this chapter, the FSR photon impact on the $Z \rightarrow \mu\mu$ decay is studied by the use of the FSR tool. The tool is optimised based on its performance on identifying efficiency, purity and fake rate. The MC has shown a good description of the data in terms of FSR properties. Adding the FSR to the Z corrects the mass spectrum from low mass tail to Z

pole. In addition, the degradation of the mass resolution caused by the FSR is found to be 1%. The FSR also affects the muon isolation, this is seen in the drop of isolation efficiency when FSR is identified. By subtracting the contribution of FSR from the cone around the muon, the efficiency is recovered. This variable defined for the FSR case is now added in ATLAS software.

Chapter 6

Search for $H \rightarrow ZZ^{(*)} \rightarrow 4\ell$ using 4.8 fb^{-1} of 7 TeV data and 5.8 fb^{-1} of 8 TeV data

The search for the Higgs boson is the major goal of the ATLAS experiment. Among various direct search channels, $H \rightarrow ZZ^{(*)} \rightarrow 4\ell$, where the ℓ stands for electron or muon has the most distinctive signature. The decay diagram is shown in figure 6.1. As discussed in section 1.3, this is the "golden" channel that makes the best use of excellent energy resolution and linearity of the reconstructed electrons and muons, leading to a narrow 4-lepton invariant mass on top of background events. The low branching ratio of this final state in the low mass region is compensated by the capability to fully reconstruct the mass, which produces a great sensitivity in the 110 to 600 GeV mass range.

The search for the Higgs boson decaying to four leptons is conducted in 4 different final states: $\mu^+\mu^-\mu^+\mu^-$ (4μ), $e^+e^-e^+e^-$ ($4e$), $\mu^+\mu^-e^+e^-$ ($2\mu 2e$), $e^+e^-\mu^+\mu^-$ ($2e 2\mu$). The convention is that the leading lepton pair has a reconstructed mass closer to the Z boson mass. The major background in this channel is the continuum $(Z^{(*)}/\gamma^*)(Z^{(*)}/\gamma^*)$, referred to as $ZZ^{(*)}$ hereafter. This irreducible background differs from the signal only in the way the Z bosons are produced, as shown in the Feynman diagrams in figure 6.2, and has therefore an indistinguishable final state from the signal. In the regime of $m_H < 180$ GeV, where one of the Z is off-shell and decays into low transverse momentum leptons, the reducible backgrounds from $t\bar{t}$ and $Z + jets$ become important too. The top pair produced via gluon-gluon fusion and quark-antiquark annihilation have 4 reconstructed leptons in the final state when the W boson and b quark from top decay both subsequently decay to leptons. The Z production accompanied by jets have a very large cross section. The jets are either heavy-quark jets that predominantly decay to leptons or light-quark jets that can be possibly mis-identified as leptons, which together with the two prompt leptons from the Z, form the four leptons final state. Other background contributions, from QCD

and diboson processes, though negligible, are considered in the analysis. In spite of a much larger cross section compared with the signal and ZZ^* background, the irreducible backgrounds can be well controlled through additional criteria on lepton quality such as isolation and impact parameter significance.

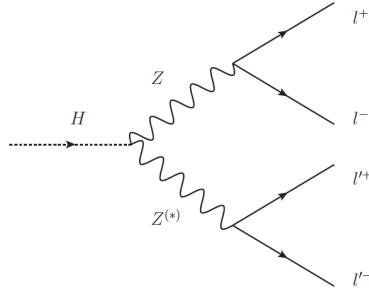


Figure 6.1: The decaying mode of $H \rightarrow ZZ^{(*)} \rightarrow 4\ell$ in ATLAS.

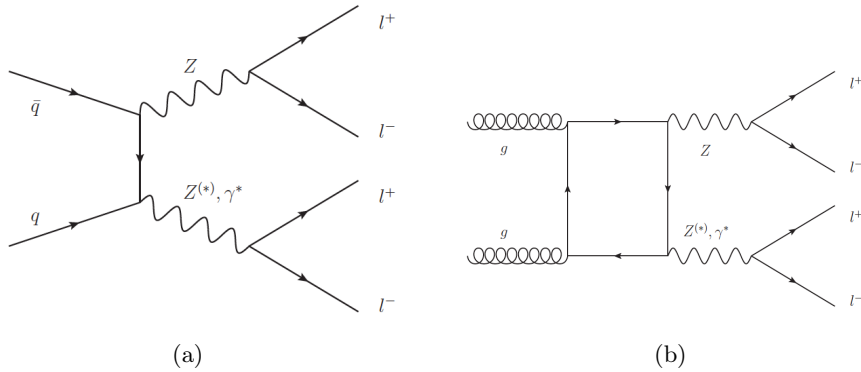


Figure 6.2: The production mode of ZZ^* in ATLAS, (a) through quark antiquark annihilation, (b) through gluon gluon fusion.

Search in this channel using the full 2011 4.8 fb^{-1} data has been published in ref. [39]. The mass regions 134–156 GeV, 182–233 GeV, 256–265 GeV, and 268–415 GeV have been excluded. Incorporating with the previous results from LEP and Tevatron (see section 1.2), one concludes that a light Higgs is preferred if it exists. Therefore, the analysis is re-optimized towards increasing the sensitivity in the low mass region, and the results, combining 2011 data and 2012 data, will be presented in every detail. Section 6.1 introduces the samples used for the analysis, including the data and simulation of signal and background processes. The optimisation of the event selection criteria is described in section 6.2. Section 6.3 presents the various techniques of data-driven methods to estimate the background. The signal mass resolution and systematic errors are discussed in section 6.4 and 6.5. The final result of the event selection is shown in section 6.6, the exclusion limits based on the result is illustrated in section 6.7, with a summary in section 6.8.

6.1 Data and Simulation Samples

The data delivered to ATLAS in 2011 and 2012 are used in the analysis and must satisfy quality requirements. To be accepted, events must have been recorded during periods when the relevant detector components were operating properly. The resulting integrated luminosity is 4.8 fb^{-1} , 4.8 fb^{-1} and 4.9 fb^{-1} for 4μ , $2e2\mu$ ($2\mu2e$), and $4e$ final states in 2011 and 5.8 fb^{-1} , 5.8 fb^{-1} and 5.8 fb^{-1} in 2012, respectively.

The GEANT4 software [37] is used to simulate the ATLAS detector, as well as the signal and background processes which are simulated, digitised and reconstructed within the ATLAS computing framework ATHENA [40]. Additional pp interactions in the same and adjacent bunch crossings (pile-up) are included in the simulation. The Monte-Carlo (MC) samples are re-weighted to reproduce the distribution of the mean number of interactions per bunch crossing observed in the data. Section 6.1.1 introduces the MC samples used in the analysis of the signal and the corresponding cross section, and discusses theoretical uncertainties. The same information is given in section 6.1.2 for the background processes.

6.1.1 Signal

All the four production modes of the Higgs boson are considered in the search, except associated production with a top quark pair, which has a negligible cross section. The simulation of $H \rightarrow ZZ^{(*)} \rightarrow 4\ell$ is done by POWHEG Monte Carlo (MC) event generator, [41, 42], which calculates separately the gluon fusion and vector-boson fusion production mechanisms with matrix elements up to next-to-leading order (NLO). The Higgs boson transverse momentum (p_T) spectrum in the gluon fusion process is re-weighted to follow the calculation of Ref. [43], which includes QCD corrections up to NLO and QCD soft-gluon re-summations up to next-to-next-to-leading logarithm (NNLL). POWHEG is interfaced with PYTHIA [34] for showering and hadronization, which in turn is interfaced with PHOTOS [44] for quantum electrodynamics (QED) radiative corrections in the final state and to TAUOLA [45, 46] for the simulation of τ lepton decays. PYTHIA is used to simulate the production of a Higgs boson in association with a W or a Z boson.

The Higgs boson production cross sections and decay branching ratios, as well as their uncertainties, are taken from Refs. [10, 11]. Different schemes are used for 7 TeV and 8 TeV. The cross section calculations for 7 TeV do not take into account the width of the Higgs boson, which is implemented through the zero-width-approximation (ZWA), while for 8 TeV data, the complex-pole-scheme (CPS) for ggF and VBF ($m_H > 300 \text{ GeV}$) is adopted. The difference between the two schemes at $m_H = 125 \text{ GeV}$ is minor (0.1%), but becomes sizeable in the range $m_H = 200 - 300 \text{ GeV}$. In the absence of a full calculation, the possible size of such effects is included as a signal normalisation systematic uncertainty and parameterised as a function of m_H : $150\% \times m_H^3 [\text{TeV}]$, for $m_H \geq 300 \text{ GeV}$ [11].

The cross sections for the gluon-fusion process have been calculated to NLO [47–49], and NNLO [50–52] in QCD. In addition, QCD soft-gluon re-summations calculated in

NNLL approximation are applied for the gluon-fusion process [53]. NLO electroweak (EW) radiative corrections are also applied [54, 55]. These results are compiled in Refs [56–58] assuming factorisation between QCD and EW corrections. The QCD scale uncertainties for $m_H = 125$ GeV amount to ${}^{+7}_{-8}\%$. The uncertainty in the production cross section due to uncertainties in the parton distribution function (PDF) and α_s is $\pm 8\%$, and is estimated by following the prescription in Ref [59] and by using the PDF sets of CTEQ [60], MSTW [61] and NNPDF [62].

The cross sections for vector-boson fusion process are calculated with full NLO QCD and EW corrections [63–65], whereas approximate NNLO QCD corrections are also available [66]. The uncertainties in the production cross section from the QCD scale and PDF are estimated to be $\pm 1\%$ and $\pm 4\%$, respectively.

The cross sections for the associated WH/ZH production processes are calculated at NLO [67] and at NNLO [68] in QCD, and NLO EW radiative corrections [69] are applied. The uncertainties from the QCD scale and PDF are the same as in VBF process, which is $\pm 1\%$ and $\pm 4\%$, respectively.

The Higgs boson decay branching ratio [70] to the four-lepton final state is predicted by PROPHECY4F [71, 72], which includes the complete NLO QCD+EW corrections, interference effects between identical final-state fermions, and leading two-loop heavy Higgs boson corrections to the four-fermion width. Table 6.1 gives the production cross sections and branching ratios for $H \rightarrow ZZ^{(*)} \rightarrow 4\ell$ at 7 and 8 TeV, which are used to normalize the signal MC, for several Higgs boson masses.

6.1.2 Background

The $ZZ^{(*)}$ continuum background produced from quark-antiquark annihilation and gluon fusion are modelled by the POWHEG [73] and GG2ZZ [74], respectively. The cross section and the shape of the $ZZ^{(*)}$ system invariant mass are predicted by MCFM [75, 76], at QCD NLO, the numbers corresponding to 7 TeV energy are listed in table 6.2. The uncertainty is $\pm 5\%$ from the QCD scale and $\pm 4\%$ ($\pm 8\%$) from the PDF and α_s for quark (gluon) initiated processes.

ALPGEN [77] is used to model the Z + jets process, which is composed of Z + light jets and $Zb\bar{b}$ samples. The Z + light jets sample includes both $Zc\bar{c}$ in the massless c -quark approximation and $Zb\bar{b}$ from parton showers. The $Zb\bar{b}$ sample uses matrix element calculations that take into account the b -quark mass. Since ALPGEN does not include any form of showering or hadronization, the interface of ALPGEN output to the external showering package introduces the risks of double counting of identical jets produced via the matrix element calculation and via the parton shower. This double counting is removed by the MLM [78] matching scheme, but not for b -jets. Therefore, $b\bar{b}$ pairs with separation $\Delta R = \sqrt{(\Delta\phi)^2 + (\Delta\eta)^2} > 0.4$ between the b -quarks are taken from the matrix-element calculation, whereas for $\Delta R < 0.4$ the parton-shower $b\bar{b}$ pairs are used. The simulation of

Table 6.1: Higgs boson production cross sections for gluon fusion, vector-boson fusion and associated production with a W or Z boson in pp collisions [10] at $\sqrt{s} = 7, 8$ TeV [10]. The quoted uncertainties correspond to the total theoretical systematic uncertainty. The production cross section for associated production with a W or Z boson is negligibly small for $m_H > 300$ GeV. The decay branching ratio for $H \rightarrow 4\ell$, with $\ell = e$ or μ , is reported in the last column [10].

m_H [GeV]	$\sigma(gg \rightarrow H)$ [pb]	$\sigma(qq' \rightarrow Hqq')$ [pb]	$\sigma(q\bar{q} \rightarrow WH)$ [pb]	$\sigma(q\bar{q} \rightarrow ZH)$ [pb]	$\text{BR}(H \rightarrow ZZ^{(*)} \rightarrow 4\ell)$ [10^{-3}]
$\sqrt{s} = 7$ TeV					
125	$15.3^{+3.0}_{-2.3}$	1.21 ± 0.03	$0.57^{+0.02}_{-0.03}$	0.32 ± 0.02	0.13
130	$14.1^{+2.7}_{-2.1}$	1.15 ± 0.03	0.50 ± 0.02	0.28 ± 0.01	0.19
190	$5.9^{+1.0}_{-0.9}$	0.69 ± 0.02	0.125 ± 0.005	0.074 ± 0.004	0.94
400	$2.03^{+0.32}_{-0.33}$	$0.162^{+0.009}_{-0.005}$	—	—	1.21
600	0.37 ± 0.06	$0.058^{+0.005}_{-0.002}$	—	—	1.23
$\sqrt{s} = 8$ TeV					
125	19.5 ± 2.9	$1.56^{+0.04}_{-0.05}$	0.70 ± 0.03	0.39 ± 0.02	0.13
130	18.1 ± 2.6	1.49 ± 0.04	0.61 ± 0.03	0.35 ± 0.02	0.19
190	7.9 ± 1.1	$0.91^{+0.03}_{-0.02}$	0.156 ± 0.007	0.094 ± 0.006	0.94
400	2.9 ± 0.4	0.25 ± 0.01	—	—	1.21
600	0.5 ± 0.1	0.097 ± 0.004	—	—	1.23

this process is not directly used in the analysis, but rather the normalised control samples from data. The cross sections for inclusive Z boson and $Zb\bar{b}$ production are obtained from the QCD NNLO FEWZ [79, 80] and MCFM, respectively, as shown in table 6.2 for 7 TeV. The $t\bar{t}$ background is modelled using MC@NLO [81]. The corresponding cross section comes from approximate NNLO calculation using HATHOR [82]. The effect of the QCD scale uncertainty on the cross section is $^{+4}_{-9}\%$, while the effect of PDF and α_s uncertainties is $\pm 7\%$. This background is also estimated from control samples of data. Both ALPGEN and MC@NLO are interfaced to HERWIG [83] for parton shower hadronization and to JIMMY [84] for the underlying event simulation.

6.2 Event Selection and Optimization

A series of criteria are imposed in order to select good quality data for identifying a possible signal. The criteria include trigger requirements, described in section 6.2.1, lepton quality in section 6.2.2, kinematics and the topology of the event in section 6.2.3 and additional lepton requirements to reduce background: e.g. isolation performance in section 6.2.4. The invariant mass resolution after all selections is further improved by applying a Z mass constraint to the leading di-lepton for $m_{4\ell} < 190$ GeV and to both di-leptons for higher masses. Further discussion on the Z mass constraint will be presented in section 6.4. The complete event selection scheme is shown in table 6.3. In addition, event candidates are

Table 6.2: Background Samples and their cross-sections in fb at 7 TeV. The numbers after " \times " are k-factors.

ID	Process	Cross-section [fb]
107650	AlpgeJimmy $Zee + 0p$	827375
107651	AlpgeJimmy $Zee + 1p$	166625
107652	AlpgeJimmy $Zee + 2p$	50375
107653	AlpgeJimmy $Zee + 3p$	14000
107654	AlpgeJimmy $Zee + 4p$	3375
107655	AlpgeJimmy $Zee + 5p$	1000
107660	AlpgeJimmy $Z\mu\mu + 0p$	822125
107661	AlpgeJimmy $Z\mu\mu + 1p$	166000
107662	AlpgeJimmy $Z\mu\mu + 2p$	49500
107663	AlpgeJimmy $Z\mu\mu + 3p$	13875
107664	AlpgeJimmy $Z\mu\mu + 4p$	3500
107665	AlpgeJimmy $Z\mu\mu + 5p$	1000
107670	AlpgeJimmy $Z\tau\tau + 0p$	828125
107671	AlpgeJimmy $Z\tau\tau + 1p$	167375
107672	AlpgeJimmy $Z\tau\tau + 2p$	50375
107673	AlpgeJimmy $Z\tau\tau + 3p$	13750
107674	AlpgeJimmy $Z\tau\tau + 4p$	3500
107675	AlpgeJimmy $Z\tau\tau + 5p$	1000
116960	Zeebb, $Z \rightarrow ee$ ($ll > 30$ GeV) + 0p [$m_{4\ell}$ 60/12 GeV]	20.701
116961	Zeebb, $Z \rightarrow ee$ ($ll > 30$ GeV) + 1p [$m_{4\ell}$ 60/12 GeV]	18.8029
116962	Zeebb, $Z \rightarrow ee$ ($ll > 30$ GeV) + 2p [$m_{4\ell}$ 60/12 GeV]	10.505
116963	Zeebb, $Z \rightarrow ee$ ($ll > 30$ GeV) + 3p [$m_{4\ell}$ 60/12 GeV]	7.30463
116965	$Z\mu\mu bb$ ($ll > 30$ GeV) + 0p [$m_{4\ell}$ 60/12 GeV]	21.516
116966	$Z\mu\mu bb$ ($ll > 30$ GeV) + 1p [$m_{4\ell}$ 60/12 GeV]	19.6674
116967	$Z\mu\mu bb$ ($ll > 30$ GeV) + 2p [$m_{4\ell}$ 60/12 GeV]	10.516
116968	$Z\mu\mu bb$ ($ll > 30$ GeV) + 3p [$m_{4\ell}$ 60/12 GeV]	7.93834
116950	$Z\mu\mu bb$ ($ll > 30$ GeV) + 0p 3l filter, veto on $m_{4\ell}$ 60/12 GeV	756.32×1.4
116951	$Z\mu\mu bb$ ($ll > 30$ GeV) + 1p 3l filter, veto on $m_{4\ell}$ 60/12 GeV	432.25×1.4
116952	$Z\mu\mu bb$ ($ll > 30$ GeV) + 2p 3l filter, veto on $m_{4\ell}$ 60/12 GeV	176×1.4
116953	$Z\mu\mu bb$ ($ll > 30$ GeV) + 3p 3l filter, veto on $m_{4\ell}$ 60/12 GeV	96.75×1.4
116955	$Z\mu\mu bb$ ($ll > 30$ GeV) + 0p 3l filter, veto on $m_{4\ell}$ 60/12 GeV	730.24×1.4
116956	$Z\mu\mu bb$ ($ll > 30$ GeV) + 1p 3l filter, veto on $m_{4\ell}$ 60/12 GeV	432.25×1.4
116957	$Z\mu\mu bb$ ($ll > 30$ GeV) + 2p 3l filter, veto on $m_{4\ell}$ 60/12 GeV	179.3×1.4
116958	$Z\mu\mu bb$ ($ll > 30$ GeV) + 3p 3l filter, veto on $m_{4\ell}$ 60/12 GeV	92.3962×1.4
105200	$t\bar{t}$ (at least 1lepton filter)	91550.6
109346	$t\bar{t}$ (with $m_{\ell\ell} > 60$ GeV filter and $m_{\ell\ell} > 12$ GeV)	515.2
109292	$ZZ \rightarrow 4\ell$ 3LepFilter	91.54

required to have reconstructed primary vertices with at least three tracks.

Table 6.3: Summary of the event selection requirements. The two lepton pairs are denoted as m_{12} and m_{34} . The threshold values for m_{34} are defined through linear interpolation of the values in Table 6.6.

Event Preselection	
Electrons	
“MultiLepton” quality GSF electrons with $E_T > 7$ GeV and $ \eta < 2.47$	
Muons	
combined or segment-tagged muons with $p_T > 6$ GeV and $ \eta < 2.7$	
calo-tagged muons with $p_T > 15$ GeV and $ \eta < 0.1$	
standalone muons with $p_T > 6$ GeV, $2.5 < \eta < 2.7$ and $\Delta R > 0.2$ from closest segment-tagged	
Event Selection	
Kinematic Selection	Require at least one quadruplet of leptons consisting of two pairs of same-flavour opposite-charge leptons fulfilling the following requirements: p_T thresholds for three leading leptons in the quadruplet 20, 15 and 10 GeV Leading di-lepton mass requirement $50 \text{ GeV} < m_{12} < 106 \text{ GeV}$ Sub-leading di-lepton mass requirement $m_{threshold} < m_{34} < 115 \text{ GeV}$ Remove quadruplet if alternative same-flavour opposite-charge di-lepton gives $m_{\ell\ell} < 5 \text{ GeV}$ $\Delta R(\ell, \ell') > 0.10(0.20)$ for all same (different) flavour leptons in the quadruplet.
Isolation	Lepton track isolation ($\Delta R = 0.20$): $\Sigma p_T / p_T < 0.15$ Electron calorimeter isolation ($\Delta R = 0.20$): $\Sigma E_T / E_T < 0.20$ Muon calorimeter isolation ($\Delta R = 0.20$): $\Sigma E_T / E_T < 0.30$ Stand-Alone muons calorimeter isolation ($\Delta R = 0.20$): $\Sigma E_T / E_T < 0.15$
Impact Parameter Significance	Apply impact parameter significance cut to all leptons of the quadruplet. For electrons : $d_0 / \sigma_{d_0} < 6.5$ For muons : $d_0 / \sigma_{d_0} < 3.5$

6.2.1 Trigger

The trigger signatures for the online selection of four-lepton events are single and di-lepton triggers. One requires that the event passes either the single or the di-lepton trigger, and the 4 leptons that are later selected, should contain the lepton that matches to the single trigger or the two leptons that match to the di-lepton trigger. The transverse momentum threshold of the leptons varies with the level of instantaneous luminosity and pile up. The corresponding threshold for muons is 18 GeV for the single trigger, and 10 GeV for the di-muon trigger for 2011 data. Furthermore the leptons that match the trigger should have p_T above 20 GeV and 12 GeV respectively. For electrons, the threshold for single trigger is 20 GeV, increased to 22 GeV as luminosity raises, and 12 GeV for di-lepton trigger, thus putting the limit on the matched electron p_T at 21 GeV, 23 GeV and 13 GeV. During the 2012 data taking, because of the rise in c.m. energy, pileup increases, and the thresholds for muons and electrons set to 24 GeV for single trigger and isolation cuts are introduced.

The isolation cuts are applied at Event Filter level only and require the sum of the p_T of tracks, in a cone of size $\Delta R < 0.2$ around the lepton track, to be less than 10% of the lepton p_T . In addition, an asymmetric di-muon trigger is used by requiring one muon with $p_T > 18$ GeV and another with $p_T > 8$ GeV. The summary of the triggers used in 2011 and 2012 is presented in tables 6.4 and 6.5. The trigger efficiency with respect to the offline analysis requirements for a simulated Higgs signal (gluon-fusion with $m_H = 130$ GeV) is:

- 4μ : 98.2% (2011), 97.6% (2012)
- $2e2\mu$: 98.8% (2011), 97.3% (2012)
- $4e$: 99.7% (2011) , 99.7% (2012)

Trigger efficiencies in data and MC are measured using tag-and-probe methods based on $Z \rightarrow \mu\mu$ and $Z \rightarrow ee$ events. Efficiencies are computed in bins of the phase space $\xi_i = (p_{Ti}, \eta_i, \phi_i)$ and are defined for p_T values above the trigger threshold. Differences between trigger efficiencies in data and MC are accounted for by re-weighting MC events according to the single-lepton efficiencies computed in phase-space bins η_i , denoted as $\epsilon(\eta_i)$, of all reconstructed leptons in the event. The trigger efficiency scale factor is computed as:

$$SF_{trigger} = \frac{[1 - \Pi_i(1 - \epsilon(\eta_i))]_{Data}}{[1 - \Pi_i(1 - \epsilon(\eta_i))]_{MC}} \quad (6.1)$$

Table 6.4: Triggers used in the Data. In each data taking period, the OR of single- and di-lepton triggers is used to select each signature.

Single-lepton triggers				
Period	B-I	J	K	L-M
4μ	EF_mu18_MG	EF_mu18_MG_medium	EF_mu18_MG_medium	EF_mu18_MG_medium
$4e$	EF_e20_medium	EF_e20_medium	EF_e22_medium	EF_e22vh_medium1
$2e2\mu$	4μ OR $4e$			
Di-lepton triggers				
Period	B-I	J	K	L-M
4μ	EF_2mu10_loose	EF_2mu10_loose	EF_2mu10_loose	EF_2mu10_loose
$4e$	EF_2e12_medium	EF_2e12_medium	EF_2e12T_medium	EF_2e12Tvh_medium
$2e2\mu$	4μ OR $4e$			

6.2.2 Object selection

Electron candidates consist of electromagnetic clusters matched with an inner detector track using the distance between the cluster position and the extrapolated position of the track at the calorimeter. In the 2011 electron reconstruction, the matching between track and cluster was very loose because the bremsstrahlung was not taken into account

Table 6.5: Summary of the triggers that will be used during the 2012 data taking for the three analysis channels. When multiple chains are indicated, it is intended that the OR among them is requested.

Channel	Single-lepton	Di-lepton
4e	e24vhi_medium1	2e12Tvh_medium1
4 μ	mu24i_tight	2mu13, mu18_mu8_EFFS
2e2 μ	e24vhi_medium1, mu24i_tight	2e12Tvh_medium1, 2mu13, mu18_mu8_EFFS, e12Tvh_medium1_mu10, e24vhi_loose1_mu8

in the pattern recognition. The electrons, identified with *loose* ++ criteria are used to provide good separation between isolated electrons and jets, with the addition of the E_{ratio} cut for $E_T < 10$ GeV (as in medium++) [85]. In 2012, as introduced in section 2.3.1, GSF refitted tracks associated with electromagnetic clusters considerably improves electron reconstruction efficiency in the low momentum regime. The identification making use of new information is called *MultiLepton* criteria.

Muon candidates are reconstructed by matching ID tracks with either complete or partial tracks reconstructed in the Muon Spectrometer. All four types of muons described in section 2.3.2 are used in the analysis. The combined muons and the segment-tagged muons are used in the barrel region ($|\eta| < 2.5$), with additional criteria on inner detector hits: a minimum number of pixel and SCT hits, and the outliers in TRT not exceeding a certain fraction of all TRT hits. The detector conditions are taken into account in these cuts, by adding the dead sensors to the hit counts. To extend the muon reconstruction coverage, standalone muons in the forward region ($2.5 < |\eta| < 2.7$) without inner detector coverage are also used, with the requirement that the track must cross 3 stations to guarantee good quality. In the barrel region where there is no Muon Spectrometer hardware coverage ($|\eta| < 0.1$), calo-tagged muons are used. They are very loosely reconstructed, thus the p_T threshold is higher than for other types of muons. The same requirements on the number of hits in the inner detector as combined ones are also imposed.

For both electrons and muons, the transverse impact parameter relative to the primary vertex should satisfy $|d_0| < 0.2$ mm and the z-coordinate of the track at the point of closest approach to the vertex in the transverse plane $|z_0| < 1.0$ mm (if there is an inner detector track associated).

6.2.3 Quadruplet selection and Optimisation

The candidate quadruplet is formed by selecting two opposite sign, same flavour di-lepton pairs in an event. Muons are required to have $p_T > 6$ GeV and $|\eta| < 2.7$, while electrons are required to have $E_T > 7$ GeV and $|\eta| < 2.47$. The four leptons of the quadruplets are required to be well separated, $\Delta R = \sqrt{\Delta\eta^2 + \Delta\phi^2} > 0.10$, for same flavour leptons and $\Delta R > 0.20$ for different flavour leptons. The di-lepton of the quadruplet with a mass m_{12} closest to the nominal Z boson mass is called the leading di-lepton, while the second di-

lepton of the quadruplet with a mass m_{34} is the sub-leading one. For each event there is a mass window requirement applied to the invariant mass of each of the two di-leptons. The limits of the mass windows are chosen event-by-event using the reconstructed four-lepton invariant mass, resulting in a single mass spectrum for each background regardless of the assumed Higgs mass. m_{12} is required to be between 50 and 106 GeV. m_{34} is required to exceed a threshold, $m_{threshold}$, which varies as a function of the four-lepton invariant mass, $m_{4\ell}$, and should always be below 115 GeV. A set of threshold values is shown in table 6.6, where the actual value used is obtained by linear interpolation between these mass points. In the case where more than one quadruplets survive the kinematic selection, the one with m_{12} closest the m_Z mass is retained, if multiple quadruplets have the same m_{12} , the one with the highest m_{34} is selected.

Table 6.6: Summary of thresholds applied to m_{34} for reference values of $m_{4\ell}$. For other $m_{4\ell}$ values, the selection requirement is obtained via linear interpolation.

$m_{4\ell}$ (GeV)	≤ 120	130	150	160	165	180	≥ 190
threshold (GeV)	17.5	22.5	30	30	35	40	50

The kinematic cuts on the four lepton transverse momentum and the invariant mass of the leading and sub-leading pairs, are optimised to maximise the sensitivity in the mass region between 120 and 130 GeV. The optimisation procedure, is conducted in the 4μ channel and $4e + 2\mu 2e$ channel. The signal sensitivity is quantified by the p_0 value, which is the probability that the expected background in a 6 GeV window around the signal mass fluctuates to an observed number of events larger or equal to the sum of the expected signal plus background events in the same mass window. The expected events, are taken directly from MC in the 4μ case, and partially constrained from data control samples in the case of the sub-leading electron pair, due to the small number of events remaining after final selection in MC. The p_0 value, can be expressed in terms of equivalent number of Gaussian standard deviation Z_0 , using the χ^2 asymptotic approximation

$$Z_0 = \sqrt{2 \left((s+b) \ln \left(1 + \frac{s}{b} \right) - s \right)} \quad (6.2)$$

where s and b are the number of signal and background events respectively. Another way to estimate p_0 is based on a simple Poisson marginal probability integral with a linear extrapolation between the two closest integers to the expected signal plus background number of events. The two methods give similar results.

The procedure is based on finding the largest significance that a set of cuts can provide, and if a small dependency of the expected significance is observed the choice was made to be conservative and reduce the reducible background contribution. One found that in the 4μ final state, m_{12} and the p_T of the least energetic lepton are the most sensitive

variables. The other variables, since they have little effects on the significance, are chosen to be tightened with respect to the previous analysis [39]. Combining all the informations, the value of optimal cut position for a 125 GeV Higgs mass signal is shown in table 6.7 compared with the previous analyse. The minimum p_T cut of the muon is determined from the optimisation while the cut for electron is determined by the availability of the scale factor provided by the performance group.

Table 6.7: Value of optimal cut position for a 125 GeV Higgs mass signal obtained from the optimization procedure.

Variable	Optimal Cut	Published cut
m_{12}	50 GeV	15 GeV around Z mass
m_{34}	20 GeV (at $m_{4\mu} = 125$ GeV)	17.5 GeV (at $m_{4\mu} = 125$ GeV)
P_{t1}	20 GeV	20 GeV
P_{t2}	15 GeV	20 GeV
P_{t3}	10 GeV	7 GeV
P_{t4}	6 GeV (μ) 7 GeV (e)	7 GeV

6.2.4 Extra selection and Efficiency

The normalised track isolation discriminant is defined as the sum of the transverse momenta of tracks, Σp_T , inside a cone of $\Delta R < 0.20$ around the lepton, divided by the lepton p_T . Summed tracks are of good quality and pass a minimum p_T cut (at least four silicon hits and $p_T > 1$ GeV). Each lepton is required to have a normalised track isolation smaller than 0.15. The normalised calorimetric isolation discriminant for muons is defined as the sum of the calorimeter cells, ΣE_T , inside an isolation cone of 0.20 around the muon, divided by the muon p_T . In the case of electrons, the normalised calorimetric isolation is computed as the sum of the topological cluster transverse energies inside a cone of 0.2 around the electron cluster divided by the electron p_T , the cells corresponding to the core of the electron cluster being excluded from the sum. Then energy loss of muon in the calorimeter is also subtracted from the sum of transverse energies when calculating the isolation. Muons are required to have a normalised calorimetric isolation less than 0.30, while for electrons the corresponding value is lowered to 0.20 in 2012 to reduce pileup effects. For both the track- and calorimeter-based isolation any contributions arising from other leptons of the quadruplet are subtracted. The impact parameter significance, d_0/σ_{d0} , is required to be lower than 3.5 for muons and 6.5 for electrons. The electron impact parameter is affected by Bremsstrahlung and is thus broader.

The efficiency of these extra criteria for data and MC is presented in this section. For the signal leptons, efficiency scale factors (SF), i.e. the efficiencies of data relative to MC, are needed for any cross section measurement or limit estimate. Unlike the SF for the pre-selection cuts, which are provided by the Combined Performance groups, the SFs

for the additional isolation and impact parameter cuts, which are specific to this analysis are determined in this work. For this, the full 2011 and 2012 data samples passing the data-quality requirements for electrons and muons are used.

The efficiencies of signal electrons and muons satisfying the extra criteria are retrieved respectively from $Z \rightarrow ee$ and $Z \rightarrow \mu^+\mu^-$ events using tag-and-probe methods. The basic idea is to calculate the ratio of Z events in a mass window of the Z mass PDG value, with and without requiring the probe lepton to pass the extra cuts. The number of Z events is determined from data by the fit of invariant mass of tag-and-probe electron or muon pairs. Templates from MC are used to model the Z signal as well as the background distributions for $t\bar{t}$ and $Z \rightarrow \tau\tau$ with normalisation according to the luminosity. The background contribution from QCD is described by an exponential function in the case of $Z \rightarrow ee$ and a template of same sign tag-and-probe pairs from data for $Z \rightarrow \mu^+\mu^-$. The events are chosen in a mass window around the Z nominal PDG value, and the size is 5 GeV and 3 GeV respectively for electron and muon pairs.

The tag lepton, always defined as the tighter one in the pair, is required to have higher p_T and a charge opposite to the probe lepton. It should be isolated to make sure the selected events are clean since the cuts on the probe lepton are rather loose. The tag electron must pass the tight++ requirement, $E_T > 15$ GeV, $|\eta| < 1.37$ and be matched with a trigger electron. The tag muon on the other hand, is required to be a combined muon passing all inner detector hits requirements with $p_T > 20$ GeV, $|z_0| < 10$ mm, to avoid cosmic and cavern background.

The mass fit of the tag-and-probe pair is done in different transverse energy bins of the probe lepton. The efficiency of passing the extra selection is calculated for data and MC, as the ratio between the two: the SF, are shown in figure 6.3. The scale factor is close to 1, with a maximum deviation of 2% for electrons and 1% for muons in the low momentum region. The systematic uncertainties have two sources: the size of the mass window and the sample in the template. Varying the window from 3 to 8 GeV and substituting the Z signal sample from ALPGEN to PYTHIA gives the uncertainties marked by the bands on Figure 6.3. The maximum uncertainty is 4% for electrons and 2% for muons.

6.3 Background estimation

Correct estimation of background events that enter the final selection is essential to the determination of signal significance. MC prediction provides a reference, but as the number of collected data increases, it always confronts the problem of lacking statistics. Moreover, one should not entirely rely on MC, the accuracy of MC should be verified by data in different control-regions. Using data to estimate background events is preferable. Various data-driven background estimation techniques have been developed in the analysis in the challenging low mass region between 120–180 GeV, where the off-shell Z gives low transverse momentum leptons and increases the diversity of background sources other than the $ZZ^{(*)}$

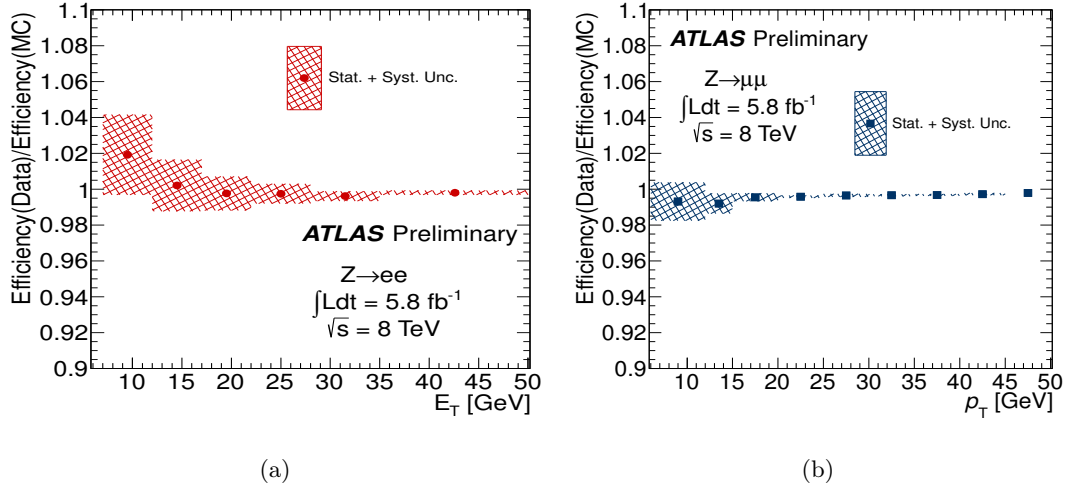


Figure 6.3: Ratio of the isolation and impact parameter efficiencies between data and simulation, estimated with the Tag & Probe method, using (a) $Z \rightarrow ee$ and (b) $Z \rightarrow \mu\mu$ events.

continuum. In the case of a sub-leading muon pair, $pp \rightarrow Zb\bar{b} \rightarrow 4\ell$ and $pp \rightarrow t\bar{t} \rightarrow 4\ell$ make up the main background, as the heavy flavour quarks are the dominant fake source of muons, while for the sub-leading electron pair, $pp \rightarrow Z + \text{jets} \rightarrow 4\ell$ becomes the dominant background, where various types of jets fake electrons. Because the background is of different origin, the $Z(QQ \rightarrow \mu^+\mu^-)$ and the $Z(XX \rightarrow e^+e^-)$ processes are studied separately.

Though the data driven methods vary with the final states and even within the same final state, all the methods share the basic scheme that is shown in figure 6.4. A control region that is enriched in background is built, and the composition from different sources are identified based on the characteristic of each. Then for every single composition, the transfer factors that the events in the control region fall also in the signal region are obtained usually from MC, and by summing up the contribution from all parts the yields in signal region are obtained.

6.3.1 Estimate of the $Z + \mu^+\mu^-$ background

$t\bar{t}$ and $Zb\bar{b}$ background estimation using a fit on m_{12}

As introduced in the beginning of the section, heavy flavour quarks are the most important source of fake muons, which makes $t\bar{t}$ and $Zb\bar{b}$ the main background in the $Z + \mu\mu$ final state. To estimate this contribution, a control region, enriched in $b\bar{b}$, is constructed. In this control region the m_{12} distribution has a peak at the Z -mass due to $Zb\bar{b}$, on top of a flat distribution from $t\bar{t}$ events. The number of events from the two sources in the control region can be extracted by fitting data, given their distinctive shapes. Then the yields can

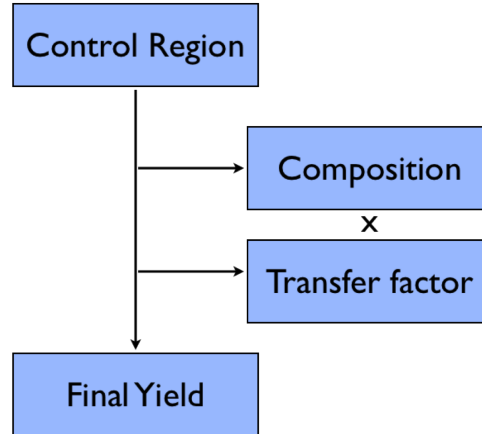


Figure 6.4: The basic scheme of background estimation methods.

be extrapolated to the signal region by applying the cut efficiency from MC, which has been verified with data.

Since the b quark is characterised by a secondary vertex, which results in a muon with large IP significance ($d_0/\sigma d_0$), one can define the control region by applying the standard selection to all leptons, except to the leptons of the sub-leading pair, one of which being required to fail the IP significance cut. This also efficiently removes $ZZ^{(*)}$ contribution in the region, leaving only $t\bar{t}$ and $Zb\bar{b}$. No isolation requirement is applied to the sub-leading pair to increase statistics. The m_{12} distribution is presented in Figure 6.5, where one clearly sees the side-band regions dominated by $t\bar{t}$ and a peak at the Z-mass dominated by $Z + jets$ backgrounds most of which is $Zb\bar{b}$. The ZZ^* is very small, which makes it possible to simultaneously estimate both $t\bar{t}$ and $Zb\bar{b}$ backgrounds by a single fit. For the fitting procedure, the $t\bar{t}$ component is described by a second order Chebychev polynomial, and for the $Zb\bar{b}$ component, a Breit Wigner line-shape convoluted with a Crystal-Ball resolution function is used. The parameters of the polynomial, the Breit Wigner and the Crystall-Ball function are determined from MC, by separately fitting $Zb\bar{b}$ and $t\bar{t}$ samples in the same control region, and a fluctuation within 10% of their nominal values are allowed in the fit of data. In Figure 6.5 the results of the fit, which are compatible with the MC expectations, are presented for 2011 and 2012 data.

The yields obtained for $t\bar{t}$ and $Zb\bar{b}$ from the fit are anti-correlated, with a linear correlation coefficient of -0.4 .

Extrapolation to the signal region In order to calculate the expected background in the signal region, a transfer factor obtained from MC is used. There are two ways of getting the transfer factor, one simple and direct way is to calculate from MC the ratio of the number of events expected in the signal region and the control region.

$$f_{\text{transfer}} = \frac{n_{SR}}{n_{CR}}$$

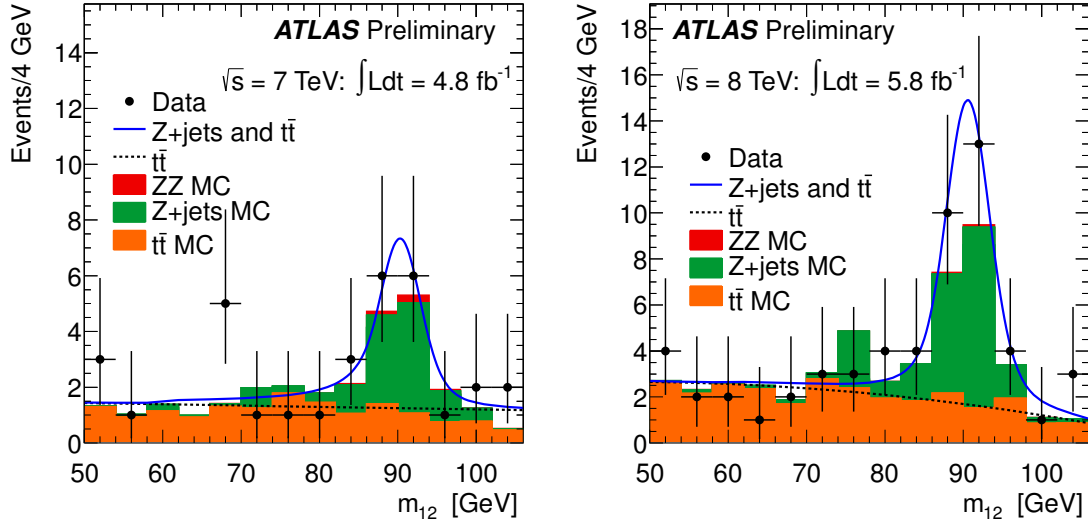


Figure 6.5: Distribution of m_{12} in the control region where the isolation requirement is not applied to the two sub-leading muons, and at least one of these muons fails the impact parameter significance requirement for 2011 (left) and 2012 (right) data. The fit used to obtain the yields for $t\bar{t}$ and $Z + \text{jets}$ is presented and the MC expectations are also shown for comparison.

where n_{SR} and n_{CR} are the number of events in the signal and in the control region, respectively.

The second method, is based on the efficiency of a single b-like muon to pass the IP significance and the isolation requirement, and on linking the control region and the signal region by the following formula:

$$f_{\text{transfer}} = \epsilon_{iso}^2 \epsilon_{d_0}^2 / (1 - \epsilon_{d_0}^2)$$

where ϵ_{d_0} and ϵ_{iso} are the efficiencies of the sub-leading muons to satisfy the IP and isolation selection criteria. Both methods rely on MC, the former being limited by the statistics: if the MC sample has only a few events surviving the final selection, the transfer factor has a large statistical uncertainty. The second method, uses one overall muon efficiency thus ignoring the dependency on muon momentum and position. To ensure a similar phase space is used in the efficiency calculation and the control region, the efficiency is calculated from MC events by averaging all muons in sub-leading pairs in the control region. This method solves the statistic problem of the first method, but ignores the correlation between the IP significance cut and the isolation cut. Given the available MC samples, $Zb\bar{b}$ takes the first method to get the transfer factor while $t\bar{t}$ uses the second formula. In Table 6.8, the efficiencies for the 2012 analysis used to calculate the transfer factors are presented, while in Table 6.9 the resulting transfer factors used are shown. The difference of the transfer factors from the two methods are included in the systematic uncertainty.

Table 6.8: Efficiencies of IP significance and isolation requirements for $t\bar{t}$ and $Z + b\bar{b}$ used to calculate the transfer factor in events that fulfill the $Z + \mu\mu$ selection, with a sub-leading di-muon.

	IP efficiency	isolation efficiency
$Zb\bar{b}$	49.6 ± 1.5	21.9 ± 1.3
$t\bar{t}$	46.3 ± 1.7	10.7 ± 1.5

Table 6.9: Transfer factors for $t\bar{t}$ and $Z + b\bar{b}$ in events that fulfill the $Z + \mu\mu$ selection, where the muons make the subleading pair.

	transfer factor (%)
$Zb\bar{b}$	$3.3 \pm 0.3 \pm 1.0$
$t\bar{t}$	$0.3 \pm 0.1 \pm 0.1$

Verification of MC The transfer factor, which characterises the b-like muon behaviour, is evaluated from MC. It is important to verify that the MC describes well the variables involved in the extrapolation, in this case the isolation and IP significance variables of muons. To this end a $Z + \mu$ control region is formed to study the agreement between the $t\bar{t}$ MC and data, where the extra μ is b-like and the Z is required to fulfil the leading pair criteria as in the four-lepton analysis. To enrich the control region with $t\bar{t}$ events, at least one b-tagged jet is required. A b-tagging algorithm is used that combines secondary vertex and impact parameter significance, with a neural network (JetCOMBNN). A jet is considered as b-tagged if the b-tag weight is larger than -1.25 and has $p_T > 20$ GeV. This requirement has 80% efficiency for b-jets in top MC events. To remove $Z + \text{jets}$, a $E_T^{\text{miss}} > 50$ (80) GeV requirement is applied in the 2011 (2012) analysis. Figure 6.6 shows the E_T^{miss} distribution after the b-tag requirement.

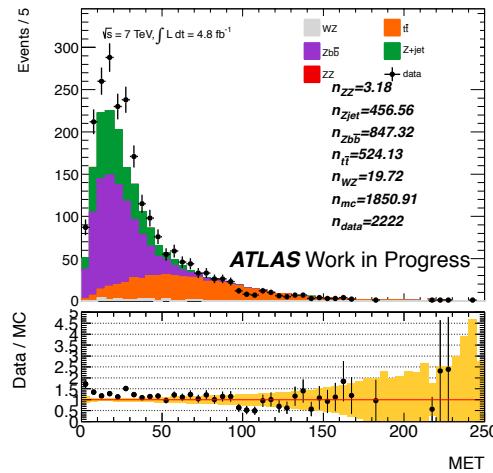


Figure 6.6: Distribution of MET in $Z + \mu(1 \text{ b-jet})$ control region of 2011 data and MC.

The efficiencies of track/calorimeter isolation and IP significance requirements are derived using the extra μ . Figure 6.7 shows the data/MC distribution of the IP significance, track and calorimeter isolation (left) and the efficiency comparison (right). Overall, the $t\bar{t}$ MC reproduces the data well, the MC efficiency agrees with data within the statistical error at the value of cut ($d_0/\sigma_{d_0} < 3.5$, caloIso <0.3 , trackIso < 0.15), except for the calorimeter isolation, where a 10% difference is seen. Therefore, a 10% systematic error per muon is assigned to the transfer factor. The systematic uncertainties on the efficiencies of the extra muon, estimated by varying the E_T^{miss} cut and the number of required b-tagged jets, are within the statistical errors shown in the plot.

Final results The final estimated numbers of $t\bar{t}$ and $Z + b\bar{b}$ events in the signal region are given in Table 6.10 and Table 6.11 for 2011 and 2012 data. These fit results are split in 4μ and $2e2\mu$ channels according to the ratio between their entries in the inverted IP control region taken from MC.

Table 6.10: Estimated number of $t\bar{t}$ and $Z + b\bar{b}$ events in the signal region of 2011 data.

	$t\bar{t}$	$Z + b\bar{b}$
4μ data fit	$0.022 \pm 0.010 \pm 0.011$	$0.250 \pm 0.103 \pm 0.020$
4μ MC	$0.018 \pm 0.007 \pm 0.009$	$0.180 \pm 0.016 \pm 0.014$
$2e2\mu$ data fit	$0.020 \pm 0.009 \pm 0.010$	$0.201 \pm 0.083 \pm 0.016$
$2e2\mu$ MC	$0.016 \pm 0.006 \pm 0.008$	$0.144 \pm 0.013 \pm 0.012$

Table 6.11: Estimated number of $t\bar{t}$ and $Z + b\bar{b}$ events in the signal region of 2012 data.

	$t\bar{t}$	$Z + b\bar{b}$
4μ data fit	$0.044 \pm 0.015 \pm 0.015$	$0.506 \pm 0.127 \pm 0.159$
4μ MC	$0.052 \pm 0.013 \pm 0.017$	$0.286 \pm 0.025 \pm 0.090$
$2e2\mu$ data fit	$0.040 \pm 0.013 \pm 0.013$	$0.405 \pm 0.102 \pm 0.127$
$2e2\mu$ MC	$0.047 \pm 0.011 \pm 0.016$	$0.226 \pm 0.020 \pm 0.070$

$t\bar{t}$ checks using the $e\mu + \mu\mu$ control region

The $t\bar{t}$ background estimation is cross checked by an alternative method, which is based on a control region where the leading pair is of a different flavour. Indeed theoretically for $t\bar{t}$ the leptons which constitute the leading pair in the four lepton analysis come from W decay, thus leaving equal possibility of being electrons and muons. By requiring the leading pair to be of opposite flavour rules out all other backgrounds in the analysis since they all include true Z. The $e^\pm\mu^\mp$ pair should also have the invariant mass between 50 and 106 GeV, and satisfy the extra requirements of isolation and IP significance. Furthermore,

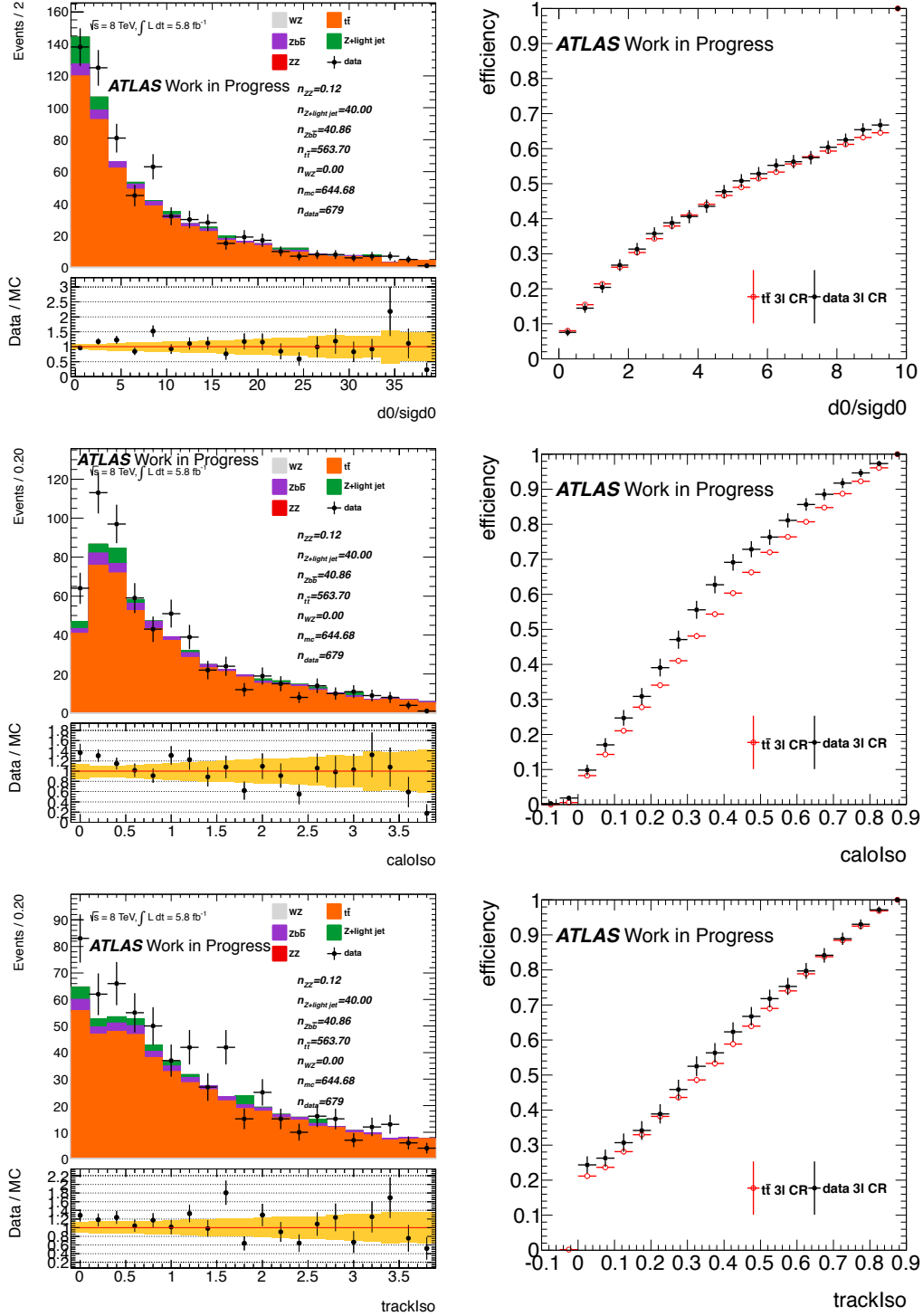


Figure 6.7: Distribution of isolation and IP significance variables in the $Z + \mu$ control region (left) and efficiency (right); 2012 data are shown here.

the p_T should be explicitly larger than 20 and 15 GeV. The sub-leading muon pair, passing all object criteria and the m_{34} invariant mass requirement, is not required to pass the

extra selection. Such selection selects events mostly from $t\bar{t}$, as Table 6.12 shows. The contamination from QCD events is found to be small, and $t\bar{t}$ MC shows good agreement with data.

Table 6.12: Observed and expected $e^\pm\mu^\mp + \mu\mu$ events for 2012 data (5.8 fb^{-1}).

	$e^\pm\mu^\mp + \mu^+\mu^-$	$e^\pm\mu^\mp + \mu^\pm\mu^\pm$
Data	16	20
$t\bar{t}$	18.9 ± 1.1	18.6 ± 1.1
QCD	0.0 ± 1.0	2.3 ± 2.0

The number of $t\bar{t}$ events in the signal region is then estimated as follows. The transfer factor from the control region to the signal region is estimated from $t\bar{t}$ MC as the ratio of yields in the kinematic region in the control region of $ee + \mu\mu$ and $\mu\mu + \mu\mu$ events and the $e\mu + \mu\mu$ yield. It is estimated to be 0.589 ± 0.003 and 0.667 ± 0.003 for the $ee/e\mu$ and $\mu\mu/e\mu$ final states, respectively in the 2012 analysis. Furthermore, the efficiency of applying the isolation and the d_0 significance requirements on the sub-leading muon pair is estimated by averaging the $ee\mu\mu$ and $\mu\mu\mu\mu$ final states from MC, the obtained value is $(5.4 \pm 0.7)10^{-3}$.

The systematic uncertainty of this method also comes from the difference observed in efficiencies of data and MC. It is estimated in the $e\mu + \mu$ control region on the extra muon, and a final 31% uncertainty is assigned to the systematic term. Thus, the final expectations in the signal region in 2012 are:

- $2e2\mu$: 0.051 ± 0.013 (stat) ± 0.017 (syst)
- 4μ : 0.058 ± 0.015 (stat) ± 0.019 (syst)

This result is compatible with the result from the m_{12} fit method.

6.3.2 Estimate of the $Z+ee$ background

The background of $Z+ee$ final state comes from fake sub-leading electrons, most are QCD jets, non-isolated decay electrons from heavy flavour quark, or background electrons from converted photons. The origin of electrons is known in MC samples, based on the official ATLAS truth matching and classification tool. The electrons are in general categorised as:

- Isolated electrons (e), if they match a true electron originating from a Z or W boson.
- Hadron Fakes (f), if they do not match a true electron, muon or tau.
- Non-isolated electrons (b), if they match a true electron originating from $b(c)$ -mesons.

- Background electrons (c), if they match a true electron originating from a photon. These electrons (from photons) can be further divided depending upon the origin of the photon, for example the photon may arise from a neutral pion decay, from the Bremsstrahlung cascade of an electron coming from the decay of a Z boson, or from initial or final state radiation.

In the four-lepton analysis, electrons from all categories but the first (isolated electron) constitute a potential background to the signal. Among this background are the hadron fakes and background electrons in the Z +jet sample, and non-isolated electrons in $t\bar{t}$ sample. The estimation of the background in $Z + ee$ final state is thus based on the categories of fake electron instead of the individual samples, since in each sample, there may be a mixing of different fake sources. There are three methods to evaluate the background, which will be introduced in this section.

$Z + XX$ estimation using categories

In this method, the different categories mentioned above are defined in a control region, where the identification of the sub-leading electron pair is relaxed to gain statistics, and then each composition is extrapolated to the signal region using their respective transfer factors. As the classification information is only available in MC truth, not in data, the electrons are first classified based on discriminating reconstruction variables, as "Electron (E)", "Conversion (C)" or "Fake (F)". The classification based on reconstructed variables is called reconstruction classification (E,F,C), and the one based on MC truth is called truth classification (e,f,b). All events in the control region, denoted as $Z+XX$, where the X can be E,C or F, are then classified into 9 categories, e.g. EE,EF,FE etc., where the ordering depends on the p_T . Similarly, the events can also be classified into 16 truth categories, e.g. ee, ef, eb etc. The probability for each truth category falling in a given reconstruction category can be derived from MC and used in data; in this way, the data events are reassigned from a reconstruction category to a truth category. The efficiency of each truth category to satisfy full electron identification as well as the extra cuts are evaluated in the $Z+X$ control region. As the $ZZ^{(*)}$ background is also included in the control region, its contribution must be removed in the end using MC expectation.

Reconstruction-based electron categories The different sources of electron backgrounds can largely be identified by using discriminating reconstruction variables.

Electron(E) $f_1 > 0.1$, has B-Layer (if expected), if ($|\eta| < 2.0$), then η -dependent r_{TRT} (high threshold TRT hits ratio) cut based on electron working group recommendation, else R_ϕ (energy deposit ratio in 3x3/3x7 cluster) > 0.9 .

Photon(C) no B-Layer (if expected) or number of pixel hits < 2 (if not expected B-Layer).

Fakes(F) everything else.

Table 6.13: Data/MC comparison for different categories in the $Z(\text{ee})+XX(\text{ee})$ control region.

All		
	Data	MC
EE	32	22.66
EC	6	6.04
EF	18	19.05
CE	4	8.84
CC	1	5.26
CF	12	8.81
FE	16	5.73
FC	6	6.49
FF	12	17.36
Total	107	100.23

Table 6.14: Data/MC comparison for different categories in the $Z(\mu\mu)+XX(\text{ee})$ control region.

All		
	Data	MC
EE	31	24.88
EC	2	1.87
EF	26	15.29
CE	6	5.13
CC	6	4.18
CF	15	15.26
FE	12	8.42
FC	7	4.33
FF	16	33.56
Total	121	112.91

Definition of the $Z+XX$ control sample Events are selected following the standard analysis selection, but the electron identification is replaced by looser criteria for the sub-leading di-lepton. Isolation and impact parameter criteria are not applied to the sub-leading di-lepton. The relaxed identification cuts for the sub-leading di-lepton are:

- At least 7 Si hits.
- At least 1 Pixel hits.
- R_{had} (E_T leakage ratio into hadronic calorimeter with exclusion of energy in tile), R_η , $w_{\eta 2}$, w_{stot}

as applied in the loose++ for 2011 selection or MultiLepton selection in 2012. For 2012 data, requirements on f_3 , $\Delta\phi$ (the angular matching between the track and the electromagnetic cluster), r_{TRT} (for crack region) are added.

The number of observed and expected events in each category of the control region is presented in Table 6.13 and Table 6.14 for the 2012 analysis. General agreement between data and MC is seen.

Composition in truth category and transfer factor In the $Z+XX$ control region, each of the 9 reconstruction categories contain a mixture of the 16 truth categories, the fraction is known in MC and given in Table 6.16 for 2012 data. To analyse the data, toy pseudo-experiments are used based on the inputs from the table. The truth composition for each event is decided by the pseudo-experiment, where the central value in the table defines the nominal expected fraction varying with Poisson uncertainty. Subsequently, the transfer factor is multiplied for each category in order to get the final estimation in

Table 6.15: Efficiency of the remaining electron identification criteria (to complete the MultiLepton selection), and the isolation and impact parameter cuts for different categories for the leading and sub-leading electrons for $Z(ee)+XX$.

	e	b	c	f
Leading Electron				
E	0.839 ± 0.017	0.172 ± 0.023	0.229 ± 0.008	0.201 ± 0.006
C	0.695 ± 0.017	0.104 ± 0.081	0.258 ± 0.006	0.074 ± 0.012
F	0.633 ± 0.044	0.385 ± 0.063	0.188 ± 0.010	0.196 ± 0.003
Sub-Leading Electron				
E	0.796 ± 0.026	0.232 ± 0.021	0.171 ± 0.009	0.124 ± 0.005
C	0.632 ± 0.016	0.150 ± 0.084	0.181 ± 0.005	0.052 ± 0.009
F	0.505 ± 0.049	0.441 ± 0.049	0.114 ± 0.011	0.111 ± 0.002

the signal region. The transfer factor is a product of efficiencies of each electron in the sub-leading pair to pass the remaining identification criteria and the additional selections. This transfer factor of each electron, which depends both on the truth category and the reconstruction category, is a 3×4 matrix obtained from MC. To have enough statistics to obtain such a matrix, a $Z+X$ control region is set up, where the X satisfies the same criteria as in the $Z+XX$ control region. Considering the efficiency dependency on the electron transverse momentum, the p_T of X in the $Z+X$ control region is re-weighted to those in $Z+XX$. Table 6.15 shows the transfer factor matrix for 2012 data.

Final result After subtracting the ZZ^* contribution, the final result for 2011 and 2012 are

- $Z \rightarrow ee + XX = 3.1 \pm 0.6 \pm 0.5$ events (2011) $3.9 \pm 0.7 \pm 0.8$ events (2012)
- $Z \rightarrow \mu\mu + XX = 2.6 \pm 0.4 \pm 0.4$ events(2011) $4.9 \pm 0.8 \pm 0.7$ events(2012)

The same method is also tested in $Z+XX$ same sign control region, where the sub-leading pair is required to be of the same sign, to exclude ZZ^* . The final yields for 2012 is

- $Z \rightarrow ee + XX = 3.2 \pm 0.6 \pm 0.5$ events (2011) $3.1 \pm 0.5 \pm 0.6$ events (2012)
- $Z \rightarrow \mu\mu + XX = 3.7 \pm 0.9 \pm 0.6$ events(2011) $4.1 \pm 0.6 \pm 0.8$ events(2012)

$Z+XX$ estimation using Same Sign events

The main part of the $Z+XX$ background originates from random combinations of jets, photons, heavy quarks and mis-pairings of electrons as demonstrated in the introduction section. Thus, one can measure this particular background using events with a same-sign sub-leading di-lepton. In this section the full analysis criteria are applied to select

Table 6.16: Yields used for the purity calculation in the $Z+XX(ee)$ control regions. Capital letters denote Reconstruction categories, while small letters denote true categories.

$ee + ee$																
	ee	eb	ec	ef	be	bb	bc	bf	ce	cb	cc	cf	fe	fb	fc	ff
EE	16.46	0.14	0.02	0.59	0.08	0.53	0.00	0.03	0.01	0.02	0.00	0.79	1.86	0.00	0.00	0.99
EC	0.58	0.00	0.97	0.02	0.00	0.00	0.63	0.00	0.00	0.00	1.73	0.00	0.00	0.00	2.10	0.00
EF	2.56	0.04	0.02	10.53	0.00	0.06	0.00	0.07	0.00	0.00	0.00	0.62	0.00	0.00	0.00	2.68
CE	0.47	0.00	0.00	4.43	0.00	-0.00	0.00	0.00	0.03	0.06	0.00	2.02	0.00	0.00	0.00	0.00
CC	0.01	0.00	0.00	0.00	0.00	0.00	0.00	0.00	1.41	0.00	1.30	0.00	0.00	0.00	2.53	0.00
CF	0.07	0.00	0.00	1.27	0.00	0.00	0.00	0.00	0.01	0.00	0.00	6.94	0.00	0.00	0.00	0.53
FE	2.00	0.00	0.00	0.00	0.01	0.06	0.00	0.00	0.00	0.00	0.00	0.00	1.04	1.55	0.01	1.03
FC	0.08	0.00	0.01	0.00	0.00	0.00	0.00	0.00	0.00	0.00	0.00	0.00	0.00	0.00	6.40	0.00
FF	0.28	0.00	0.00	0.04	0.00	-0.01	0.00	1.34	0.00	0.00	0.00	0.00	0.02	0.01	0.00	11.58

$\mu\mu + ee$																
	ee	eb	ec	ef	be	bb	bc	bf	ce	cb	cc	cf	fe	fb	fc	ff
EE	18.68	0.19	0.02	0.03	0.03	0.56	0.01	0.05	0.01	1.45	0.00	0.94	0.00	0.04	1.07	0.00
EC	0.54	0.00	0.05	0.00	0.01	0.00	0.05	0.00	0.00	0.00	0.00	0.00	0.98	0.00	0.23	0.00
EF	2.67	-0.01	0.00	0.75	0.00	0.14	0.02	1.39	0.00	0.00	0.00	1.89	0.01	0.01	0.00	4.85
CE	0.51	0.00	1.80	0.00	0.00	0.04	0.00	0.00	0.01	0.01	1.03	1.73	0.00	0.00	0.00	0.00
CC	0.01	0.00	1.84	0.00	0.00	0.00	0.00	0.00	1.15	0.00	1.18	0.00	0.00	0.00	0.00	0.00
CF	0.06	0.01	0.00	8.00	0.00	0.00	0.00	0.00	0.00	0.00	0.00	6.04	0.00	0.00	0.00	1.15
FE	2.53	0.00	0.00	0.00	-0.01	0.12	0.00	0.02	0.00	0.00	0.00	0.00	0.02	0.11	1.47	3.36
FC	0.07	0.00	0.00	0.00	0.00	0.01	0.01	0.00	0.00	0.00	0.00	0.00	0.05	0.00	0.79	0.00
FF	0.39	0.00	0.00	0.01	0.00	0.00	0.01	0.05	0.00	0.00	0.00	1.95	0.00	-0.03	2.01	25.87

events with same-sign sub-leading di-leptons, while the leading di-lepton is required to be opposite-sign. The same sign number of events that survive the full selection is:

- $4e = 4$ (2011) 4 (2012)
- $2\mu 2e = 2$ (2011) 6 (2012)

Control Region with $3l + X$

Alternatively, the estimation of the background in the $Z+ee$ final state can be made with the truth categories, without the introduction of reconstruction categories. This eliminates the uncertainty of transfer from one classification to the other. Furthermore, instead of relaxing the identification on both sub-leading electrons, one can choose only one, so that only one decomposition is needed. A control region with three leptons selected as standard analysis and a relaxed electron is built. Quadruplets are selected as in the previous analysis and all the cuts are applied to the three highest p_T leptons, whereas for the least energetic electron only a cut on the of hits ($n_{Silicon} > 7$ and $n_{Pixel} > 0$) is required, and neither the electron identification nor isolation and IP significance selection criteria are applied. The sub-leading pair is required to be same sign to exclude $ZZ^{(*)}$ contamination.

Templates and closure test The composition problem now is simplified to determine the contribution from the 3 truth categories(b, f, c) to the signal region, the true electron category(e), known as signal, is not considered in the background estimation. This can be achieved by a two dimensional fit that disentangles the 3 components. The variables used are the n_{blayer} , which is the number of hits in the innermost layer of the Pixel Detector in the barrel region, used to discriminate between hadrons and conversions, and the TRT ratio, which is the fraction of high threshold hits in the TRT. The distributions of b-layer hits and TRT ratio are shown in Figure 6.8 for each component.

A different naming convention is used here, the γ denotes the conversion, f denotes hadrons and b represents the heavy flavor. Distributions shown in the plots of Figure 6.8 are then used as templates for each component, to determine the respective contribution in the control region. The templates are obtained from a $Z+X$ control region to gain statistics. The Z satisfies the same selection criteria as in the standard analysis and the additional electron fulfills the same requirement of X in $3l+X$ control region. To take into account the effect of different p_T spectrum, the p_T of X in $Z+X$ control region is reweighted the one in $3l+X$.

Fit on data These templates are fitted to the observed data in the $3\ell + X$ control region, where also a cut on R_η is applied to decrease the hadron component with respect to the others. First, a closure test is made by performing the fit on a sample taken from MC, shown in Figure 6.9. The lines in the plot represent the result from the fit while the different color histograms are the components read from MC. The closure test shows that

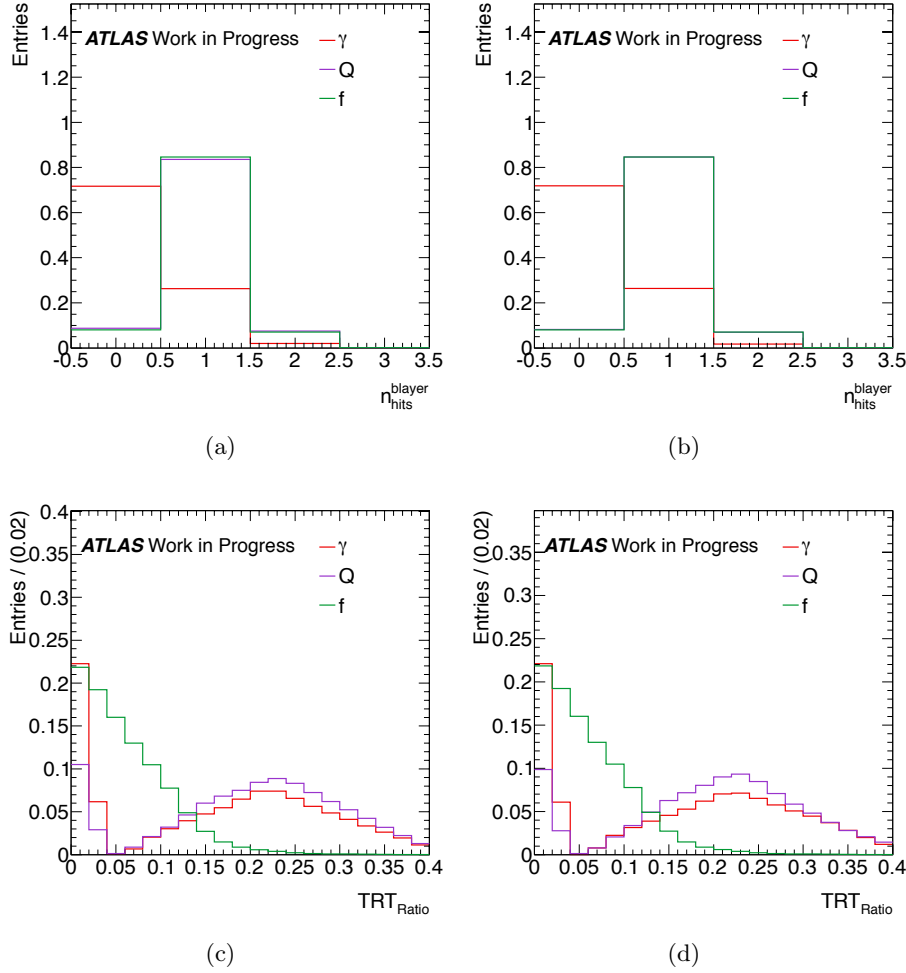


Figure 6.8: Distributions of $n_{B-Layer}$, TRT_{Ratio} for the different sources of background in ALPGEN MC (Z +jets and $Z+b\bar{b}$), taken from the Z +additional lepton control region. (a) and (b) are the distributions for $n_{B-Layer}$, in the $Z(2\mu)+e$ and $Z(2e)+e$ case and for the whole η range; (c) and (d) show the distribution of TRT_{Ratio} , separately for the $Z(2\mu)+e$ and $Z(2e)+e$ channels.

the fit can reproduce the contribution from each truth component. After this test the procedure is applied to the data, producing the results in Figure 6.10 and Table 6.17.

The two dimensional fit is performed assuming that the two variables (n_{blayer} , TRT_{ratio}) are non-correlated. A fit with two dimensional templates that correctly takes into account possible correlations is performed and an almost identical result is obtained, proving the non-correlation assumption. The validity of this method was studied by substituting other variables for the TRT ratio as to distinguish electron from hadron: e.g. f_1 , which is shown in figure 6.11 or the distance in eta between the extrapolated impact point of the track at the calorimeter and the cluster barycenter using the strips ($\Delta\eta_1$). The difference in the results form part of the systematic error. As seen from the fit plots, the b component takes

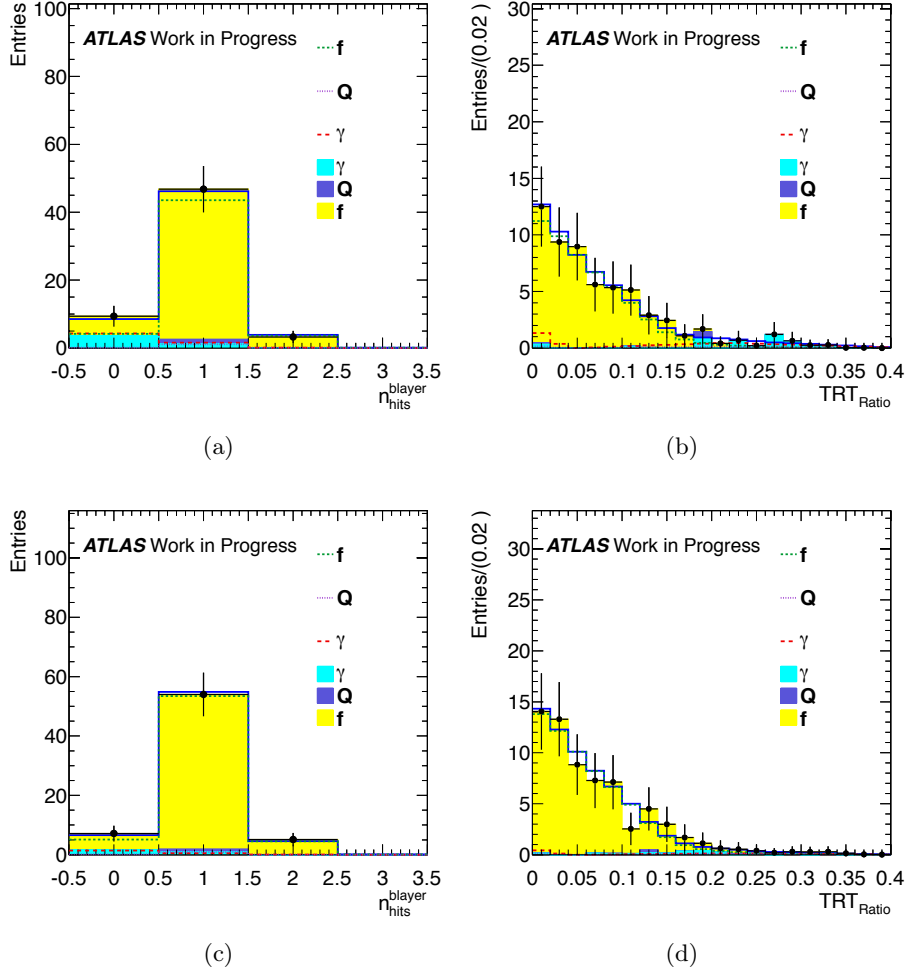


Figure 6.9: Example of closure test done performing the simultaneous fit in the $2\mu 2e$ case (a) and (b) and in the $4e$ case (c), (d) on ALPGEN MC (Z +jets and $Z + b\bar{b}$).

a very small fraction in the control region, hence the fit is insensitive to disentangling the component. Therefore, the number of b component is constrained in the fit, using MC prediction, and a 50% fluctuation on it is allowed. The difference in the final fit result by relaxing the constraint is taken again as systematic error.

The yields obtained for the different background components within a fitted region are anti-correlated, with a linear correlation coefficient r : -0.08 between C and Q , -0.04 between Q and f , and $r = -0.15$ between C and f . In this case, the conservative quadratic sum of the statistical uncertainties of the different components is used as the final statistical uncertainty.

Transfer Factor The transfer factor to the signal region, includes the efficiency of passing remaining electron identification and additional isolation/IP requirements, and is obtained from the MC $Z+X$ control region. The number is shown in Table 6.17 for $2\mu 2e$

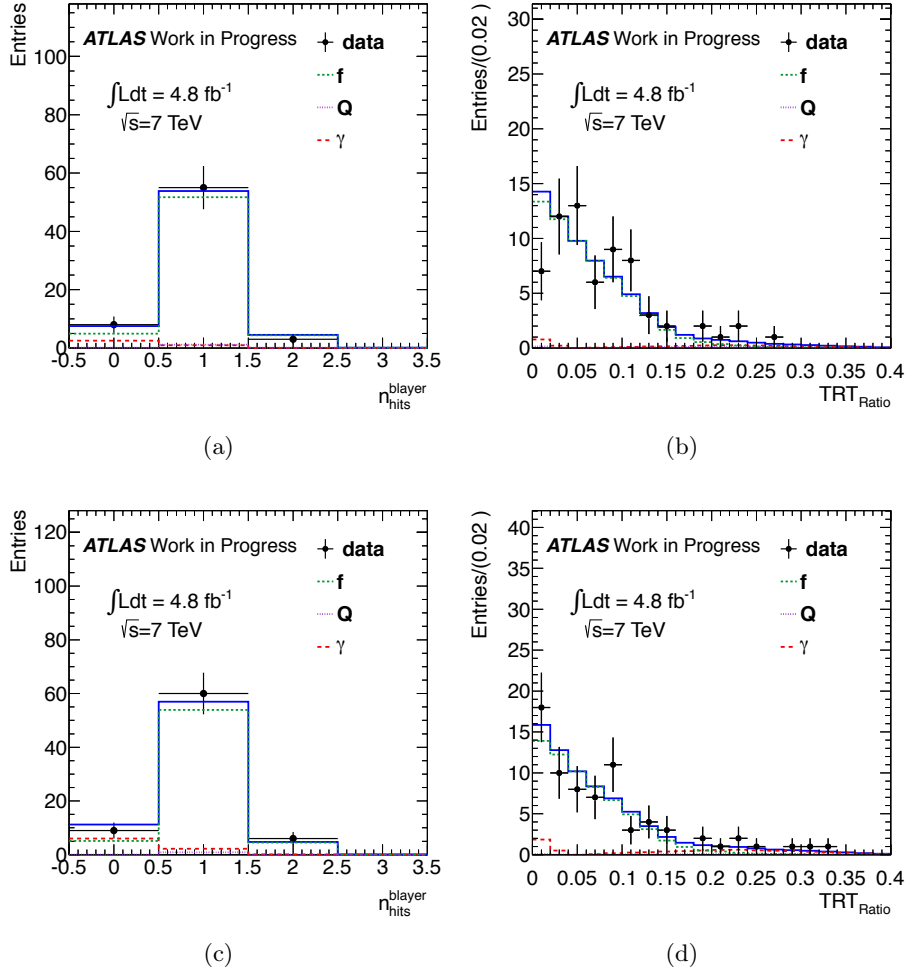


Figure 6.10: The results of a simultaneous fit to (a) $n_{\text{hits}}^{\text{blayer}}$ and (b) $\text{TRT}_{\text{Ratio}}$ for the background components in the $2\mu 2e$ channel are presented. In (c) and (d) the corresponding results for the $4e$ channel are given. The sources of background electrons are denoted as: light jets faking an electron (f), photon conversions (γ), electrons from heavy quark semi-leptonic decays (Q).

and $4e$ final states receptively. The systematic term, which comes from the MC/data disagreement shown in $Z+X$ control region, is 5% in 2011 and 10% in 2012.

Final result The final result obtained from this method is:

- $Z \rightarrow ee + XX = 2.2 \pm 0.5 \pm 0.3$ (2011) $3.0 \pm 0.4 \pm 0.4$ (2012)
- $Z \rightarrow \mu\mu + XX = 1.9 \pm 0.4 \pm 0.4$ (2011) $3.5 \pm 0.5 \pm 0.5$ (2012)

The three methods are consistent with each other considering the statistic uncertainty.

Table 6.17: Fit results for the yield of each component estimated from 2011 data.

$2\mu 2e$			
Component	Fit yields	Transfer factor	Yields in signal region
f	$61.10^{+8.33}_{-7.67}$	0.0202 ± 0.0010	$1.23^{+0.17}_{-0.15}$
Q	$1.41^{+0.68}_{-0.68}$	0.2142 ± 0.0107	$0.30^{+0.15}_{-0.15}$
C	$3.48^{+2.93}_{-2.48}$	0.1000 ± 0.0050	$0.35^{+0.29}_{-0.25}$
$4e$			
f	$63.60^{+8.61}_{-7.94}$	0.0190 ± 0.0010	$1.21^{+0.16}_{-0.15}$
Q	$1.01^{+0.49}_{-0.49}$	0.1987 ± 0.0099	$0.20^{+0.10}_{-0.10}$
C	$8.32^{+4.06}_{-3.61}$	0.0995 ± 0.0050	$0.83^{+0.40}_{-0.36}$

6.3.3 Summary of backgrounds

The results of all the background estimation methods are summarised in Table 6.18 and table 6.19 for 2011 and 2012 analysis, respectively. The “†” symbol indicates the estimated number of events used for the background normalisation, the others being cross-checks. The first uncertainty is statistical, while the second is systematic. Compatible results from various data-driven methods are acquired.

The m_{12} and m_{34} distributions, for events selected by the analysis when relaxing the isolation and impact parameter requirements for the sub-leading di-lepton, are presented in figure 6.12 combining the 2011 and 2012 analyse. The events are divided according to the flavour of the sub-leading lepton pair into $\ell\ell + \mu\mu$ and $\ell\ell + ee$ samples. In (a) the m_{12} and in (c) the m_{34} distributions are presented for $\ell\ell + \mu\mu$ events. In (b) the m_{12} and in (d) the m_{34} distributions are presented for $\ell\ell + ee$ events. The kinematic selection of the analysis is applied. Requirements on the isolation and impact parameter significance are applied to the first lepton pair only. The irreducible backgrounds are normalised to the central value obtained from data-driven methods. The shape and normalisation of the backgrounds are in good agreement with data. This is observed both for large values of m_{34} , where the $ZZ^{(*)}$ background dominates, and for low m_{34} values.

6.4 Higgs mass resolution and Z mass constraint

The Higgs mass resolution is obtained from an unbinned maximum likelihood fit of a gaussian model to the MC for the four final states separately. The resolution at 130 GeV is around 2 GeV, and the 4μ channel has the narrowest peak among all the final states, which is 2.13 GeV as shown in Figure 6.13. The Z mass constraint is applied at the end of the selection. It constrains the momenta of the leptons originating from the real Z boson. It estimates the true Z mass, event by event, by maximising the probability density function

$$p(m_Z^{\text{truth}}) \propto p(m_{2\ell}|m_Z^{\text{truth}}) \cdot p(m_Z^{\text{truth}})$$

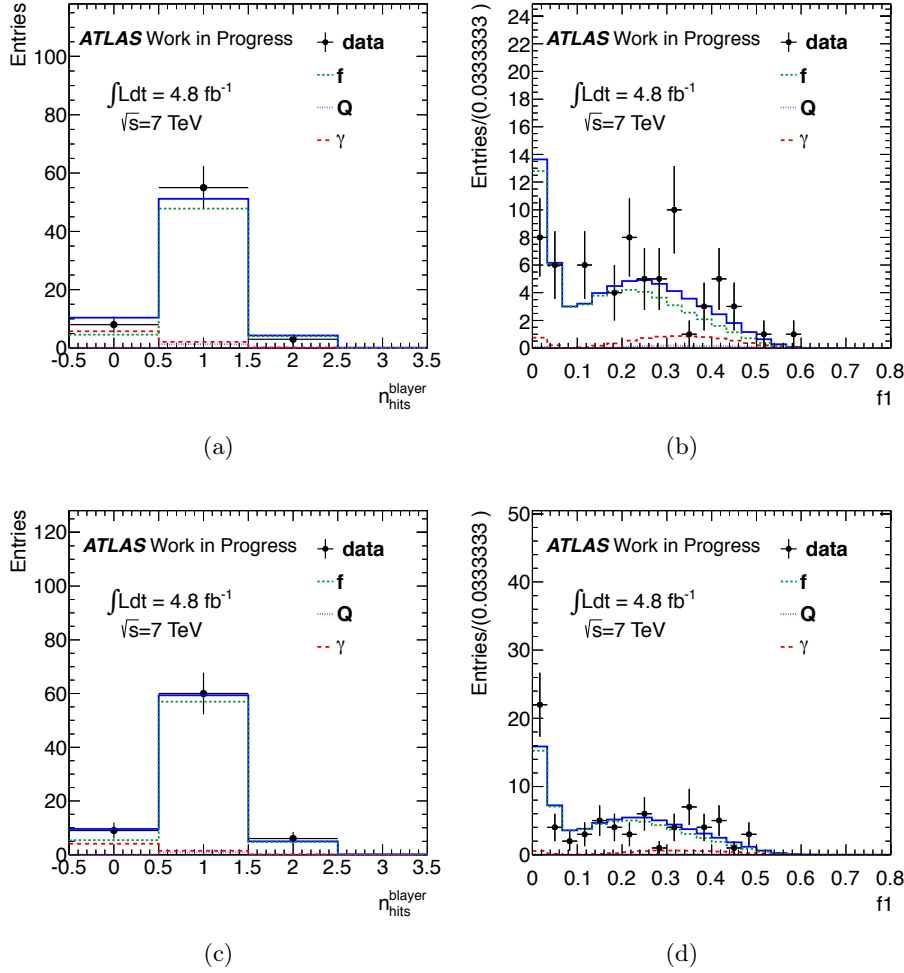


Figure 6.11: The results of a simultaneous fit to (a) $n_{\text{hits}}^{\text{blayer}}$ and (b) $f1$ for the background components in the $2\mu 2e$ channel are presented. In (c) and (d) the corresponding results for the $4e$ channel are given. The sources of background electrons are denoted as: light jets faking an electron (f), photon conversions (γ), electrons from heavy quark semi-leptonic decays (Q).

The first term of the right-hand side of the equation represents the resolution model for the di-lepton mass, the second term represents the prior p.d.f. for the true Z mass. Terms independent of m_Z^{truth} have been neglected since they do not take part in the maximisation.

A gaussian resolution model is used for $p(m_{2\ell}|m_Z^{\text{truth}})$, with zero bias and the gaussian standard deviation being obtained by propagating the lepton momentum uncertainties to $m_{2\ell}$, while a Breit–Wigner p.d.f. is used as truth Z mass model $p(m_Z^{\text{truth}})$.

The Higgs mass resolution is improved by around 10% when the Z mass constraint is applied at the end of the selection, as shown in Figure 6.13 for the 2012 analysis.

Table 6.18: Summary of the background estimates for the $\sqrt{s} = 7$ TeV data sample. The “†” symbol indicates the estimated number of events used for the background normalisation, the others being cross-checks. The first uncertainty is statistical, while the second is systematic.

Method	Estimated number of events
4μ	
m_{12} fit: Z + jets contribution	$0.25 \pm 0.10 \pm 0.08^\dagger$
m_{12} fit: $t\bar{t}$ contribution	$0.022 \pm 0.010 \pm 0.011^\dagger$
$t\bar{t}$ from $e^\pm\mu^\mp + \mu^\pm\mu^\mp$	$0.025 \pm 0.009 \pm 0.014$
$2e2\mu$	
m_{12} fit: Z + jets contribution	$0.20 \pm 0.08 \pm 0.06^\dagger$
m_{12} fit: $t\bar{t}$ contribution	$0.020 \pm 0.009 \pm 0.011^\dagger$
$t\bar{t}$ from $e^\pm\mu^\mp + \mu^\pm\mu^\mp$	$0.024 \pm 0.009 \pm 0.014$
$2\mu2e$	
$\ell\ell + e^\pm e^\mp$	$2.6 \pm 0.4 \pm 0.4^\dagger$
$\ell\ell + e^\pm e^\pm$	$3.7 \pm 0.9 \pm 0.6$
$3\ell + \ell$ (same-sign)	$2.0 \pm 0.5 \pm 0.3$
$4e$	
$\ell\ell + e^\pm e^\mp$	$3.1 \pm 0.6 \pm 0.5^\dagger$
$\ell\ell + e^\pm e^\pm$	$3.2 \pm 0.6 \pm 0.5$
$3\ell + \ell$ (same-sign)	$2.2 \pm 0.5 \pm 0.3$

6.5 Systematic uncertainties

Various systematic uncertainties are considered in the analysis, which include terms related to leptons identification, extra lepton criteria, signal modelling, background estimation and theoretical uncertainties of signal and background cross sections.

Lepton The uncertainty of the lepton reconstruction and identification efficiencies, and of the momentum resolution and scale, are determined using samples of W , Z and J/ψ decays [86]. The uncertainty of the muon identification and reconstruction efficiency results in a relative acceptance uncertainty of the signal and the $ZZ^{(*)}$ background which is uniform over the mass range of interest, and amounts to $\pm 0.16\%$ ($\pm 0.12\%$) for the 4μ ($2e2\mu$) channel. The uncertainty of the electron identification efficiency results in a relative acceptance uncertainty of $\pm 3.0\%$ ($\pm 1.7\%$) for the $4e$ ($2e2\mu$) channel at $m_{4\ell} = 600$ GeV and reaches $\pm 8.0\%$ ($\pm 4.6\%$) at $m_{4\ell} = 110$ GeV. The effects of muon momentum resolution and scale uncertainty are found to be negligible. The effect of the uncertainty of the energy resolution for electrons is negligible, while the uncertainty of the electron energy scale results in an uncertainty of less than $\pm 0.7\%$ ($\pm 0.4\%$) on the mass scale of the $m_{4\ell}$ distribution for the $4e$ ($2e2\mu$) channel.

Table 6.19: Summary of the background estimates for the $\sqrt{s} = 8$ TeV data. The “†” symbol indicates the estimated number of events used for the background normalisation, the others being cross-checks. The first uncertainty is statistical, while the second is systematic.

Method	Estimated number of events
4μ	
m_{12} fit: $Z + \text{jets}$ contribution	$0.51 \pm 0.13 \pm 0.16^\dagger$
m_{12} fit: $t\bar{t}$ contribution	$0.044 \pm 0.015 \pm 0.015^\dagger$
$t\bar{t}$ from $e^\pm\mu^\mp + \mu^\pm\mu^\mp$	$0.058 \pm 0.015 \pm 0.019$
$2e2\mu$	
m_{12} fit: $Z + \text{jets}$ contribution	$0.41 \pm 0.10 \pm 0.13^\dagger$
m_{12} fit: $t\bar{t}$ contribution	$0.040 \pm 0.013 \pm 0.013^\dagger$
$t\bar{t}$ from $e^\pm\mu^\mp + \mu^\pm\mu^\mp$	$0.051 \pm 0.013 \pm 0.017$
$2\mu2e$	
$\ell\ell + e^\pm e^\mp$	$4.9 \pm 0.8 \pm 0.7^\dagger$
$\ell\ell + e^\pm e^\pm$	$4.1 \pm 0.6 \pm 0.8$
$3\ell + \ell$ (same-sign)	$3.5 \pm 0.5 \pm 0.5$
$4e$	
$\ell\ell + e^\pm e^\mp$	$3.9 \pm 0.7 \pm 0.8^\dagger$
$\ell\ell + e^\pm e^\pm$	$3.1 \pm 0.5 \pm 0.6$
$3\ell + \ell$ (same-sign)	$3.0 \pm 0.4 \pm 0.4$

Extra Selection The selection efficiency of the isolation and impact parameter requirements is studied using data for both isolated and non-isolated leptons. Isolated leptons are obtained from $Z \rightarrow \ell\ell$ decays, while additional leptons reconstructed in events with $Z \rightarrow \ell\ell$ decays constitute the sample of non-isolated leptons. Additional checks are performed with non-isolated leptons from semi-leptonic b - and c -quark decays in a heavy-flavour enriched di-jet sample. Good agreement is observed between data and simulation and the systematic uncertainty is, in general, estimated to be small with respect to the other systematic uncertainties.

Signal Selection An additional uncertainty on the signal selection efficiency is added in the 2011 analysis only, but is not needed in the 2012 analysis due to an improved modelling of the signal kinematics. This additional uncertainty is evaluated by varying the Higgs boson p_T spectrum in the gluon fusion process according to the PDF and QCD scale uncertainties.

Background Estimation The background uncertainties of the data driven methods have already been presented in Sections 6.1.2. The overall uncertainty of the integrated luminosity for the complete 2011 dataset is $\pm 1.8\%$ and is described in Refs. [87, 88]. For the

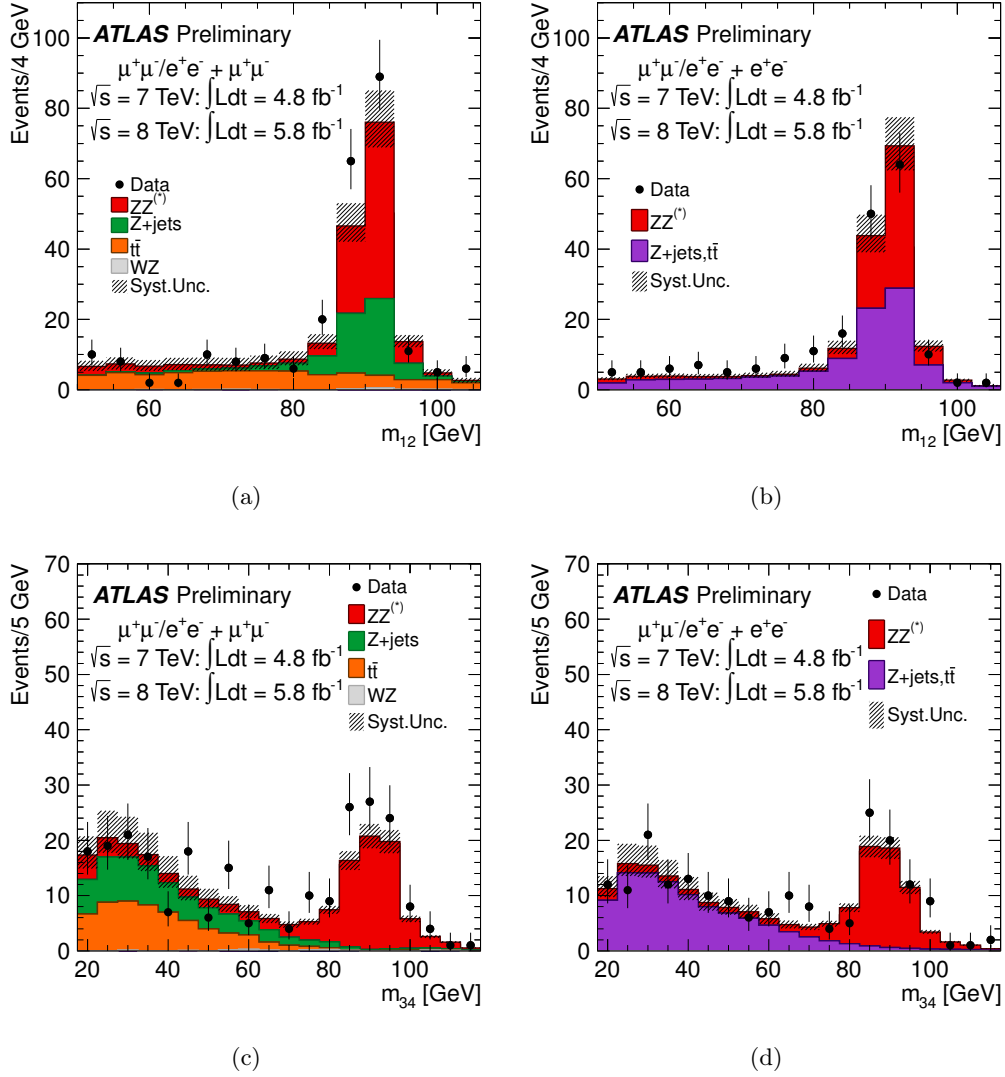


Figure 6.12: Invariant mass distributions of the lepton pairs in the control sample defined by a Z boson candidate and an additional same-flavour lepton pair, for the $\sqrt{s} = 8$ TeV and $\sqrt{s} = 7$ TeV datasets combined. The sample is divided according to the flavour of the additional lepton pair.

2012 dataset the corresponding preliminary uncertainty is $\pm 3.6\%$ based on the calibration described in Ref. [88].

Uncertainty on theory The theory-related systematic uncertainty, for both signal and $ZZ^{(*)}$ background, has been discussed in Section 6.1.

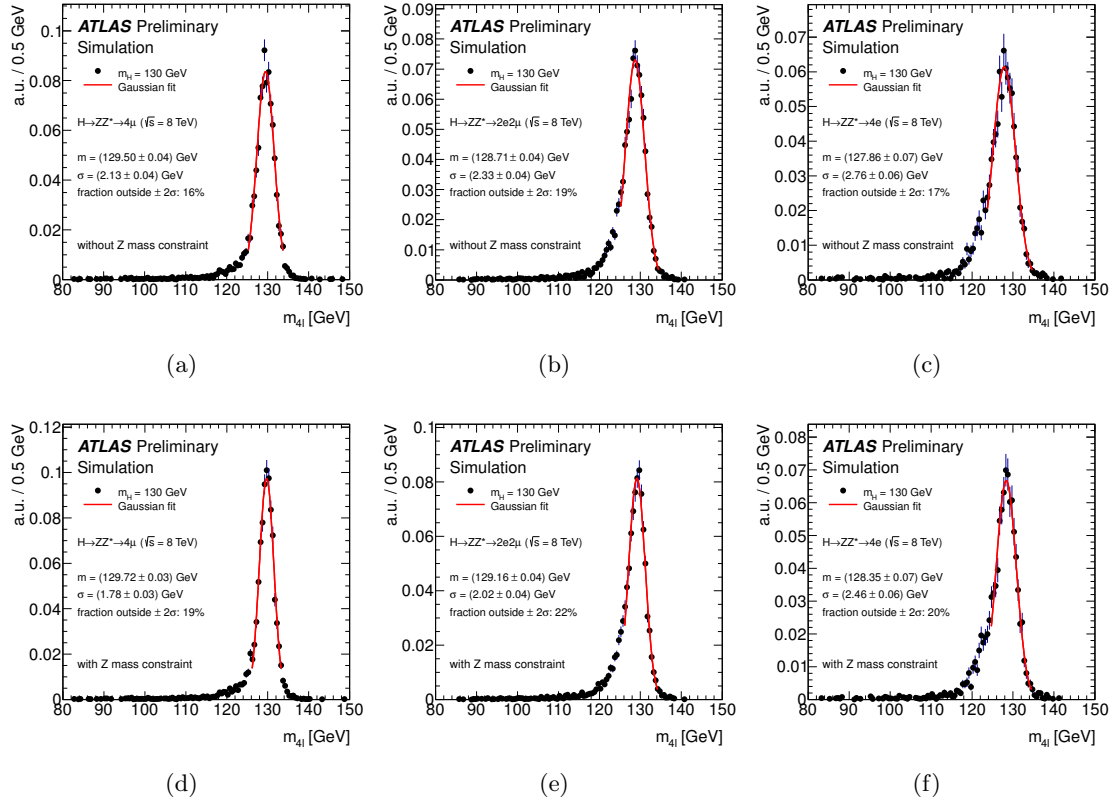


Figure 6.13: Invariant mass distributions for simulated (a) $H \rightarrow ZZ^{(*)} \rightarrow 4\mu$, (b) $H \rightarrow ZZ^{(*)} \rightarrow 2e2\mu$ and (c) $H \rightarrow ZZ^{(*)} \rightarrow 4e$ events for $m_H = 130$ GeV, at $\sqrt{s} = 8$ TeV. The fitted range for the Gaussian is chosen to be: -2σ to 2σ (-1.5σ to 2.5σ) for the 4μ ($2e2\mu/4e$) channel. The slightly reduced mean values arise from radiative losses which are more explicit in channels involving electrons [86]. In (d), (e) and (f) the corresponding results after applying the Z mass constraint are shown.

6.6 Results of event selection

In Table 6.20, the number of events observed in each final state are summarised and compared with the expected backgrounds, separately for $m_{4\ell} < 160$ GeV and $m_{4\ell} \geq 160$ GeV, and to the expected signal for various m_H hypotheses. Table 7.4 presents the observed and expected number of events, in a window of ± 5 GeV around various hypothesised Higgs boson masses, for the 5.8 fb^{-1} at $\sqrt{s} = 8$ TeV and the 4.8 fb^{-1} at $\sqrt{s} = 7$ TeV datasets as well as for their combination.

The expected $m_{4\ell}$ distributions for the total background and several signal hypotheses are compared with the data in Fig. 7.9. Figure 6.15 presents the same distributions, for the low mass range 80–250 GeV.

Table 6.20: The observed numbers of events and the final estimate for the expected backgrounds, separated into “Low mass” ($m_{4\ell} < 160$ GeV) and “High mass” ($m_{4\ell} \geq 160$ GeV) regions. The expected numbers of signal events is also shown for various Higgs boson mass hypotheses. For signal and background estimates, the corresponding total uncertainty is given.

	4μ		$2e2\mu/2\mu2e$		$4e$	
	Low mass	High mass	Low mass	High mass	Low mass	High mass
$\sqrt{s} = 8 \text{ TeV}$						
Int. Luminosity	5.8 fb^{-1}		5.8 fb^{-1}		5.9 fb^{-1}	
$ZZ^{(*)}$	6.3 ± 0.3	27.3 ± 2.0	3.9 ± 0.2	41.4 ± 3.1	2.9 ± 0.3	17.7 ± 1.4
$Z + \text{jets, and } t\bar{t}$	0.4 ± 0.2	0.15 ± 0.07	3.9 ± 0.9	1.4 ± 0.3	2.9 ± 0.8	1.0 ± 0.3
Total Background	6.7 ± 0.3	27.4 ± 2.0	7.8 ± 1.0	42.8 ± 3.1	5.8 ± 0.8	18.7 ± 1.4
Data	4	34	11	61	7	25
$m_H = 125 \text{ GeV}$	1.4 ± 0.2		1.7 ± 0.2		0.8 ± 0.1	
$m_H = 150 \text{ GeV}$	4.5 ± 0.6		5.9 ± 0.8		2.7 ± 0.4	
$m_H = 190 \text{ GeV}$	8.2 ± 1.0		12.5 ± 1.7		5.3 ± 0.8	
$m_H = 400 \text{ GeV}$	3.9 ± 0.5		6.6 ± 0.9		2.9 ± 0.4	
$\sqrt{s} = 7 \text{ TeV}$						
Int. Luminosity	4.8 fb^{-1}		4.8 fb^{-1}		4.9 fb^{-1}	
$ZZ^{(*)}$	4.6 ± 0.2	18.6 ± 1.3	2.4 ± 0.2	28.0 ± 2.1	1.4 ± 0.1	10.5 ± 0.8
$Z + \text{jets, and } t\bar{t}$	0.2 ± 0.1	0.07 ± 0.03	2.1 ± 0.5	0.7 ± 0.2	2.3 ± 0.6	0.8 ± 0.2
Total Background	4.8 ± 0.2	18.6 ± 1.3	4.5 ± 0.5	28.7 ± 2.0	3.6 ± 0.6	11.3 ± 0.9
Data	8	25	5	28	4	18
$m_H = 125 \text{ GeV}$	1.0 ± 0.1		1.0 ± 0.2		0.4 ± 0.1	
$m_H = 150 \text{ GeV}$	3.0 ± 0.4		3.4 ± 0.5		1.4 ± 0.2	
$m_H = 190 \text{ GeV}$	5.1 ± 0.7		7.4 ± 1.1		2.8 ± 0.4	
$m_H = 400 \text{ GeV}$	2.3 ± 0.3		3.8 ± 0.6		1.6 ± 0.3	

Table 6.21: The numbers of expected signal and background events together with the number of observed events, in a window of ± 5 GeV around the hypothesized Higgs boson mass for the 5.8 fb^{-1} at $\sqrt{s} = 8$ TeV and the 4.8 fb^{-1} at $\sqrt{s} = 7$ TeV datasets as well as for their combination.

	$\sqrt{s} = 8 \text{ TeV}$			$\sqrt{s} = 7 \text{ TeV}$			$\sqrt{s} = 8 \text{ TeV and } \sqrt{s} = 7 \text{ TeV}$					
m_H	exp.	signal	exp. bkg	obs	exp.	signal	exp. bkg	obs	exp.	signal	exp. bkg	obs
4μ												
120	0.68±0.09	0.62±0.04	2	0.48±0.07	0.40±0.02	2	1.16±0.16	1.03±0.06	4			
125	1.24±0.17	0.77±0.05	4	0.85±0.13	0.49±0.03	2	2.09±0.30	1.26±0.07	6			
130	1.87±0.25	0.85±0.05	2	1.38±0.21	0.53±0.03	1	3.26±0.46	1.38±0.07	3			
$2e2\mu/2\mu2e$												
120	0.81±0.11	1.17±0.15	2	0.48±0.08	0.66±0.08	1	1.29±0.19	1.82±0.17	3			
125	1.45±0.20	1.32±0.17	3	0.84±0.13	0.75±0.09	2	2.29±0.33	2.07±0.20	5			
130	2.25±0.31	1.35±0.17	2	1.27±0.20	0.78±0.10	1	3.52±0.51	2.14±0.20	3			
$4e$												
120	0.34±0.05	0.78±0.15	1	0.15±0.02	0.56±0.11	1	0.49±0.08	1.34±0.19	2			
125	0.62±0.09	0.90±0.17	2	0.28±0.05	0.64±0.12	0	0.90±0.14	1.54±0.21	2			
130	0.91±0.14	0.96±0.17	1	0.42±0.07	0.68±0.13	0	1.33±0.21	1.63±0.22	1			

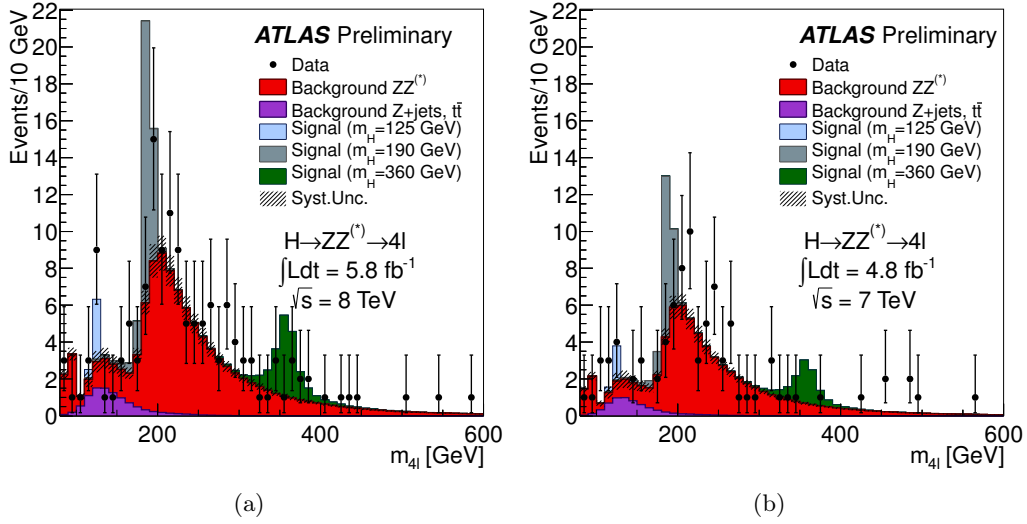


Figure 6.14: The distribution of the four-lepton invariant mass, $m_{4\ell}$, for the selected candidates compared with the background expectation in the range 80–600 GeV for the (a) $\sqrt{s} = 8$ TeV and (b) $\sqrt{s} = 7$ TeV datasets. The error bars represent the 68.3% central confidence intervals. The signal expectation for several m_H hypotheses is also shown. The resolution of the reconstructed Higgs boson mass is dominated by detector resolution at low m_H values and by the Higgs boson width at high m_H .

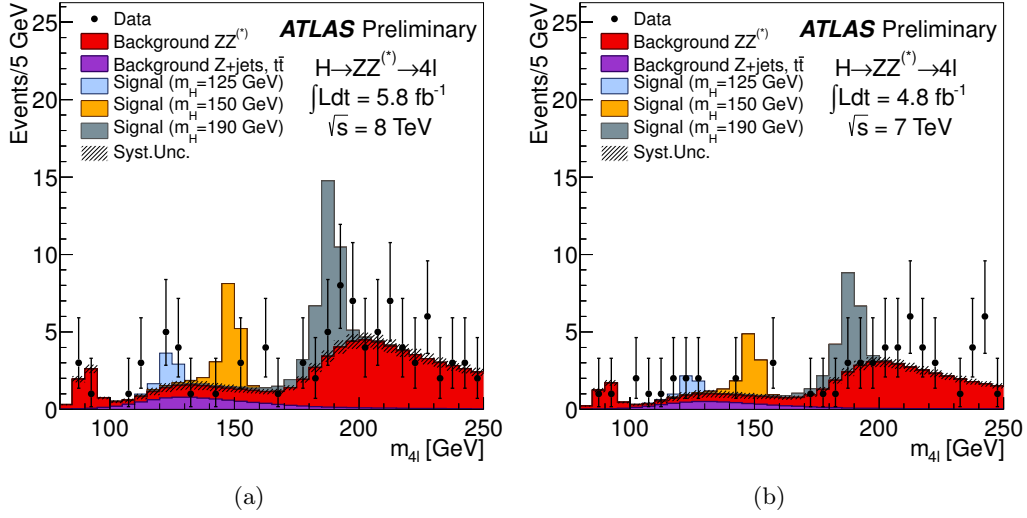


Figure 6.15: The distribution of the four-lepton invariant mass, $m_{4\ell}$, for the selected candidates compared to the background expectation in the 80–250 GeV mass range for the (a) $\sqrt{s} = 8$ TeV and (b) $\sqrt{s} = 7$ TeV datasets. Error bars represent 68.3% central confidence intervals. The signal expectation for several m_H hypotheses is also shown.

6.7 Exclusion limits and p -values

Based on the number of events remaining in the final selection, upper limits are set on the Higgs boson production cross section at 95% CL, using the CL_s modified frequentist formalism [89] with the profile likelihood ratio test statistic [90]. A brief introduction of the CL_s method and frequentist formalism will be presented in section 6.7.1 and 6.7.2. The final exclusion limits will be discussed in section 6.7.3.

6.7.1 The CL_s method

A test statistic q is used to distinguish between the hypothesis of data containing signal and background ($s + b$) or containing background only (b). The PDF of q for $s + b$ and b only should be discriminative, using the actual data results in a value q_{obs} of the test variable. In order to determine which of the two hypotheses is favoured, ($s+b$) or (b), the p -value is defined. It is a probability which measures the compatibility of the data with the chosen hypothesis. If $f(q|s + b)$ denotes the PDF of q under the assumption of $s + b$ model, then the p -value can be expressed as

$$p_{s+b} = P(q \geq q_{\text{obs}} | s + b) = \int_{q_{\text{obs}}}^{\infty} f(q|s + b) dq. \quad (6.3)$$

In a similar way, one takes the p -value of the background-only hypothesis to be

$$p_b = P(q \leq q_{\text{obs}}|b) = \int_{-\infty}^{q_{\text{obs}}} f(q|b) dq . \quad (6.4)$$

This is called the " CL_{s+b} " method. The smaller the p -value, the less data is compatible with the model. The conventional 95% confidence level of exclusion is defined as $1 - \alpha = 95\%$ if the p value satisfies $p_{s+b} < \alpha$, where α equals to 0.05.

This procedure is not appropriate when the test statistics can not distinguish between the different hypotheses. This can happen if the expected number of signal events is much less than the number of background events, which can be the case in Higgs searches. The value of α can easily approach 5%, thus excluding the signal hypotheses. To avoid this problem, the CL_s [89] is defines as

$$CL_s \equiv \frac{p_{s+b}}{1 - p_b} < \alpha . \quad (6.5)$$

so that when the PDF's $f(q|b)$ and $f(q|s+b)$ values are widely apart, $1 - p_b$ is only slightly less than unity, not affecting the original exclusion; on the contrary, if the two distributions are close to each other, $1 - p_b$ becomes small, and thus the p -value of $s + b$ is increased to be protected from unreasonable exclusion.

Since CL_s is always larger than $CL_{(s+b)}$, it is more conservative when the limit is excluded. The p -value is transformed into significance, under the assumption that its PDF is a Gaussian. The significance is the standard deviation of σ from the central value, expressed in numbers of σ .

6.7.2 Frequentist Limit Setting

The counting experiment yields a total number of n events, which equals to $\mu s + b$, where s is the number of signal events for the assumed Higgs mass, b denotes the number of background events. μ is the strength of the signal with respect to the Standard Model expectation. For the limit setting procedure, the distribution of the reconstructed mass for the four leptons is considered. The likelihood function is the product of Poisson probabilities for $\mu s + b$ in all bins of the invariant mass distribution. The nuisance parameters that characterise the shape of the signal and background PDFs of the variable mass, denoted as θ , is usually constrained in the likelihood function with poisson functions. To test a hypothesised value of μ the profile likelihood ratio is defined as

$$\lambda(\mu) = \frac{L(\mu, \hat{\vec{\theta}})}{L(\hat{\mu}, \hat{\vec{\theta}})} . \quad (6.6)$$

Here $\hat{\vec{\theta}}$ in the numerator denotes the value of $\vec{\theta}$ that maximizes L for the specified μ , i.e., it is the conditional maximum-likelihood (ML) estimator of $\vec{\theta}$ (and thus is a function of μ). The denominator is the maximized (unconditional) likelihood function, i.e., $\hat{\mu}$ and $\hat{\vec{\theta}}$

are their ML estimators [90].

The profiled likelihood λ is between 0 and 1, a large value implying good agreement of data and the μ hypothesis. Equivalently the test statistic expressed as

$$t_\mu = -2 \ln \lambda(\mu) \quad (6.7)$$

indicates compatibility if its value is large. Thus the p-value is computed

$$p_\mu = \int_{t_{\mu, \text{obs}}}^{\infty} f(t_\mu | \mu) dt_\mu, \quad (6.8)$$

where $t_{\mu, \text{obs}}$ is the value of the statistic t_μ observed from the data and $f(t_\mu | \mu)$ denotes the pdf of t_μ under the assumption of a signal strength μ . The confidence interval derived from this definition is two-sided, i.e., the excluded value of μ can be of either side of the $\hat{\mu}$. To set an upper limit for μ which is one side only, one defines

$$\tilde{q}_\mu = \begin{cases} -2 \ln \tilde{\lambda}(\mu) & \hat{\mu} \leq \mu \\ 0 & \hat{\mu} > \mu \end{cases} = \begin{cases} -2 \ln \frac{L(\mu, \hat{\theta}(\mu))}{L(0, \hat{\theta}(0))} & \hat{\mu} < 0, \\ -2 \ln \frac{L(\mu, \hat{\theta}(\mu))}{L(\hat{\mu}, \hat{\theta})} & 0 \leq \hat{\mu} \leq \mu, \\ 0 & \hat{\mu} > \mu. \end{cases} \quad (6.9)$$

The reason for setting $q_\mu = 0$ for $\hat{\mu} > \mu$ is that when setting an upper limit, one would not regard data with $\hat{\mu} > \mu$ as representing less compatibility with μ than the obtained data, and therefore this is not taken as part of the rejection region of the test. For $\mu \geq 0$, if one finds data such that $\hat{\mu} < 0$, then the best level of agreement between the data and any physical value of μ occurs for $\mu = 0$.

The upper limit set on μ for observed data, is obtained by iteration on the μ value to find the one that satisfies the p-value $p_\mu = 5\%$. The pdf of the test statistic, is generated by toy MC experiments under μ and $\hat{\theta}(\mu, \text{obs})$ which is the conditional MLE(maximum likelihood estimator) based on observed data. The confidence interval of $(0, \mu_{up})$ contains the true value of μ in 95% of the cases if the experiment is repeated many times. Thus if $\mu_{up} < 1$ at a hypothesis mass, the true value of μ cannot be 1, and the standard model will be excluded.

The expected limit is set, by taking toy MC experiments as data, which are generated according to $\mu = 0$ and $\hat{\theta}(0, \text{obs})$. For each pseudo data event, the process of calculating the p-value and the upper μ limit is repeated as is done in the case of the observed limit. A distribution of μ_{up} is formed and its median is taken as expected limit, the 68% and 95% bands of the μ_{up} distribution will be denoted as the 1σ and 2σ bands.

6.7.3 Results

The test statistic is evaluated using a maximum-likelihood fit of signal and background models to the observed $m_{4\ell}$ distribution using the CL_s modified frequentist formalism.

Figures 6.16, 6.17 and 7.10 show the observed and expected 95% CL cross section upper limits, as a function of m_H , for the $\sqrt{s} = 8$ TeV data, the $\sqrt{s} = 7$ TeV data and for the combination of the two datasets. Combining the two datasets, the SM Higgs boson is excluded at 95% CL in the mass ranges 131–162 GeV and 170–460 GeV. The expected exclusion ranges are 124–164 GeV and 176–500 GeV.

The significance of an excess is given by the probability, p_0 , where the 0 denotes the μ value and implies it is the background only model. In Figure 6.19 the local p_0 , obtained using the asymptotic approximation of Ref. [90], is presented as a function of the m_H hypothesis for the combination of $\sqrt{s} = 8$ and 7 TeV data samples. For comparison, the results for the two data samples are given separately in Fig. 7.11. In the combined analysis of the two datasets, the lowest local p_0 value is 0.018% (3.6 standard deviations), at $m_H = 125$ GeV. The probability that such an excess occurs anywhere in the full mass range considered in this search (*i.e.*, the *look-elsewhere effect* on the above p_0 value), is evaluated using the method of Ref. [91], in the mass range between 110 GeV and 141 GeV (*i.e.*, the mass range not previously excluded at the 95% C.L. by the LHC experiments [92]). The *global* p_0 of the excess located at $m_H = 125$ GeV is 0.65%, or 2.5 standard deviations. In the high mass region ($m_H > 160$ GeV), the lowest p_0 is at 1.9% (2.1 standard deviations), at $m_H = 266$ GeV. In Fig. 7.13(a) the signal strength parameter $\mu = \sigma/\sigma_{SM}$ is presented as a function of m_H for the combination of the two data samples. The corresponding result in the case where a SM Higgs signal of $m_H = 125$ GeV is injected is shown in Fig. 7.13(b). The bands illustrate the μ interval corresponding to $-2 \ln \lambda(\mu) < 1$, where λ is the profile likelihood ratio test statistic, and represents an approximate $\pm 1\sigma$ variation. The fitted signal strength divided by the expected SM rate is denoted with $\hat{\mu}$. The expected $\hat{\mu}$ has an asymmetric shape and because the expected SM rate rises rapidly with m_H in the low mass region, the expected $\hat{\mu}$ is increased below the injected signal mass and slightly exceeds one for a small mass range.

Figure 7.14 presents the best μ and m_H fit and the profile likelihood ratio contours that, in the asymptotic limit, would correspond to 68% and 95% confidence levels.

6.8 Summary

A search for the SM Higgs boson in the decay channel $H \rightarrow ZZ^{(*)} \rightarrow 4\ell$ based on 4.8 fb^{-1} of data recorded with the ATLAS detector at $\sqrt{s} = 7$ TeV during 2011 and 5.8 fb^{-1} recorded at $\sqrt{s} = 8$ TeV during 2012 has been presented. The SM Higgs boson is excluded at 95% CL in the mass ranges 131–162 GeV and 170–460 GeV. An excess of events is observed around $m_H = 125$ GeV, whose p_0 value is 0.018% (3.6 standard

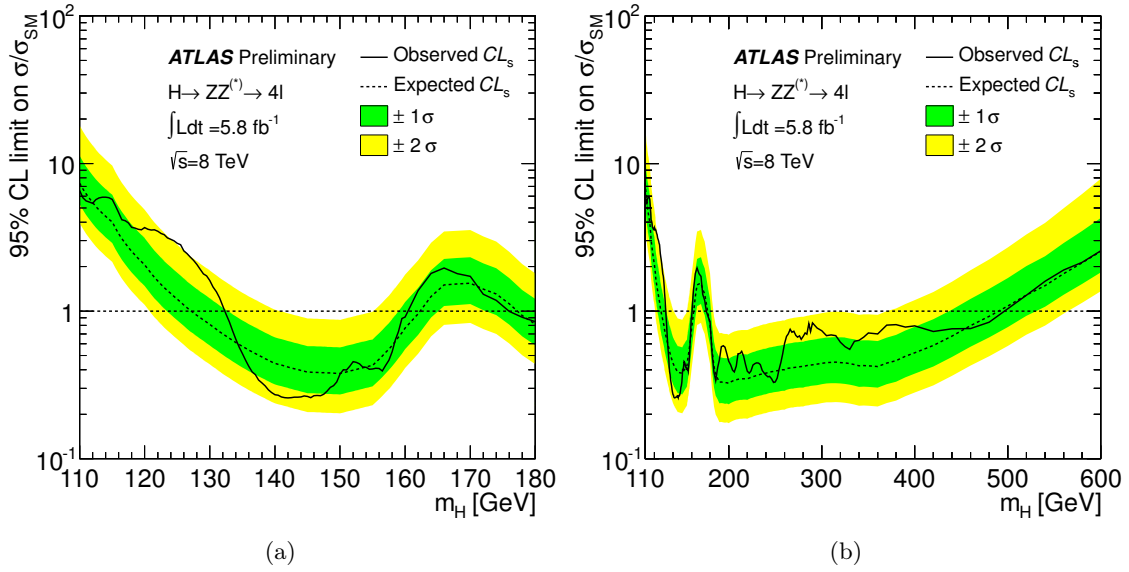


Figure 6.16: The expected (dashed) and observed (full line) 95% CL upper limits on the Standard Model Higgs boson production cross section as a function of m_H , divided by the expected SM Higgs boson cross section, for the $\sqrt{s} = 8$ TeV data sample. The dark (green) and light (yellow) bands indicate the expected limits with $\pm 1\sigma$ and $\pm 2\sigma$ fluctuations, respectively; (a) shows the low mass range, and (b) the full range under consideration.

deviations) in the combined analysis of the two datasets.

6.9 Combination with other search channels

As section 1.3 introduced, $H \rightarrow ZZ^{(*)} \rightarrow \ell^+\ell^-\ell^+\ell^-$ is not the only sensitive searching channel in ATLAS. The result of combining with other production modes was first published in [93] and also [94], which includes, $H \rightarrow \gamma\gamma$ and $H \rightarrow WW$ analysis of 8 TeV and 7 TeV data, and previously published results of searches for $b\bar{b}$ and $\tau^+\tau^-$ in the 7 TeV data.

$H \rightarrow \gamma\gamma$ analysis The search for the SM Higgs boson through the decay $H \rightarrow \gamma\gamma$ is performed in the mass range between 110 GeV and 150 GeV. The invariant mass of the two photons is evaluated using the photon energies measured in the calorimeter. Photon candidates are required to pass identification criteria based on shower shapes in the electromagnetic calorimeter and on energy leakage into the hadronic calorimeter. With the selection [94], in the diphoton invariant mass range between 100 GeV and 160 GeV, 23788 and 35251 diphoton candidates are observed in the 7 TeV and 8 TeV data samples, respectively. Data-driven techniques [95] are used to estimate the numbers of $\gamma\gamma$, γj and $j j$ events in the selected sample. The description of the Higgs boson signal is obtained from MC, while the background is estimated from data by fitting the diphoton mass spec-

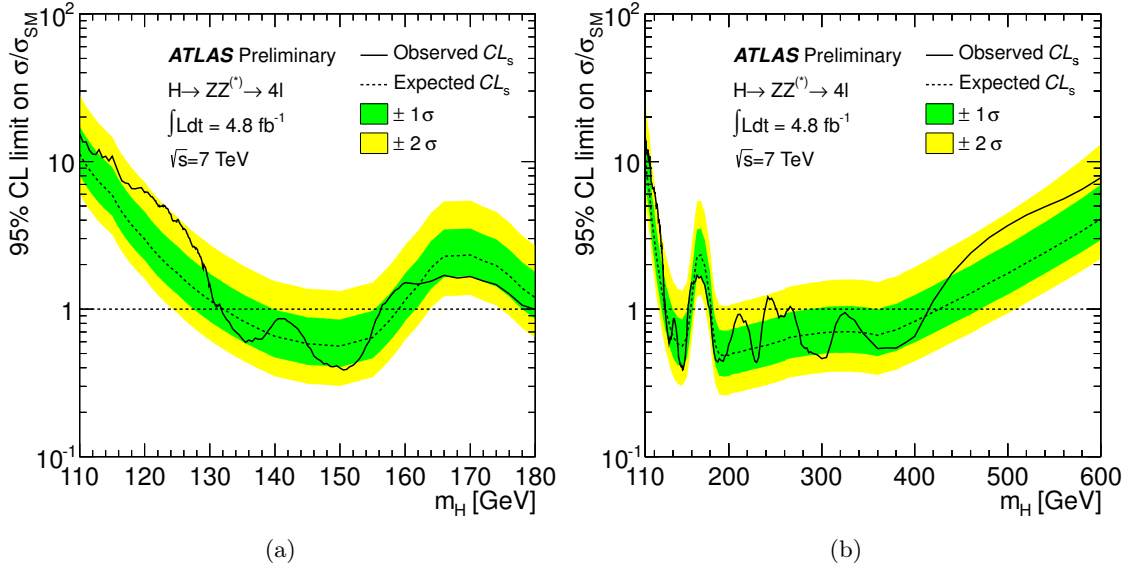


Figure 6.17: The expected (dashed) and observed (full line) 95% CL upper limits on the SM Higgs boson production cross section as a function of m_H , divided by the expected SM Higgs boson cross section for the $\sqrt{s} = 7$ TeV data sample. The dark (green) and light (yellow) bands indicate the expected limits with $\pm 1\sigma$ and $\pm 2\sigma$ fluctuations, respectively; (a) shows the low mass range, and (b) the full range under consideration.

trum in the mass range 100–160 GeV with a selected model with free parameters of shape and normalisation. The events are separated into ten mutually exclusive categories having different mass resolutions and signal-to-background ratios. The distributions of the invariant mass, $m_{\gamma\gamma}$, of the diphoton events, summed over all categories, are shown in figure 6.23. The result of a fit including a signal component fixed to $m_H = 126.5$ GeV and a background component described by a fourth-order Bernstein polynomial is superimposed. The statistical analysis of the data employs an unbinned likelihood function constructed from those of the ten categories of the 7 TeV and 8 TeV data samples. To demonstrate the sensitivity of this likelihood analysis, the mass spectrum is obtained after weighting events with category-dependent factors reflecting the signal-to-background ratios.

$H \rightarrow WW$ channel The analysis of $H \rightarrow WW$ is focused on the mass range $110 < m_H < 200$ GeV. Only the $e\mu$ final state is considered in the 8 TeV analysis since it provides more than 85% of the sensitivity of the search and the higher luminosity results in a larger Drell-Yan background in the same-flavour final states. Stringent requirements are used for the leptons and due to the presence of neutrinos in the final state, events are required to have large E_T^{miss} . The background rate and composition depend significantly on the jet multiplicity, as does the signal topology. Therefore the analysis is subdivided into 0-jet, 1-jet and 2-jet search channels. The WW, W+jet and top backgrounds are estimated from data-driven techniques, and the small backgrounds from Drell-Yan and diboson processes

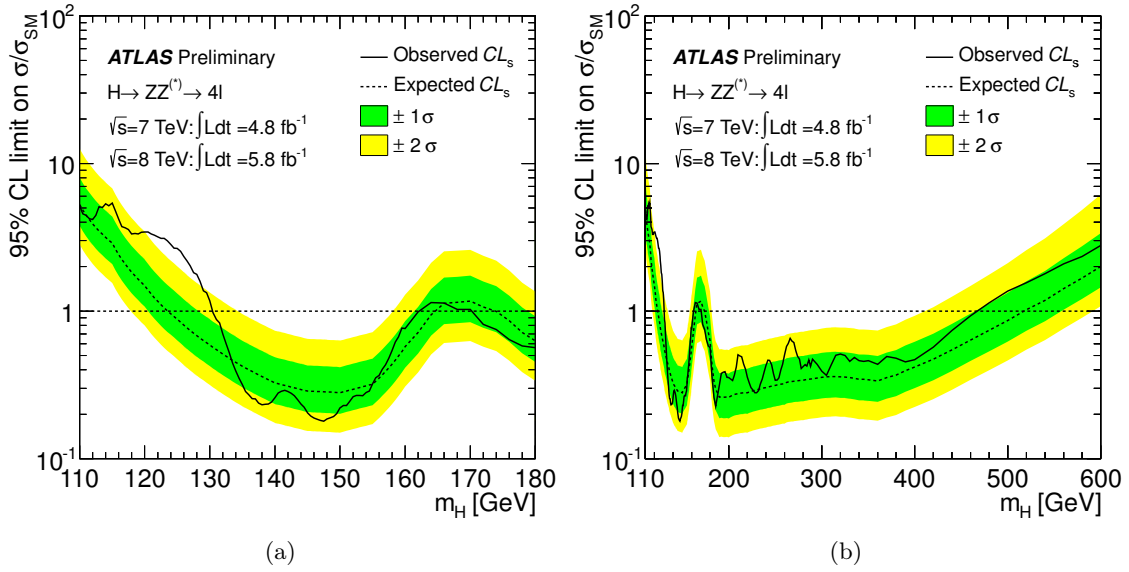


Figure 6.18: The expected (dashed) and observed (full line) 95% CL upper limits on the Standard Model Higgs boson production cross section as a function of m_H , divided by the expected SM Higgs boson cross section, for the combination of the $\sqrt{s} = 7$ TeV and $\sqrt{s} = 8$ TeV data samples. The dark (green) and light (yellow) bands indicate the expected limits with $\pm 1\sigma$ and $\pm 2\sigma$ fluctuations, respectively; (a) shows the low mass range, and (b) the full range under consideration.

other than WW, as well as the WW background for the 2-jet analysis, are estimated using MC simulation. Figure 6.24 shows the distribution of the transverse mass after all selection criteria in the 0-jet and 1-jet channels combined, and for both lepton channels together.

Combined results The individual search channels that enter the combination are summarized in Table 6.22.

In the absence of a signal, this should allow the exclusion of the SM Higgs boson for all masses between 110 and 582 GeV, as shown in 6.25. This range overlaps with the lower bound from LEP (114.4 GeV); if the entire range had been excluded, this would have shown the SM to be deeply flawed. Our data exclude a SM Higgs boson signal at 95% CL in two mass regions, 111 to 122 GeV and 131 to 559 GeV. In the region around 126 GeV, this analysis is more than sensitive enough to exclude a SM Higgs boson signal at 95% CL; the failure to do so means that the possibility of a discovery must be considered.

The largest local significance for the combined data is for a SM Higgs boson mass of $m_H \sim 126$ GeV, at which it reaches 6.0σ , corresponding to a probability of an upward fluctuation of the background of 1.0×10^{-9} . This significance is slightly higher than, but consistent with, the expected SM Higgs boson signal at this mass, as seen in figure 6.26. The observed significances for the statistically independent 7 and 8 TeV data samples both peak at ~ 126 GeV, at which they are 3.6σ and 4.9σ , respectively. Uncertainties in the

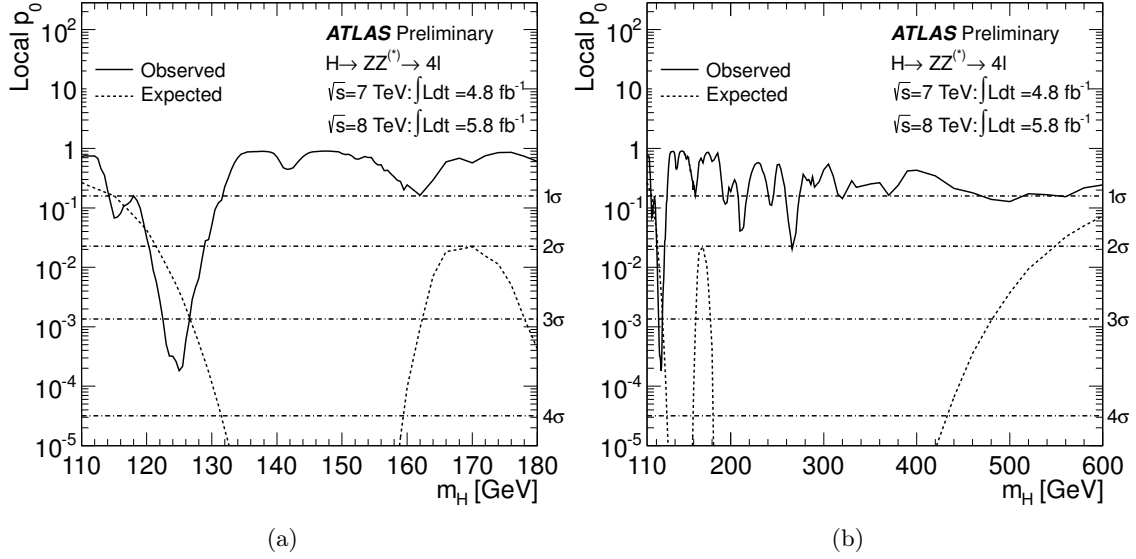


Figure 6.19: The observed local p_0 for the combination of the 2011 and 2012 datasets (solid line) in a) low mass region b) full mass region. The dashed curve shows the expected median local p_0 for the signal hypothesis when tested at the corresponding m_H . The horizontal dashed lines indicate the p_0 values corresponding to local significances of 1σ , 2σ , 3σ and 4σ .

relative energy scales of the detector for electrons and muons reduce the combined local significance to 5.9σ . The global significance of the excess is $\sim 5.1\sigma$, increasing to 5.3σ in the range 110–150 GeV, which is approximately the mass range not excluded at the 99% CL by the LHC combined SM Higgs boson search [139] and the indirect constraints from the global fit to precision electroweak measurements.

The mass of the observed new particle is estimated using the profile likelihood ratio $\lambda(m_H)$ for $H \rightarrow ZZ^{(*)} \rightarrow 4\ell$ and $H \rightarrow \gamma\gamma$, the two channels with the highest mass resolution. The signal strength is allowed to vary independently in the two channels, although the result is essentially unchanged when restricted to the SM hypothesis $\mu = 1$. The leading sources of systematic uncertainty come from the electron and photon energy scales and resolutions. The resulting estimate for the mass of the observed particle is 126.0 ± 0.4 (stat) ± 0.4 (sys) GeV.

The best-fit signal strength $\hat{\mu}$ is shown in Fig. 6.27 as a function of m_h . The observed excess corresponds to $\hat{\mu} = 1.4 \pm 0.3$ for $m_H = 126$ GeV, which is consistent with the SM Higgs boson hypothesis $\mu = 1$.

Conclusion The high degree of statistical significance and simultaneous observation in multiple channels and data sets in this search for the SM Higgs boson demonstrate that we have observed a new particle with properties consistent with those of the SM Higgs boson. The excess is driven by the two channels with the highest mass resolution, $H \rightarrow ZZ^{(*)} \rightarrow$

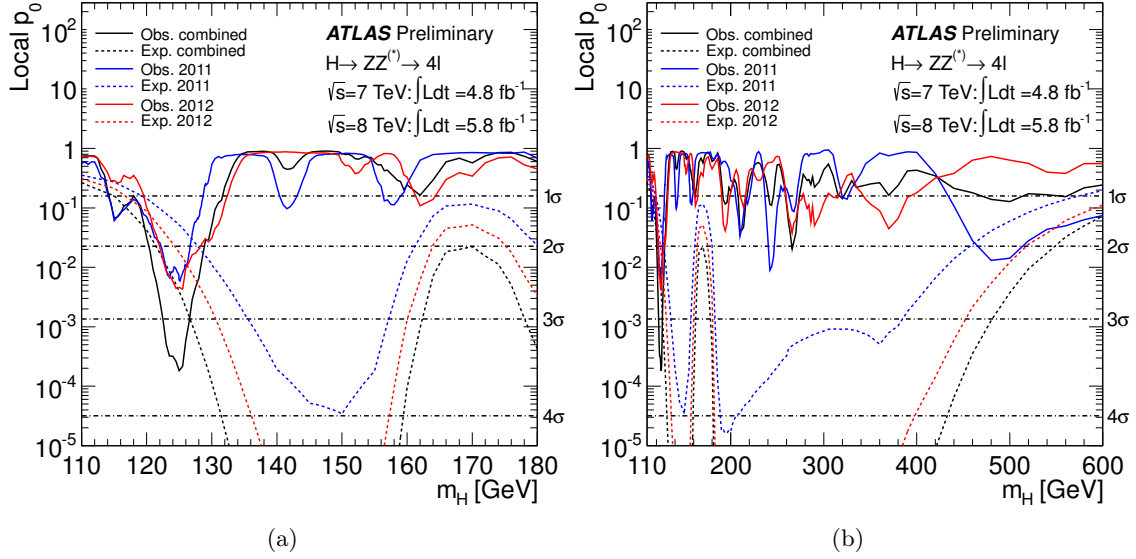


Figure 6.20: The observed local p_0 for the combination of the 2011 and 2012 datasets (solid black line) in a) low mass region b) full mass region; the $\sqrt{s} = 7 \text{ TeV}$ and $\sqrt{s} = 8 \text{ TeV}$ data results are shown in solid lines (blue and red, respectively). The dashed curves show the expected median local p_0 for the signal hypothesis when tested at the corresponding m_H . The horizontal dashed lines indicate the p_0 values corresponding to local significances of 1σ , 2σ , 3σ and 4σ .

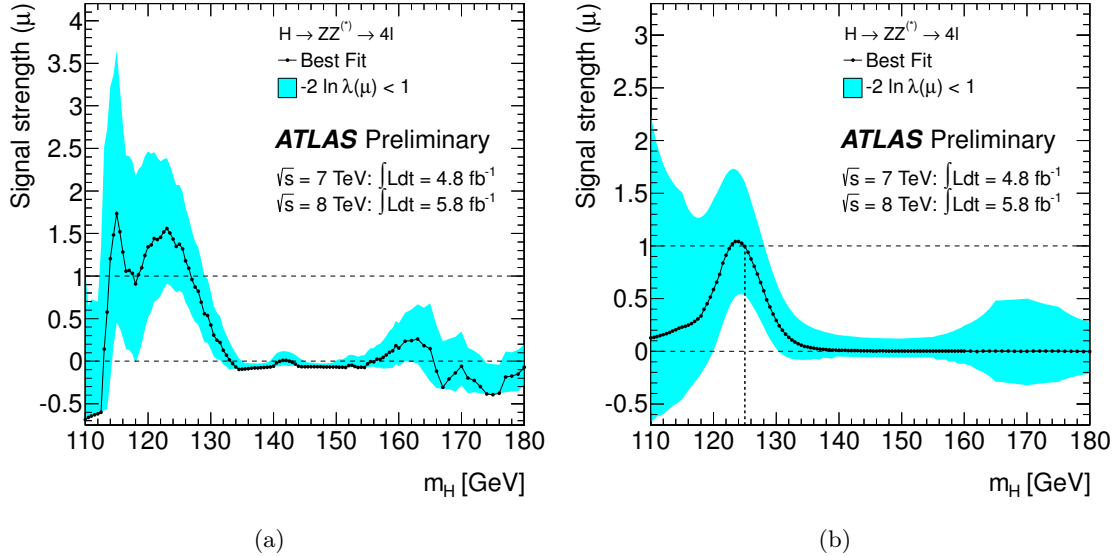


Figure 6.21: The signal strength parameter $\mu = \sigma/\sigma_{SM}$ obtained from a fit to the data is presented (a) for the combined fit to the 2011 and 2012 data samples and (b) for the expected value of μ as a function of m_H when a SM Higgs signal with $m_H = 125 \text{ GeV}$ is injected.

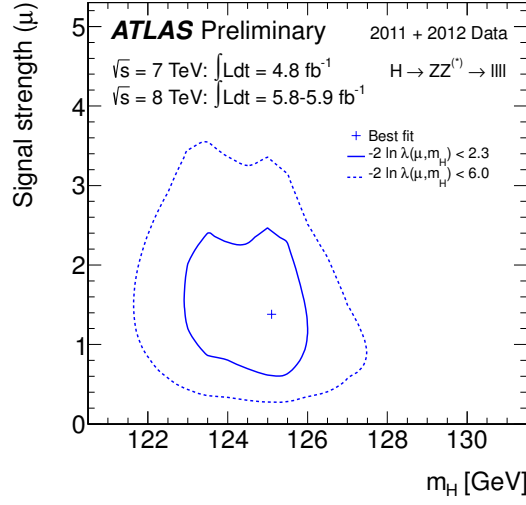


Figure 6.22: Best fit values for μ and m_H , and likelihood ratio contours that, in the asymptotic limit, correspond to 68% and 95% level contours in the (μ, m_H) plane.

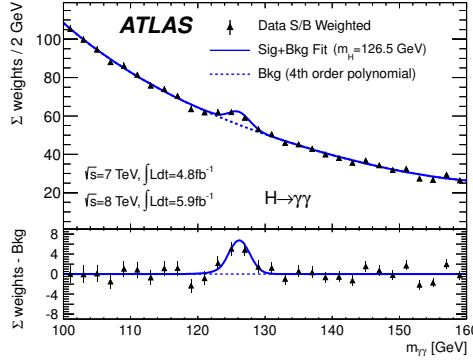


Figure 6.23: Distribution of the mass, $m_{\gamma\gamma}$, of weighted di-photon candidates. The selected events are weighted by factors that reflect the signal-to-background ratio predicted for a SM Higgs boson. The result of a fit to the data of the sum of a signal component fixed to $m_H = 126.5$ GeV and a background component described by a fourth-order polynomial are superimposed. The residuals of the weighted data with respect to the fitted background are displayed at the bottom [94].

$\ell^+\ell^-\ell^+\ell^-$ and $H \rightarrow \gamma\gamma$, and the equally sensitive but low-resolution $H \rightarrow WW^{(*)} \rightarrow \ell\nu\ell\nu$ channel. Taking into account the entire mass range of the search, 110–600 GeV, the global significance of the excess is 5.1σ , which corresponds to $p_0 = 1.7 \times 10^{-7}$. These results provide conclusive evidence for the discovery of a new particle with mass 126.0 ± 0.4 (stat) ± 0.4 (sys) GeV. The signal strength parameter μ has the value 1.4 ± 0.3 at the fitted mass, which is consistent with the SM Higgs boson hypothesis $\mu = 1$. The decays to pairs of vector bosons whose net electric charge is zero identify the new particle as a neutral boson.

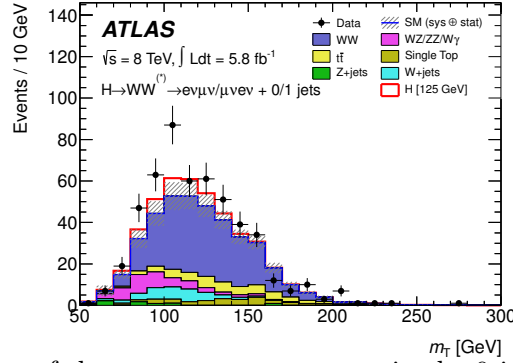


Figure 6.24: Distribution of the transverse mass, m_T , in the 0-jet and 1-jet analyses with both $e\mu$ and μe channels combined, for events satisfying all selection criteria. The expected signal for $m_H = 125$ GeV is shown stacked on top of the background prediction. The W +jets background is estimated from data, and WW and top background MC predictions are normalised to the data using control regions. The hashed area indicates the total uncertainty on the background prediction [93].

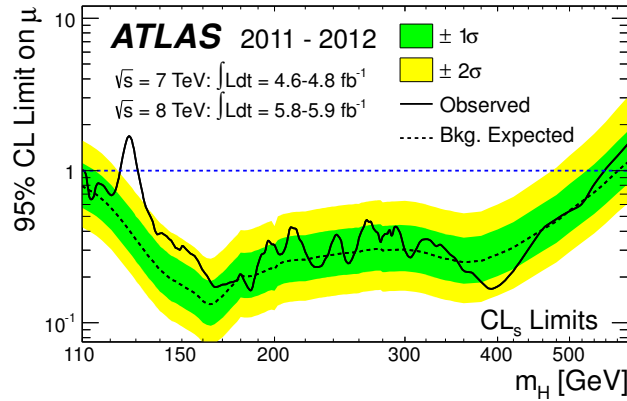


Figure 6.25: Combined search results: The observed (solid) 95% CL limits on the signal strength as a function of m_h and the expectation (dashed) under the background-only hypothesis. The dark and light shaded bands show the $\pm 1\sigma$ and $\pm 2\sigma$ uncertainties on the background-only expectation [93].

Table 6.22: Summary of the individual channels entering the combination. The transition points between separately optimised m_h regions are indicated where applicable. In channels sensitive to associated production of the Higgs boson, V indicates a W or Z boson. The symbols \otimes and \oplus represent direct products and sums over sets of selection requirements, respectively.

Higgs Boson Decay	Subsequent Decay	Sub-Channels	m_h Range [GeV]	$\int L dt$ [fb $^{-1}$]	Ref.
2011 $\sqrt{s}=7$ TeV					
$H \rightarrow ZZ^{(*)}$	4ℓ	$\{4e, 2e2\mu, 2\mu2e, 4\mu\}$	110–600	4.8	[96]
	$\ell\ell\nu\bar{\nu}$	$\{ee, \mu\mu\} \otimes \{\text{low, high pile-up}\}$	200–280–600	4.7	[97]
	$\ell\ell q\bar{q}$	$\{b\text{-tagged, untagged}\}$	200–300–600	4.7	[98]
$H \rightarrow \gamma\gamma$	–	10 categories $\{p_T \otimes \eta_\gamma \otimes \text{conversion}\} \oplus \{2\text{-jet}\}$	110–150	4.8	[99]
$H \rightarrow WW^{(*)}$	$\ell\nu\ell\nu$	$\{ee, e\mu/\mu e, \mu\mu\} \otimes \{0\text{-jet, 1-jet, 2-jet}\} \otimes \{\text{low, high pile-up}\}$	110–200–300–600	4.7	[100]
	$\ell\nu qq'$	$\{e, \mu\} \otimes \{0\text{-jet, 1-jet, 2-jet}\}$	300–600	4.7	[101]
$H \rightarrow \tau\tau$	$\tau_{\text{lep}}\tau_{\text{lep}}$	$\{e\mu\} \otimes \{0\text{-jet}\} \oplus \{\ell\ell\} \otimes \{1\text{-jet, 2-jet, } VH\}$	110–150	4.7	[102]
	$\tau_{\text{lep}}\tau_{\text{had}}$	$\{e, \mu\} \otimes \{0\text{-jet}\} \otimes \{E_T^{\text{miss}} < 20 \text{ GeV}, E_T^{\text{miss}} \geq 20 \text{ GeV}\} \oplus \{e, \mu\} \otimes \{1\text{-jet}\} \oplus \{\ell\} \otimes \{2\text{-jet}\}$	110–150	4.7	
	$\tau_{\text{had}}\tau_{\text{had}}$	$\{1\text{-jet}\}$	110–150	4.7	
$VH \rightarrow Vbb$	$Z \rightarrow \nu\nu$	$E_T^{\text{miss}} \in \{120 - 160, 160 - 200, \geq 200 \text{ GeV}\}$	110–130	4.6	[103]
	$W \rightarrow \ell\nu$	$p_T^W \in \{< 50, 50 - 100, 100 - 200, \geq 200 \text{ GeV}\}$	110–130	4.7	
	$Z \rightarrow \ell\ell$	$p_T^Z \in \{< 50, 50 - 100, 100 - 200, \geq 200 \text{ GeV}\}$	110–130	4.7	
2012 $\sqrt{s}=8$ TeV					
$H \rightarrow ZZ^{(*)}$	4ℓ	$\{4e, 2e2\mu, 2\mu2e, 4\mu\}$	110–600	5.8	[96]
$H \rightarrow \gamma\gamma$	–	10 categories $\{p_T \otimes \eta_\gamma \otimes \text{conversion}\} \oplus \{2\text{-jet}\}$	110–150	5.9	[99]
$H \rightarrow WW^{(*)}$	$e\nu\mu\nu$	$\{e\mu, \mu e\} \otimes \{0\text{-jet, 1-jet, 2-jet}\}$	110–200	5.8	[104]

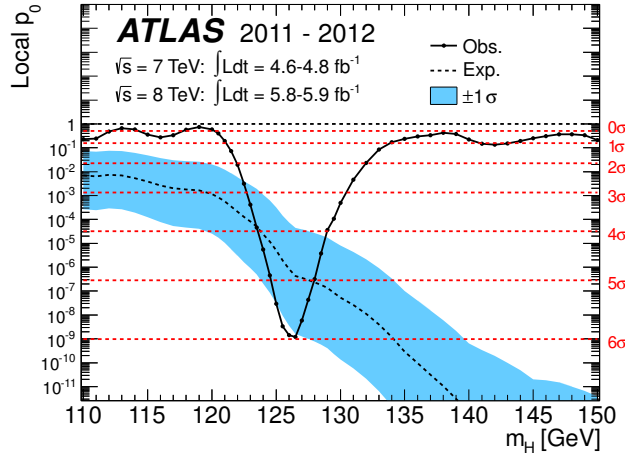


Figure 6.26: The observed (solid) local p_0 as a function of m_h in the low mass range. The dashed curve shows the expected local p_0 under the hypothesis of a SM Higgs boson signal at that mass with its $\pm 1\sigma$ band. The horizontal dashed lines indicate the p -values corresponding to significances of 1 to 6 σ [93].

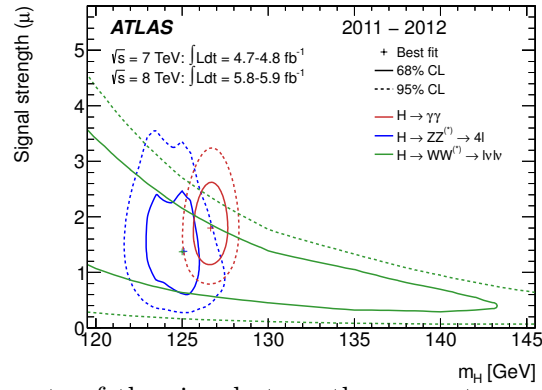


Figure 6.27: Measurements of the signal strength parameter μ for $m_h=126$ GeV for the individual channels and their combination [93].

Chapter 7

Updated results of the new Higgs-like particle in the four lepton decay channel with the ATLAS detector

In the summer of 2012, ATLAS reported the observation of a new particle in the search for the SM Higgs based on 4.9 fb^{-1} at $\sqrt{s} = 7 \text{ TeV}$ and 5.8 fb^{-1} at $\sqrt{s} = 8 \text{ TeV}$ [93, 105]. The most sensitive channels are $H \rightarrow ZZ^{(*)} \rightarrow 4\ell$, $H \rightarrow \gamma\gamma$, and $H \rightarrow WW^{(*)} \rightarrow e\nu\mu\nu$. The search for the SM Higgs boson through the decay $H \rightarrow ZZ^{(*)} \rightarrow 4\ell$, where $\ell = e$ or μ , provides good sensitivity over a wide mass range. This chapter updates the results presented in chapter 6. It includes a re-analysis of the $\sqrt{s} = 7 \text{ TeV}$ data corresponding to an integrated luminosity of 4.6 fb^{-1} collected in 2011, combined with an analysis of $\sqrt{s} = 8 \text{ TeV}$ data corresponding to an integrated luminosity of 20.7 fb^{-1} which corresponds to the full data sample collected in 2012.

The analysis remains largely the same, with only a few changes. The electron identification has been tightened to improve the background rejection for the final states with a pair of electrons forming the lower mass Z^* boson, only for $\sqrt{s} = 8 \text{ TeV}$ data. The mass pairing has been improved to reduce the mis-pairing in the 4μ and $4e$ final states. This reduces the $ZZ^{(*)}$ background at low mass and improves both the Z -mass constraint and the spin measurements. The minimum requirement on m_{34} has been relaxed to increase the sensitivity. Also, a treatment for the inclusion of final state radiation (FSR) has been introduced.

A more detailed description of the selection changes will be given in section 7.1. More specifically, the study of the impact of FSR on the analysis will be presented in section 7.2. The refinement of the background estimation techniques is described in section 7.3. The final result of event selection will be shown in section 7.4. By using the result, the exclusion limits and the mass measurement will be presented. Furthermore, an improvement of the mass measurement can be achieved by including the per event uncertainty, which is not

included in the analysis yet. A study to estimate the per event mass uncertainty is shown in section 7.5. In addition to the main analysis, a spin-parity analysis and a search for Higgs production in the VBF and VH modes is also performed for the first time, and the results will be briefly presented in section 7.6.

7.1 Event Selection

The analysis is optimised after the observation of the new particle, to further improve the sensitivity for a low mass SM Higgs boson. The bulk of the selection remains the same as described in section 6.2. The changes are the following:

Data quality selection In contrast with the previous data quality selection, which was specific to the final states $4e$, $2e2\mu/2\mu2e$ and 4μ , a single selection is made for all final states. This reduces the available luminosity of 2011 data from 4.9 fb^{-1} to 4.6 fb^{-1} .

Electron Identification The electron identification is tightened to better reject the Z +jet background. Specifically, the electron calorimeter requirements have been tightened in the transition region of the detector, and the pixel tracking requirements became stricter to improve conversion rejection. These tighter requirements are applied to all the 2012 data.

Jet Identification Jets are used in the classification of events into VBF-like, VH-like and ggF-like categories, which will be described in section 7.6. Jets are reconstructed from topological clusters [106] using an anti- k_T algorithm [107] with a distance parameter $R = 0.4$. The topological clusters are then corrected from the electromagnetic energy scale to the hadronic energy scale using a p_T - and η -dependent jet energy scale (JES) determined with Monte Carlo simulations [108, 109] (2011) and with data [110] (2012). The latter significantly decreases the JES uncertainty. The pile-up correction was also improved for the full 2012 dataset; it is now based on the jet area and event p_T density; this results in reduced pile-up uncertainties, improved jet energy resolution at low p_T , and higher suppression of fake pile-up jets.

Jets due to pile-up are removed by requiring that at least 50% (75% for 2011) of the tracks associated with the jet (within $\Delta R = 0.4$ around the jet axis) must originate from the primary vertex. This is implemented as a cut on the absolute value of the “jet vertex fraction,” respectively $|\text{JVF}| > 0.75$ for 7 TeV data and Monte Carlo and $|\text{JVF}| > 0.5$ for 8 TeV data and Monte Carlo.

As a pre-selection cut, the jets are required to have $p_T > 25 \text{ GeV}$ for $|\eta| < 2.5$ and $p_T > 30 \text{ GeV}$ for $2.5 < |\eta| < 4.5$. To reject jets not associated with real energy deposits in the calorimeters, they are also required to pass the standard “looser” (“very loose” known as “loose--”) quality cuts for ATLAS jets [111]. To avoid double-counting objects in the

event, a jet is removed if a selected electron is found within $\Delta R < 0.2$ around the jet axis. The jet selection is summarised in Table 7.1.

Table 7.1: Summary of jet selection for 7 TeV and 8 TeV data and Monte Carlo.

Identification	Anti- k_T $R = 0.4$ topological jets
Kinematic cuts	$p_T > 25$ GeV (30 GeV) $ \eta < 2.5$ (> 2.5)
Quality	Looser quality cuts
pile-up	$ JVF > 0.75$ (7 TeV) $ JVF > 0.5$ (8 TeV)

Quadruplet selection Instead of choosing the best quadruplet among the multiple combinations in each event, the optimised selection only allows one quadruplet per event from the beginning. This quadruplet is formed by an opposite sign same flavour di-lepton pair, which has the invariant mass closest to the nominal Z boson mass. This pair is chosen as the leading di-lepton, while the sub-leading is composed of the opposite sign same flavour pair which has the highest invariant mass. For each event, the requirement imposed on the leading pair remains the same as in the previous selection, which is 50-106 GeV, while for the sub-leading one, the criteria is relaxed to increase the sensitivity. The invariant mass of the sub-leading pair, m_{34} , is required to be in the range $m_{\min} < m_{34} < 115$ GeV, where m_{\min} is 12 GeV for $m_{4\ell} < 140$ GeV and rises linearly to 50 GeV at $m_{4\ell} < 190$ GeV.

The selection optimisation related to FSR photons will be introduced in detail in the next section, and the impact on the analysis will be studied.

7.2 FSR impact on $H \rightarrow ZZ^{(*)} \rightarrow 4\ell$ analysis

Due to the presence of two Z bosons in the $H \rightarrow ZZ$ decay, possible FSR can severely distort the mass spectrum of the reconstructed Higgs. The impact is estimated by adding the reconstructed FSR candidate selected by the FSR tool (introduced in chapter 5), or by adding a true FSR photon directly to the final mass. The selection for the FSR photon is $E_T > 3.5$ GeV, $\Delta R < 0.15$ and the shower sampling fraction $f_1 > 0.1$, and only one FSR photon is selected per muon. In the case of multiple candidates, the one closest to the muon is chosen. The fraction of events identified with FSR in the 4μ final state is 1%. In order not to increase the background to the Higgs signal, the FSR photons are not added to the invariant mass of leading or sub-leading pairs, so that it will not affect the event selection. Only events that pass the final selection will be investigated, and if FSR is found, it is added to the 4 lepton invariant mass. The possible resolution improvement and spectrum change are studied. Note that this study is performed before the selection optimisation, thus small differences are expected in the final result. But because the FSR is

only added to the leading pair, whose selection is not changed, the effect due to a different selection is assumed to be negligible.

The performance of the tool for a low mass Higgs (125 GeV) and high mass Higgs (200 GeV) after all analysis cuts have been applied, is checked. Figure 7.1 shows the invariant mass before and after adding the FSR candidates, and the contamination from muon ionisation and UE events are small with the configuration of the selection. The ratio of $m_{4\mu\gamma}/m_{4\mu}$ is shown in figure 7.2 in each mass bin; a significant reduction of the invariant mass tails by up to 40% is observed, while at the pole mass of the resonance a moderate increase at the level of 7% is seen. The same test is done with a high mass Higgs sample, $m_H = 200$ GeV, as presented in figure 7.3 and 7.4. As both Z are on-shell, the effect of FSR is more pronounced, a 40% reduction of the tail and a 10% in the peak are seen.

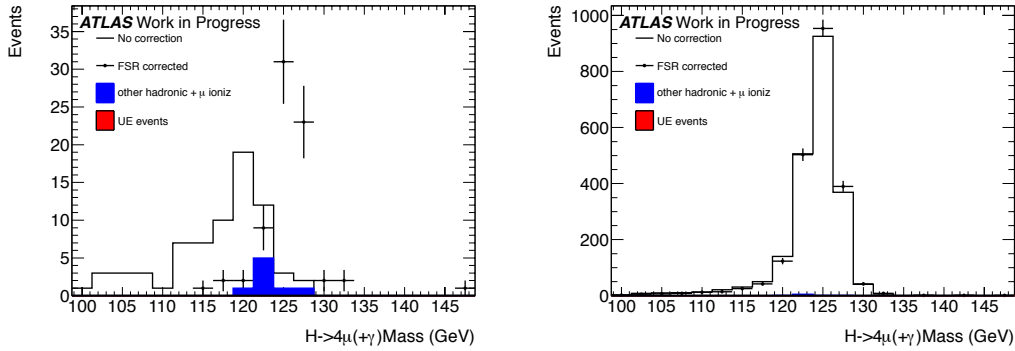


Figure 7.1: $H(125) \rightarrow 4\mu + \gamma$ invariant mass for FSR corrected events only (left) and for all events (right), after all analysis cuts have been applied.

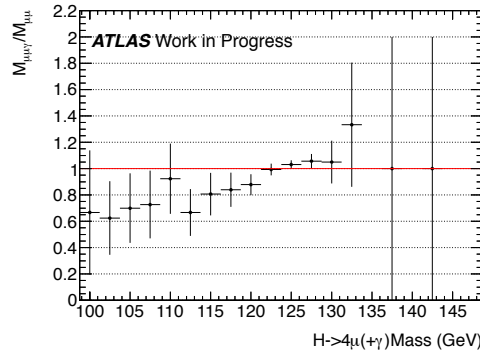


Figure 7.2: Ratio of $M_{H(125) \rightarrow 4\mu + \gamma} / M_{H(125) \rightarrow 4\mu}$ histograms to show the relative reduction of the tails and the increase of the bulk of the invariant mass after the addition of FSR photons.

The effects of the FSR addition to the background in the $H \rightarrow 4\ell$ analysis has also been studied. The main goal here is to examine whether any significant increase of the reducible and irreducible backgrounds is observed, given that the addition of FSR moves events to slightly higher 4ℓ invariant masses. In figure 7.5, the effect of the FSR on the

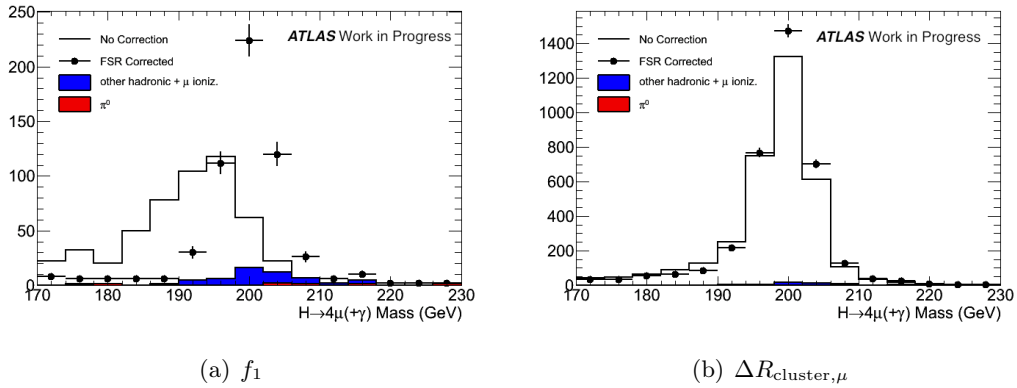


Figure 7.3: $H(200) \rightarrow 4\mu + \gamma$ invariant mass for FSR corrected events only (left) and for all events (right), after all analysis cuts have been applied.

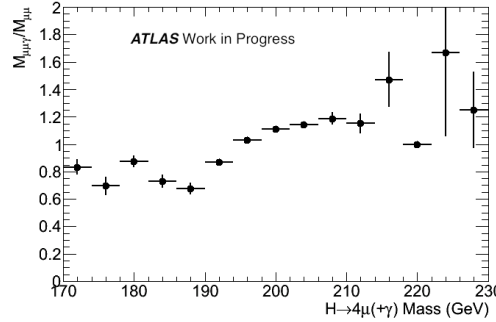


Figure 7.4: Ratio of $M_{H(200) \rightarrow 4\mu + \gamma} / M_{H(200) \rightarrow 4\mu}$ histograms to show the relative reduction of tails and increase of the bulk of the invariant mass after the addition of FSR photons.

$ZZ^{(*)}$ background is shown after all the analysis cuts. Based on these results, no increase on this background is seen. The effects on $Zb\bar{b}$ and $t\bar{t}$ backgrounds are also studied, similar results hold and the main conclusion is that no increase of any of the backgrounds is observed.

To investigate the overall effect of FSR on the mass scale, adding FSR in various ways is tested to compare the changes relative to the default selection. Figure 7.6 (a) shows the reconstructed 4μ mass of the $m_H = 125$ GeV MC sample of the events that pass the final selection. A 2-sigma Gaussian fit is performed to determine the mean value and resolution of the spectrum. Figure 7.6 (b) shows the mass after adding the reconstructed FSR selected by the tool; the resolution is compatible with the original one, while the central value moves 44 MeV towards the injected Higgs mass. Such a small effect is expected, as the rate of FSR identified by the tool is small. To estimate the maximum impact of FSR photons, instead of adding those selected by the tool, FSR photons at the generator level are added to the reconstructed mass as shown in 7.6 (c). As no E_T threshold is imposed on the photon, and this result is not affected by the tool efficiency, the overall effect is more dramatic: the resolution improves by 8% and a 300 MeV shift to the true mass is observed. This

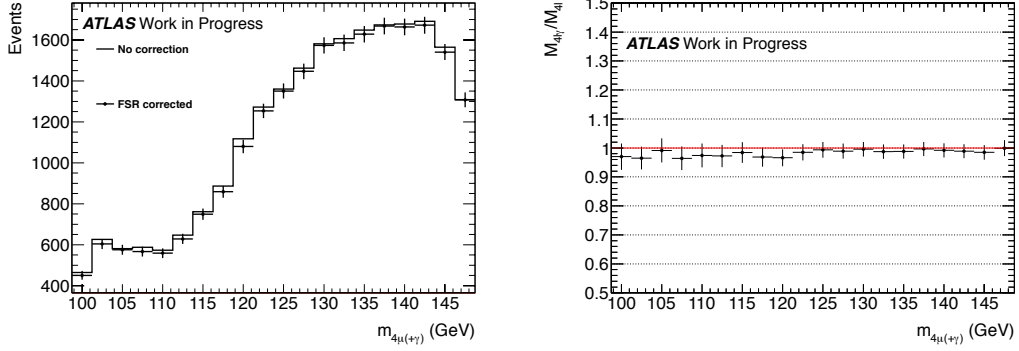


Figure 7.5: $ZZ^{(*)} \rightarrow 4\mu + \gamma$ invariant mass of background events before and after FSR addition after all analysis cuts have been applied (left). The relative change of the invariant mass after the FSR addition (right) shows that there is no increase in the $ZZ^{(*)}$ background.

is compatible with the mass resolution of the events without generated FSR photons, as shown in 7.6 (d).

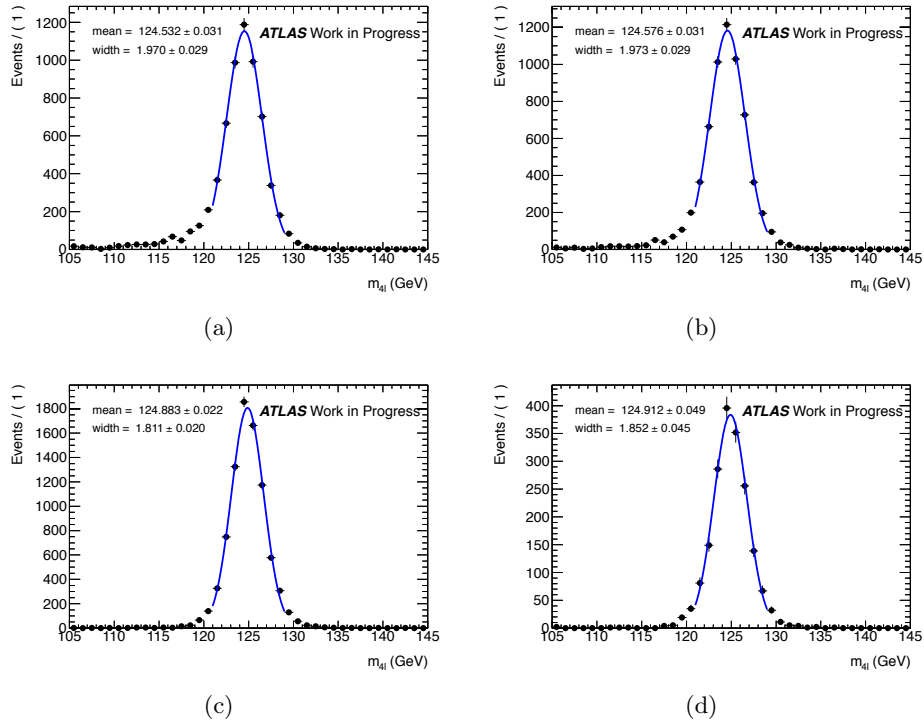


Figure 7.6: $H \rightarrow ZZ^{(*)} \rightarrow 4\mu$ invariant mass after all analysis cuts have been applied. a) contains all the events, b) adding the selected reconstructed FSR c) adding all generator level FSR d) contains only events without FSR at generator level.

To investigate the effect on the data candidates, the events having at least one FSR photon among the muons, after all selection criteria are applied on 13 fb^{-1} of 2012 and 4.6 fb^{-1} of 2011 data, are given in tables 7.2 and 7.3. Most of the events are in the high

mass region as expected. One extra candidate event in the $2\mu 2e$ final state was found in the low mass region not present in the standard analysis, where its reconstructed invariant mass moved from 109 GeV to 123 GeV when adding an FSR photon.

type	RunNumber	EventNumber	$m_{4\ell}$	$m_{4\ell}^{fsr}$	m_{12}	m_{12}^{fsr}	m_{34}	m_{34}^{fsr}
4μ	203353	26647061	242.54	268.89	91.53	91.53	86.98	104.33
4μ	203636	34504484	337.53	342.66	88.57	90.58	86.26	86.26
4μ	204564	149682166	281.83	290.63	88.34	91.55	86.99	86.99
4μ	204763	64671324	220.33	307.22	93.95	93.95	61.55	91.34
4μ	205112	58173349	319.11	391.50	100.19	100.19	74.51	93.87
$2\mu 2e$	203258	114413312	185.53	194.08	88.12	96.71	95.26	95.26
$2\mu 2e$	203680	10638148	175.39	187.68	84.76	98.62	79.99	79.99
$2\mu 2e$	209161	96479632	109.03	123.62	71.63	84.02	34.89	34.89
$2e 2\mu$	204474	89082513	184.28	201.38	95.22	95.22	78.48	96.30
$2e 2\mu$	205112	25095415	168.15	182.99	89.44	89.44	71.57	84.99
$2e 2\mu$	206409	74123032	239.91	258.15	85.04	85.04	66.61	95.50
$2e 2\mu$	207664	85286083	290.99	328.82	88.20	88.20	78.48	90.59
$2e 2\mu$	207865	91045473	169.91	180.73	90.20	90.20	66.85	75.09
$2e 2\mu$	208354	118769851	307.48	337.40	95.39	95.39	81.39	92.23

Table 7.2: The list of the candidates with at least one FSR photon found in 2012 data.

type	RunNumber	EventNumber	$m_{4\ell}$	$m_{4\ell}^{fsr}$	m_{12}	m_{12}^{fsr}	m_{34}	m_{34}^{fsr}
$2\mu 2e$	191218	1072214	250.59	261.12	93.23	98.54	87.07	87.07

Table 7.3: The list of the candidates with at least one FSR photon found in 2011 data.

The impact of lowering the transverse energy threshold from 3.5 GeV to 1 GeV when selecting the FSR photons is also investigated, by searching for topo-clusters with $E_T > 1$ GeV. The left plot of figure 7.7 from ref. [33] shows the correlation between the discriminant variables used in the FSR selection namely f_1 and ΔR . The events include the FSR photons and the background coming from the muon ionisation and from hadrons in a $Z \rightarrow \mu\mu$ MC sample. The same distribution is produced for the 2012 data, the ZZ MC background and the 125 GeV MC signal events passing all standard analysis cuts as shown on the right plot of figure 7.7. The population of the data (shown as dots) in the "FSR signal region" of $f_1 > 0.1$ comes from candidate events in the high mass region (> 180 GeV). The red dot represents one candidate event in the low mass $120 \text{ GeV} < m_H < 130 \text{ GeV}$ region and we observe that it is on the edge of the FSR signal and the hadronic background regions.

The FSR is added at the end of the selection in the updated analysis of 20.7 fb^{-1} of 2012 data. New optimisation is adjusted to cope with the increased pileup present in the data. The low transverse energy FSR candidates are also used to improve the correction. The topo-clusters with $1.0 < E_T < 3.5$ GeV are added to the standard electron/photon

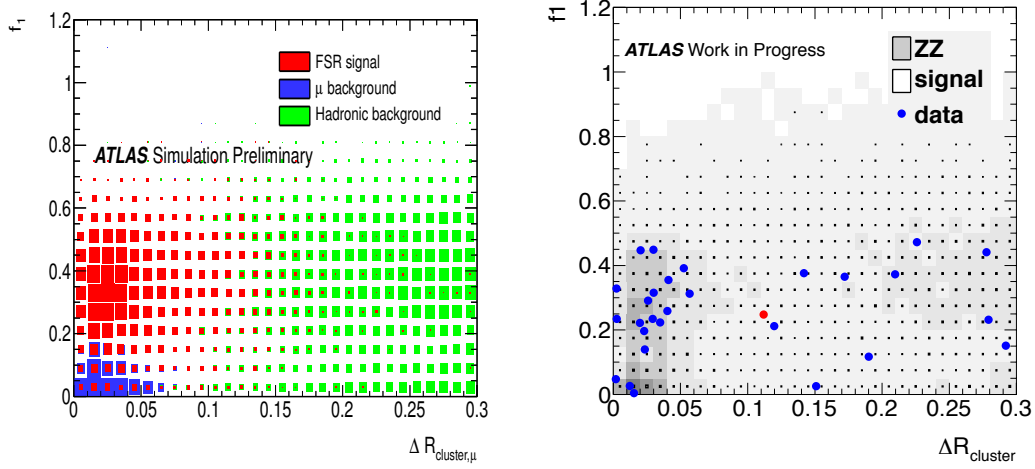


Figure 7.7: Left: Correlation between the discriminant variables f_1 and ΔR for FSR photons and background from muon ionisation and hadrons in a $Z \rightarrow \mu\mu$ MC sample. Right: a population in FSR signal region comes from high mass region. The red dot on the right plot is from $120 \text{ GeV} < m_H < 130 \text{ GeV}$ $H \rightarrow 4\mu$ candidate, and sits on the edge of the FSR signal and hadronic background regions.

candidates. To suppress backgrounds, a stricter cut of $f_1 > 0.2$ is applied. Only the leading di-muon pairs which have invariant mass between 66 and 89 GeV are considered for FSR candidates, and the correction is turned off if $m_{\mu\mu\gamma} > 100 \text{ GeV}$. The average efficiency of this correction is 70%, and the purity is 85%, where the fakes come from pileup and muon ionisation.

7.3 Background Estimation

As in the previous analysis, the level of the irreducible ZZ^* background is estimated using MC simulations normalised to the theoretical cross section, while the rate and composition of the reducible $\ell\ell$ +jets and $t\bar{t}$ background processes are evaluated with data-driven methods. The data-driven methods are similar to the ones used in the discovery analysis, with the following refinement:

$\ell\ell + \mu\mu$ background The $\ell\ell + \mu\mu$ reducible background arises from $t\bar{t}$ and $Z + \text{jets}$, where the $Z + \text{jets}$ component has a heavy quark $Zb\bar{b}$ part and another from π/K in-flight decays. In the previous analysis, only $Zb\bar{b}$ is considered for establishing the control region of enhanced $b\bar{b}$. In the optimised analysis, the π/K in-flight decays contribution is also studied in another control region where the track isolation requirement for the sub-leading lepton pair is reverted. The same method is used to estimate the overall number of $Z + \text{jets}$, by fitting the m_{12} distribution where the $t\bar{t}$ and $Z + \text{jets}$ shapes are well separated. The residual number of events from a Z boson mass fit after removing the $Z + b\bar{b}$ estimate previously obtained is interpreted as a π/K in-flight decay contribution. The π/K in-flight

decay contributes $\sim 20\%$ to the $Z + \text{jets}$ background. The m_{12} distributions for events selected by the analysis when removing the isolation and impact parameter requirements for the sub-leading di-lepton in this channel are presented in Figure 7.8 (a). The shape and normalisation of the backgrounds are in good agreement with data.

$\ell\ell + ee$ background A sample of reconstruction-level objects identified as electron candidates will contain true isolated electrons, electrons from heavy flavour semi-leptonic decays (Q), electrons from photon conversion (γ) or light jets mis-reconstructed as electrons and denoted as fake electrons (f). The contribution from each category is estimated in a control region by relaxing the electron selection criteria for the electrons of the sub-leading pair. The efficiency of the extrapolation of the background yield in each category from the control region to the signal region is obtained from MC. In the previous analysis, these efficiencies were independent of the electron kinematics, which has been checked in the optimisation and proved to have a sizeable effect. Thus p_T, η dependent transfer factors are used in the new analysis. Also, as a cross check, the control region composed of same-sign sub-leading electron pairs is used to perform the same estimation, in order to remove the ZZ contamination. The m_{12} distributions for events without isolation and impact parameter requirements for the sub-leading di-lepton in this channel are presented in Figure 7.8 (b).

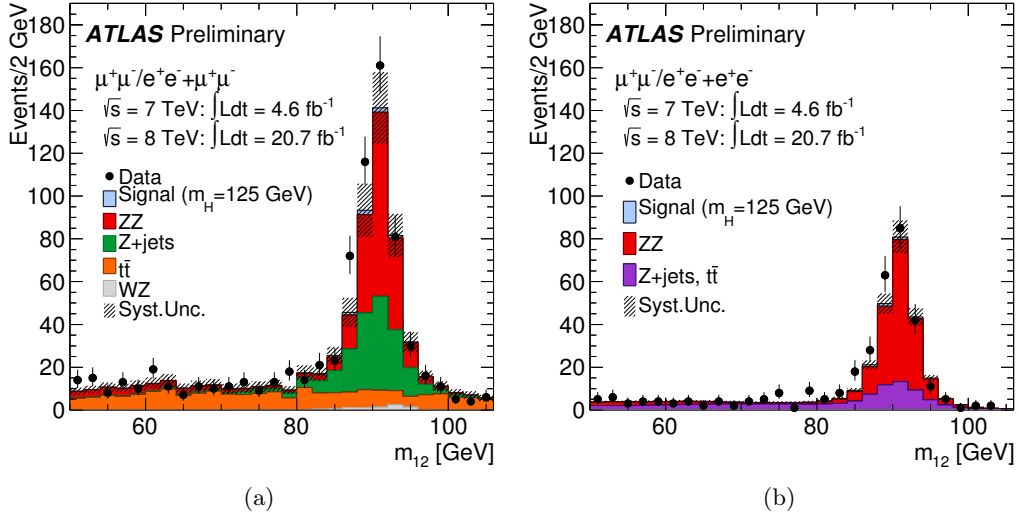


Figure 7.8: Invariant mass distributions of the lepton pairs in the control sample defined by a Z boson candidate and an additional same-flavour lepton pair, for the $\sqrt{s} = 8 \text{ TeV}$ and $\sqrt{s} = 7 \text{ TeV}$ data combined. In (a) and (b) the m_{12} distributions are presented for $\ell\ell + \mu\mu$ and $\ell\ell + ee$ events. Isolation and impact parameter significance requirements are applied to the first lepton pair only. The MC is normalised to the data-driven background estimations.

7.4 Results

Table 7.4 presents the observed and expected events, in a window of ± 5 GeV around a 125 GeV hypothesized Higgs boson mass, for the 20.7 fb^{-1} at $\sqrt{s} = 8 \text{ TeV}$ and the 4.6 fb^{-1} at $\sqrt{s} = 7 \text{ TeV}$ data sets as well as their combination. The FSR correction has affected seven of the 225 events with a leading muon pair, with one event in the 120 to 130 GeV mass window. Relative to Ref. [112], the $ZZ^{(*)}$ background has been reduced by $\sim 15\%$ in the 4μ and $4e$ modes due to the changes in the kinematic selection, and the overall S/B has improved from 1.2 to 1.5, in part due to the improved electron identification.

Table 7.4: The number of expected signal for the $m_H=125 \text{ GeV}$ hypothesis and background events together with the number of observed events, in a window of $\pm 5 \text{ GeV}$ around 125 GeV for 20.7 fb^{-1} at $\sqrt{s} = 8 \text{ TeV}$ and 4.6 fb^{-1} at $\sqrt{s} = 7 \text{ TeV}$ as well as for their combination.

$\sqrt{s} = 8 \text{ TeV}$							
	total signal	signal (in window)	$ZZ^{(*)}$	$Z + \text{jets}, t\bar{t}$	S/B	expected	observed
4μ	5.8 ± 0.7	5.3 ± 0.7	2.3 ± 0.1	0.50 ± 0.13	1.9	8.1 ± 0.9	11
$2\mu 2e$	3.0 ± 0.4	2.6 ± 0.4	1.2 ± 0.1	1.01 ± 0.21	1.2	4.8 ± 0.7	4
$2e 2\mu$	4.0 ± 0.5	3.4 ± 0.4	1.7 ± 0.1	0.51 ± 0.16	1.5	5.6 ± 0.7	6
$4e$	2.9 ± 0.4	2.3 ± 0.3	1.0 ± 0.1	0.62 ± 0.16	1.4	3.9 ± 0.6	6
total	15.7 ± 2.0	13.7 ± 1.8	6.2 ± 0.4	2.62 ± 0.34	1.6	22.5 ± 2.9	27
$\sqrt{s} = 7 \text{ TeV}$							
4μ	1.0 ± 0.1	0.97 ± 0.13	0.49 ± 0.02	0.05 ± 0.02	1.8	1.5 ± 0.2	2
$2\mu 2e$	0.4 ± 0.1	0.39 ± 0.05	0.21 ± 0.02	0.55 ± 0.12	0.5	1.0 ± 0.1	1
$2e 2\mu$	0.7 ± 0.1	0.57 ± 0.08	0.33 ± 0.02	0.04 ± 0.01	1.6	0.9 ± 0.1	2
$4e$	0.4 ± 0.1	0.29 ± 0.04	0.15 ± 0.01	0.49 ± 0.12	0.5	0.9 ± 0.1	0
total	2.5 ± 0.4	2.2 ± 0.3	1.17 ± 0.07	1.12 ± 0.17	1.0	4.3 ± 0.5	5
$\sqrt{s} = 8 \text{ TeV}$ and $\sqrt{s} = 7 \text{ TeV}$							
4μ	6.8 ± 0.8	6.3 ± 0.8	2.8 ± 0.1	0.55 ± 0.15	1.9	9.6 ± 1.0	13
$2\mu 2e$	3.4 ± 0.5	3.0 ± 0.4	1.4 ± 0.1	1.56 ± 0.33	1.0	6.0 ± 0.8	5
$2e 2\mu$	4.7 ± 0.6	4.0 ± 0.5	2.1 ± 0.1	0.55 ± 0.17	1.6	6.6 ± 0.8	8
$4e$	3.3 ± 0.5	2.6 ± 0.4	1.2 ± 0.1	1.11 ± 0.28	1.2	4.8 ± 0.8	6
total	18.2 ± 2.4	15.9 ± 2.1	7.4 ± 0.4	3.74 ± 0.93	1.6	27.0 ± 3.4	32

The expected $m_{4\ell}$ distributions for the total background and one signal hypothesis are compared to the combined $\sqrt{s} = 8 \text{ TeV}$ and $\sqrt{s} = 7 \text{ TeV}$ data in Fig. 7.9(a) for the low mass range 80–170 GeV, and in Fig. 7.9(b) for the full 80–900 GeV mass range.

Upper limits are set on the Higgs boson production cross section at 95% CL, using the CLs modified frequentist formalism [89] with the profile likelihood ratio test statistic [90]. The test statistic is evaluated using a maximum-likelihood fit of signal and background models to the observed $m_{4\ell}$ distribution. Figure 7.10 shows the observed and expected 95% CL cross section upper limits, as a function of m_H , for the combined $\sqrt{s} = 8 \text{ TeV}$ and $\sqrt{s} = 7 \text{ TeV}$ data sets. The expected exclusion range for the SM Higgs boson is from

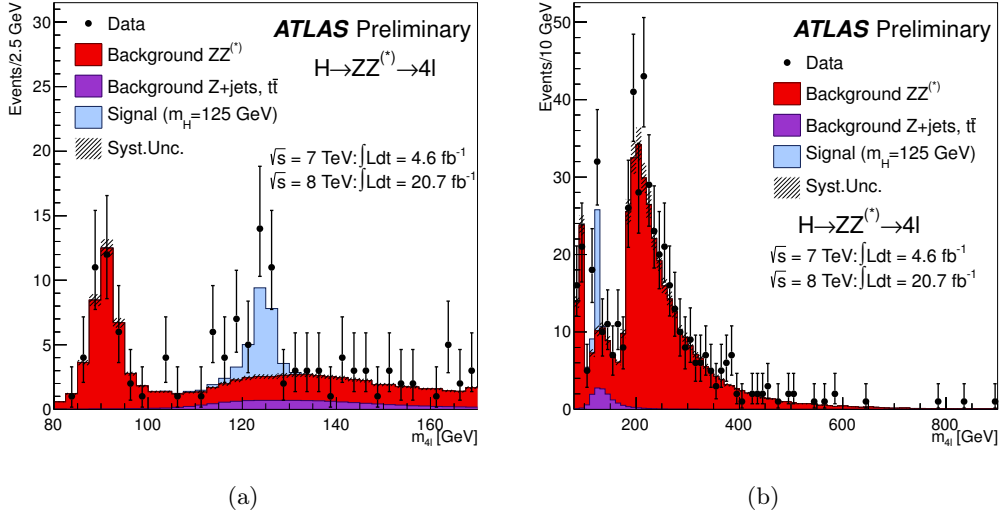
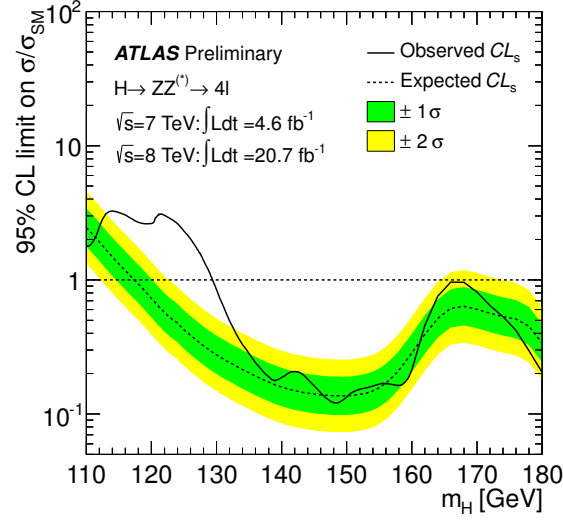


Figure 7.9: The distribution of the four-lepton invariant mass, $m_{4\ell}$, for the selected candidates compared to the background expectation for the combined $\sqrt{s} = 8$ TeV and $\sqrt{s} = 7$ TeV data sets in the low mass range (a) 80 – 170 GeV and the full mass range (b) 80 – 900 GeV. The signal expectation for the $m_H=125$ GeV hypothesis is also shown. The resolution of the reconstructed Higgs boson mass is dominated by detector resolution at low m_H values and by the Higgs boson width at high m_H .

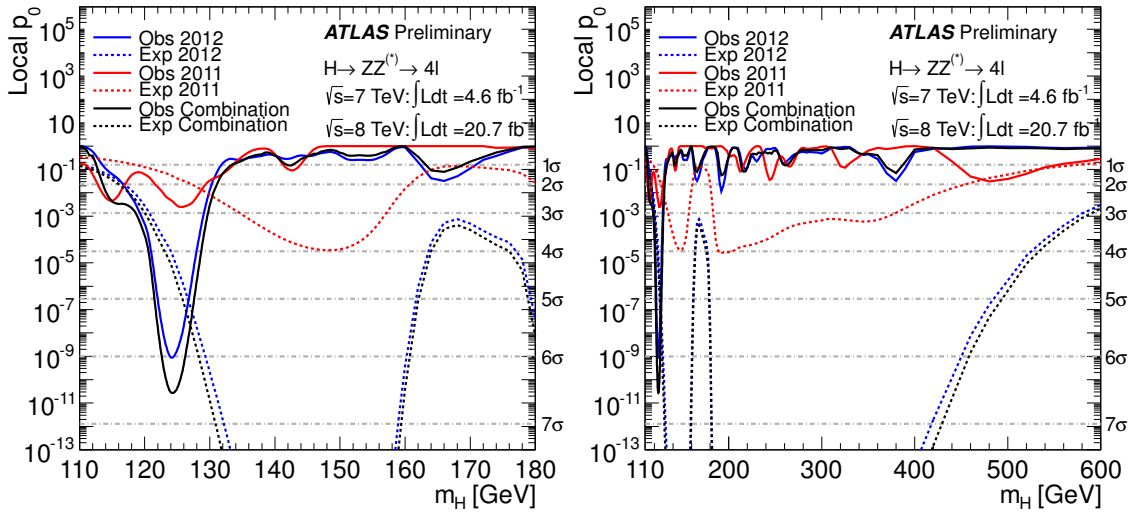
118 GeV to 600 GeV. However, a weaker observed exclusion is obtained in the low mass region due to a significant excess of events: the observed exclusion region starts from around 130 GeV.

The significance of an excess is given by the probability, p_0 , that a background-only experiment is more signal-like in terms of the test statistic than the observed data. In Fig. 7.11 the local p_0 , obtained using the asymptotic approximation of Ref. [90], is presented as a function of the m_H hypothesis for the combination of $\sqrt{s} = 8$ and $\sqrt{s} = 7$ TeV data samples. Results for each of the 7 TeV and 8 TeV datasets are also given separately in Fig. 7.11. Figure 7.12(a) shows the profile likelihood as a function of m_H for the combined 2011 and 2012 data samples. The profile likelihood is shown both with (solid curve) the mass scale systematics from electrons MSS(e) and muons MSS(μ) and without MSS(e) and MSS(μ) (dashed curve). Figure 7.12(b) shows the corresponding profile likelihood as a function of m_H for the four channels. The value of the fitted mass from the profile likelihood is $m_H = 124.3^{+0.6}_{-0.5}$ (stat) $^{+0.5}_{-0.3}$ (syst) GeV, where the systematic uncertainty is dominated by the energy and momentum scale uncertainties. The three channels, 4μ , $2e2\mu$ and $4e$, which predominately contribute to the overall fitted mass value agree well as can be seen in Fig. 7.12(b) where the likelihood curves cross approximately at the 1σ level ($-2\ln\Lambda = 1$). The global signal strength factor μ acts as a scale factor on the total number of events predicted by the Standard Model for each of the Higgs boson signal processes. In Fig. 7.13(a) μ is presented as a function of m_H for the combination of the



(a)

Figure 7.10: The expected (dashed) and observed (full line) 95% CL upper limits on the Standard Model Higgs boson production cross section as a function of m_H in the low mass region, divided by the expected SM Higgs boson cross section, for the combination of the $\sqrt{s} = 7$ TeV and $\sqrt{s} = 8$ TeV data samples. The dark (green) and light (yellow) bands indicate the expected limits with $\pm 1\sigma$ and $\pm 2\sigma$ fluctuations, respectively.



(a)

(b)

Figure 7.11: The observed local p_0 for the combination of the 2011 and 2012 data sets (solid black line); the $\sqrt{s} = 7$ TeV and $\sqrt{s} = 8$ TeV data results are shown in solid lines (blue and red, respectively). The dashed curves show the expected median local p_0 for the signal hypothesis when tested at the corresponding m_H . The horizontal dashed lines indicate the p_0 values corresponding to local significances of 1σ , 2σ , 3σ and 4σ .

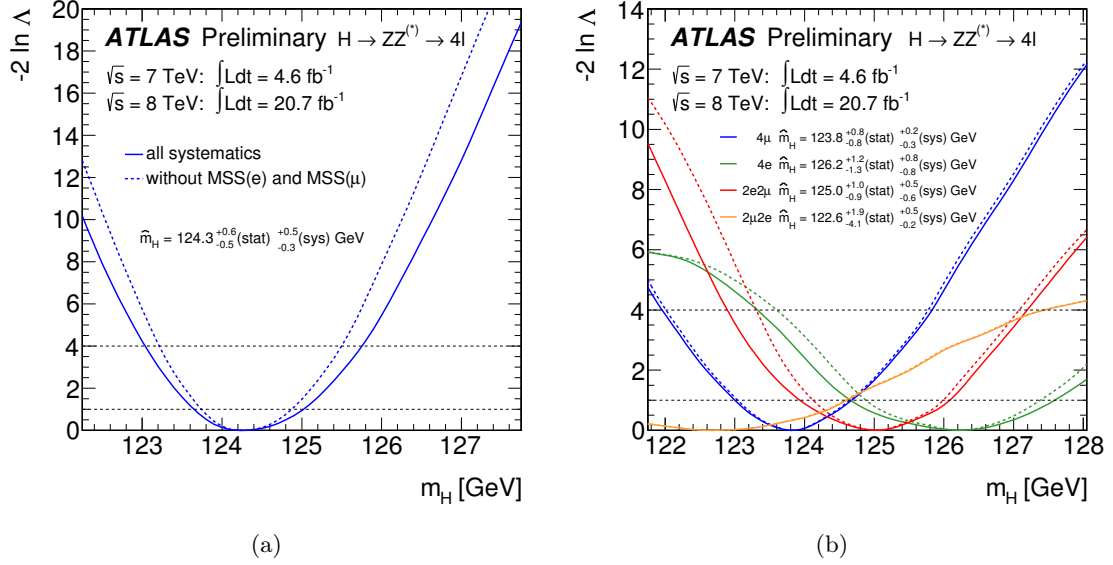


Figure 7.12: (a) The profile likelihood as a function of m_H for the 2011 and 2012 combined data samples, and (b) the profile likelihood as a function of m_H for the individual channels for the $\sqrt{s} = 8$ TeV data sample. The profile likelihoods are shown both with (solid) the mass scale systematics from electrons (MSS(e)) and from muons (MSS(μ)) and without (dashed), i.e. with the corresponding nuisance parameters fixed to their best fit values. The 68% CL uncertainty is determined by the points where the profile likelihood curve crosses 1.

two data samples. The corresponding result in the case where a SM Higgs boson signal of $m_H = 125$ GeV is added to the simulated background events is shown in Fig. 7.13(b). The fitted signal strength divided by the expected SM rate is denoted by μ . The bands illustrate the μ interval of the test statistic $-2 \ln \lambda(\mu) < 1$, where λ is the profile likelihood ratio, and represents an approximate $\pm 1\sigma$ variation.

Figure 7.14(a) presents the best μ and m_H fit values and the profile likelihood ratio contours that, in the asymptotic limit, would correspond to 68% and 95% confidence levels, again shown both with (dark dashed curve) MSS(e) and MSS(μ) and without (lighter dashed curve). The value of the signal strength μ at the best fit for m_H (125 GeV) is $1.7^{+0.5}_{-0.4}$. For a value of $m_H = 125.5$ GeV, $\mu = 1.5 \pm 0.4$.

7.5 4μ invariant mass error

As seen from the previous section, the accumulated data in ATLAS makes the mass measurement of the Higgs boson feasible. Intrinsically, each reconstructed mass has an uncertainty which comes from the leptons due to the finite detector resolution. The resolution is not constant and depends on the region traversed by the leptons. Assigning the correct uncertainty to each event thus is essential to provide an accurate mass estimation. Given

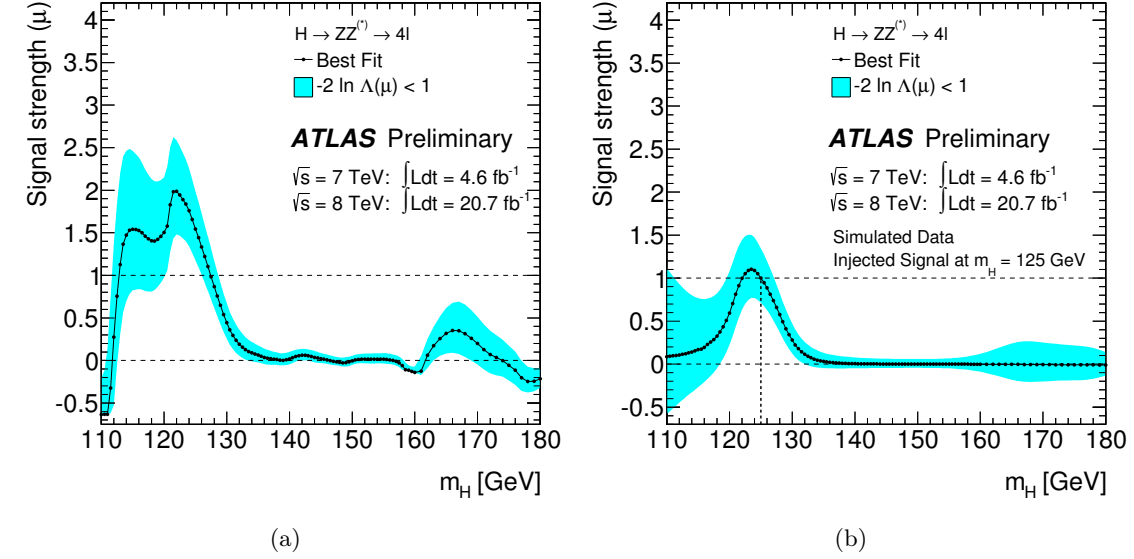


Figure 7.13: (a) The signal strength parameter $\mu = \sigma/\sigma_{SM}$ obtained from a fit to the data is presented for the combined fit to the 2011 and 2012 data samples. (b) The signal strength μ is shown as a function of m_H when a simulated SM Higgs boson signal with $m_H = 125 \text{ GeV}$ is injected onto simulated backgrounds.

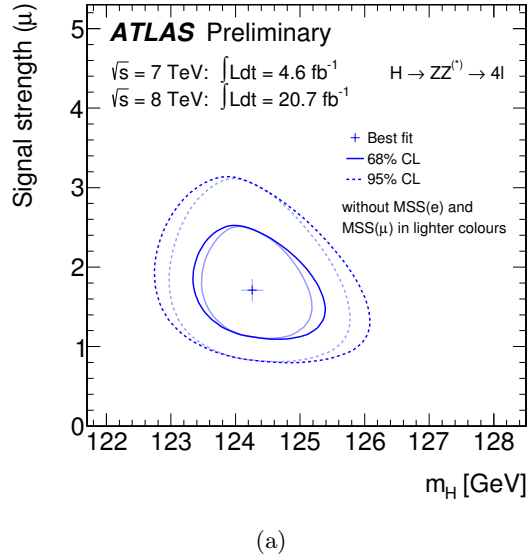


Figure 7.14: (a) Likelihood ratio contours in the μ , m_H plane that, in the asymptotic limit, correspond to 68% and 95% level contours, again shown with (dark dashed) and without (lighter dashed) MSS(e) and MSS(μ).

that the mass measurement is mostly driven by the 4μ channel, an attempt to calculate the per event mass error based on the muon momentum resolution is performed. In the analysis, the mass error is calculated through the four lepton covariance matrix. More

specifically, in the 4μ final state, the 5×5 track covariance matrices of each muon is converted into the (p_x, p_y, p_z, E) representation, which is a 4×4 matrix. Then the error of the invariant mass of this four body decay is computed as the following:

$$\begin{aligned}
 J &= \left(\frac{\partial m}{\partial p_{x1}}, \frac{\partial m}{\partial p_{y1}}, \frac{\partial m}{\partial p_{z1}}, \frac{\partial m}{\partial p_{E1}}, \dots, \frac{\partial m}{\partial p_{x4}}, \frac{\partial m}{\partial p_{y4}}, \frac{\partial m}{\partial p_{z4}}, \frac{\partial m}{\partial p_{E4}} \right) \\
 C_{comb} &= \begin{pmatrix} C_1 & & & \\ & C_2 & & \\ & & C_3 & \\ & & & C_4 \end{pmatrix} \\
 \sigma_m^2 &= J \cdot C_{comb} \cdot J^T
 \end{aligned} \tag{7.1}$$

where the $C_{1,2,3,4}$ are the error matrix of the leptons.

As an alternative, a study starting with the estimation of the muon momentum resolution based on the reconstructed momentum will be introduced in section 7.5.1. The estimation is then validated on $Z \rightarrow \mu\mu$ MC, by reproducing the momentum spectrum and Z boson invariant mass, which will be shown in section 7.5.2. The 4μ mass error is calculated by analytically propagating the error of each muon to the mass. This will be introduced in section 7.5.3. The estimated uncertainty on the Higgs mass will be shown as well.

7.5.1 Muon momentum resolution

All the types of muons used in the $H \rightarrow ZZ^{(*)} \rightarrow 4\ell$ analysis are studied for the single muon resolution estimation. This means that the momentum measurements are either obtained from ID (tagged muons and calo muons), or from MS (standalone muons), or the combination of the two (combined muons). As introduced in section 2.2.3, the resolution of an ID measurement can be expressed as:

$$\frac{\sigma_{ID}}{p_T} = p_1^{ID} \oplus p_2^{ID} p_T, \tag{7.2}$$

where the multiple scattering is reflected in the first term and the intrinsic resolution contributes to the second term. Correspondingly, the MS measurement resolution can be expressed as

$$\frac{\sigma_{MS}}{p_T} = \frac{p_0^{MS}}{p_T} \oplus p_1^{MS} \oplus p_2^{MS} p_T, \tag{7.3}$$

where p_0^{MS} , p_1^{MS} and p_2^{MS} are related respectively to the energy loss in the calorimeter, multiple scattering and intrinsic resolution. The combined muon resolution is a statistical

combination of the two resolutions, following the formula

$$\sigma_{CB} = \frac{\sqrt{2}\sigma_{ID}\sigma_{MS}}{\sqrt{\sigma_{MS}^2 + \sigma_{ID}^2}}. \quad (7.4)$$

As the resolution is commonly expressed in terms of p_0 , p_1 and p_2 in the above cases, the overall resolution of all types of muons is approximated as

$$\frac{\sigma}{p_T} = \frac{p_0}{p_T} + p_1 + p_2 p_T. \quad (7.5)$$

In other words, the muon resolution will be assumed to have a Gaussian distribution of width σ . The parameters p_0 , p_1 and p_2 differ in the various pseudo-rapidity ranges and are obtained by fitting the resolution distributions. The ZZ MC sample is used to provide the muon resolution distribution, the muons being selected with the same criteria as in the $H \rightarrow ZZ^{(*)} \rightarrow 4\ell$ analysis. The resolution is defined as $(p_T^{reco} - p_T^{truth})/p_T^{reco}$, where the p_T^{reco} is the reconstructed p_T and p_T^{truth} is the generated muon p_T . The distribution is then divided into the following regions, according to the different geometry in ID and MS.

- $0 < |\eta| < 0.1$, the $\eta \sim 0$ crack region,
- $0.1 < |\eta| < 1.05$, the barrel region,
- $1.05 < |\eta| < 1.3$, the barrel region where the EE chambers are missing,
- $1.3 < |\eta| < 1.7$, the transition region,
- $1.7 < |\eta| < 2.0$, the end-cap region,
- $2.0 < |\eta| < 2.5$, CSC region, no TRT coverage.

The resolution distributions are fitted with Gaussians in intervals of p_T of 2 GeV. The means and widths of the Gaussian obtained from the fit are plotted as a function of the mean p_T in the interval, as shown in Figure 7.15 and Figure 7.16. As seen from the figures, the resolutions in different η regions exhibit very different characteristic. In general, the resolution is small in the barrel region and relatively larger in the end-cap region. The intrinsic resolution plays a more important role in the transition region than in the other regions, as reflected in the steeper slope. The σ and the mean of the Gaussian dependency on p_T are then fitted with the equation 7.4. The fitted parameters p_0 , p_1 and p_2 are shown in the plots.

The choice of the regions only depends on η for the moment, but there can be also dependency on ϕ , considering the geometry in the MS. Due to the different radial layout and material presence, one would expect different resolutions in small and large sections. Moreover, the special chamber layout in the feet region where barrel toroid supports are located and in the rail region where the calorimeter module supports are located causes

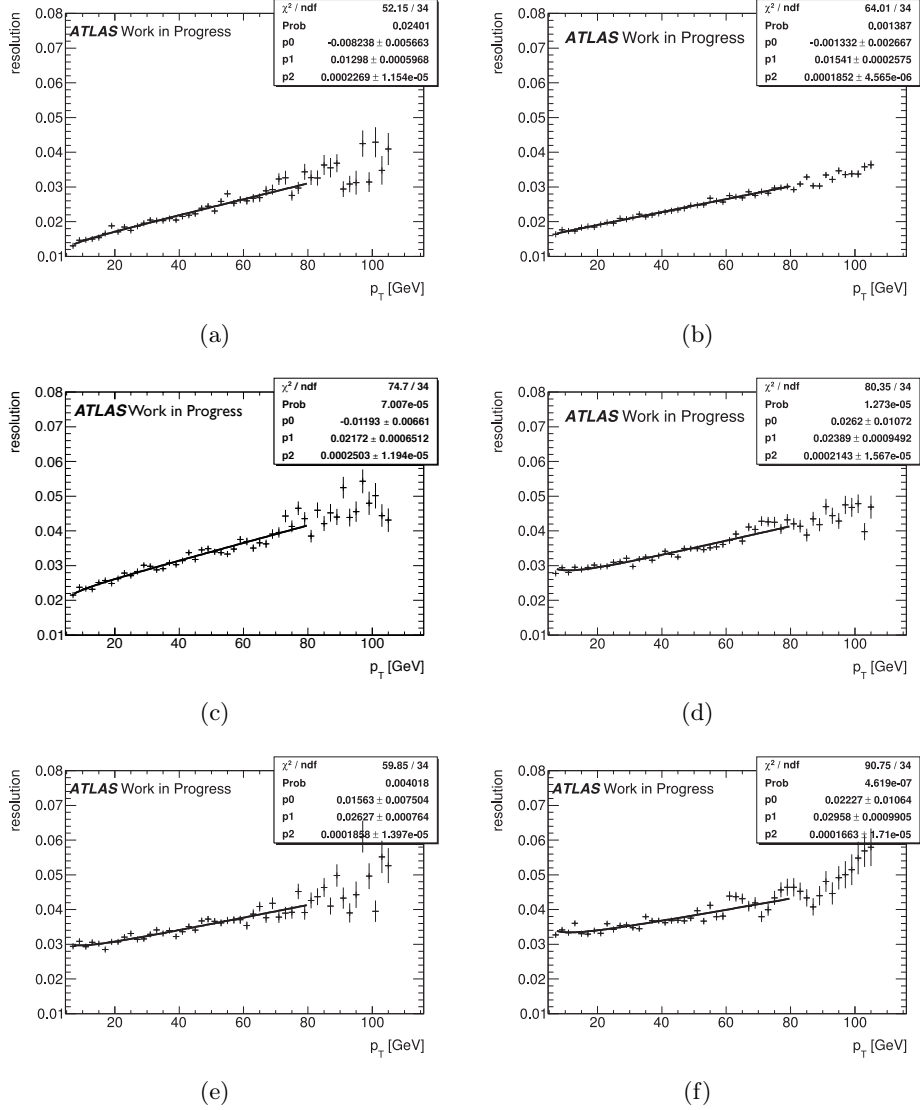


Figure 7.15: The Gaussian width of the resolution distribution as a function of p_T in region (a) $0 < |\eta| < 0.1$, (b) $0.1 < |\eta| < 1.05$, (c) $1.05 < |\eta| < 1.3$, (d) $1.3 < |\eta| < 1.7$, (e) $1.7 < |\eta| < 2.0$, (f) $2.0 < |\eta| < 2.5$. A fit is performed in each region, using the approximation $\frac{p_0}{p_T} + p_1 + p_2 p_T$, the parameters obtained from the fit are shown in the plots.

different resolutions too. Figure 7.17 shows the resolution distribution in the large, small, feet and rail regions, respectively. The feet region clearly has the worse resolution, and the intrinsic resolutions differ between the four types as seen in the slopes. Therefore, the momentum resolutions are estimated both in slices of η and ϕ .

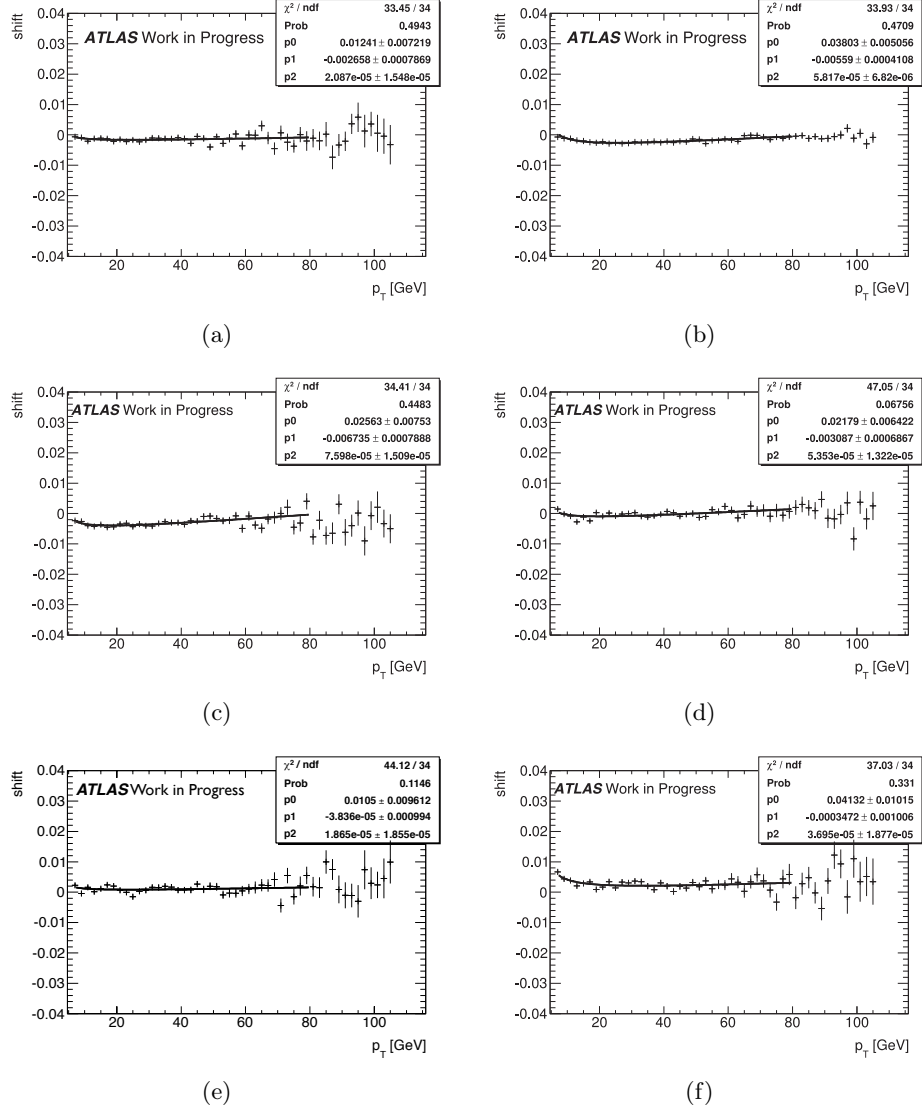


Figure 7.16: The Gaussian mean value of the resolution distribution as a function of p_T in region (a) $0 < |\eta| < 0.1$, (b) $0.1 < |\eta| < 1.05$, (c) $1.05 < |\eta| < 1.3$, (d) $1.3 < |\eta| < 1.7$, (e) $1.7 < |\eta| < 2.0$, (f) $2.0 < |\eta| < 2.5$. A fit is performed in each region, using the approximation $\frac{p_0}{p_T} + p_1 + p_2 p_T$, the parameters obtained from the fit are shown in the plots.

7.5.2 Muon momentum resolution validation

By using the parameters p_0 , p_1 and p_2 obtained by the above procedure, one can calculate the resolution of any muon. These parameters need to be validated first, in the sense that the calculated resolution does not deviate from the real one. This can be tested by assigning the calculated resolution to the generated momentum of the muons. If the reconstructed momentum spectrum can be reproduced, then the parameters will be validated as describing the resolution well.

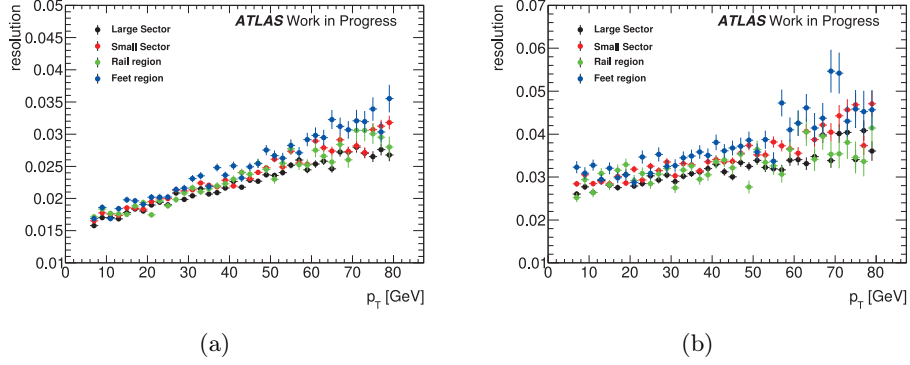


Figure 7.17: The Gaussian width in large, small, feet and rail regions as a function of p_T in (a) $0.1 < |\eta| < 1.05$ (b) $1.05 < |\eta| < 1.3$.

The validation is performed with a $Z \rightarrow \mu\mu$ MC sample. For each MC event, two muons are selected as in the $H \rightarrow ZZ^{(*)} \rightarrow 4\ell$ analysis, and the generated transverse momentum of each muon is known. Depending on the η and ϕ of the muon, the resolution is calculated using the corresponding p_0 , p_1 and p_2 . A "pseudo smearing" procedure is then performed. The estimated resolution is multiplied by a random number following a Gaussian distribution, and added to the generated p_T . The value obtained will be treated as the "toy" p_T , and compared to the reconstructed value. Figure 7.18 (a) shows the distribution of the p_T spectrum of the selected muons, in red the toy p_T and in black the reconstructed p_T . The two distributions agree very well, which is also reflected in the mean and RMS value of the distributions. The invariant mass of the two muons, using the reconstructed p_T and the toy p_T , are compared in Figure 7.18 (b). The two distributions agree very well with each other, which proves the validity of the resolution calculation.

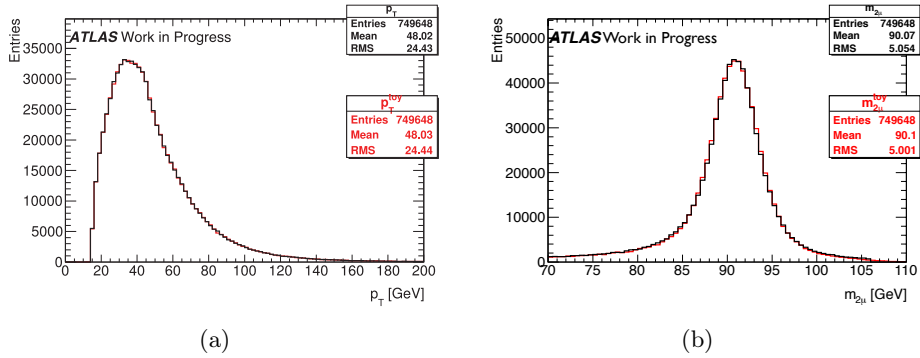


Figure 7.18: Using the parameterised resolution function, the muon "toy" p_T spectrum (a) and di-muon invariant mass (b) are compared with the reconstructed p_T and mass.

To further check the parameters defining the resolution, the *pull* is defined as $(p_T^{reco} - p_T^{truth})/resolution$. If the resolution correctly reflects the uncertainty in the p_T measurement, the distribution will be a Gaussian centred at 0 with a width of 1. As Figure 7.19 (a) shows,

after fitting the pull distribution, the Gaussian has a width of 0.957, which indicates that the parameterised function describes the resolution within an error of 4.3%. As a comparison, the resolution that only depends on η is also checked, and the pull distribution is shown in Figure 7.19 (b). The width of the Gaussian illustrates that, by using the ϕ information, the overall accuracy improves by 1.6%.

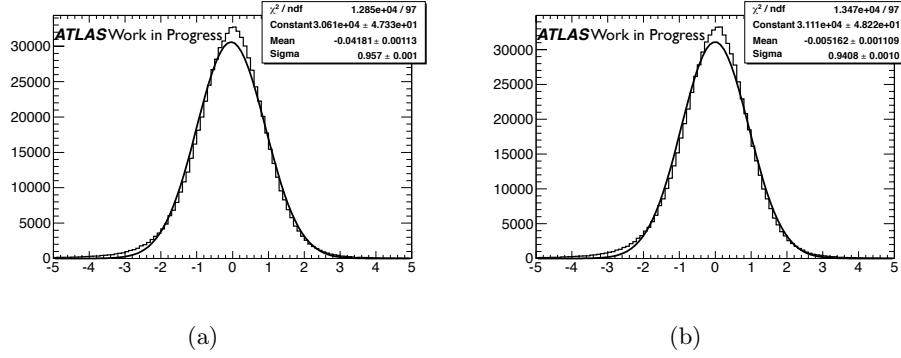


Figure 7.19: The pull distribution of p_T using the parameterised p_T uncertainty which is dependant on (a) η and ϕ , (b) η only.

There are various ways to estimate the uncertainty of the p_T measurement, the method described above is one of them. One can also use the covariant matrix of the basic measurement parameters (d_0 , z_0 , q/p , θ , ϕ) to derive the uncertainty. This is also the standard procedure adopted in the $H \rightarrow ZZ^{(*)} \rightarrow 4\ell$ analysis. The correlation between the resolution obtained from the two methods are shown in Figure 7.20. A good correlation is seen, and most of the entries are seen in the $\sigma_{p_T} < 5$ region. Figure 7.20 (b) shows the zoomed correlation in the region, where the linear correlation is evident. In general, the uncertainty estimated with the parameterisation is larger than the one obtained with the matrix.

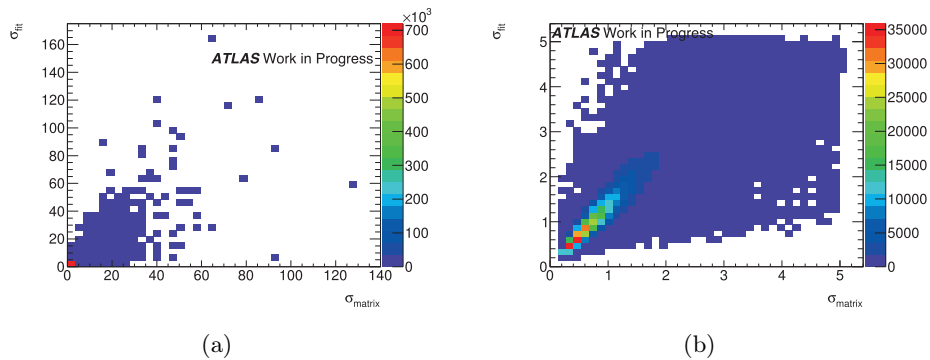


Figure 7.20: The p_T uncertainty correlation between the method based on the parameterisation and the covariance matrix method, in (a) the full range, (b) zoomed region where entries are below 5. A linear correlation is observed.

7.5.3 Muon resolution and 4μ mass error

The per muon p_T uncertainty validated above is then used to derive the overall uncertainty of the 4μ mass. The derivation uses the following formula

$$\sigma_m = \sqrt{\sum_{i=0}^4 \left(\frac{\sigma_i}{\sin\theta_i P_i} \sum_{j \neq i} P_i P_j \right)^2} \quad (7.6)$$

where the σ_i denotes the uncertainty of the i^{th} muon p_T , P_i denotes the 4-momentum of the i^{th} muon. The mass error is estimated with the ZZ MC sample. The selected events pass all the $H \rightarrow ZZ^{(*)} \rightarrow 4\ell$ analysis criteria. Repeating the toy procedure explained in section 7.5.2, the invariant mass obtained from the toy and the reconstructed mass are compared in Figure 7.21 (a). As seen from the plot, the invariant mass is well reproduced. Then the pull of the mass is defined as $(m_{4\mu}^{reco} - m_{4\mu}^{truth})/\sigma_m$, where $m_{4\mu}^{reco}$ and $m_{4\mu}^{truth}$ are the reconstructed and generated 4μ invariant mass, and σ_m is calculated with Equation 7.6. As seen in Figure 7.21 (b), the pull distribution is Gaussian, with mean value around 0 and width 1.003. This means that the mass uncertainty is well modelled.

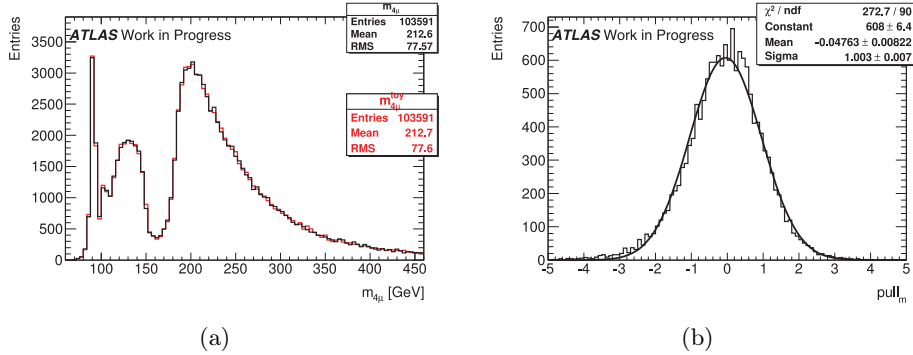


Figure 7.21: (a) The 4μ invariant mass distribution obtained from the toy compared to the reconstructed one, (b) the pull distribution of the invariant mass of ZZ MC sample.

The test is also performed on the signal sample, where $m_H = 125$ GeV. Figure 7.22 (a) and (b) show the invariant mass and the pull distribution, respectively. Similar to the ZZ case, the uncertainty is well modelled, as illustrated by the well reproduced invariant mass and the Gaussian distribution of the pull.

The estimation of the mass uncertainty is then performed with the data. Table 7.5 shows the mass uncertainty of each candidate selected in the 4μ final state in the range $120 < m_H < 130$, using 20.7 fb^{-1} TeV data. The mass uncertainty of a 125 GeV Higgs is therefore around 2 GeV. As a reference, the uncertainty obtained from the covariant matrix is shown. The resolutions that are solely η dependent and η, ϕ dependent are compared as well. Overall agreement in the three methods is obtained within the statistical uncertainty.

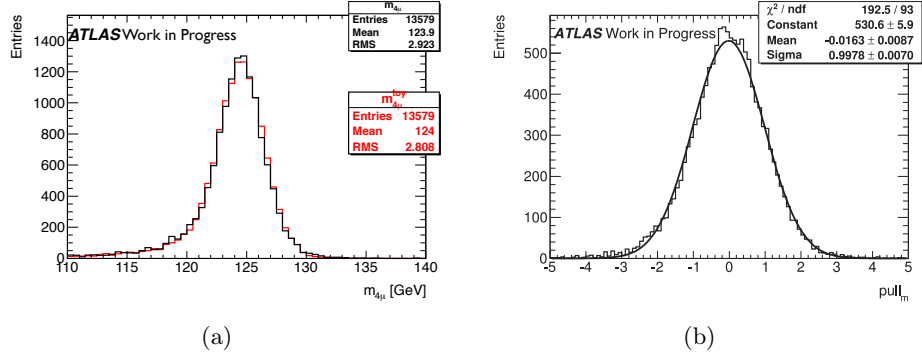


Figure 7.22: (a) The 4μ invariant mass distribution of the toy compared to the reconstructed one, (b) the pull distribution of the invariant mass of the signal $m_H = 125$ GeV MC sample.

$m_{4\mu}$ [GeV]	$\sigma(m_{4\mu})$ (covariance matrix) [GeV]	$\sigma(m_{4\mu})$ (η dependent parameterisation) [GeV]	$\sigma(m_{4\mu})$ (η, ϕ dependent parameterisation) [GeV]
124.355	2.107	1.846 ± 0.044	1.882 ± 0.082
123.327	1.304	1.424 ± 0.021	1.392 ± 0.037
123.840	2.491	2.170 ± 0.077	2.005 ± 0.074
129.173	2.096	2.027 ± 0.062	1.920 ± 0.068
123.188	2.110	2.683 ± 0.100	2.848 ± 0.143
129.634	1.829	2.044 ± 0.056	1.986 ± 0.087
126.935	2.194	2.189 ± 0.052	2.276 ± 0.129
122.804	2.154	2.533 ± 0.088	2.349 ± 0.126
124.619	2.557	2.286 ± 0.078	2.476 ± 0.150
123.648	2.026	1.983 ± 0.049	2.085 ± 0.095
124.058	1.507	1.479 ± 0.036	1.477 ± 0.063
120.933	2.082	2.082 ± 0.067	2.215 ± 0.129

Table 7.5: The estimated uncertainty on the 4μ invariant mass of the candidates found in 8 TeV 20.7 fb $^{-1}$ data, in the range $120 < m_H < 130$ GeV.

7.6 Higgs production search in VBF and VH modes and Spin-Parity measurement

7.6.1 Higgs production search in VBF and VH modes

To separately measure the cross sections for the ggF, VBF, and VH production mechanisms, each $H \rightarrow 4\ell$ candidate selected with the criteria described above is assigned to one of three categories (VBF-like, VH-like, or ggF-like), depending on its characteristics. The VBF-like category is defined by events with two forward jets in opposite hemispheres. The VBF kinematic requirements for jets are $p_T > 25$ (30) GeV for $|\eta| < 2.5$ ($2.5 < |\eta| < 4.5$). The

two highest p_T jets are required to be separated by more than 3 units in pseudo-rapidity and have an invariant mass greater than 350 GeV. Events which do not satisfy the VBF-like criteria are tested to be VH-like. Events are classified as VH-like if there is a lepton (e or μ), in addition to the four leptons forming the Higgs candidate, with $p_T > 10$ GeV and satisfying the same lepton requirements. Events which are not classified as VBF-like nor VH-like fall into the ggF-like category.

Applying the categorisation criteria to the selected four lepton candidates, eight VBF-like candidates and one VH-like candidate are selected. One VBF-like candidate is found in a window of ± 5 GeV around 125 GeV. Its reconstructed invariant mass is 123.5 GeV. In this mass window, 0.76 ± 0.15 events are expected for a SM Higgs boson with 60% VBF purity and a signal-to-background ratio of about 5, after profiling the nuisance parameters. Above 160 GeV, there are six VBF-like candidates in agreement with 4.0 ± 1.4 events expected from $ZZ^{(*)}$ production. The one observed VH candidate has a mass of 270 GeV, to be compared with 0.9 ± 0.3 $ZZ^{(*)}$ events expected.

7.6.2 Spin-Parity measurement

Two independent methods are developed to perform the spin-parity analysis on events selected in the main analysis between $115 < m_H < 130$ GeV. Six hypotheses for spin/parity states are tested, namely J^P 0^+ , 0^- , 1^+ , 1^- , 2^+ , 2^- . One method uses a boosted decision tree (BDT) in a multivariate analysis. The other one uses the theoretical differential decay rate for the angles, m_{12} and m_{34} , corrected for detector acceptance and analysis selection, to construct a likelihood ratio base on matrix elements (MELA) [113] as a discriminant between the different spin-parity hypotheses.

Both the BDT and J^P -MELA approaches show similar results. MC pseudo-experiment studies show that the results from the two methods are consistent, taking into account the limited statistics and the fact that the two methods are not fully correlated. The results of these two different analyses both support the conclusion that the SM expectation of $J^P = 0^+$ is clearly preferred. The alternative spin and parity hypotheses are excluded assuming purely ggF production, at the following CLs confidence levels for the J^P -MELA (BDT) analysis: 99.7% (97.8%) for 0^- , 99.5% (99.8%) for 1^+ , 97.0% (93.9%) for 1^- , and 81.8% (83.1%) for 2_m^+ .

7.7 Summary

Updated search results for the newly observed Higgs-like particle have been presented, using 4.8 fb^{-1} of data at $\sqrt{s} = 7 \text{ TeV}$ and 20.7 fb^{-1} at $\sqrt{s} = 8 \text{ TeV}$ recorded by the ATLAS detector. An excess of events above background is seen with the smallest p_0 of 2.7×10^{-11} (6.6 standard deviations) appearing at $m_H = 124.3 \text{ GeV}$. The fitted mass is $m_H = 124.3_{-0.5}^{+0.6} (\text{stat})_{-0.3}^{+0.5} (\text{syst}) \text{ GeV}$, and the signal strength (the ratio of the observed

cross-section to the expected SM cross-section) of the Higgs-like particle at this mass is found to be $1.7^{+0.5}_{-0.4}$.

For the first time the $H \rightarrow ZZ^{(*)} \rightarrow 4\ell$ candidate events have been categorised, allowing the study Higgs couplings via ggF/ttH and VBF/VH production. A VBF-like candidate has been found at 123.5 GeV, where approximately 0.5 events is expected with S/B around 1 if one includes ggF Higgs production as background.

Finally, an updated analysis of the spin and parity of the new particle has been briefly presented. Hypothesis tests comparing the SM $0^+ J^P$ hypothesis with 0^- , 1^+ , 1^- , 2_m^+ and 2^- have been performed, assuming purely ggF production. The SM spin and parity 0^+ remain the favoured hypotheses over the 0^- , 1^+ , 1^- , and 2^+ states, while remaining inconclusive for the 2^- comparison.

Conclusion

The ATLAS detector at the LHC is composed of multiple sub-systems which allow particle identification and accurate momentum and energy measurements. Analysis of the collision data, no matter which physics process is concerned, rely on the quality of these measurements.

From the perspective of hardware construction, the muon measurement depends on how well the position of the detection element is known. The study of the MDT chambers has shown that, several μm deviation of the wire pitch can cause a sagitta deviation of $60 \mu m$, which exceeds the expected resolution. In addition, this affects the muon trajectory reconstruction. X-ray tomography scan provides the actual position of the wires, which once included in the geometry database of the detector, will improve the reconstruction quality.

From the perspective of on-line object reconstruction, the algorithms can be optimised to further improve the performance. The proposed optimisation of the muon term in the missing transverse energy, which fully considers the conditions and quality of the reconstruction process for muons, improves the MET measurement. For the reconstruction of muons, extending the pseudo-rapidity region such that combined muons use ID tracklets improves the impact parameter and the momentum measurement without increasing the fake rate.

As an important process in the Standard Model, the $Z \rightarrow \mu\mu$ decay is essential for measuring the Z boson mass and decaying cross section, and is also the major background in many searches. The FSR impact on the Z mass spectrum is studied both by simulation and with data. With the threshold at 3 GeV, it is found that $\sim 2\%$ of the muons radiate FSR photons. The impact is larger when the FSR photon energy is smaller. For data, a dedicated FSR tool is used to select candidates, and to reduce fake FSR photons; a set of requirements is imposed based on the performance of the tool. In the case of a FSR photon, the reconstructed $\mu\mu$ mass has been shown to be distorted, as well as the resolution degraded. Thus the FSR tool is proposed to be used in analyses related to $Z \rightarrow \mu\mu$. In addition, the FSR degrades the muon isolation performance, a new variable where the contribution from the FSR is subtracted is proposed and validated.

The search of $H \rightarrow ZZ^{(*)} \rightarrow 4\ell$ is presented. The analysis is optimised for the low Higgs mass, and the leptons considered are electrons and muons. The main background

comes from the continuum $ZZ^{(*)}$, which is irreducible and estimated from the simulation. The reducible background $Zb\bar{b}$ and $t\bar{t}$ in the $Z + \mu\mu$ final state and the $Z + jet$ in the $Z + ee$ final state are estimated from data, using various data-driven methods. It has been shown that the backgrounds are well understood in the control regions enriched with background events. Using these background estimations and taking into account the systematic uncertainties, the final exclusion limits are derived. Using 4.8 fb^{-1} 7 TeV data and 5.8 fb^{-1} 8 TeV data, and combining with results from other search channels, we claim the discovery of a new particle whose mass is around 126.5 GeV and whose properties are compatible with a Standard Model scalar boson.

With more data collected at 8 TeV, $\sim 20.7 \text{ fb}^{-1}$, the analysis in the $H \rightarrow ZZ^{(*)} \rightarrow 4\ell$ is updated with some changes in the selection, including the additional FSR photons in the final mass. A 6.6σ excess above the background at the mass $m_H = 124.3 \text{ GeV}$ is seen. The measurement of the new particle mass is estimated to be $m_H = 124.3_{-0.5}^{+0.6} \text{ (stat)}_{-0.3}^{+0.5} \text{ (syst)} \text{ GeV}$, and the signal strength (the ratio of the observed cross-section to the expected SM cross-section) of the Higgs-like particle at this mass is found to be $1.7_{-0.4}^{+0.5}$. The events are also categorised according to the production mechanism, ggF or VBF; a VBF-like candidate has been found at 123.5 GeV. The spin and parity of the new particle has been analysed and favours 0^+ , which is compatible with the particle being the SM scalar boson.

The LHC has provided a huge quantity of data since its first physics run in 2009. It has been operating below its design capacity of 14 TeV. To reach its full potential, a "Long Shutdown 1" (LS1) has begun on 14 February, 2013. During these two years of shutdown, a consolidation of the accelerator will be in process, as well as the upgrade of the detectors. After that, the LHC will re-start operation at the design energy, producing more data for the physics analyses. This will benefit the Higgs boson studies, including the mass measurement, spin-parity and coupling properties.

Bibliography

- [1] M. R.E. and S. E. C. G, *Chirality Invariance and the Universal Fermi Interaction*, Phys. Rev. 109, 1860 (1958) .
- [2] *The LEP Electroweak Working Group*, <http://lepewwg.web.cern.ch/LEPEWWG/>.
- [3] Particle Data Group Collaboration, J. B. et al., *Review of particle physics*, Phys. Rev. D86, 010001 (2012) .
- [4] A. Djouadi, *The Anatomy of electro-weak symmetry breaking. I: The Higgs boson in the standard model*, Phys. Rept. **457** (2008) 1–216, [arXiv:0503172](https://arxiv.org/abs/0503172) [hep-ph].
- [5] LEP Working Group for Higgs boson searches Collaboration, R. Barate et al., *Search for the standard model Higgs boson at LEP*, Phys. Lett. **B565** (2003) 61–75, [arXiv:0306033](https://arxiv.org/abs/0306033) [hep-ex].
- [6] CDF and D0 Collaborations Collaboration, *Combined CDF and D0 Upper Limits on Standard Model Higgs Boson Production with up to 8.6 fb^{-1} of Data*, [arXiv:0901.0512](https://arxiv.org/abs/0901.0512) [hep-ex].
- [7] The TEVNPH Working Group, CDF and D0 Collaborations Collaboration, *Updated Combination of CDF and D0 Searches for Standard Model Higgs Boson Production with up to 10.0 fb^{-1} of Data*, [arXiv:1207.0449](https://arxiv.org/abs/1207.0449) [hep-ex].
- [8] The LEP Electroweak Working Group Collaboration.
<http://lepewwg.web.cern.ch/LEPEWWG/plots/winter2012/>.
- [9] GFitter group Collaboration. <http://gfitter.desy.de/Files/>.
- [10] LHC Higgs Cross Section Working Group, S. Dittmaier, C. Mariotti, G. Passarino, and R. Tanaka (Eds.), *Handbook of LHC Higgs Cross Sections: 1. Inclusive Observables*, CERN-2011-002 (CERN, Geneva, 2011) , [arXiv:1101.0593](https://arxiv.org/abs/1101.0593) [hep-ph].
- [11] LHC Higgs Cross Section Working Group, S. Dittmaier, C. Mariotti, G. Passarino, and R. Tanaka (Eds.), *Handbook of LHC Higgs Cross Sections: 2. Differential Distributions*, CERN-2012-002 (CERN, Geneva, 2012) , [arXiv:1201.3084](https://arxiv.org/abs/1201.3084) [hep-ph].
- [12] LHC Higgs Cross Section Working Group Collaboration.
<https://twiki.cern.ch/twiki/bin/view/LHCPhysics/CrossSections>.
- [13] L. Evans and P. Bryant, *LHC Machine*, JINST **3** (2008) S08001.
- [14] ATLAS Collaboration, G. Aad et al., *The ATLAS Experiment at the CERN Large Hadron Collider*, JINST **3** (2008) S08003.

- [15] *ATLAS: Detector and physics performance technical design report.*, vol. 1. CERN-LHCC-99-14, 1999.
- [16] ATLAS Collaboration, G. Aad et al., *Expected Performance of the ATLAS Experiment - Detector, Trigger and Physics*. 2009. [arXiv:0901.0512 \[hep-ex\]](#).
- [17] T. A. Collaboration, *Improved electron reconstruction in ATLAS using the Gaussian Sum Filter-based model for bremsstrahlung*, ATLAS-CONF-2012-047 (2012) .
- [18] M. C. P. W. Group, *Pile-up Dependence of the ATLAS Muon Performance*, ATL-COM-PHYS-2011-1640 (CERN, Geneva, 2011) .
- [19] D. et al., *THE HIGH-PRECISION X-RAY TOMOGRAPH FOR QUALITY CONTROL. OF THE ATLAS MDT MUON SPECTROMETER*, CERN-OPEN-97-023 (July 1997) .
- [20] M. J. Woudstra, *Precision of the ATLAS muon spectrometer*, CERN-THESIS-2003-015 .
- [21] *ATLAS muon spectrometer: Technical Design Report*. CERN, Geneva, 1997.
- [22] W. Andreazza, *The ATLAS Muon Chamber Quality Control with the X-Ray Tomograph at CERN*, Nuclear Science Symposium Conference Record, 2001 IEEE **2** 914 – 918.
- [23] S. e. a. Schuh, *Long-term geometry stability of ATLAS MDT chambers studied with a high-precision X-ray tomograph*, Nuclear Science Symposium Conference Record, 2005 IEEE **2** 1024 – 1028.
- [24] <http://muondoc.home.cern.ch/muondoc/Software/DetectorDescription/>.
- [25] F. Bauer, *MDT deformations and as-built parameter Sagitta contribution*, <http://indico.cern.ch/conferenceDisplay.py?confId=76104>.
- [26] P.-F. Giraud, *Muon alignment 2012*, <http://indico.cern.ch/conferenceDisplay.py?confId=188904>.
- [27] P. Kluit, *MS - ID z misalignments in Barrel and Endcap and “telescoping” effect*, <http://indico.cern.ch/conferenceDisplay.py?confId=205224>.
- [28] W. L. et al., *Calorimeter clustering algorithms: Description and performance*, ATL-LARG-PUB-2008-002 (2008) .
- [29] A. Collaboration, *Properties of Jets and Inputs to Jet Reconstruction and Calibration with the ATLAS Detector Using Proton-Proton Collisions at 7 TeV*, ATLAS-CONF-2010-053 (2010) .

- [30] A. Collaboration, *Electron and photon reconstruction and identification in ATLAS: expected performance at high energy and results at 900 GeV*, ATLAS-CONF-2010-005 .
- [31] A. Collaboration, *Jet energy scale and its systematic uncertainty in proton-proton collisions at $\sqrt{s} = 7$ TeV in ATLAS 2010 data*, ATLAS-CONF-2011-032 .
- [32] A. Collaboration, *E_T^{miss} Studies for the $H \rightarrow W^+W^-\ell\nu\ell\nu$ Search*, ATL-COM-PHYS-2011-1757 .
- [33] A. Collaborations, *Reconstruction of collinear final-state-radiation photons in Z decays to muons in $\sqrt{s} = 7$ TeV proton-proton collisions*, .
- [34] T. Sjostrand, S. Mrenna, and P. Z. Skands, *PYTHIA 6.4 Physics and Manual*, JHEP **05** (2006) 026, [arXiv:hep-ph/0603175](#).
- [35] P. N. S. Frixione and C. Oleari, *Matching NLO QCD computations with Parton Shower simulations: the POWHEG method*, JHEP **11** **070** (2007) .
- [36] *PHOTOS Monte Carlo: a precision tool for QED corrections in Z and W decays*, Eur. Phys. J. **C45** (2006) 97.
- [37] S. Agostinelli et al., *GEANT4: A simulation toolkit*, Nucl. Instrum. Meth. **A** **506** (2003) 250–303.
- [38] ATLAS Collaboration, *Muon Momentum Resolution in First Pass Reconstruction of pp Collision Data Recorded by ATLAS in 2010*, 2011. ATLAS-COM-CONF-2011-003.
- [39] T. A. Collaboration, *Search for the Standard Model Higgs boson in the decay channel $H \rightarrow ZZ^{(*)} \rightarrow 4\ell$ with 4.8 fb^{-1} of pp collision data at $\sqrt{s} = 7$ TeV with ATLAS*, Phys.Lett. B710 (2012) 383–402 (2012) .
- [40] ATLAS Collaboration, ATLAS Collaboration, *The ATLAS simulation Infrastructure*, Eur. Phys. J. **C** **70** (2010) 823–874, [arXiv:1005.4568 \[physics.ins-det\]](#).
- [41] S. Alioli, P. Nason, C. Oleari, and E. Re, *NLO Higgs boson production via gluon fusion matched with shower in POWHEG*, JHEP **04** (2009) 002, [arXiv:0812.0578 \[hep-ph\]](#).
- [42] P. Nason and C. Oleari, *NLO Higgs boson production via vector-boson fusion matched with shower in POWHEG*, JHEP **02** (2010) 037, [arXiv:0911.5299 \[hep-ph\]](#).

- [43] D. de Florian, G. Ferrera, M. Grazzini, and D. Tommasini, *Transverse-momentum resummation: Higgs boson production at the Tevatron and the LHC*, JHEP **11** (2011) 064, [arXiv:1109.2109 \[hep-ph\]](#).
- [44] P. Golonka and Z. Was, *PHOTOS Monte Carlo: A Precision tool for QED corrections in Z and W decays*, Eur. Phys. J. **C 45** (2006) 97–107, [arXiv:hep-ph/0506026](#).
- [45] S. Jadach, Z. Was, R. Decker, and J. H. Kuhn, *The tau decay library TAUOLA: Version 2.4*, Comput. Phys. Commun. **76** (1993) 361–380.
- [46] P. Golonka et al., *The tauola-photos-F environment for the TAUOLA and PHOTOS packages, release II*, Comput. Phys. Commun. **174** (2006) 818–835.
- [47] A. Djouadi, M. Spira, and P. M. Zerwas, *Production of Higgs bosons in proton colliders: QCD corrections*, Phys. Lett. **B 264** (1991) 440–446.
- [48] S. Dawson, *Radiative corrections to Higgs boson production*, Nucl. Phys. **B 359** (1991) 283–300.
- [49] M. Spira, A. Djouadi, D. Graudenz, and P. M. Zerwas, *Higgs boson production at the LHC*, Nucl. Phys. **B 453** (1995) 17–82, [arXiv:hep-ph/9504378](#).
- [50] R. V. Harlander and W. B. Kilgore, *Next-to-next-to-leading order Higgs production at hadron colliders*, Phys. Rev. Lett. **88** (2002) 201801, [arXiv:hep-ph/0201206](#).
- [51] C. Anastasiou and K. Melnikov, *Higgs boson production at hadron colliders in NNLO QCD*, Nucl. Phys. **B 646** (2002) 220–256, [arXiv:hep-ph/0207004](#).
- [52] V. Ravindran, J. Smith, and W. L. van Neerven, *NNLO corrections to the total cross section for Higgs boson production in hadron hadron collisions*, Nucl. Phys. **B 665** (2003) 325–366, [arXiv:hep-ph/0302135](#).
- [53] S. Catani, D. de Florian, M. Grazzini, and P. Nason, *Soft-gluon resummation for Higgs boson production at hadron colliders*, JHEP **07** (2003) 028, [arXiv:hep-ph/0306211](#).
- [54] U. Aglietti, R. Bonciani, G. Degrossi, and A. Vicini, *Two-loop light fermion contribution to Higgs production and decays*, Phys. Lett. **B 595** (2004) 432–441, [arXiv:hep-ph/0404071](#).
- [55] S. Actis, G. Passarino, C. Sturm, and S. Uccirati, *NLO Electroweak Corrections to Higgs Boson Production at Hadron Colliders*, Phys. Lett. **B 670** (2008) 12–17, [arXiv:0809.1301 \[hep-ph\]](#).

- [56] D. de Florian and M. Grazzini, *Higgs production at the LHC: updated cross sections at $\sqrt{s} = 8$ TeV*, [arXiv:1206.4133 \[hep-ph\]](#).
- [57] C. Anastasiou, S. Buehler, F. Herzog, and A. Lazopoulos, *Inclusive Higgs boson cross-section for the LHC at 8 TeV*, JHEP **1204** (2012) 004, [arXiv:1202.3638 \[hep-ph\]](#).
- [58] J. Baglio and A. Djouadi, *Higgs production at the LHC*, JHEP **03** (2011) 055.
- [59] M. Botje et al., *The PDF4LHC working group interim recommendations*, 2011. [arXiv:1101.0538 \[hep-ph\]](#).
- [60] H.-L. Lai et al., *New parton distributions for collider physics*, Phys. Rev. **D 82** (2010) 074024, [arXiv:1007.2241 \[hep-ph\]](#).
- [61] A. D. Martin, W. J. Stirling, R. S. Thorne, and G. Watt, *Parton distributions for the LHC*, Eur. Phys. J. **C 63** (2009) 189–285, [arXiv:0901.0002 \[hep-ph\]](#).
- [62] R. D. Ball et al., *Impact of heavy quark masses on parton distributions and LHC phenomenology*, Nucl. Phys. **B 849** (2011) 296–363, [arXiv:1101.1300 \[hep-ph\]](#).
- [63] M. Ciccolini, A. Denner, and S. Dittmaier, *Strong and electroweak corrections to the production of Higgs+2jets via weak interactions at the LHC*, Phys. Rev. Lett. **99** (2007) 161803, [arXiv:0707.0381 \[hep-ph\]](#).
- [64] M. Ciccolini, A. Denner, and S. Dittmaier, *Electroweak and QCD corrections to Higgs production via vector-boson fusion at the LHC*, Phys. Rev. **D 77** (2008) 013002, [arXiv:0710.4749 \[hep-ph\]](#).
- [65] K. Arnold et al., *VBFNLO: A parton level Monte Carlo for processes with electroweak bosons*, Comput. Phys. Commun. **180** (2009) 1661–1670, [arXiv:0811.4559 \[hep-ph\]](#).
- [66] P. Bolzoni, F. Maltoni, S.-O. Moch, and M. Zaro, *Higgs production via vector-boson fusion at NNLO in QCD*, Phys. Rev. Lett. **105** (2010) 011801, [arXiv:1003.4451 \[hep-ph\]](#).
- [67] T. Han and S. Willenbrock, *QCD correction to the $p p \rightarrow W H$ and $Z H$ total cross-sections*, Phys. Lett. **B 273** (1991) 167–172.
- [68] O. Brein, A. Djouadi, and R. Harlander, *NNLO QCD corrections to the Higgs-strahlung processes at hadron colliders*, Phys. Lett. **B 579** (2004) 149–156, [arXiv:hep-ph/0307206](#).
- [69] M. L. Ciccolini, S. Dittmaier, and M. Kramer, *Electroweak radiative corrections to associated WH and ZH production at hadron colliders*, Phys. Rev. **D 68** (2003) 073003, [arXiv:hep-ph/0306234](#).

- [70] A. Djouadi, J. Kalinowski, and M. Spira, *HDECAY: A program for Higgs boson decays in the standard model and its supersymmetric extension*, Comput. Phys. Commun. **108** (1998) 56–74, [arXiv:hep-ph/9704448](#).
- [71] A. Bredenstein, A. Denner, S. Dittmaier, and M. M. Weber, *Precise predictions for the Higgs-boson decay $H \rightarrow WW/ZZ \rightarrow 4\text{leptons}$* , Phys. Rev. D **74** (2006) 013004, [arXiv:hep-ph/0604011](#).
- [72] A. Bredenstein, A. Denner, S. Dittmaier, and M. M. Weber, *Radiative corrections to the semileptonic and hadronic Higgs-boson decays $H \rightarrow WW/ZZ \rightarrow 4\text{ fermions}$* , JHEP **02** (2007) 080, [arXiv:hep-ph/0611234](#).
- [73] T. Melia, P. Nason, R. Rontsch, and G. Zanderighi, *W^+W^- , WZ and ZZ production in the POWHEG BOX*, JHEP **1111** (2011) 078, [arXiv:1107.5051 \[hep-ph\]](#).
- [74] T. Binoth, N. Kauer, and P. Mertsch, *Gluon-induced QCD corrections to $pp \rightarrow ZZ \rightarrow \ell\bar{\ell}\ell'\bar{\ell}'$* , [arXiv:0807.0024 \[hep-ph\]](#).
- [75] J. M. Campbell and R. K. Ellis, *An update on vector boson pair production at hadron colliders*, Phys. Rev. D **60** (1999) 113006, [arXiv:hep-ph/9905386](#).
- [76] J. M. Campbell, R. K. Ellis, and C. Williams, *Vector boson pair production at the LHC*, JHEP **07** (2011) 018, [arXiv:1105.0020 \[hep-ph\]](#).
- [77] M. L. Mangano et al., *ALPGEN, a generator for hard multiparton processes in hadronic collisions*, JHEP **07** (2003) 001, [arXiv:hep-ph/0206293](#).
- [78] M. L. Mangano, M. Moretti, F. Piccinini, and M. Treccani, *Matching matrix elements and shower evolution for top-quark production in hadronic collisions*, JHEP **01** (2007) 013, [arXiv:hep-ph/0611129 \[hep-ph\]](#).
- [79] K. Melnikov and F. Petriello, *Electroweak gauge boson production at hadron colliders through $O(\alpha_s^2)$* , Phys. Rev. D **74** (2006) 114017, [arXiv:hep-ph/0609070](#).
- [80] C. Anastasiou, L. J. Dixon, K. Melnikov, and F. Petriello, *High precision QCD at hadron colliders: Electroweak gauge boson rapidity distributions at NNLO*, Phys.Rev. D **69** (2004) 094008, [arXiv:hep-ph/0312266 \[hep-ph\]](#).
- [81] S. Frixione, P. Nason, and B. R. Webber, *Matching NLO QCD and parton showers in heavy flavour production*, JHEP **08** (2003) 007, [arXiv:hep-ph/0305252](#).
- [82] M. Aliev et al., *HATHOR: HAdronic Top and Heavy quarks crOss section calculatoR*, Comput. Phys. Commun. **182** (2011) 1034, [arXiv:1007.1327 \[hep-ph\]](#).

- [83] G. Corcella et al., *HERWIG 6: an event generator for hadron emission reactions with interfering gluons (including super-symmetric processes)* , JHEP **01** (2001) 010.
- [84] J. M. Butterworth, J. R. Forshaw, and M. H. Seymour, *Multiparton interactions in photoproduction at HERA*, Z. Phys. **C 72** (1996) 637–646, [arXiv:hep-ph/9601371](#).
- [85] ATLAS Collaboration, *Electron performance measurements with the ATLAS detector using the 2010 LHC proton-proton collision data*, 2011. ATLAS-COM-PHYS-2011-546.
- [86] ATLAS Collaboration, *Electron performance measurements with the ATLAS detector using the 2010 LHC proton-proton collision data*, [arXiv:1110.3174 \[hep-ex\]](#). submitted to Eur. Phys. J. C.
- [87] ATLAS Collaboration, *Luminosity Determination in pp Collisions at $\sqrt{s} = 7$ TeV Using the ATLAS Detector at the LHC*, Eur. Phys. J. **C 71** (2011) 1630, [arXiv:1101.2185 \[hep-ex\]](#).
- [88] ATLAS Collaboration, *Luminosity Determination in pp Collisions at $\sqrt{s} = 7$ TeV using the ATLAS Detector in 2011*, ATLAS-CONF-2011-116 <http://cdsweb.cern.ch/record/1376384>.
- [89] A. L. Read, *Presentation of search results: The $CL(s)$ technique*, J. Phys. G **28** (2002) 2693–2704.
- [90] G. Cowan, K. Cranmer, E. Gross, and O. Vitells, *Asymptotic formulae for likelihood-based tests of new physics*, Eur. Phys. J. **C 71** (2011) 1554, [arXiv:1007.1727 \[physics.data-an\]](#).
- [91] E. Gross and O. Vitells, *Trial factors for the look elsewhere effect in high energy physics*, Eur. Phys. J. **C 70** (2010) 525–530, [arXiv:1005.1891 \[physics.data-an\]](#).
- [92] ATLAS and C. Collaborations, *Combined Standard Model Higgs boson searches with up to 2.3 fb^{-1} of pp collisions at $\sqrt{s} = 7 \text{ TeV}$ at the LHC*, ATLAS-CONF-2011-157 (2011) .
- [93] A. Collaboration, *Observation of a new particle in the search for the Standard Model Higgs boson with the ATLAS detector at the LHC*, Phys. Lett. B **716** (2012) 1–29.
- [94] T. A. Collaboration, *A Particle Consistent with the Higgs Boson Observed with the ATLAS Detector at the Large Hadron Collider*, Science **338** (2012) 1576–1582.

- [95] T. A. Collaboration, *Search for the Standard Model Higgs boson in the two photon decay channel with the ATLAS detector at the LHC*, Phys.Lett.B **705** (2011) 452–470.
- [96] ATLAS Collaboration, *Observation of an excess of events in the search for the Standard Model Higgs boson in the $H \rightarrow ZZ^{(*)} \rightarrow 4\ell$ channel with the ATLAS detector*, . ATLAS-CONF-2012-092.
- [97] ATLAS Collaboration, *Search for a Standard Model Higgs boson in the $H \rightarrow ZZ \rightarrow ll\nu\nu$ decay channel using 4.7 fb^{-1} of $\sqrt{s} = 7 \text{ TeV}$ data with the ATLAS detector*, .
- [98] ATLAS Collaboration, *Search for a Standard Model Higgs boson in the mass range 200-600 GeV in the $H \rightarrow ZZ \rightarrow llqq$ decay channel*, .
- [99] ATLAS Collaboration, *Observation of an excess of events in the search for the Standard Model Higgs boson in the gamma-gamma channel with the ATLAS detector*, . ATLAS-CONF-2012-091.
- [100] ATLAS Collaboration, *Search for the Standard Model Higgs boson in the $H \rightarrow WW^{(*)} \rightarrow \ell\nu\ell\nu$ decay mode with 4.7 fb^{-1} of ATLAS data at $\sqrt{s} = 7 \text{ TeV}$* , . Phys. Lett. **B 716**.
- [101] ATLAS Collaboration, *Search for the Higgs boson in the $H \rightarrow WW \rightarrow \ell\nu jj$ decay channel at $\sqrt{s} = 7 \text{ TeV}$ with the ATLAS detector*, .
- [102] ATLAS Collaboration, *Search for the Standard Model Higgs boson in the $H \rightarrow \tau^+\tau^-$ decay mode in $\sqrt{s} = 7 \text{ TeV}$ pp collisions with ATLAS*, .
- [103] ATLAS Collaboration, *Search for the Standard Model Higgs boson produced in association with a vector boson and decaying to a b-quark pair with the ATLAS detector*, .
- [104] ATLAS Collaboration, *Observation of an Excess of Events in the Search for the Standard Model Higgs Boson in the $H \rightarrow WW^{(*)} \rightarrow \ell\nu\ell\nu$ Channel with the ATLAS Detector*, . ATLAS-CONF-2012-098.
- [105] C. Collaboration, *Observation of a new boson at a mass of 125 GeV with the CMS experiment at the LHC*, Phys. Lett. B **716** (2012) 30–61.
- [106] W. Lampl et al., *Calorimeter Clustering Algorithms: Description and Performance*, ATLAS note ATL-LARG-PUB-2008-002, CERN, 2008.
- [107] M. Cacciari, G. P. Salam, and G. Soyez, *Anti-KT jet clustering Algorithm*, JHEP **04** (2008) 063.

- [108] ATLAS, *Properties of Jets and Inputs to Jet Reconstruction and Calibration with the ATLAS Detector Using Proton-Proton Collisions at $\sqrt{s} = 7$ TeV*, Tech. Rep. ATLAS-CONF-2010-053, CERN, Geneva, Jul, 2010.
- [109] ATLAS, *ATLAS jet energy scale uncertainties using tracks in proton proton collisions at $\sqrt{s} = 7$ TeV*, Tech. Rep. ATLAS-CONF-2011-067, CERN, Geneva, May, 2011.
- [110] ATLAS Jet/EtMiss Combined Performance Group,
<https://twiki.cern.ch/twiki/bin/viewauth/AtlasProtected/ApplyJetCalibration2012>.
- [111] ATLAS Jet/EtMiss Combined Performance Group, *How to clean jets*, <https://twiki.cern.ch/twiki/bin/view/AtlasProtected/HowToCleanJets2012>.
- [112] ATLAS Collaboration, *Updated results and measurements of properties of the new Higgs-like particle in the four lepton decay channel with the ATLAS detector*, ATLAS-CONF-2012-169 (2012) .
- [113] S. Bolognesi, *et al.*, *On the spin and parity of a single-produced resonance at the LHC*, Phys. Rev. **D86** (2012) 21.

Acknowledgements

This documentation is a summary of the three years work of my thesis in CEA Saclay, yet what has not been written is what a special time I had during these three years. I'd like to give the most sincere thanks to my supervisor Samira Hassani, who supported me all through my thesis, who taught me so many things, not only the knowledge of physics, detectors, but also the spirit of being a serious, responsible physicist. I'm really grateful for your thoughtful caring for my life and your great efforts for my future. You certainly have shown me how wonderful a supervisor could be. I feel very lucky that I have worked with you. I wish you all the best, and considering all the troubles I made in the past, I hope you can have a pleasant and peaceful time in the future. I would like to also thank Claude Guyot for accepting to be my supervisor, who helped me a lot during the three years, and gave advices on the work and the thesis.

Thanks to all the members of the committee for accepting this work, who read my thesis and gave valuable opinions. Special thanks to Ketevi Assamagan, who as my rapporteur, read my thesis in detail and provided useful comments, as a colleague, taught me from the beginning about physics analysis, and as a friend, helped a lot on my personal life. Thanks to Yves Sirois, my rapporteur, for the detailed reading of my thesis, and all the new perspectives you gave; to Djouadi Abdelhak, for your very intriguing comment on the analysis work as a theorist; to Ludovico Pontecorvo, for your discussion on the performance work and the knowledge that you taught me; to Philippe Bloch to chair my defense and the useful comments you gave.

Thanks very much to the Service de Physique des Particules for giving me the opportunity to complete my Ph.D in CEA Saclay, special thanks to Ursula Bassler, Didier Vilanova. The ATLAS group in Saclay is extremely friendly and helpful, Ahmimed and Pierre-Francois, Laurent, I can't remember how many times I bothered you to discuss about work, thank you all for all the helps that you offer. Thanks to Jean-Francois, for introducing me all the fantastic things about muon, the painful Athena framework, all your interesting explanation. Thanks to Florian for your patience when we worked on the tomography, and thanks to Andrea for passing by my office and saying Ciao each time! Thanks to Vanina for your company at Saclay, and Pillepe (Schune) when I occupied your office for a month. Thank you Rosy, it's a real pleasure to work and share an office with you in CERN, and I appreciate a lot for your warm care. Thank you Philippe (Schwem-

ling) for your advice on the defense and for sign my paper on your holiday time. The great thanks to Jean, who corrected my thesis with extraordinary dedication. Thank you very much for the great amount of time you devoted, for your concern of my defense and my life. Thanks to Traudl, for your correction and the guidance of the manuscript. Thanks for coming to my office every time, explaining the mistakes I made in writing. Of course, I'd like to thank all the "girls of Samira", Camilla, Dimitra, Joany and Sofia, you are so nice! I had a great time with you and I'm so glad to have your companies. And yes, I need to give special thanks to Joany and Sofia, for "feeding" me during the summer school. Also, thanks to Henso and Homero, for your hospitality and help. It was fun to have you all! Thanks to Joany and Heberth for all the helps on administration.

Thanks to Christos, for your ideas and helps on the work, I learnt a lot during all the discussion we had. It's very interesting to work with you. Thanks to Kostas, for helping when I started in the group, for the trust and support you gave, for all the discussion on the analysis. I'm glad that we worked together and really happy to be part of the discovery with you guys. Thanks to Stathes, it is a pleasant collaboration with you, and I liked your smart ideas a lot. Thanks to Eleni too, for sharing your experience with me, and thank you for all the encouragement. Special thanks to Xiangyang, for encouraging me joining this wonderful group, and for all your help.

To my parents, though very far away in China, who support me all the time. To Wang Mi, for all the fun time we had, and for your sweet support, hope you can have a wonderful defend coming soon. My great great thanks to Banban, thank you so much for everything! Also thanks to the friends who are not in France now, Yu Jie, Xu Chao, Eve, and Van for taking care of me when I first came to Saclay. Thanks to all the "Chinese Mafia" here, who made my three years so memorable. Finally, thanks to my dearest friends, Lu Qing, Wu Tingting, Wu Xian, life will be so different without you!